Additive Manufacturing of Graphene Nanoplatelets and Hexagonal Boron Nitride Composites via Stereolithography

A Thesis Submitted to

The University of Manchester

For the degree of

Doctor of Philosophy

In the Faculty of Science and Engineering

2019

Kirstie R. Ryan

School of Natural Sciences

Department of Materials

Contents

1 Introduction **17**
1.1 Research Aims and Objectives 18
1.2 Organisation of Thesis 19
1.3 References 20
2 Literature Review **21**
2.1 Introduction 22
2.2 Properties and Applications of 2D Materials 22
2.2.1 Production Methods of 2D Materials 24
2.3 Properties of GNP and BN Polymer Composites 28
2.3.1 GNP and BN Hybrids 30
2.4 Additive Manufacturing Technologies 32
2.4.1 History of Additive Manufacturing 32
2.4.2 AM Process 33
2.4.3 Ink-Jet Printing 35
2.4.4 Selective Laser Sintering 36
2.3.5 Direct-Ink Writing 38
2.4.6 Fuse Deposition Modelling 39
2.4.7 Stereolithography (SLA) 40
2.5 Ink Design 49
2.5.1 Rheological Properties of Inks 50
2.5.2 Ink Dispersions 53
2.6 Applications and Properties of 3D Printed 2D Material-based Polymer Composites 54
2.6.1 3D Printed Graphene and BN-based Composites 55
2.6.2 Stereolithographic Printed Graphene and BN-based Composites 56
2.7 Conclusion 58
2.8 References 60
3 Materials and Method **72**
3.1 2D Material Synthesis 73
3.2 UV-Curable Composite Ink Formulation 73
3.4 Printing 76
3.5 Characterisations 79
3.6 References 93
4 GNP and hBN Ink Formulation for Stereolithographic Printed Parts **94**
4.1 Introduction 95
4.2 UV Ink Selection 97

4.2.1 Free Radical Polymerisation Reaction: 98
4.3 Characterisation of GNP and hBN Nanoplatelets 99
4.4 Compatibility of GNP and hBN with PEGDA 100
4.5 Rheology of Inks 102
4.6 Scattering Effects of Printing GNP and hBN-based Inks using the Window Panes Test 109
4.6.1 Concentration Dependence of 2D Material-based Inks 112
4.6.2 Dose Dependence (E0) of 2D Material-based Inks 114
4.6.3 Particle Size Dependence of 2D Material-based Inks 115
4.7 General Discussion 120
4.8 References 123
5 Properties of 3D Printed GNP and hBN-based Composites 125
5.1 Introduction 126
5.2 Adjusting the 3D Printability of Composites 127
5.2.1 Support Generation 128
5.2.2 Print Speeds & Raster Pattern 129
5.2.3 Resolution 130
5.2.4 Examples of Printed Parts 133
5.3 Properties of 2D-Material Printed Composites 135
5.3.1 Thermomechanical and Spectroscopic Analysis 135
5.3.2 Mechanical Properties 137
5.3.3 Electrical Properties 142
5.3.4 Thermal Properties 143
5.4 General Discussion 148
5.5 References 153
6 Hybrid SLA Inks for Thermal Management Applications 159
6.1 Introduction 160
6.2 Printing of Hybrids 161
6.2.1 Hybrid Selection 161
6.2.2 Rheology 162
6.2.3 Window Panes 163
6.3 Properties of Hybrids 165
6.3.1 Surface Morphology of Hybrids 167
6.3.2 Mechanical Properties of Hybrids 168
6.3.3 Electrical and Thermal Properties of Hybrids 170
6.4 Heat Sinks 173

6.4.1 Heat Sink Design 176
6.5 General Discussion 177
6.5.1 Printability of Hybrids 178
6.5.2 Properties of Hybrid Composites 178
6.5.3 Hybrids for Thermal Management Applications 179
6.6 References 181
7 Conclusion 185
7.1 References 187
8 Suggestion for Future Works 188
8.1 References 190
9 Appendix 191
9.1 Particle Sizing Data 192
9.2 Herschel-Bulkley Fitting of Composite Inks 193
9.3 Optimum Printing Parameters from the '*Window Panes'* Test 195
9.4 Thermal Properties of BN and GNP Composites 197
9.5 Properties of Hybrid Composites 201
9.6 References 204

List of Figures

Figure 1 Family of 2D Materials including transition metal dichalcogenides, hexagonal boron nitride, MXenes etc. [3] 23
Figure 2 Structure of (a) graphene and (b) h-BN.[27] 23
Figure 3 schematic showing a simple diagram of the quality of flakes produced against price for mass production, for different exfoliation methods.[20] 25
Figure 4 Exfoliation methods showing (a) ion intercalation, (B) ion exchange and (c) sonication.[2] 26
Figure 5 Representative image of (a) SEM image of hBN nanoplatelets. (b) SEM image of hBN nanoplatelets after exfoliation. (c) AFM image of BN nanoplatelets (d) height profiles from AFM data indicating the thickness of the flakes. [27] 28
Figure 6 Schematic of Owais et al. preparation of functionalised GNP-BN short carbon fibre-epoxy composites. [60] 31
Figure 7 Schematic representation of GNP-hBN hybrid, blue disks represent GNP red spheres represent hBN.[57] 32
Figure 8 Pictograph of additive manufacturing technologies. [157] 33
Figure 9 Additive manufacturing process. 34
Figure 10 Diagram of the working principle of ink-jet printing. [158] 36
Figure 11 Images of printed parts using Ink-jet printing. (a) Copper ink printed electrodes and solar cells.[159] (b) Ink-jet printed microfluidic device. [160] 36
Figure 12 Diagram of SLS process. [73] 37
Figure 13 Images of SLS printed parts. [161], [70] 37
Figure 14 Schematic of robocasting [77] 38
Figure 15 Photograph showing a 3D printed functional light emitting diode array made out of silver-thermoplastic polyurethane (Ag TPU) fabricated using DIW. [162] 39
Figure 16 Examples of FDM printed parts[164] [84] [165] [166] 40
Figure 17 Schematic of the working principles of FDM.[163] 40
Figure 18 Schematic of working principle of 'vat' polymerisation Stereolithography. 41
Figure 19 Parabolic cross section of UV laser produced on resin surface. 42
Figure 20 Electromagnetic spectrum[167] 44
Figure 21 Schematic of photo-polymerisation. 46
Figure 22 Chemical structure representing an acrylate functionality and acrylate radical. [102] 46
Figure 23 Chemical structure of BAPO. 47
Figure 24 Chemical structure of Igacure 2959. 47
Figure 25 Chemical structure of Irgacure 184. 47
Figure 26 Chemical structure of PEGDA. 48
Figure 27 Example of SLA printed parts.[168][118][117] 48
Figure 28 Diagram of filler agglomerates forming in a resin. [133] 54
Figure 29 3D-printed graphene structures using DIW. Images showing filament pile (d) and woodpile structures (e) printed through a 150 μm nozzle with a highly concentrated GO/BCS ink (2.5 wt.% GO)[81] 55
Figure 30 (a) Process of producing graphene-based inks for bioelectronics applications.[150] (b) 3D printed lumbor spine replica and double helix (60 vol. % hBN).[148] (c) Ink-jet printed graphene and BN transistors. [147] (d) FDM printed graphene electrodes for energy storage applications. [149] 56
Figure 31 Photograph and SEM image of GO scaffolds made by stereolithography.[153] 57
Figure 32 Stereolithography printed polymer and GO reinforced polymer (0.5 wt.%)[154] 57
Figure 33 (A) Tensile strength comparison of GO nanocomposite printed using SLA and casted. (B) GO printed composite. [155] 58
Figure 34 BNNP SLA printed scaffolds. (b) 0 wt. %, (c) 1 wt. %, (d) 5 wt. %.[156] 58
Figure 35 Speed mixing results of GNP and UV curable ink.(Left image) Results from mixing a small amount of PEGDA with GNP flakes to produce a course paste, (right image) Smooth resin after the rest of the UV has been added to the paste. 75

Figure 36 Schematic of printed window panes showing a series of 5 panes Cd1 representing the thinnest pane to Cd5 the thickest pane 77
Figure 37 Graph showing a typical representation of the working curve from the window panes test. The measured cure depth (C_d) is plotted against the exposure energy (E_0) on an ln scale. The gradient of the curve provides the D_p value, how far the laser can penetrate through the resin where the intensity of the laser reaches 1/e of its original value. The x-intercept is the E_c value were below this exposure energy curing will not occur. 77
Figure 38 Schematic showing the working set-up of SEM (above), schematic showing the interaction of the incident electron beam with the sample and the associated characteristic interactions used to create the SEM image (below).[8] 80
Figure 39 Schematic showing the working principles of AFM. 81
Figure 40 Schematic showing the principle workings of an FTIR spectrometer. 82
Figure 41 Schematic representing the main three types of rotational techniques: (a) concentric cylinder (b) torsion using cone geometry (c) torsion using parallel plates. 83
Figure 42 Discovery DH-3 Rheometer by TA Systems. 84
Figure 43 Spectrum of electromagnetic radiation. 85
Figure 44 DSC thermogram showing the transitions of a typical thermoplastic in relation to temperature changes. 86
Figure 45 Schematic of working principle of the laser flash technique (above). Representation of a typical graph produced from laser flash technique (below). [15] 88
Figure 46 Setup for thermal imaging of heat sinks on rGO aerogel. 89
Figure 47 Photograph of typical set up for tensile tests. 90
Figure 48 Photograph of typical set up of 3-point bend test. 91
Figure 49 (a) Schematic of 2-point probe electrical resistivity measurement set-up. (b) Photograph of measurement set up using 3D printed BN part. 92
Figure 50 Overview of factors relating to SLA printing. The highlighted region will be explored and discussed in this chapter. 96
Figure 51 The effect of using different photoinitiators to cure PEGDA 575. Starting printing parameters: Ec: 12 mJ/ cm^2, Dp: 3.7 mm. 98
Figure 52 Mechanism of free-radical polymerisation of PEGDA and BAPO, hv represents the photon from the UV light. [17] 99
Figure 53 Typical SEM images of the lateral flake size distribution of (a) BN, (b) GNP and (c) eBN.n=100 100
Figure 54 Sedimentation results of BN (top) and GNP (bottom) in PEGDA at 0, 4, 8 and 36 hours .101
Figure 55 Normalised UV-Vis spectrum of UV ink PEGDA, BN: PEGDA (1 wt. %) and GNP: PEGDA (1 wt. %), full UV-vis spectra (left) zoomed in image (right). 101
Figure 56 Effects of filler volume fraction on the viscosity of (a) BN-based inks and (b) GNP-based inks. The numbers next to GNP and BN represent the weight percentage of the platelets in the PEGDA inks, e.g. BN 2= 2 wt. % BN and 98 wt. % of PEGDA. 103
Figure 57 Effect of particle size dependency on the viscosity of BN-based inks. 104
Figure 58 Oscillation amplitude ramp of (a) BN 8 (b) BN 20 and (c) GNP 8. 105
Figure 59 Difference in the shear thinning parameter n with varying BN and GNP concentrations. .106
Figure 60 Yield stress as a function of concentration of (a) BN and (b) GNP particles, derived from Herschel-Bulkley. Difference in reference viscosity K, with (c) BN and (d) GNP. 107
Figure 61 Comparison of models to find $\tau\gamma$ with increasing volume % of (a) BN particles and (b) GNP particles. 109
Figure 62 (a) Images of printed window pane labelled GNP and hBN. (b) Example of plotted window panes graph to find the E_c and D_p values for composite inks. (c) Cure depth as a function of concentration with increasing E_0 for BN-based inks and (d) GNP-based inks. Initial set parameters were E_c: 12 mJ/cm^2 and D_p: 3.7 mm. 112
Figure 63 Cure depth vs inverse volume fraction for GNP concentrations at 980 mJ /cm^2 and λ=365 nm. Initial printing parameters: E_c: 12 mJ/cm^2 and D_p: 3.7 mm. 113
Figure 64 Cure depth vs inverse volume fraction for BN concentrations at E_0 980mJ /cm^2 and λ= 365 nm. Initial printing parameters: E_c: 12 mJ/cm^2 and D_p: 3.7 mm. 114

Figure 65 Cure depth of BN 4 wt. % and GNP 4 wt. %. Initial printing parameters: E_c: 12 mJ/cm^2 and D_p: 3.7 mm. 115
Figure 66 Cure depth of BN 20 and eBN 20 inks. Initial printing parameters: E_c: 30 mJ/cm^2 and D_p: 4.2 mm. 116
Figure 67 Scematic of curing between individual layers during the SLA printing process.(adapted from Formlabs) [4] 127
Figure 68 (a) Example of point supports for flexure-test samples BN 1, and (b) slippage between layers of GNP 1 tensile test specimen. 128
Figure 69 Photographs of the outcomes of changing the raster pattern of the SLA laser using 1 wt. % GNP ink. 130
Figure 70 Optical microscope image of 3D printed layers of UV ink. 130
Figure 71 Theoretical width of cure of UV ink when the E_c=12 mJ/cm^2 (set parameters for all GNP-based inks and BN-based inks below 8 wt. %) and E_c=30 mJ/cm^2 (set parameters for BN 20 wt. % inks). 132
Figure 72 3D printed GNP-based composites 1 wt. %. 133
Figure 73 3D printed BN-based composites 20 wt. %. 134
Figure 74 (a) Tg results of printed composites with varying concentrations of GNP and BN. (b) Example of DSC results of BN 20 wt. % and 4 wt. % displaying 2rd heating curve. 136
Figure 75 FTIR of UV polymer, BN-based composite and GNP-based composite. 136
Figure 76 TGA data of (a) BN -based polymer composites and (b) GNP-based composites, showing the loss in mass as a percentage with increasing temperature. 137
Figure 77 Three-point bend results of (a) BN and (b) GNP printed composites via SLA. 138
Figure 78 Example of stress stress/strain curves of printed composites (a). Tensile test results of (b) BN (c) GNP printed composites via SLA. 140
Figure 79 SEM micrographs of the flexural fracture surface of 3D printed composites with 2, 8 and 20 wt. % BN (top, middle and bottom images, respectively). Arrows indicate agglomerates for BN 2, pull-out for BN 8 and flakes for BN 20. 141
Figure 80 SEM micrographs of the flexural fracture surface of 3D printed composites with 1, 0.25 wt. % GNP (top and bottom images, respectively). Arrows indicate agglomerates for GNP 0.25, flakes for GNP 1. 142
Figure 81 (a) Electrical conductivity as a function of filler volume of BN and GNP. (b) Typical current/voltage graph from two-point probe tests for GNP 1 wt.% and GNP 2 wt.%. 143
Figure 82 SEM image of BN 20 the arrows highlighting the random orientation of flakes within the polymer matrix (left). Measured thermal conductivity of BN composites (right). 144
Figure 83 Thermal conductivity of BN 20 and eBN 20 (left). Thermal conductivity of GNP-based composites (right). 145
Figure 84 Thermal enhancement factor (%) of BN and GNP-based composites compared to UV polymer (calculations based on thermal conductivity measured at 90 °C). 145
Figure 85 Thermal conductivity as a function of volume fraction of nanoplatelets, measured at 90 °C. 146
Figure 86 Results of the thermal conductivities of BN composites, black line represents the experimental values obtained, the blue and red lines represent the fitting of Agari's equation and Maxwell-Eucken to the experimental values. 148
Figure 87 Comparison of thermal conductivities of BN-based polymer composites including ABS (35 wt. %)[55], Poly (imide) (30 wt. %)[56], Elax^{TM} 260 (20 wt. %)[57] , Epoxy TMBPDGE-DDM (50 wt.%)[58], TPU (50 wt.%)[59] , PEGDA (20 wt. %)(this work), CNF (cellulose Nano-fibre functionalised BN (30 wt. %))[60], PDMS (15 wt. %)[61], Polyimide (10 wt. %)[62], PVA (20 wt. %)[63], Epoxy (20 wt. %)[64]. 150
Figure 88 Comparison of thermal conductivities of GNP-based polymer composites including PEGDA (4 wt. %) (This work), PDMS: graphene foam (0.7 wt. %)[65], Silicon Rubber (16 wt. %)[66], PLA (6 wt. %)[67], PC (20 wt.%)[35], PE (10 wt. %)[68], Cyclic butylene terephthalate (CBT) (20 wt. %)[69], Epoxy (5 wt. %)[70], PA12 (2 wt. %)[71], Epoxy (1 wt. %)[72]. 151
Figure 89 Representation of hybrid BN and µGNP flakes within the UV polymer ink. 162
Figure 90 Rheological flow data of Hybrids. 163

Figure 91 Cure depths from 'Window panes' test of hybrid 1, 7 and BN 20. 164
Figure 92 Example of printed part using hybrid 7 ink. 165
Figure 93 SEM image of printed layers of (a) hybrid 1 and (b) hybrid 7. The blue arrows point towards the voids between the layers. 165
Figure 94 TGA data of hybrid composites, showing the loss in mass as a percentage with increasing temperature. 166
Figure 95 FTIR showing the infrared spectrum of Hybrids 1, 7 and the UV polymer. 167
Figure 96(a) Fracture surface of hybrid 7 the white regions pointed with blue arrows represents the BN flakes. (b) Fracture surface of hybrid 1 the white regions pointed with blue arrows represents the BN flakes. 168
Figure 97 Tensile data of Hybrids 1, 7, composite BN 20 and the UV ink PEGDA/BAPO. 169
Figure 98 Flexure results of Hybrids 1, 7, composite BN 20 and the UV ink PEGDA/BAPO. 170
Figure 99 (a) Thermal conductivity of hybrid composites. (b) Thermal Diffusivity of hybrids. 172
Figure 100 Thermal enhancement factor of hybrid composites. Hybrid 1 (19:1, BN: eBN) Hybrid 7 (19.8:0.2, BN: eGNP) and BN 20 (20 wt.% BN) 172
Figure 101 Photograph of composite heat sinks, from left to right GNP 1, H 1 and H7. The heat design shown here is the plate fin array consisting of 10 fins in total. 173
Figure 102 Schematic of the heat flow through the heat sink as a result of joule heating of the rGO aerogel 174
Figure 103 Temperature profiles of different composite heat sinks. 175
Figure 104 IR camera images of Hybrid 1and Hybrid 7 heat sinks 175
Figure 105 (a) Heat sink designs of hybrid 1 composite with rGO aerogel joule heater providing homogeneous source of heat to the sinks (b) temperature profile of the different designs of heat sinks displaying heat dissipation over time, (c) IR images of the heat dissipation of different designs of heat sinks printed using Hybrid 1. 177
Figure 106 Representative AFM data for GNP nanoplatelets n=14. 192
Figure 107 Representative AFM data for BN nanoplatelets n=12. 192
Figure 108 Herschel–Bulkley fitting of all BN-based inks, raw data from flow sweeps. 193
Figure 109 Herschel–Bulkley fitting of PEGDA and GNP-based inks, raw data from flow sweeps. 194
Figure 110 Thermal diffusivity of BN-based inks measured from 30°C to 150 °C. 197
Figure 111 Thermal diffusivity of GNP-based inks measured from 30°C to 150 °C. 198
Figure 112 Coefficient of thermal expansion of composites. 198
Figure 113 Agari's equation applied to the thermal conductivity of BN composites to find the C_1 and C_2 values. 200
Figure 114 SEM image of eGNP nanoplatelets 201
Figure 115 Working curve of all iterations of hybrids from the window panes test. 201
Figure 116 TGA results showing change in mass over temperature of all hybrid compositions. 202
Figure 117 Glass transition temperature of hybrid composites. 202
Figure 118 CT data of Hybrid 1. The white areas represent the BN flakes dispersed within the polymer matrix (black areas) scale bar is 5 mm. 203
Figure 119 CT data of Hybrid 1, the blue circles highlight the voids within the sample. The white areas represent the BN flakes dispersed within the polymer matrix (black areas). 203
Figure 120 Joule heating of rGO Aerogel 204
Figure 121 Joule heating of rGO Aerogel 204
Figure 124 Image of 3D printed BN polar bear on rGO aerogel showing the difference in temperature gradients.40.5 °C. 204
Figure 123 Image of 3D printed BN polar bear on rGO aerogel showing the difference in temperature gradients. 204
Figure 124 Image of 3D printed BN polar bear on rGO aerogel showing the difference in temperature gradients. 204

List of Tables

Table 1 Thermal conductivities of GNP and BN polymer composites. 29
Table 2 Reported electrical conductivities of GNP polymer composites. 30
Table 3 Summary of Additive manufacturing techniques. [119] 49
Table 4 Concentration of 2D materials in PEGDA resin used to describe the naming of the composites. 74
Table 5 Properties of Photoinitiators. 97
Table 6 Mean average data of size distributions of GNP, BN and eBN flakes from SEM. 100
Table 7 Comparison of models to find $\tau\gamma$ for BN inks. 108
Table 8 Comparison of models to find $\tau\gamma$ for GNP inks. 108
Table 9 General properties of UV inks and filler materials that effect scattering behaviours. 110
Table 10 Calculated Q values for BN 2 wt. %. 118
Table 11 Calculated Q values for GNP 2 wt. %. 118
Table 12 Calculated Q values for BN 8 and GNP 8 inks. 119
Table 13 Calculated Q values for BN 20 and eBN 20 inks. 119
Table 14 Adjustments of parameters in structural supports of SLA printed parts. 128
Table 15 Dimensional results from changing raster pattern of the SLA laser. 129
Table 16 Measured resolution of 3D printed composites. 131
Table 17 Weight retention of composites from TGA data. 137
Table 18 Thermal conductivity components of composites measured at 90 °C, were ρ (g/cm^3) is the density of the composite, C_p (T) (J/g °C) is the specific heat capacity, a (T) is the thermal diffusivity (mm/cm^2) and λ (T) is the thermal conductivity (W.m^{-1}.K^{-1}) (see appendix for full range of values). 146
Table 19 Varying ratios of hybrids containing bulk BN, eBN and eGNP. 161
Table 20 T_g results of composites BN 20 and Hybrids1 and 7. 167
Table 21 Intrinsic properties of polymer matrix and fillers. 170
Table 22 Thermal and electrical properties of hybrid composites. Were ρ (g/cm^3) is the density of the composite, C_p (T) (J/g °C) is the specific heat capacity, a (T) is the thermal diffusivity (mm/cm^2) and λ (T) is the thermal conductivity (W.m^{-1}.K^{-1}). 171
Table 23 Measurements of hybrid 1 heat sinks with varying fin numbers. 177
Table 24 Particle sizing of BN and GNP flakes 192
Table 25 The calculated D_p and E_c values from the Window Panes test results, derived from Beer-Lamberts equation. 195
Table 26 Glass transition temperatures (°C) of all composites containing GNP and BN. 200

List of Equations

(1) 42
(2) 43
(3) 50
(4) 50
(5) 51
(6) 52
(7) 52
(8) 52
(9) 53
(10) 53
(11) 53
(12) 77
(13) 102
(14) 106
(15) 111
(16) 111
(17) 117
(18) 117
(19) 117
(20) 117
(21) 118
(22) 118
(23) 131
(24) 147
(25) 147
(26) 195
(27) 196
(28) 196
(29) 196
(30) 196
(31) 196
(32) 196
(33) 197

Word count: 51054

List of Abbreviations

°C	Degrees Celsius
µm	Micrometre
2D	Two-dimensional
3D	Three-dimensional
ABS	Acrylonitrile butadiene styrene
AFM	Atomic Force Microscopy
AM	Additive Manufacturing
ASTM	American standards and Testing
BAPO	Phenylbis (2,4,6-trimethylbenzoyl)phosphine oxide)
BNNS	Boron nitride nanosheets
CAD	Computer-aided Design
C_d	Cure depth
cm	Centimetre
DMA	Dynamic Mechanical Analysis
D_p	Depth of penetration
DSC	Differential scanning calorimetry
DSPC	Direct shell production casting
E’	Storage modulus
E’’	Loss modulus
E_c	Critical exposure energy
E_o	Exposure Energy
FDM	Fuse deposition Modelling
FTIR	Fourier transformation infrared spectrometer
G'	Storage modulus
G"	Loss modulus
GGO	Giant graphene oxide
GNP	Graphene Nanoplatelets
GO	Graphene oxide
hBN	Hexagonal Boron Nitride
HDPE	High density polyethylene
IPA	Isopropanol
LOM	Laminated object manufacturing
LPE	Liquid phase exfoliation
M	Mega
mm	Millimetre
MoS_2	Molybdenum disulphide
M_w	Molecular weight
Pa	Pascal
PC	Polycarbonate
PEGDA	Poly (ethylene glycol) diacrylate
PI	Photoinitiator
PLA	Polylactic acid

PP	Polypropylene
Q	Extinction coefficient efficiency term
rGO	Reduced graphene oxide
rpm	Revolutions per minute
SEM	Scanning Electron Microscopy
SGC	Solid ground curing
SLA	Stereolithography Apparatus
SLS	Selective laser sintering
STL	Stereolithography
TEM	Transition electron microscopy
T_g	Glass transition temperature
TGA	Thermogravimetric analyses
UTS	Ultimate tensile strength
UV	Ultraviolet
W_c	Width of cure
XRD	X-ray diffraction

Abstract

The ability to utilise graphene and related 2D materials within additive manufacturing sparks a promising future for developing multi-functional composites on a commercial scale. 2D materials can be exfoliated into platelets with high aspect ratios and re-dispersed within a polymer resin to produce inks suitable for 3D printing. Such inks can be combined with a photoinitiator to form photocurable inks for the use in stereolithography. This work presents the manufacture of 3D printed boron nitride (BN) and graphene nano-platelets (GNP) composites with enhanced thermal conductivities for potential uses in thermal management applications.

Key manufacturing parameters, such as the critical exposure and depth of penetration from the SLA laser are investigated to facilitate formulation and printing of 3D structures. The scattering effects of the 2D materials are explored using semi-empirical models to understand why the maximum printable solid loadings of the inks are 20 wt. % and 4 wt. % for BN and GNP respectively.

The intrinsically high thermal properties of GNP (3000 $W.m^{-1}.K^{-1}$) (XG Sciences) and BN (400 $W.m^{-1}.K^{-1}$) can be applied for thermal management in electronics to produce efficient systems with increased operating times eliminating short-circuiting from occurring. An increase in thermal conductivity of over 233 % has been observed with the addition of 20 wt. % BN (0.70 $W.m^{-1}.K^{-1}$) and 200 % for 4 wt. % GNP (0.55 $W.m^{-1}.K^{-1}$) when compared to the UV polymer (0.21 $W.m^{-1}.K^{-1}$). An increase in mechanical properties of the polymer matrix has also been observed with BN and GNP platelets acting as reinforcements.

GNP and BN can be coupled to form hybrids with synergetic capabilities for improved thermal and mechanical properties of polymers. The electrically insulating hexagonal BN platelets have been dispersed with GNP platelets to form photo-curable hybrid inks for SLA. The hybrids showed a maximum thermal enhancement of 238 % Hybrid 1 (0.71 $W.m^{-1}.K^{-1}$) compared to UV polymer (0.21 $W.m^{-1}.K^{-1}$) and an electrical resistivity of 1.81 $x10^{10}$ Ω.m. Heat sinks containing hybrid materials were 3D printed and tested for potential applications in thermal management of electronic devices by measuring the heat transfer through the printed structure over time. The hybrid heat sinks reached the set temperature 43 % faster than the control displaying improved heat transfer and heat dissipation required for heat sink applications.

Declaration

No portion of the work referred to in the thesis has been submitted in support of an application for another degree or qualification of this or any other university or other institute of learning.

Copyright Statement

i. The author of this thesis (including any appendices and/or schedules to this thesis) owns certain copyright or related rights in it (the "Copyright") and s/he has given The University of Manchester certain rights to use such Copyright, including for administrative purposes.

ii. Copies of this thesis, either in full or in extracts and whether in hard or electronic copy, may be made only in accordance with the Copyright, Designs and Patents Act 1988 (as amended) and regulations issued under it or, where appropriate, in accordance Presentation of Theses Policy You are required to submit your thesis electronically Page 11 of 25 with licensing agreements which the University has from time to time. This page must form part of any such copies made.

iii. The ownership of certain Copyright, patents, designs, trademarks and other intellectual property (the "Intellectual Property") and any reproductions of copyright works in the thesis, for example graphs and tables ("Reproductions"), which may be described in this thesis, may not be owned by the author and may be owned by third parties. Such Intellectual Property and Reproductions cannot and must not be made available for use without the prior written permission of the owner(s) of the relevant Intellectual Property and/or Reproductions.

iv. Further information on the conditions under which disclosure, publication and commercialisation of this thesis, the Copyright and any Intellectual Property and/or Reproductions described in it may take place is available in the University IP Policy (see http://documents.manchester.ac.uk/DocuInfo.aspx?DocID=2442 0), in any relevant Thesis restriction declarations deposited in the University Library, The University Library's regulations (see http://www.library.manchester.ac.uk/about/regulations/) and in The University's policy on Presentation of Theses

Acknowledgements

I am very grateful for all those who have helped and contributed to my PhD. Firstly, I would like to give thanks to EPSRC for funding this research and enabling the opportunity to present my work.

I would like to give thanks to my supervisor Dr Suelen Barg and the Nano 3D research group for all their support and advice it has been a pleasure working with you all. I would also like to thank Professor Brian Derby my co-supervisor and all of the Derby research group, for all the fruitful discussions and help throughout my PhD.

A special thank you to Mr Andy Wallwork and Dr Rachel Saunders I will be forever grateful for all your support and time you have spent helping me to reboot and fix the SLA.

I would like to give thanks to Natalie Ishmael, Jason Hui, Hui Ding, Petar Gerganov and Will Lowenhardt for your friendship and support throughout my PhD.

To Dave, Joe, Craig, Chris, Scott and Rich thank you all for your friendship making my time in Manchester unforgettable.

A special thank you to Joseph Neilson firstly for all your help and support throughout my PhD. But also all of your support outside of the PhD, this journey would have been a lot less fun without you in my life.

Finally, I would like to thank my parents Stephen Ryan and Pauline Ryan for their continued support and belief in me throughout my academic life.

1 Introduction

Additive manufacturing (AM) often referred to as 3D printing, is an advanced manufacturing technique used to build 3D objects using a layer-by-layer method. A computer-aided design (CAD) image can be used to produce complex geometries and structures that can be readily edited and printed in relatively quick processing times with minimal labour and little to no material waste. These prospects of 3D printing offer an exciting opportunity for many industries including electronics, thermal management, biomedical, fashion, automotive, aerospace to name a few.

Stereolithography (SLA) was one of the first AM techniques to be developed and still to this day produces 3D parts with high resolutions in the *z, x* and *y*-axis compared with other printing technologies on the market. Although SLA is known for printing parts with smooth surface finishes and good dimensional tolerances, the printing of functional parts is yet to be developed and refined. The addition of fillers (structural and functional) to SLA polymer resins opens up opportunities for the development of advanced composites.[1][2][3][4] However, some challenges include the dispersion of fillers within the polymer resin, high viscosities outside of the printable range and scattering effects produced by the SLA laser interacting with the filler.[5][6] There has been progress in the development of ceramic-based SLA resins, with significant developments in the maximum solid loading of these resins and their associated mechanical properties.[7] However, the domain of 2D material-based resins is yet to be explored, with only a few reports on printing with graphene oxide (GO) and BN.[3][8][9][2]

The interesting chemical and physical properties of many 2D layered materials such as graphene and hBN offer an exciting new field for 3D printing parts with excellent electrical, thermal and mechanical properties. Although there have been numerous publications on the production and characterisation of these materials there are still significant gaps in the literature on the use of 2D materials in additive manufacturing.

1.1 Research Aims and Objectives

This research is motivated by the ever-growing demand for the manufacture of multi-functional 3D printed parts. Dependent on the chemistry and composition of the material each ink can require extensive alterations for the 3D printing technology used. The research aims to develop UV curable 2D material-based composite inks for 3D printing of multi-functional parts via stereolithography. The outcomes are to establish new ways in which 2D materials can be used in advanced manufacturing techniques for the potential applications in the field of thermal management of electronics.

This research is divided up into the following objectives:

1. Synthesis of UV-curable 2D material-based resins.
2. Establish the effects that 2D materials have on the printability of the inks used in SLA, including effects on rheological properties and scattering effects of the SLA laser interacting with the filler materials during printing.
3. Consideration of maximum solid loading of 2D materials in SLA inks, and the consequence this has on the scattering of light from the printer's laser.
4. Analyse the effects of the mechanical, electrical and thermal properties of the printed composites.
5. Research on GNP and hBN hybrid composites for prospective use in thermal management applications.

1.2 Organisation of Thesis

Chapter 1: Introduction

Research background and motivation including the aims and objectives of the study.

Chapter 2: Literature Review

This chapter is divided up into further sub-sections reviewing previously published work on the synthesis, properties and applications of 2D materials, and the comparison of additive manufacturing technologies and their printed products. This chapter also identifies the gap in the development of 2D material-based inks for 3D printing technologies.

Chapter 3: Materials and Methods

This chapter is used to explain all the experimental works carried out in this research including the parameters and procedures used for Chapters 4-6.

Chapter 4: GNP and BN Ink Formulation for Stereolithographic Printed Parts

Chapter 4 presents the characterisation and analyses of the synthesised 2D material-based composite inks. Including preliminary printing results of 2D structures.

Chapter 5: Properties of 3D Printed GNP and hBN Composites

This chapter presents the challenges of printing 3D structures using stereolithography. The chemical, mechanical and physical properties are discussed and analysed against previously published work.

Chapter 6: Hybrid SLA Inks for Thermal Management Applications

Chapter 6 explores the development and printability of hybrid composites containing GNP and hBN, with focus on the thermal, mechanical and electrical properties of the hybrids. The hybrids are then tested for potential uses in thermal management applications by 3D printing heat sinks and monitoring their heat transfer over time.

Chapter 7: Conclusion

This chapter presents the general conclusions established in this research.

Chapter 8: Future Works

This chapter provides suggestions for future areas of research to continue towards.

1.3 References

[1] U. Kalsoom, A. Peristyy, P. N. Nesterenko, and B. Paull, "A 3D printable diamond polymer composite: A novel material for fabrication of low cost thermally conducting devices," *RSC Adv.*, vol. 6 pp. 38140-38147, 2016.

[2] J. Bustillos, D. Montero-Zambrano, A. Loganathan, B. Boesl, and A. Agarwal, "Stereolithography-based 3D printed photosensitive polymer/boron nitride nanoplatelets composites," *Polym. Compos.*, vol. 40, no. 1, pp. 379–388, 2019.

[3] J. Z. Manapat, J. D. Mangadlao, B. D. B. Tiu, G. C. Tritchler, and R. C. Advincula, "High-Strength Stereolithographic 3D Printed Nanocomposites: Graphene Oxide Metastability," *ACS Appl. Mater. Interfaces*, vol. 9, no. 11, pp. 10085–10093, 2017.

[4] M. Rosa, C. Barou, and V. Esposito, "Zirconia UV-curable colloids for additive manufacturing via hybrid inkjet printing-stereolithography," *Mater. Lett.*, vol. 215, pp. 214–217, 2018.

[5] M. L. Griffith and J. W. Halloran, "Scattering of ultraviolet radiation in turbid suspensions," *J. Appl. Phys.*, vol. 81, no. 6, pp. 2538–2546, 1997.

[6] C. Hinczewski, S. Corbel, and T. Chartier, "Ceramic suspensions suitable for stereolithography," *J. Eur. Ceram. Soc.*, vol. 18, no. 6, pp. 583–590, 1998.

[7] G. A. Brady and J. W. Halloran, "Stereolithography of ceramic suspensions," *Rapid Prototyp. J.*, vol. 3, no. 2, pp. 61–65, 2005.

[8] D. Lin *et al.*, "3D stereolithography printing of graphene oxide reinforced complex architectures.," *Nanotechnology*, vol. 26, no. 43, p. 434003, 2015.

[9] H. Korhonen *et al.*, "Fabrication of graphene-based 3D structures by stereolithography," *Phys. status solidi*, vol. 213, no. 4, pp. 982-985, 2015.

2

Literature Review

Additive Manufacturing of 2D Material-based Composites

2.1 Introduction

3D printing has been the motive force for many innovations within manufacturing, art, medicine and engineering. As the trend for using 2D materials emerges new complex manufactured 3D parts can be produced using functional materials with very interesting properties. This can lead to exciting new ventures in electronics, biomedical, thermal management, automotive and aerospace. The addition of 2D materials within a polymer matrix can provide a significant improvement to its properties whilst achieving good processability attained by the polymer. There are however associated challenges with printing these inks due to their tendencies to aggregate, altering the rheological properties, leading to further refinement for the intended AM technology. This review will explore the published research on the synthesis and production of 2D materials with a focus on GNP and hBN and the challenges and capabilities of additive manufacturing techniques with an emphasis on stereolithography.

2.2 Properties and Applications of 2D Materials

Awareness of two-dimensional materials has sparked great interest in recent years since graphene was first isolated using the now denoted 'scotch tape method' by professor Geim and Novoselov at the University of Manchester in 2004.[1] Graphene is a one-atom-thick crystalline material, consisting of a network of carbon atoms (Figure 2). Many other layered materials can be exfoliated similarly to graphene to produce new 2D materials that have versatile properties that could be very interesting for industrial applications. Layered materials are three-dimensional structures formed by weakly bonded atomic layers.[2] They consist of very strong chemical bonds in-plane, and weak out-of-plane bonds. These weak out-of-plane bonds are what enable the material to be exfoliated into 2D layers. Research into other layered materials has founded a group of 2D materials which include hexagonal boron nitride (hBN), layered metal oxides and layered metal hydroxides (LDHs), transition metal dichalcogenides (TMDs, e.g. MoS_2, WSe_2, TiS_2, WS_2, TaS_2 etc.).[3] In very recent years many more new 2D materials have been introduced into the 2D family (Figure 1), including MXenes, black phosphorus, silicone.[3] This class of materials has become key in material science, physics and chemistry due to their extraordinary properties and potential in a variety of applications.

The unique properties of 2D materials can be used in a variety of applications. These include sensing, electronics, catalysis energy storage and lithium-ion batteries, thermal management and lubrication for aerospace applications.[4][5]

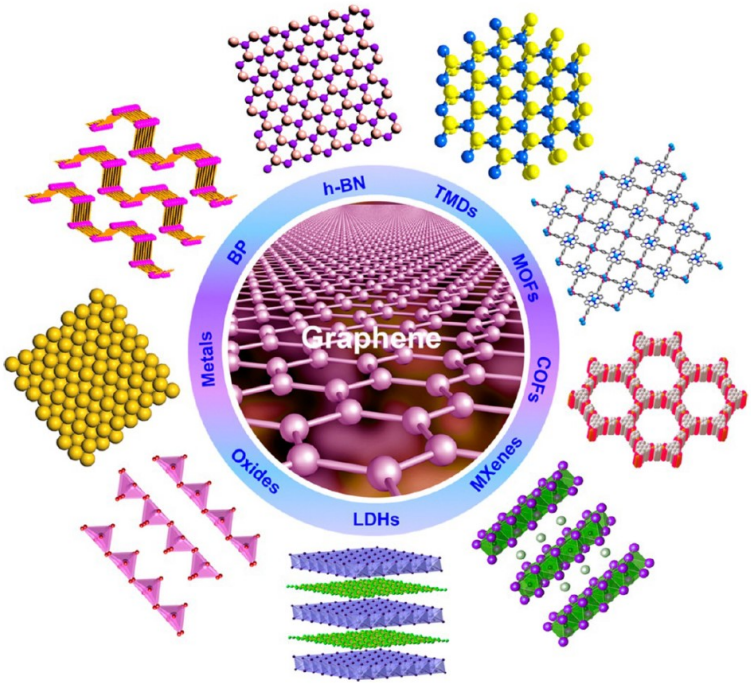

Figure 1 Family of 2D Materials including transition metal dichalcogenides, hexagonal boron nitride, MXenes etc. [3]

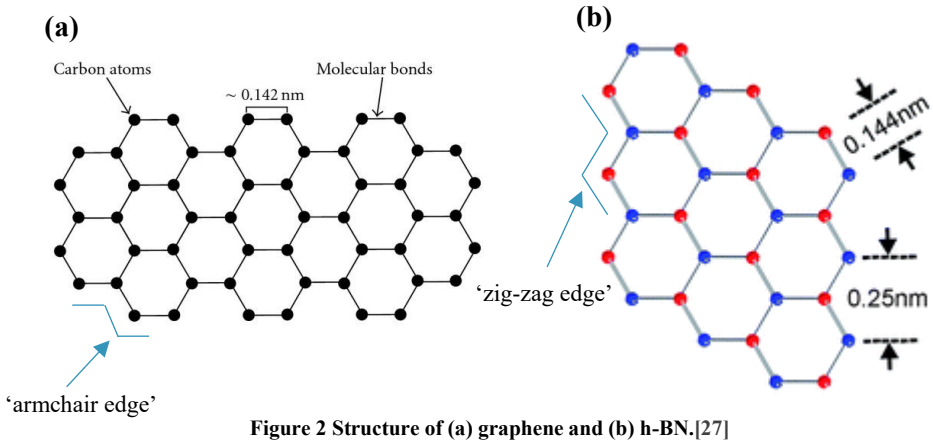

Figure 2 Structure of (a) graphene and (b) h-BN.[27]

Graphene is a flat monolayer of carbon atoms arranged in a honeycomb lattice.[6] Each carbon atom is covalently bonded to three other carbon atoms at a distance of 0.142 nm between them. Single sheets of graphene are layered on top of one another through van der Waals interactions to create 3D graphitic structures. Graphene

consists of carbon atoms that sit above the centre of the neighbouring aromatic ring known as AB stacking. The distance between the neighbouring planes is 0.335 nm. The edge sites present in monolayer graphene include armchair and zigzag (Figure 2).

Hexagonal boron nitride is known as 'white graphene' it is an III-V compound. The two-dimensional hexagonal boron nitride sheets are 2D crystals that comprise of boron and nitrogen atoms which are covalently bonded in a hexagonal manner.[7] BN comes in four main crystallographic forms, these include hexagonal (h-BN), rhombohedral (r-BN), cubic (c-BN) and wurtzite (w-BN).[8][9] Hexagonal boron nitride consists of layers of covalently bonded boron and nitrogen atoms.[8] Weak van der Waals interactions hold the layers together. It is these weak interlayer bonds that allow hBN to be exfoliated into 2D sheets. BN displays AA' stacking whereby the boron (B) atom sits above the nitrogen (N) atom of the adjacent layer (figure 2). The distance between the neighbouring BN planes is 0.333nm; this is determined by the van der Waal forces. The main edge sites present in monolayer BN, include armchair edge and zigzag edge. (Figure 2).

There are distinct differences between graphene and hBN related to their optical, electrical and chemical properties.[10] Hexagonal boron nitride is a wide band-gap electrical insulator 5.5-6 eV.[11] Whereas, graphene is a superb electrical conductor with a reported conductivities of 10^{14} S/m.[12] BN is chemically stable in oxidising atmospheres up to 1000 °C in air and 1400 °C in a vacuum.[13] Graphene is stable in oxidising atmospheres up to 400-450 °C.[13] Hexagonal boron nitride and graphene are often used in thermal management applications due to their high thermal conductivities. The thermal conductivity of BN has been reported to be ~400 W/mK in-plane and ~5 W/mK out of plane[14][14] [15][17] graphene, however, has a reported thermal conductivity of 3000 W/ mK in-plane and 6 W/mK out of plane.[18]

2.2.1 Production Methods of 2D Materials

Two main approaches are used to produce monolayer materials, including bottom-up processes and top-down processes. Top-down processes start with bulk materials that are broken down into monolayers through external forces. Such methods include liquid-phase exfoliation and mechanical cleavage. Bottom-up processes involve the assembly of individual atoms to form 2D layers.[19] Chemical vapour deposition (CVD) is an example of a bottom-up process. Each approach is done under

different time frames and costs and therefore produces flakes of varying qualities (Figure 3).

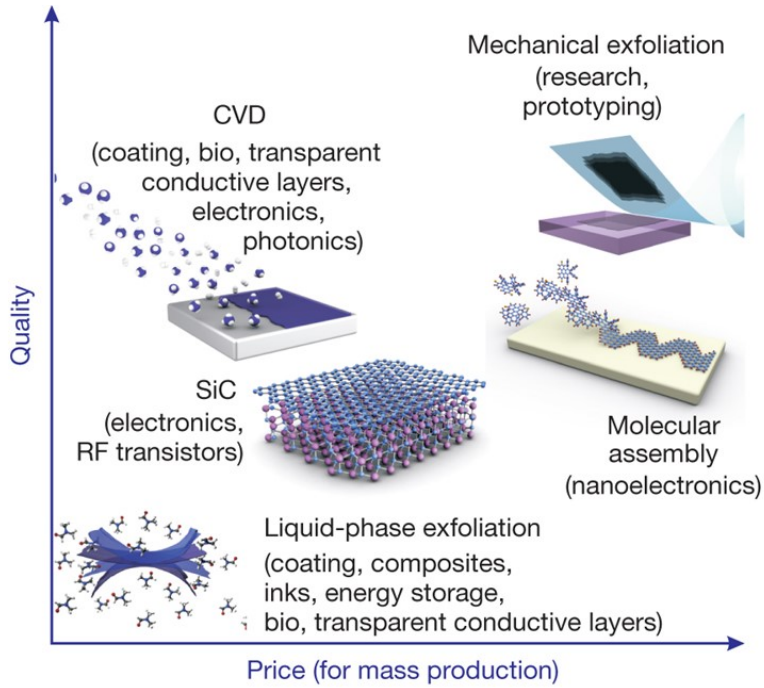

Figure 3 schematic showing a simple diagram of the quality of flakes produced against price for mass production, for different exfoliation methods.[20]

Liquid Phase Exfoliation (LPE)

Mechanical exfoliation was one of the first methods for 2D material production (graphene, scotch tape method). However, the scalability of this method is limited to long processing times and low yields. Liquid phase exfoliation, on the other hand, is a desirable method of 2D material production due to its versatility of exfoliation mediums and relatively low cost. The method involves dispersing bulk materials into an organic solvent then applying a large amount of energy via sonication to break the bonds between the layers.[21] An ultrasonic bath or probe creates an ultrasonic wave that creates cavitation bubbles, when these cavitation bubbles implode, causing fluid jets to break up the weak van der Waal interactions between the layers resulting in exfoliated sheets.[2]

Another solution-based method of exfoliation is based on the intercalation between adjacent layers of the 2D material. This method involves the absorption of molecules between layers. The intercalation of ionic species between layers increases the space between layers and reduces the adhesion of the layers. With the assist of ultra-

sonication and high input energies, the bonds between the layers are broken, allowing exfoliation of monolayers (Figure 4).[2]

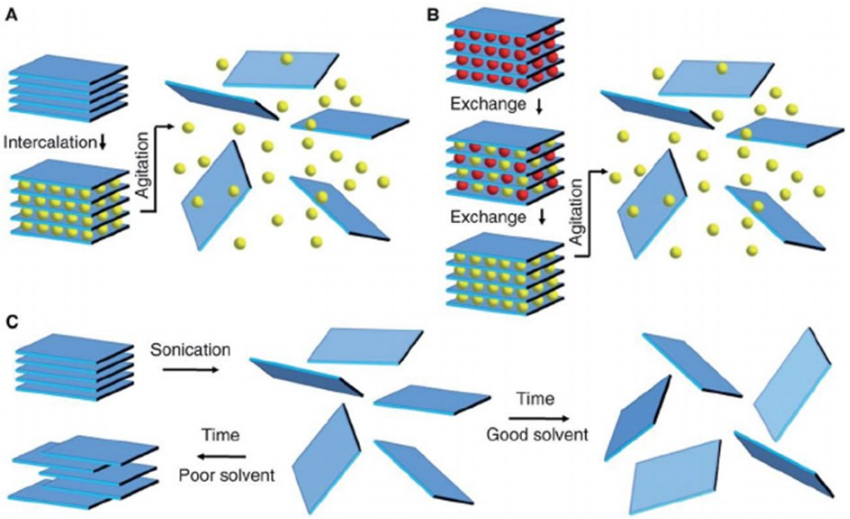

Figure 4 Exfoliation methods showing (a) ion intercalation, (B) ion exchange and (c) sonication.[2]

Coleman et al. have researched thoroughly into liquid-phase exfoliation of layered materials into two-dimensional nano-sheets. They initially began exfoliating commercial MoS_2, WS_2 and BN powders in several different solvents with varying surface tensions.[4] Their exfoliating technique involved sonication via bath and probes followed by centrifugation to size order their materials. They reported that re-aggregation of nanoplatelets could be reduced by matching the surface energy of the organic solvent to the surface energy of the 2D material being exfoliated.[4] This is because the driving force of re-aggregation is reduced when the difference in surface energy between the solvent and material is removed. The most promising solvents for exfoliating MoS_2, WS_2 and BN were found to be N-methyl-pyrrolidone (NMP) and isopropanol (IPA).

Other researchers have created their own techniques for exfoliating BN and GNP in various solvents and surfactants. Wang et al. sonicated BN in methanesulfonic acid for 8 hours in an ultrasonic bath followed by centrifugation for 90 minutes at 4000 rpm. The final concentration reported was 0.3 mg/ml, and an average lateral size of less than 500 nm, this is similar to those reported by Coleman et al. (100-500 nm).[4] Zhi et al. tried sonicating BN in N-dimethylformamide (DMF). The concentrations after exfoliation were between 0.01-0.03 mg/ml.[22] Bourlinos et al. exfoliated 2D materials in polymers to produce colloidal composites, graphite was exfoliated in the presence of polyvinylpyrrolidone, the final concentrations were found to be 0.1

mg/ml.[23] May et al. explored the exfoliation of MoS_2 and hBN in tetrahydrofuran (THF) using various polymers as stabilisers.[24] The range of concentrations achieved was found to be between 0.003-0.034 mg/ml.[24]

Several factors can affect the outcome of the exfoliated materials including sonication time, temperature, power and centrifugation speeds. Zhi et al. studied the relationship between centrifugation speeds and the thickness of the collected exfoliated materials.[22] They found that at speeds of 5000 rpm most sheets had less than 20 layers and thicknesses less than 7 nm. With speeds of 8000 rpm, Zhi et al. were able to reduce the average thickness to 3 nm (less than 10 layers).

These reports describe the process to produce few-layered 2D materials using LPE. However, the long processing times and relatively low yields of these methods may be challenging for the large quantity needed for 3D applications.

Characterisation of 2D Materials

The characterisation of exfoliated flakes is a necessary step in determining the quality of the materials produced. The key elements that determine the quality include the morphology, size, topography and the number of layers of the 2D materials.

Atomic force microscopy (AFM) can be used to detect the number of layers of exfoliated flakes. AFM uses a cantilever with an atomically sharp tip to scan over a sample to build an image profile (Figure 5). This technique is useful for displaying the topography and thickness of exfoliated flakes, with relative simplicity compared to other methods such as Raman and XRD. However, AFM has reported being quite problematic in distinguishing between the number of layers greater than 2 in graphene samples, due to folding and wrinkling of graphene sheets.[25] For BN nanoplatelets AFM has been reported to successfully measure the thickness of the platelets and therefore determining the number of layers present.[26]

Scanning electron microscopy (SEM) can be used to show the morphology and topography of 2D material nanoplatelets (Figure 5). 2D materials are characteristically smooth in their surface features however, SEM can be used to identify the morphology of flakes and therefore the lateral sizes. It is difficult to identify the thickness of the flakes or number of layers present using just SEM alone, therefore a secondary technique such as Raman or AFM is usually required.[27]

Other widely reported characterisation techniques of 2D materials include Raman, XRD and TEM.[28][29][30] These techniques are used to find the thickness and number of layers of the nanoplatelets after exfoliation rather than the lateral sizes. Therefore AFM and SEM are mainly used for characterising the shape and geometries of 2D materials. The lateral sizes of 2D materials are an important parameter for applications in 3D printing techniques as they are related to the rheological behaviour and scattering effects in SLA resins.

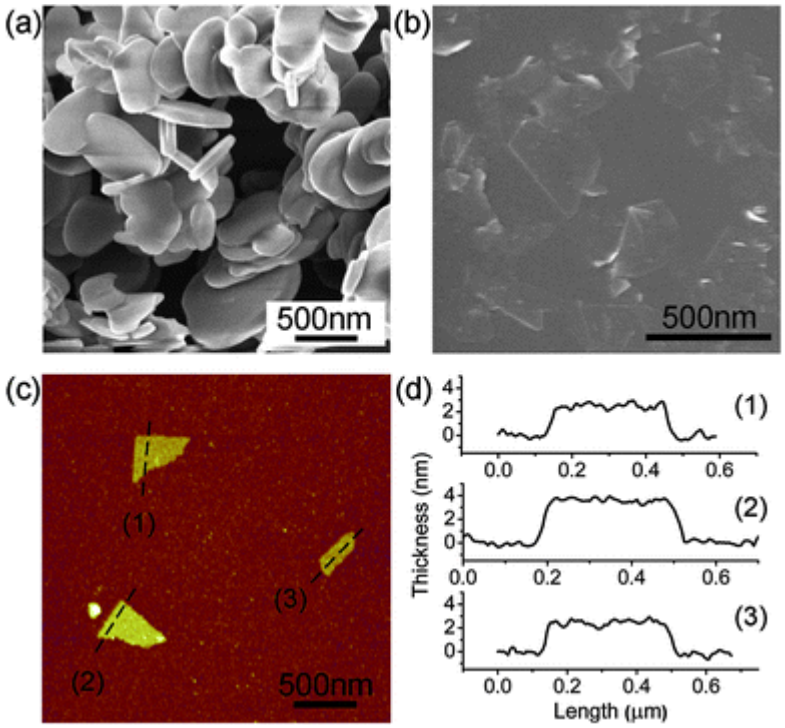

Figure 5 Representative image of (a) SEM image of hBN nanoplatelets. (b) SEM image of hBN nanoplatelets after exfoliation. (c) AFM image of BN nanoplatelets (d) height profiles from AFM data indicating the thickness of the flakes. [27]

2.3 Properties of GNP and BN Polymer Composites

Graphene nanoplatelets (GNP) and BN can be used as filler materials in polymer composites to improve their thermal, electrical and mechanical properties. Polymers are usually poor thermal conductors; therefore, the addition of thermally conductive fillers in the form of graphene and BN can produce high-performance nanocomposites (Table 1).[31] However, the thermal conductivity of a composite material is highly dependent on the thermal conductivity of the polymer matrix. Based on 24 wt. % of BN in PMMA the thermal conductivity of 3.16 W m^{-1} K^{-1} has been reported by Ebadi-Dehaghani et al. [15] A study by Wong et al. also found that the addition of 30 wt.% BN sheets in epoxy resin resulted in thermal conductivities (~1.2

W m^{-1} K^{-1}) three times that of neat epoxy.[32] The addition of BN flakes into a polymer composite will not only enhance the thermal conductivity of the polymer but will increase the elastic modulus, glass transition temperature (Tg) and yield strength.[33][13]

Similarly, the intrinsically high thermal conductivity of GNP has been reported to increase the thermal conductivity of polymer composites. Min et al. dispersed 1.89 vol. % GNP in epoxy and reported a thermal conductivity of 0.54 W m^{-1} K^{-1}, a 157 % increase from the polymer matrix alone.[34] Shtein et al. reported an ultra-high thermal conductivity (12.4 W m^{-1} K^{-1}) of their GNP (volume fraction 0.25) dispersed in epoxy (0.19 W m^{-1} K^{-1}), providing an overall increase in thermal conductivity of 6800 %.[35] An increase in thermal conductivity of polyethylene glycol/polymethyl methacrylate has been reported by Zhang et al. by dispersing GNP 8 wt. % in the polymer. The reported thermal conductivity of 2.34 W m^{-1} K^{-1} was 9 times that of the polymer matrix (0.25 W m^{-1} K^{-1}).[36] A review of some of the reported thermal conductivities of polymer composites containing BN and GNP are listed in Table 1.

Table 1 Thermal conductivities of GNP and BN polymer composites.

Polymer Matrix	Filler	Loading	Thermal Conductivity (W m^{-1} K^{-1})	Ref.
Pentaglycerine (PG)	GNP	4 wt. %	0.509	[37]
Paraffin	GNP	4 wt. %	0.29	[38]
Polybutylene terephthalate (PBT)/polycarbonate (PC)	GNP	20 vol. %	5.82 (in plane) 1.06 (through plane)	[39]
Epoxy	GNP	1 wt. %	0.33	[40]
Poly carbonate (PC)	GNP	20 wt. %	1.8	[41]
Epoxy	BN	30 wt. %	1.2	[42]
Polyimide (PI)	BN	40 wt. %	0.748	[43]
Polysiloxane	BN	15 vol. %	1.6	[44]
High density polyethylene (HDPE)	BN	50 vol. %	3.6	[45]
Epoxy	BN	9 vol. %	0.44	[46]

Graphene and its analogues are often used as fillers to provide an electrically conductive network inside a polymer matrix. Conductive polymer composites offer an exciting opportunity in the development of electronic applications, 3D printing and tissue engineering due to the versatility of polymers. Current research has reported the dispersion of GNP in polymer matrixes to achieve high electrical conductivities.

Table 2 displays reported graphene-polymer composites and their electrical conductivities. The table describes GNP-based composites to achieve electrical conductivities at ~10 wt. % solid loading, however Chandrasekaran et al. reported as little as 0.5 wt. % GNP in epoxy achieved a conductivity value of ~2 x10^{-3}.

Table 2 Reported electrical conductivities of GNP polymer composites.

Polymer Matrix	Filler	Loading	Conductivity (S m^{-1})	Ref
Polypropylene (PP)	xGNP-15	5 vol.%	0.1	[47]
Epoxy	Graphene	0.52 vol.%	1E-2	[48]
Poly methyl methacrylate (PMMA)	EG	1.00 wt.%	1E-3	[49]
High density polyethylene **(HDPE)**	EG	3.0 vol.%	1E-8	[50]
(PET)	Graphene	0.47 vol.%	7.4E-2	[51]
Poly methyl methacrylate (PMMA)	GNP	10 wt.%	~1	[52]
Poly propylene (PP)	GNP	10 wt.%	5E-3	[47]
Polyvinyl chloride (PVC)	GNP	14.8 wt.%	0.06	[53]
Polyethylene glycol (PEG)/ polymethyl methacrylate (PMMA)	GNP	2.0 wt. %	10^{-4}	[36]
Epoxy	GNP	0.5 wt. %	~2 x10^{-3}	[54]
Poly lactic acid (PLA)	GNP	15 wt. %	0.36	[55]
Epoxy	GNP	10 wt. %	0.005	[56]

2.3.1 GNP and BN Hybrids

In recent years, a trend has started to be seen in graphene/boron nitride hybrid composites for efficient thermal management of electronic devices.[57] Both materials are used in synergy to maintain graphene's high thermal conductivity, whilst BN is used as a secondary filler for its electrically insulating properties (Figure 7).[57][58][59] Work by Shtein et al. developed an epoxy graphene-BN hybrid and observed an increase in thermal conductivity of 3.06 W m^{-1} K^{-1} compared to the

polymer without fillers (0.19 W m^{-1} K^{-1}).[57] The electrical resistive and high thermal conductivity of the hybrids were then applied as potting material for electronic devices. Another approach of BN-GNP hybrids was reported by Owais et al. where they dispersed GNP and BN inside short carbon fibres within an epoxy matrix, to improve thermal conductivity and electrical resistivity for thermal management applications in electronic devices (Figure 6).[60] They reported a thermal enhancement of 350 % with their functionalised composite containing 3 wt. % carbon fibre and 5 wt. % GNP-BN (1:1) compared to neat epoxy.[60] Shao et al. saw an increase in thermal conductivity of their GNP-BNNS PA6 hybrids by 350 % with 1.6 wt. % BN and 6.8 wt. % GNP.[61] GO has also been used as a hybrid filler to BN, work by Wu et al. chemically reduced GO to form rGO that was fixed onto the surface of the BN flakes and dispersed in epoxy. They observed an increase in thermal conductivity of 390 % when 30 wt. % BN@rGO was dispersed in the polymer.[62] Yang et al. developed GNP and BN-PEG hybrids for the development of solar-thermal-electric energy conversion and storage phase change materials. [63] The hybrids consisted of 1 wt. % GNP content with varying BN content 5 wt. % 10 wt. % 20 wt.% and 30 wt. %. They found that by adding GNP as a secondary filler they increased the thermal conductivity of their 30 wt. % BN composite by 336 %.[63]

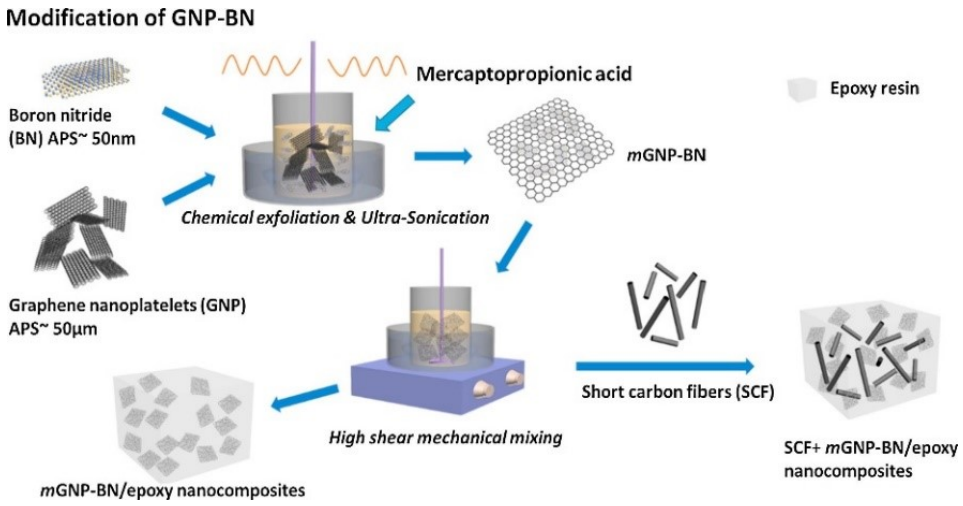

Figure 6 Schematic of Owais et al. preparation of functionalised GNP-BN short carbon fibre-epoxy composites. [60]

The combination of BN and GNP hybrids seems promising for improving the thermal conductivity and electrical resistivity of polymer composites. With key applications in thermal management of electronic devices. The ability to manufacture these materials into complex geometries through 3D printing could offer a fast and reliable solution to current methods of fabrication using expensive tooling and dies.

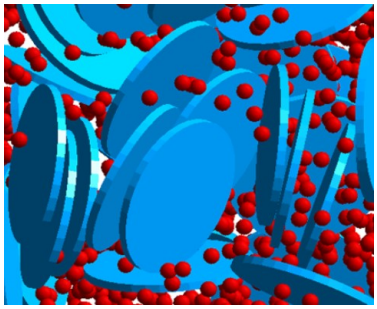

Figure 7 Schematic representation of GNP-hBN hybrid, blue disks represent GNP red spheres represent hBN.[57]

2.4 Additive Manufacturing Technologies

Additive manufacturing has gained a great amount of attention over the past few decades. The potential to fabricate three-dimensional products with minimal waste to a high degree of accuracy has sparked interest within the manufacturing sector. Unlike other forms of manufacturing the additive manufacturing process involves the fabrication of a 3D part in a layer by layer fashion, rather than subtracting material to form the object. This technique produces minimal waste materials and can be used to produce highly complex and intricate objects. Whilst eliminating the need for expensive tooling and dies.[64]

Current progress in AM techniques enables the design of complex geometries with hierarchal complexities. AM also enables the customisation of parts with integrated assemblies that can be adapted and manufactured easily without timely prototyping processes.

2.4.1 History of Additive Manufacturing

Additive manufacturing first emerged in 1987 with the creation of stereolithography by Charles Hall. Stereolithography involves the process of curing thin layers of photosensitive polymeric material with UV radiation from a laser.[65] SLA (stereolithography apparatus) was the first commercial 3D printer by 3D Systems; this further led to the creation of commercial first-generation acrylate resins. A few years later in 1991, new AM technologies were introduced into the commercial market, these systems included fuse deposition modelling (FDM), solid ground curing (SGC) and laminated object manufacturing (LOM). FDM utilises an extruded based system to build parts layer by layer using a thermoplastic filament, whilst SGC incorporates flooding each layer with UV light through a mask on a glass plate. [65] LOM operates by bonding and cutting sheet material through a guided laser. Selective

laser sintering (SLS) was the next to be introduced in 1992 and uses heat produced by a laser to fuse together powdered materials. Direct shell production casting (DSPC) was then introduced in 1993, this method uses an inkjet mechanism, by depositing a liquid binder onto a ceramic powder to form shells used in investment casting.[65] As interest grew in AM technology, demand for accessible low-cost printers was a high priority. This has led to the commercialisation of 3D printers for home printing, from Formlabs and MakerBot. The main AM technologies used today include (Figure 8):

- Stereolithography
- Ink-jet printing
- Extrusion printing, robocasting
- Direct energy deposition
- Sheet lamination
- Powder bed fusion and binder jetting processes.[66]

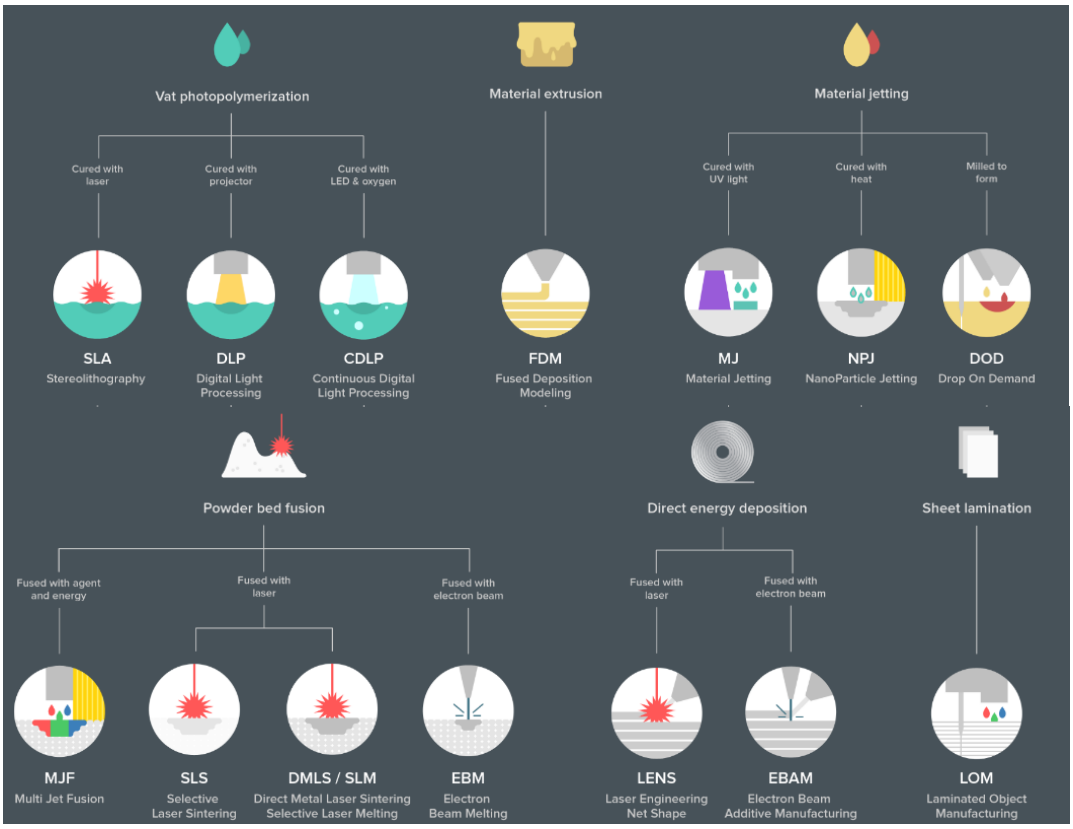

Figure 8 Pictograph of additive manufacturing technologies. [157]

2.4.2 AM Process

The AM chain for most AM technologies includes the conceptualisation of a 3D image using CAD (computer-aided design) software (Figure 9). The 3D CAD

image is then saved or converted into an stl. file. Dependent on the AM technology used, further manipulations to the original file may be required, i.e. the introduction of slicing software for the layer by layer processes or the addition of supports for any fragile parts, bridges and overhangs.[66] The build file is then sent to the 3D printer to begin the manufacturing process. Once the printer has finished printing, the parts often require post-processing including cleaning to remove excess supports and uncured residue and second stage curing processes (thermal/UV curing).

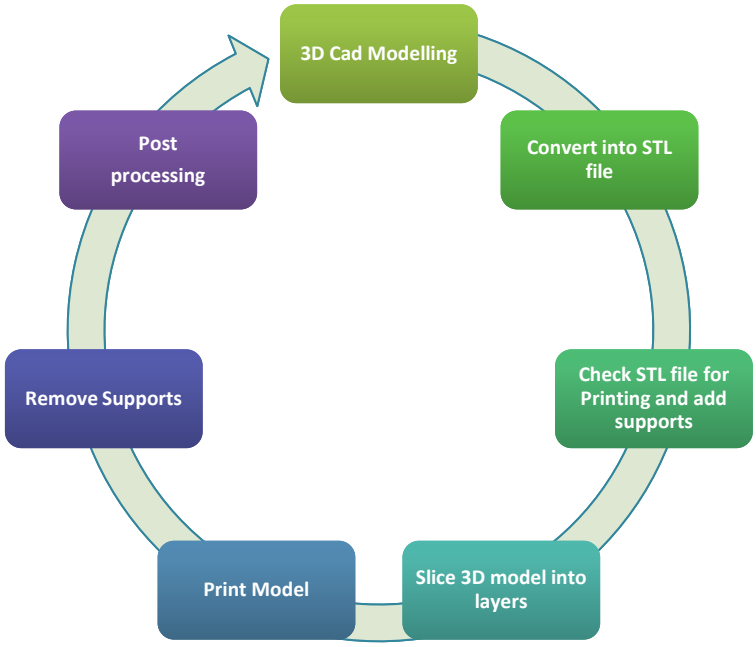

Figure 9 Additive manufacturing process.

Not all AM technologies require CAD modelling, advances in AM technologies in the medical field use 3D scanning through computerised tomography (CT), magnetic resonance imaging (MRI) and 3D ultrasounds to build a 3D image.[66] Reverse engineering can also be used to collect data for AM production, this method uses laser scanning technologies to collect surface data from varying surfaces to build measure and reconstruct an existing component. Both these methods require further interpretation and processing to extract relevant sections to be built into a model.[66]

Applications of AM parts include rapid prototyping, medical implants, braces and supports, jewellery, decorations, electronic circuit boards, art, product development, automotive and many more. One of the main limitations of AM is limited material selection. Polymers are often used for many AM processes due to their excellent

processability; however, their mechanical and physical properties limit their applications in industry.[67] One of the ways researchers have tried to combat this problem is through the addition of fibres and particles that can dramatically alter and tune the polymer properties for advanced applications. [67] However, the addition of secondary material can significantly change the properties of a resin including an increase in viscosity with increasing concentration of filler material, this can prove to be very problematic depending on the AM technology. A catalogue of parameters for each technique and the material combination would be highly beneficial for the manufacturing industry, however, as of yet this has not been achieved as material combinations and new technologies are constantly evolving.

An overview of the working principles of AM technologies including SLA, FDM, SLS, Ink-jet printing and DIW will now be explored in the following subchapters.

2.4.3 Ink-Jet Printing

Ink-jet printing is also known as material jetting is a common 3D printing technique used for ceramic-based suspensions. Ink-jet printing deposits ink in the form of droplets from the printing nozzle onto a substrate via a thermal or piezoelectric method (Figure 10). The continuous droplet pattern than solidifies through evaporation, UV light or thermal exposure forming the first layer of the printed part. A new layer of droplets are then deposited on top of the previous one and the process continues in a layer by layer fashion.[68] The inclusion of supports is essential for ink-jet printing to maintain the integrity of the 3D structure, these supports can be made from partially cured material or a soluble material which can easily be removed via washing. Factors affecting the printability of the ink include viscosity, contact angle, solid loading, density, particle sizing, speed of printing and nozzle size.[69]

One of the main advantages of ink-jet printing is the high degree of accuracy and excellent resolution in the z-axis, typical layer heights are between 16-32 microns with $\pm 0.1\%$ dimensional accuracy. Ink-jet printing attains fast print speeds this, however, can result in a coarse finish with lack of adhesion between layers.[69]

Applications of ink-jet printed parts include electronic components, conductive tracks, resistors and thin-film transistors. It is also commonly used for

prototyping and bio applications, microfluidic and micro-optical devices (Figure 11).[70][71][72]

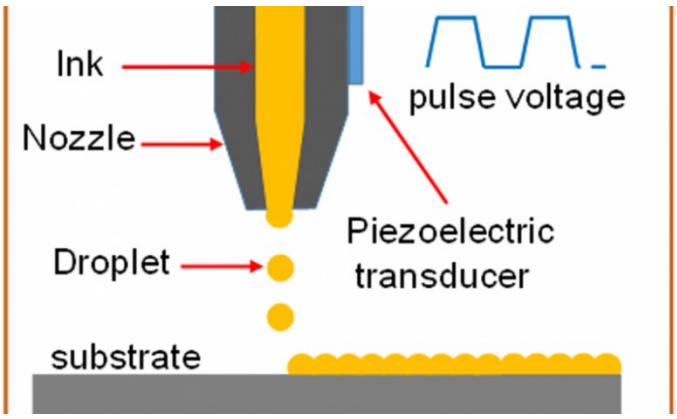

Figure 10 Diagram of the working principle of ink-jet printing. [158]

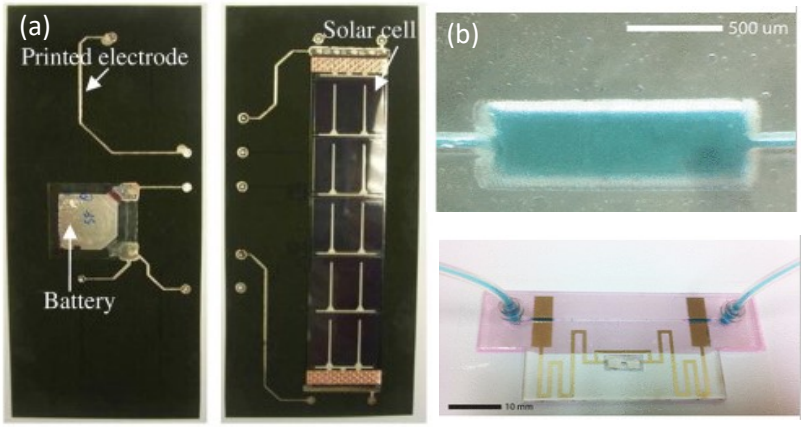

Figure 11 Images of printed parts using Ink-jet printing. (a) Copper ink printed electrodes and solar cells.[159] (b) Ink-jet printed microfluidic device. [160]

2.4.4 Selective Laser Sintering

Selective laser sintering (SLS) uses a powder bed of fine particles closely packed together on top of a build plate. A laser or binder cures the top surface of the powder in the pattern of a layer from the associated stl. file. A roller than deposits a new layer of powder directly on top of the previous one and the process continues in a layer by layer fashion (Figure 12). After the process has been completed the final printed part is removed from the printer and excess powder is removed via a vacuum. The printed parts can then be post-processed using sintering, coating and/or infiltration.[69] SLS can be used to print polymers, metals and alloy components. The key conditions of printing using SLS are the associated particle size distribution and packing density of the materials, as these factors will determine the overall density of the final part. When a liquid binder is used the rheological properties of the binder and

speed of deposition is important to ensure there is good interaction between the powder and binder. SLS that use a laser to fuse the particles together tends to produce parts with higher densities than binder deposition which are associated with high porosities. [73]

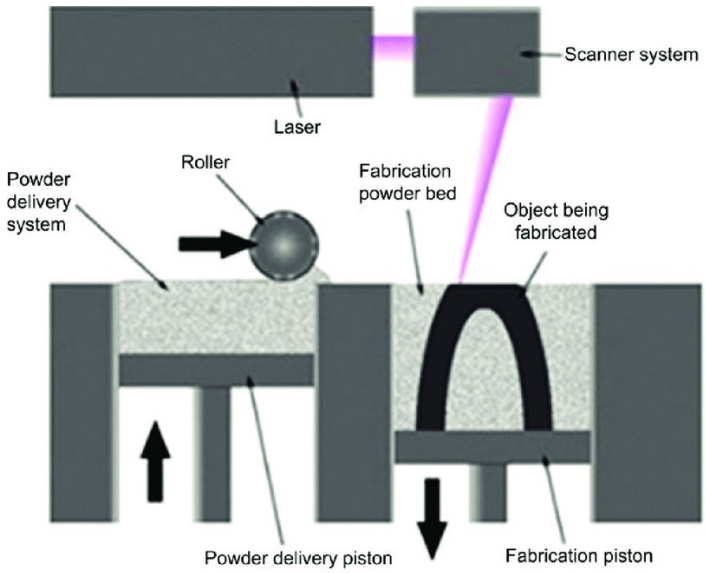

Figure 12 Diagram of SLS process. [73]

Advantages of SLS includes the ability to print parts with good tolerances and fine detailing of complex parts.[74] One of the main advantages of SLS is that the surrounding powder is used to support the part during printing eliminating the need for additional supports.[75] These attributes make SLS an attractive technique for applications in aerospace, fashion, electronics and biomedical industries (Figure 13).[75][76] The drawbacks of SLS consists of slow processing times due to the fusion of particles, coarse surfaces and the high-cost associate with the procedure.

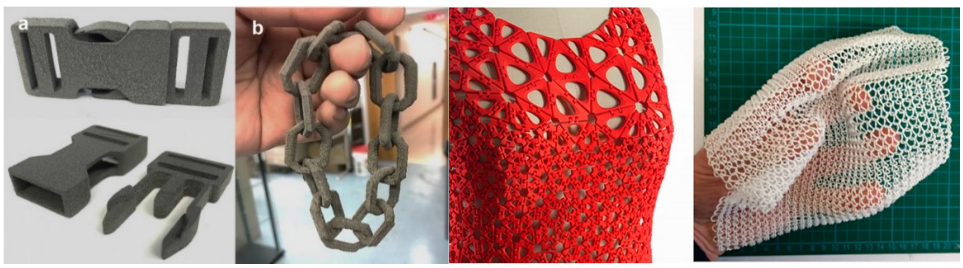

Figure 13 Images of SLS printed parts. [161], [70]

2.3.5 Direct-Ink Writing

Direct ink writing or robocasting is an extrusion-based 3D printing technique. It is used to fabricate 3D shapes generated from computer-aided design. Direct ink writing involves the squeezing of ink inside of a syringe through a nozzle onto a substrate, controlled by computer deposition (Figure 14).

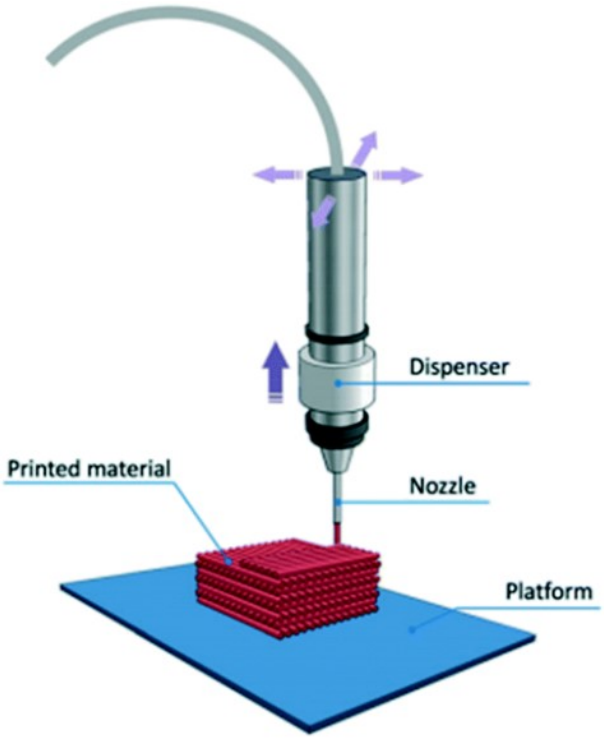

Figure 14 Schematic of robocasting [77]

DIW is used to print mainly ceramics and polymers. The fluidity of the colloidal suspension or ink is important during the printing process, as the ink is required to travel through a small nozzle. Therefore the suspension should maintain a shear-thinning behaviour during flow with quick elastic recovery.[78] Once the material has been deposited onto a substrate the extruded ink should be self-supporting to fabricate a 3D part using a layer by layer process. The layer thickness achieved from DIW is relatively large compared to other additive manufacturing techniques such as stereolithography and ink-jet printing.[77] Extrusion-based printing can be used to print parts at room temperature or in a controlled environment. However dependent on the physical and chemical properties of the ink various adjustments to the printer have been engineered. These have included printing onto temperature-controlled

plates, using a UV light for curing processes and printing into oil baths to help retain shape and topography.

Although originally used to print polymer and ceramic suspensions, recent works have shown an increase in printing inks containing 2D materials for a variety of applications from electronics to bio-applications (Figure 15).[64][79][80] 2D materials such as graphene, graphene oxide, TMDs, hBN, Mxenes can offer superior electrical, mechanical, insulating & electrochemical properties making them interesting materials to incorporate into suspensions for DIW and other additive manufacturing techniques.[81]

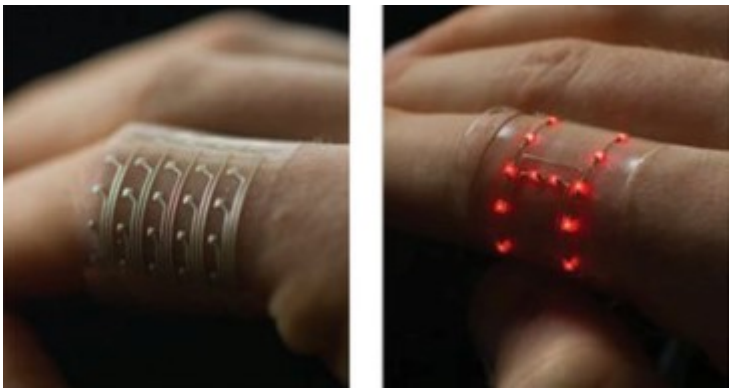

Figure 15 Photograph showing a 3D printed functional light emitting diode array made out of silver- thermoplastic polyurethane (Ag TPU) fabricated using DIW. [162]

2.4.6 Fuse Deposition Modelling

Fused deposition modelling (FDM) uses a spool of thermoplastic filament that is drawn through a heated nozzle (Figure 17). The heated nozzle converts the solid-like filament into a semi-liquid phase and deposits as droplets or rods onto a build plate where it quickly cools back down to a solid phase.[69] Essentially FDM works similar to that of a hot glue gun. The printed part is then built up in a layer-by-layer fashion with supports included in the design. Post-processing of FDM parts is usually minimal with only the removal of supports required. Materials used in FDM include thermoplastics usually (polylactic acid (PLA), acrylonitrile butadiene styrene (ABS) and polycarbonate (PC)).[82][83][84] The simplistic and safe approach of FDM has made it one of the most widely used technologies as machines are readily available and affordable for everyone. Applications of FDM printed parts include fashion and textiles, prototyping, aerospace, medical devices (Figure 16).[85][86] The limitations

of FDM, however, include poor surface finishes with low resolutions compared to other techniques, and printed parts with anisotropic properties.[87]

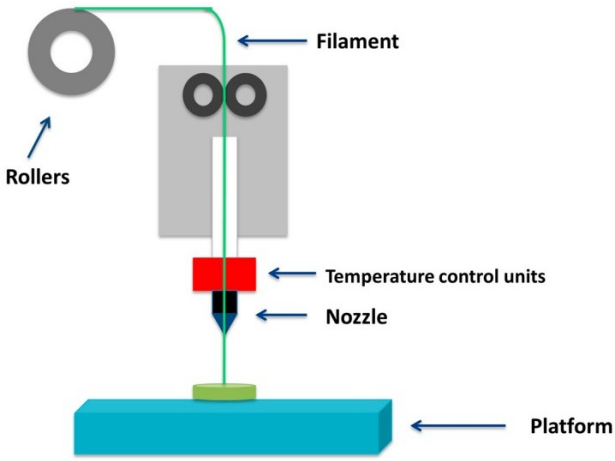

Figure 17 Schematic of the working principles of FDM.[163]

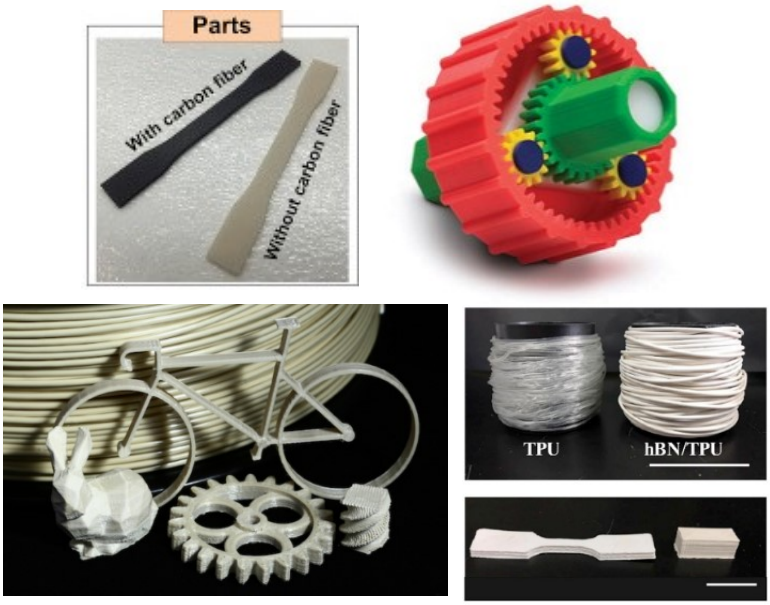

Figure 16 Examples of FDM printed parts[164] [84] [165] [166]

2.4.7 Stereolithography (SLA)

Stereolithography (SLA) was first developed in 1986 by Chuck Hull, and commercialised in 1988 by 3D systems.[88][89] The technique requires a 3D CAD model to be converted into an stl. file.[90] Slicing software is then used to deconstruct the image into layers for printing. The 3D image is then manufactured through the

curing a photopolymer using a UV radiation from a laser source. The main principles of stereolithography are:

- Components are cured when a UV beam scans across the surface of a photopolymer.
- Parts are built layer by layer, each layer is scanned by an optical scanning system and controlled by an elevation mechanism, this lowers after each layer has been cured.

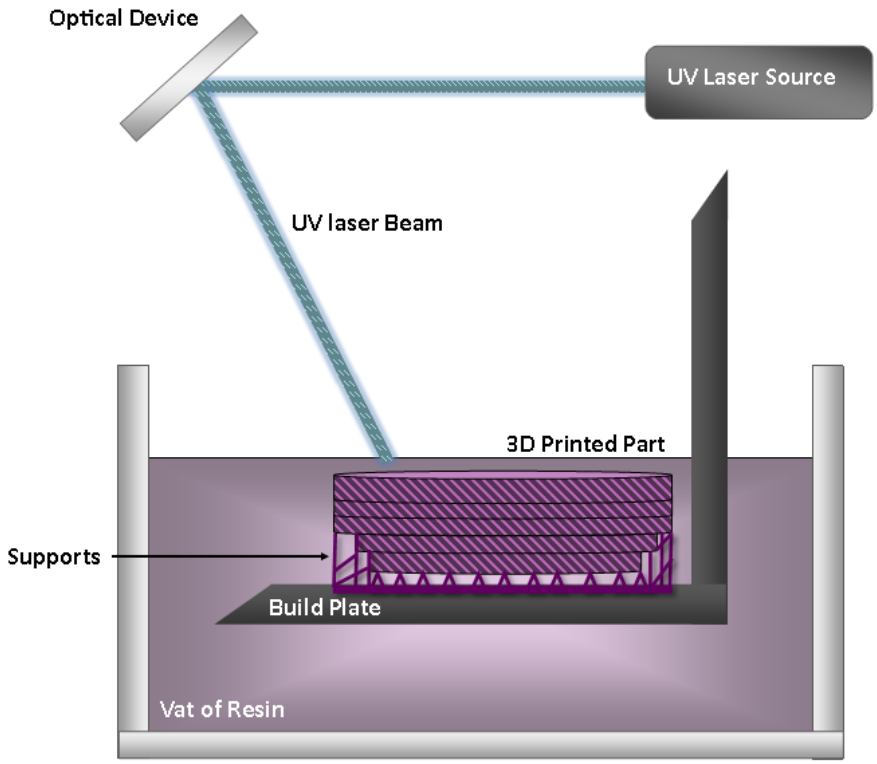

Figure 18 Schematic of working principle of 'vat' polymerisation Stereolithography.

There are two main configurations that can be used in SLA printing including a free surface approach where a UV laser traces a 2D image of the cross-section of the 3D part within a '*bath*' of photoactive resin (Figure 18).[89] After the layer is cured it is then lowered into the bath by a predefined distance and a fresh layer of polymer is then deposited on the top surface to continue the build. The second configuration of SLA is known as *'bat'* configuration and uses a constrained surface approach; like the classic free surface approach, this approach builds parts layer-by-layer. The difference in this approach is that the object is built hanging from a moveable substrate, like a bat hanging from a ceiling.[89] The build plate is placed just above a vat of resin and

is lowered down onto the surface of a vat of resin to deposit a new layer of resin. Unlike vat configuration where the laser is positioned above the vat here, the laser is situated underneath the vat for curing.

The laser polymerises the surface of the resin which represents a two-dimensional section of the sliced stl. file.[91] Each laser pass polymerises a parabolic cross-section of the resin.[92] Figure 19 represents the cross-section of the laser as it hits the surface of the liquid polymer.

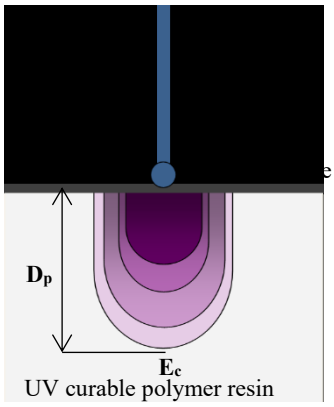

Figure 19 Parabolic cross section of UV laser produced on resin surface.

Key considerations for optimising the printing process include layer thickness, over and under-curing, speed of print, raster pattern of the laser, the temperature of the resin, the gap between the resin and zephyr blade and scattering effects from filler materials.[93][94] Therefore for each new resin formulation a new set of printing parameters is required. There are two critical parameters which are calculated and adjusted to produce a specific layer thickness, these include the depth of penetration of the laser D_p and critical exposure energy E_c. The D_p is related to the distance at which the laser penetrates through the resin from the top surface, where the energy of the laser is 1/e of its initial starting value. The E_c is the minimum amount of energy required to activate the polymerisation of the resin.[95] These parameters are related by the following working curve equation:

$$C_d = D_p \ln\left[\frac{E_0}{E_c}\right] \quad (1)$$

This equation is used to produce the working curve of the resin, C_d is the cure depth of the printed part and E_0 is the maximum energy supplied by the laser.

This equation can be used to find the optimum printing parameters of each new resin, by setting arbitrary values for the E_c and D_p values, a single layer can be printed and measured to find the thickness or C_d. The optimum E_c and D_p values can then be calculated by plotting C_d vs ln E_0, to optimise and control the thickness of each layer (z-resolution).[96]

The printing of highly loaded filler materials can present major challenges in SLA due to scattering effects and increased viscosities.[97] During printing, the filler materials can obstruct the photoinitiator from absorbing light resulting in under curing or a reduction in the C_d value. Previous work by Griffith *et al.* have studied the effect of highly loaded ceramic particles inside resins for SLA.[98] They observed the relationship between particle size, volume fraction, scattering properties and the C_d using the Beer-Lambert law:

$$C_d \propto \frac{d}{\emptyset\beta(n_{ceramic} - n_{resin})^2} \, ln\left(\frac{E_0}{E_c}\right) \quad (2)$$

Where d is the particle size, $\emptyset$ is the volume fraction of the particle inside the resin, n is the refractive index of the ceramic and resin phase and β is related to particle size and wavelength of radiation.

The equation states that the depth of cure of the resin is directly proportional to the particle size of the ceramic and the natural logarithm of the exposure energy E_0, and inversely proportional to the volume fraction of the ceramic. The cure depth is therefore also inversely proportional to the refractive index βn^2. [99][99]

Although this equation can be used for calculating the printing outcomes of resins for SLA with varying volume fractions of ceramic particles, it may not translate when

incorporating 2D materials. This is because the morphology of 2D materials are flakes/platelets as opposed to spherical ceramic particles, resulting in high surface areas and tendencies to aggregate.

SLA Resins and Photopolymers

Understanding current SLA resins and photopolymers is very important to enable the design of reinforced photocurable inks. The choice of resin will dictate the type of reaction that will take place during polymerisation, this will affect the cure time, degree of shrinkage and mechanical properties of the printed parts.[100]

Photopolymers were first developed in the late 1960s and were commercially used in the coating and printing industry.[66] Many photopolymers or radiation-curable resins react to radiation in the ultraviolet (UV) range of wavelengths between 100nm-400nm (Figure 20). These materials undergo chemical reactions to solidify known as photo-polymerisation.[66]

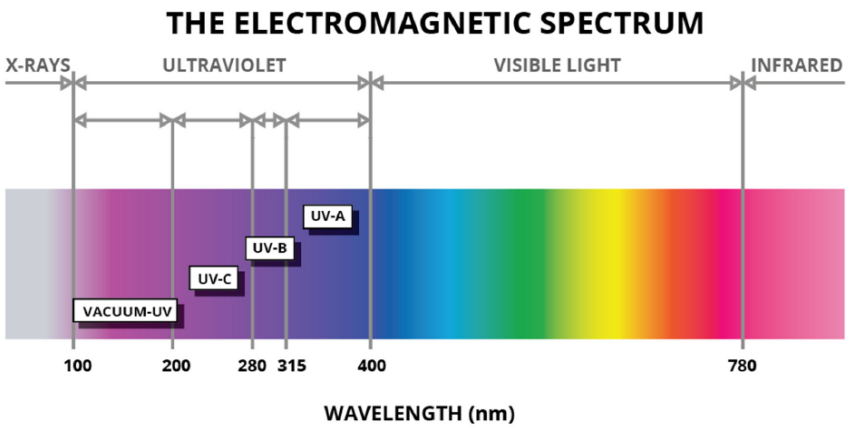

Figure 20 Electromagnetic spectrum[167]

SLA photopolymer resins usually fall into two main polymeric systems acrylates and epoxides. Acrylate resins are highly reactive however result in a significant degree of shrinkage, whereas epoxides have slower photo speeds but can produce more accurate parts.[101] Shrinkage in epoxy-based resins is ~1-2 % whereas acrylate resins have been reported to be between 5-20 %.[66] Notably, the polymerisation of epoxy-based resins is not inhibited by atmospheric oxygen, whereas acrylate-based resins are. Oxygen inhibition can be catastrophic to the polymerisation of the monomer or oligomer, as the oxygen in the air stops the molecules at the surface from polymerising, causing a wet or tacky surface. Extra measures can be taken to try and minimise the effects of oxygen inhibition, these include creating an oxygen-free

atmosphere by printing in an inert atmosphere such as argon. Sensitizers may also be used in the ink formulation to transform oxygen from a reactive to non-reactive state with free-radicals.[102] The simplest method to eliminate the effects of oxygen inhibition is by changing to an efficient photoinitiator.

Acrylate resins cure through free-radical photo-polymerisation and epoxy resins cure using cationic photo-polymerisation during the printing in SLA.[66] When SLA resins are exposed to UV light the photoinitiator converts light energy into chemical energy by forming cations or free radicals.[103] In free radical polymerisation, radicals or ions break off the initiators after UV exposure, the radicals then start to react with the monomer to initiate polymerisation. In cationic reactions, a strong acid (Lewis acid) is released from the initiator starting the bonding process.[104]

Free-Radical Polymerisation

Free-radical polymerisation is widely used in SLA as acrylate resins display superb reactivity and quick processing times. [104] Like most polymerisation systems free-radical polymerisation begins with initiation, propagation then finally termination (see below). [105]

$P\text{-}I \longrightarrow \text{-}I\bullet$ (free radical formation)

$I\bullet + M \longrightarrow I\text{-}M\bullet$ (initiation)

$I\text{-}M\bullet \longrightarrow \ldots \longrightarrow I\text{-}M\text{-}M\text{-}M\text{-}M\ldots\text{-}M\bullet$ (propagation)

$I\text{-}M\text{-}M\text{-}M\text{-}M\ldots\text{-}M\text{-}I$ (termination)

P-I photoinitiator, M molecule, ● free radical

Free radical polymerisation begins with light irradiation of the photoinitiator. The activated compound then splits into two creating two free-radicals (Figure 22). These radicals then attack the surrounding oligomer or monomer transforming it into a radical (Figure 21). The radical monomer attacks the surrounding monomers transforming them into radical monomers. This process continues by adding monomer groups to the radical monomers forming polymer chains. The polymerisation step is finally terminated by either by coupling of two radicals, whereby one radical reacts

with another radical. Or by the transference of β-hydrogen between two radicals where a saturated and unsaturated product is produced (disproportion).[106]

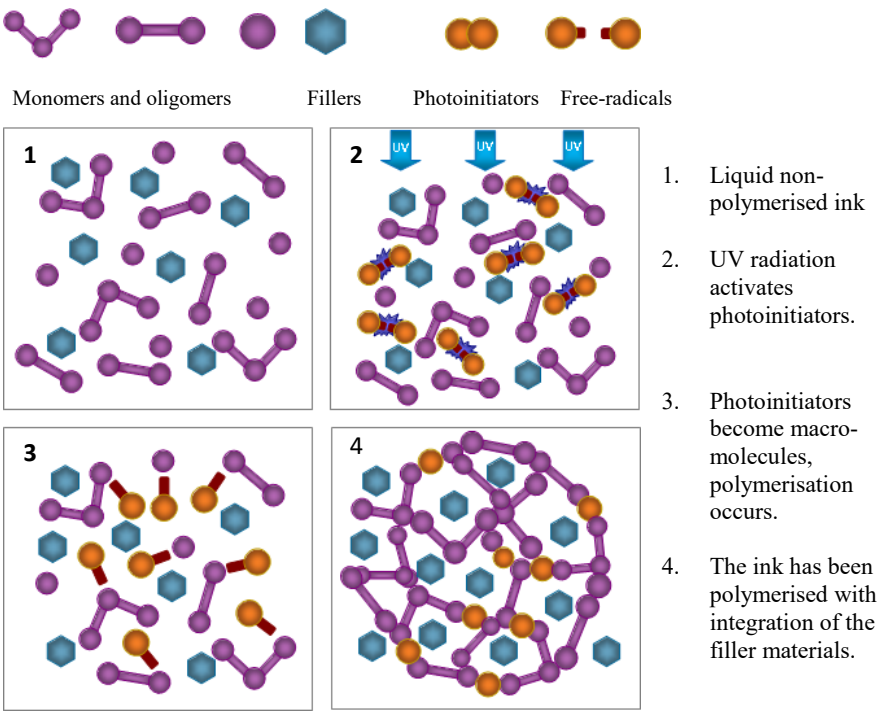

Figure 21 Schematic of photo-polymerisation.

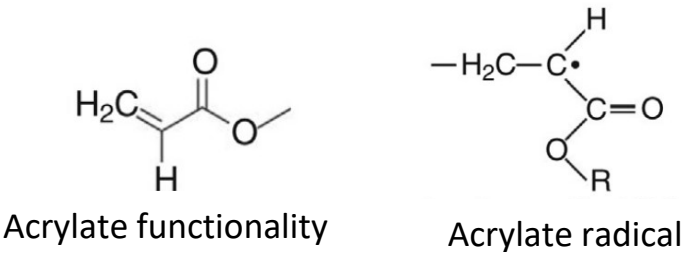

Figure 22 Chemical structure representing an acrylate functionality and acrylate radical. [102]

An example of a free-radical photoinitiator is Phenylbis (2, 4, 6-trimethylbenzoyl) phosphine oxide known as BAPO, it has the following chemical structure:

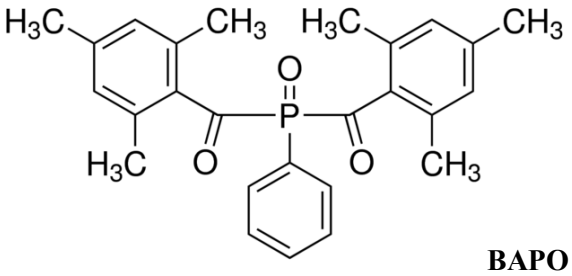

Figure 23 Chemical structure of BAPO.

Other commonly used free-radical photoinitiators include Irgacure 2959 and 184, which have the following chemical structures respectively:

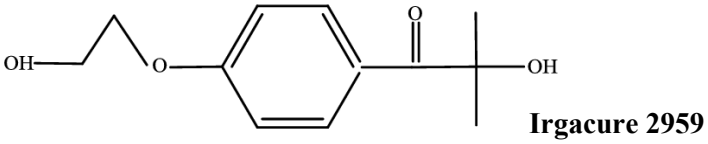

Figure 24 Chemical structure of Igacure 2959.

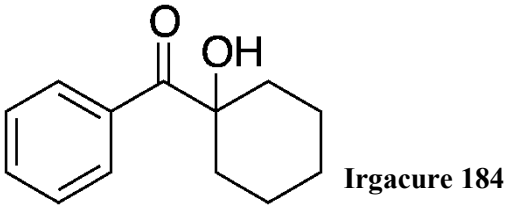

Figure 25 Chemical structure of Irgacure 184.

The photoinitiators in Figure 23,Figure 24Figure 25 have been used to polymerise acrylate resins, such as Poly(ethylene glycol) diacrylate (PEGDA) for biomedical applications and printed packaging.[107][108][109] [110]

Poly (ethylene glycol) diacrylate (PEGDA)

Poly(ethylene glycol) diacrylate (PEGDA) is a well-known oligomer used in UV curable resins due to its high reactivity and good polarity.[111] PEGDA is a PEG-based polymer with double bond acrylate groups, these side groups allow for photocrosslinking (Figure 26).[112] PEGDA is non-toxic and is available in different molecular weights for preferred cross-link densities.[113] For these reasons, it is often used in SLA resins for applications in biomedical, thermo-mechanical and electronic applications.[114][115] [116]

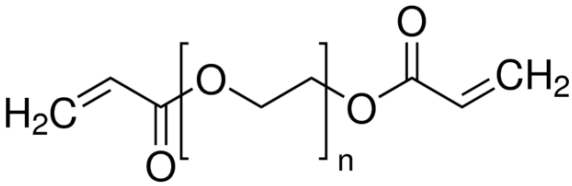

Figure 26 Chemical structure of PEGDA.

Overall the curing process involved in SLA is highly dependent on the monomer functionality and reactivity, temperature, photo speed, light intensity, depth of penetration of the laser, photoinitiator concentration, addition of fillers and stabilizers.[91] This can present many challenges when developing 2D material-based composite inks due to the vast amount of variables. However, the opportunity to print lightweight multi-functional complex parts is an exciting opportunity for the AM industry, with applications including biomedical, electronics, fashion, and aerospace, automotive and thermal management systems.[116][117][118]

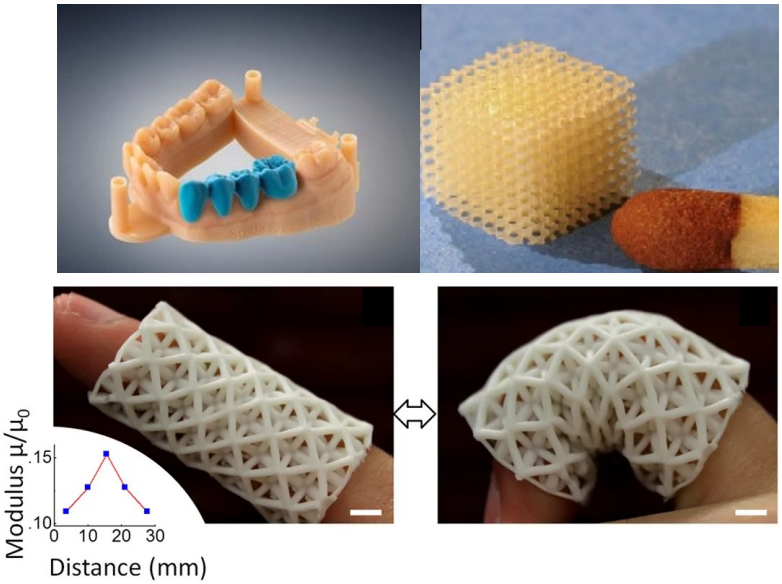

Figure 27 Example of SLA printed parts.[168][118][117]

2.4.8 Summary of AM Technologies

After reviewing the AM technologies it is clear that there are key advantages and disadvantages for each technique some of which have been listed in Table 3. The final application and resin chemistry will govern the decision for the 3D printing technique. For instance, the manufacture of metallic structures would see the implementation of SLS, whereas high viscosity fluids would be suitable for DIW. For quick and inexpensive prototyping FDM can be used, and for high resolution printed parts with good surfaces finishes, photopolymers and SLA would be the preferred choice.

Table 3 Summary of Additive manufacturing techniques. [119]

Technique	Materials	Resolution (µm)	Applications	Benefits	Drawbacks
Material jetting (Inkjet Printing)	Dispersion of particles in a liquid, ceramics polymers	~30 [120]	Biomedical Electronics	Quick print speeds	Weak bonding between layers Can cause course resolutions
Stereolithography (SLA)	UV curable monomers, ceramics	50 [121]	Prototyping Biomedical	Good resolution and quality build	Limited materials, requires large quantities of material, Slow print speeds
Powder bed fusion (selective laser sintering, SLS)	Fine powders of metals, alloys and some polymers	80-250 [119]	Electronics Biomedical Aerospace	High quality prints good resolutions	Slow print speeds, high porosity, Expensive
Extrusion-based printing (direct ink-write, DIW)	Polymers/ Ceramics	50 [122]	Biomedical Electronics prototyping advanced composites	Fast print speeds simple Low cost	Weak mechanical properties
Fuse Deposition Modelling (FDM)	Thermoplastics/ metals	50 [123]	Functional prototypes	Quick print speeds, low cost	Low resolutions/ rough surface finishes

2.5 Ink Design

Ink design for 3D printing applications usually involves the dispersion of filler material in a polymer resin. The filler material acts as the functional component of the composite whilst the polymer is used for its versatility in processing. Printable Inks

may also contain an initiator for thermal or UV curing and binders or dispersants to improve the homogeneity of the ink. This sub-chapter discusses the key characteristics of 2D material-based inks including the rheological properties and ink dispersions.

2.5.1 Rheological Properties of Inks

One of the main properties that is considered in ink design for 3D printing is the viscosity and rheological properties of the ink. As it is these properties that will determine if the ink will flow for recoating in SLA, travel through the nozzle and hold its shape for extrusion-based systems, and to control droplet generation in ink-jet printing.[124]

General Rheological Terms

To understand the rheological properties of a suspension key terms and equations should be first defined.

Viscosity

$$\mu = \frac{\tau}{\gamma} \tag{3}$$

Here μ is defined as the viscosity of the fluid, γ is the shear strain rate experienced at τ the shear stress. The viscosity is, therefore, a measurement of resistance to flow when deformed by an external force.[125]

Intrinsic Viscosity

The intrinsic viscosity η, of a suspension, is the ratio of the specific viscosity to the concentration of the solute, as the concentration reaches zero.[126] The units for intrinsic viscosity are ml/g, and can be calculated using the relative viscosity η_r of the suspension:

$$\eta_r = \frac{\eta}{\eta_0} \tag{4}$$

Herschel-Buckley

The Hershel-Buckley model is often used to model suspensions whose viscosities are effected by changing shear rates.

$$\tau = \tau_y + K\Upsilon^n \quad (5)$$

Where n is the shear-thinning coefficient and, K is the viscosity parameter and τ_y is the yield stress. When n is equal to 1 the suspension displays Newtonian behaviour when $n \leq 1$ it is considered to be shear-thinning and when $n \geq 1$ it is shear-thickening or dilatant.

The Herschel Buckley model is frequently used to find the yield stress of 3D printable resins, to understand the behaviour of the inks through the 3D printing technology under different applied stresses and shear rates. The results of which can then be applied to semi-empirical and theoretical models to find the effective viscosity of the resin for a deeper understanding of the rheological properties of the inks that can be applied to estimate or predict the behaviour of future ink designs.

Rheological Models for the Effective Viscosity of Fluids Containing Nanoparticles

The effect of nanoparticles on the rheological properties of suspensions has been heavily investigated throughout literature. Most fluids will show a Newtonian behaviour however, some fluids that contain high fractions of nanoparticles may exhibit non-Newtonian behaviour shear-thinning. With increasing volume fractions of particles the effective viscosity increases in relation to the base fluid. The ratio between these two viscosities is known as the effective viscosity ratio.[127] When the particle size is very low (submicron) even the addition of a small fraction of nanoparticles will result in shear-thinning behaviours.[128] As a general rule, the effective viscosity of a suspension increases with the increase in particle volume and or the decrease in the size of the particle.

Einstein Model

Einstein first analysed dilute suspension containing rigid uncharged spherical spheres. As the suspensions were so dilute it was deemed that the disruption of particles would not interact with one another, with the assumption that the relative viscosity of a suspension is a linear function to the intrinsic viscosity.[126] Einstein's work stated that the velocity of a fluid on the top surface of the particle is greater than on the bottom causing the particle to rotate.

$$\frac{\mu_{eff}}{\mu_{bf}} = 1 + [\eta]\phi + O(\phi^2) \quad (6)$$

μ_{eff} and μ_{bf} is the effective viscosity and baseline viscosity respectively. η is the intrinsic viscosity which is equal to 2.5 for a suspension containing spheres. This equation is only valid when the volume fraction, $\phi \leq 0.01$.[129]

Batchelor Model

Batchelor later improved upon the Einstein model by including the effects of high volume fractions of particles $\phi \geq 0.01$ on the viscosity of a suspension. Bachelor's equation takes into consideration the interaction of disturbance of one particle on another nearby particle due to Brownian motion.[130]

$$\frac{\mu_{eff}}{\mu_{bf}} = \mathbf{1 + 2.5\phi + 6.2\phi^2 + O(\phi^3)} \quad (7)$$

The value for the second-order of particles interactions has been reported to vary between 5.2 to 7.6 for spherical particles.[126]

Krieger and Dougherty Model

Krieger and Dougherty later introduced a semi-empirical model for the effective viscosity for higher concentrations of particles.[131] The model is used to identify the effective viscosity of micro/millimetre-sized particles.

$$\frac{\mu_{eff}}{\mu_{bf}} = \left(1 - \frac{\phi}{\phi_m}\right)^{-[\eta]\phi m} \quad (8)$$

Where ϕ_m is the maximum particle volume fraction at which flow occurs the value of which is usually represented as 0.605.

Experimental data by Chen et al. found that the rheological properties of their TiO_2-EG nanoparticles (diameter 25 nm) suspensions were governed by the aggregation of

the particles in the solution. They concluded that when nanoparticles are present in a suspension they mostly exist as aggregates, therefore Chen et al. put forward the following equation to include the effect of aggregation of particles:

$$\frac{\mu_{eff}}{\mu_{bf}} = \left(1 - \frac{\phi_{cs}}{\phi_m}\right)^{-[\eta]\phi m} \tag{9}$$

Where ϕ_{cs} represents the volume fraction of clustered particles.

Modified Krieger and Dougherty

The modified Krieger Dougherty model for the effective viscosity of nanofluids was later introduced to include the effects of aggregates and interfacial layer formation of particles in a suspension.[130] Particle size distribution was used to characterise the clusters in the suspension.

$$\frac{\mu_{eff}}{\mu_{bf}} = \left(1 - \frac{\phi_{esc}}{\phi_m}\right)^{-[\eta]\phi m} \tag{10}$$

Here ϕ_{esc} is the effective volume fraction of clustered spheres, which is derived from

$$\phi_{ecs} = \phi_{cs}(1 + \beta)^3 \tag{11}$$

Where β represents the thickness ratio of the interfacial layer.

2.5.2 Ink Dispersions

Good dispersion of 2D materials within a polymer resin is critical for 3D printing to improve the mechanical, thermal and electrical properties of the printed parts.[132] The main concern when dispersing 2D materials in polymer resins is their tendency to form agglomerates, these agglomerates can form pockets of trapped air in the structures (Figure 28). This can lead to voids and defects in the matrix and therefore reduce the functionality of the printed composite.[133] The reason why

nano-fillers form aggregates are because of their high surface areas and high surface energies.[134] These high surface energies produce strong interfacial interactions in the polymer resin.[135] Agglomeration of the nano-fillers can be avoided by choosing suitable organic solvents for dispersion, functionalisation of the fillers and choosing suitable production methods. There are many ways in which researchers have tried to improve the dispersions of 2D materials within a suspension with methods including ball-milling, high-speed mixers, shear mixing and ultra-sonication.[136][137] Sonication methods are used for high-frequency dispersions of 2D material composites, while ball-milling removes agglomerates from shear and compressive forces.[138] Both these methods can damage the nanoplatelets and alter the original geometries due to their harsh production methods. Speed mixing, however, can be used for a large range of viscosities and uses asymmetric centrifugal forces to mix the inks and remove any cavities, resulting in inhomogeneous mixtures of suspensions.

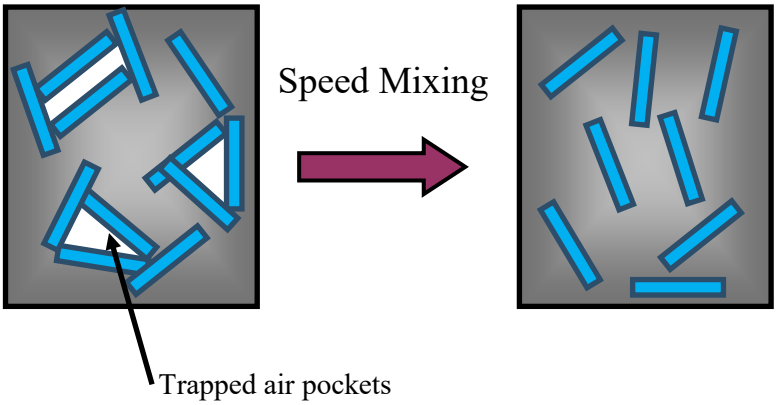

Figure 28 Diagram of filler agglomerates forming in a resin. [133]

2.6 Applications and Properties of 3D Printed 2D Material-based Polymer Composites

Applications of 3D printed 2D material-based composites is as vast as the multi-functionality of the filler. Most of the published literature focuses on the production of electronically conductive inks.[139][140][141][142] However, many of the fillers are used for reinforcement purposes of the polymer material.[143][144] An overview of some of the literature on 3D printed applications of Graphene and BN material composites will now be discussed in the following sub-chapters.

2.6.1 3D Printed Graphene and BN-based Composites

Work by You et al. incorporated 50 wt. % graphene content into a printable suspension using solvents, dispersants and thickening agents for DIW applications.[80] They observed excellent electrical stability under bending stresses by their lightweight electrically conductive inks.[80] Li et al. successfully incorporated giant graphene oxide (GGO) into suspensions for printing flexible electronics using direct-ink writing.[145] 3D printing of graphene oxide by García-Tuñon et al. have reported the development of inks containing 1.75-3 wt. % GO, the inks were printed, freeze-dried and then reduced to obtain conductive rGO structures with microscopic porosity (Figure 29).[81] Zhu et al. developed a method for printing periodic graphene aerogel microlattices via direct-ink writing.[146] Conductivities ranging from 87- 278 Sm^{-1} was achieved from their GO ink formulations containing 20-40 mg ml^{-1} respectively. The printed parts attained relatively low densities and supercompressibilities which they could tune the mechanical properties by modifying the microstructure.

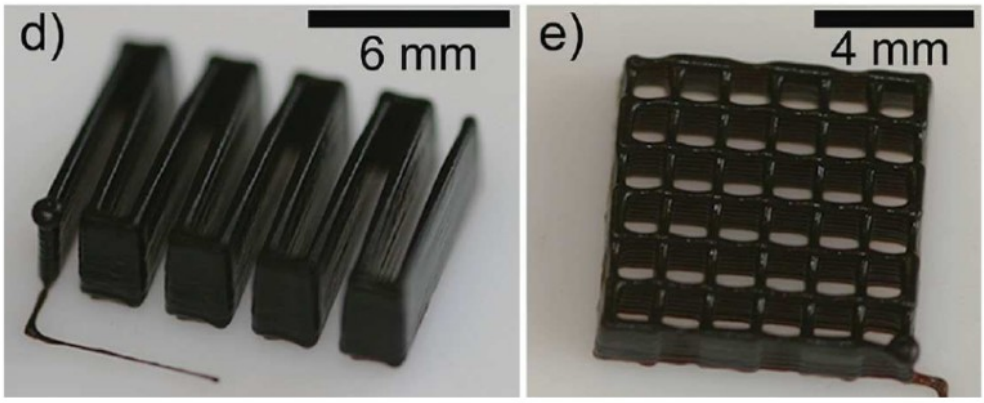

Figure 29 3D-printed graphene structures using DIW. Images showing filament pile (d) and woodpile structures (e) printed through a 150 µm nozzle with a highly concentrated GO/BCS ink (2.5 wt.% GO)[81]

Carey et al. used inkjet printing to print flexible and washable field-effect transistors for wearable electronics using heterostructures with graphene and BN inks (Figure 30).[147] BN inks with enhanced thermal conductivities of 2.1 W/mK at 40 vol. % by Guiney et al. has been reported printed using extrusion-based methods.[148] Foster et al. have used graphene and PLA to produce FDM filaments that were used to print disc electrodes for energy storage devices (Figure 30).[149] Jakus et al. produced

graphene polylactide-*co*-glycolide (PLG) inks for DIW, that were electrically conductive (800 S/m) and biocompatible for applications in bioelectronics.[150]

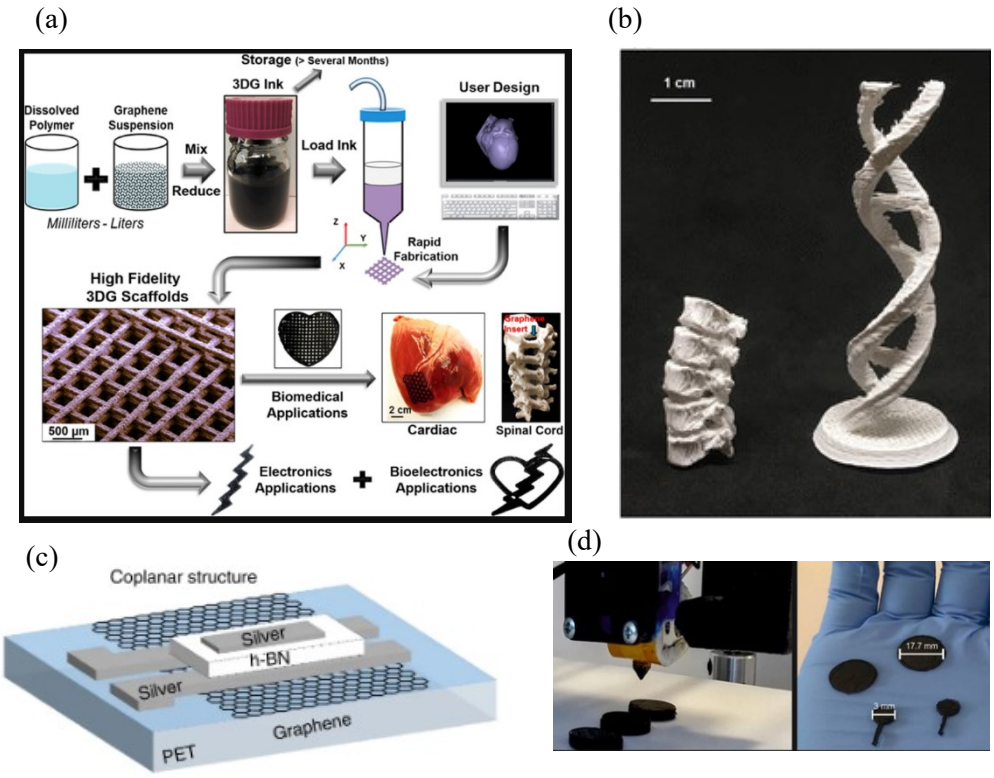

Figure 30 (a) Process of producing graphene-based inks for bioelectronics applications.[150] (b) 3D printed lumbor spine replica and double helix (60 vol. % hBN).[148] (c) Ink-jet printed graphene and BN transistors. [147] (d) FDM printed graphene electrodes for energy storage applications. [149]

2.6.2 Stereolithographic Printed Graphene and BN-based Composites

Printing of 2D-material based composites via SLA has been scarcely reported on thus far. The large aspect ratios of the platelets can produce challenges in ink dispersions, a significant increase in the viscosity and large amounts of scattering or absorption by the filler.[151][152]

Korhonen et al. conducted a study focusing on graphene printed structures using stereolithography. Korhonen et al. first produced inks containing graphene oxide dispersed in a photo-cross linkable acrylic resin. After the parts were fabricated the composite was pyrolysed under a nitrogen atmosphere to reduce the GO and decompose the polymer. The inks contained 1, 2 and 3 wt. % of GO dispersed inside a commercial polymer resin. The homogenised resins were then tested against non-graphene containing resins to determine the cure depths (C_d) and light exposures (E_0)

required to successfully 3D print. The results showed that GO containing resins experienced much lower penetration depths (D_p) than the graphene-free commercial resin. 2D 1mm thick films were printed to test the electrical conductivity of the composite and 3D porous scaffolds were printed to mimic the complex geometries for tissue engineering (Figure 31).[153]

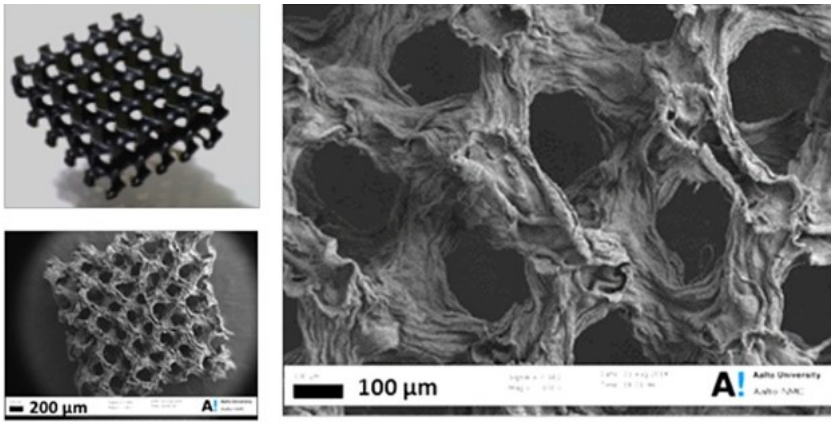

Figure 31 Photograph and SEM image of GO scaffolds made by stereolithography.[153]

Lin et al. 3D printed scaffolds containing GO via stereolithography (Figure 32). The scaffolds displayed an increase in tensile strength of 62.2 % and elongation of 12.8 % with only a 0.2 % addition of GO, resulting in a good combination of strength and ductility.[154] They tested the mechanical properties of the 3D printed parts, finding that an increase in ductility was caused by an increase in crystallinity of the GO reinforced polymer. Further compression tests revealed a metal-like failure model of the GO nanocomposites.[154]

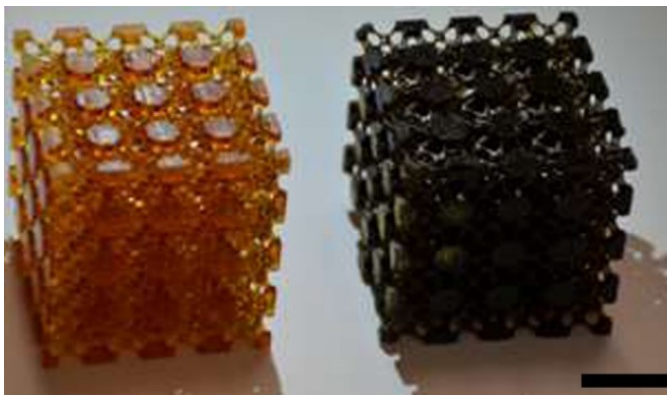

Figure 32 Stereolithography printed polymer and GO reinforced polymer (0.5 wt.%)[154]

Research by Manapat et al. also used dispersed GO in a commercial SLA resin to improve strength properties. They reported a tensile strength increase of 673.6 % with the inclusion of 1 wt. % GO (Figure 33).[155]

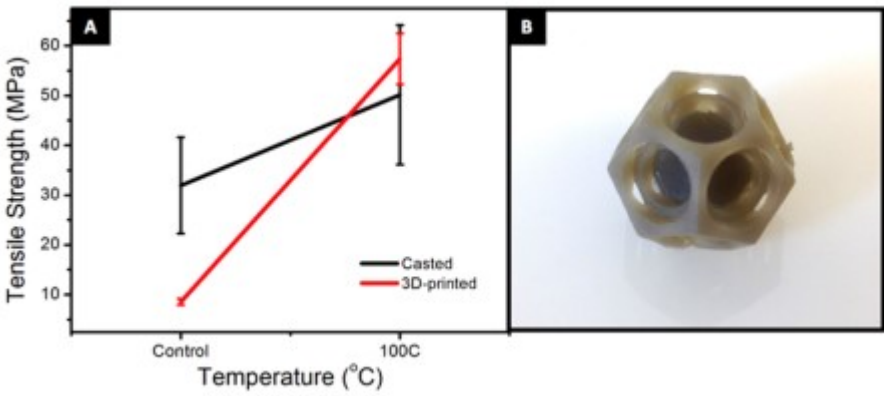

Figure 33 (A) Tensile strength comparison of GO nanocomposite printed using SLA and casted. (B) GO printed composite. [155]

Recently Bustillios et al. reported the dispersion of boron nitride nanosheets (BNNS) in a commercial resin (FLGPCL02, Formlabs Inc.) for SLA applications (Figure 34). They used BNNS as a reinforcement filler for printing scaffolds and found that their 1 wt. % composites damping response had a loss tangent two times higher than the polymer without filler. However, they also reported a decrease in compressive strength in the 3D printed scaffolds attributed to poor curing due to excess scattering from the BN sheets.[156]

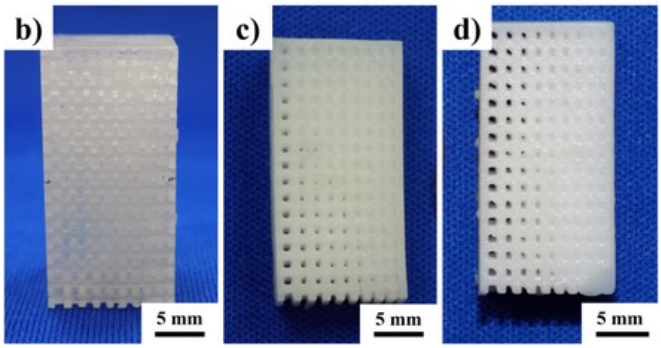

Figure 34 BNNP SLA printed scaffolds. (b) 0 wt. %, (c) 1 wt. %, (d) 5 wt. %.[156]

2.7 Conclusion

This project aims to develop UV-curable 2D material-based composite inks for 3D printing of multi-functional parts via SLA.

The unique properties of GNP and hBN have been highlighted in 2.2, both GNP and hBN show high thermal conductivities and can enhance the thermal conductivity of polymer composites significantly even at relatively low loadings ~2 wt. %. Notably,

GNP is considered an electrical conductor while BN is an electrical insulator. The combination of the two as hybrids creates a synergetic effect for improved thermal conductivity while maintaining electrical insulating properties for potential applications in thermal management of electronic devices.

Although there have been some reports of 2D material-based composites, there are few reports in the literature using additive manufacturing to create these composites. The diverse array of 3D printing technologies offers different qualities in resolution, part dimensions, tolerances and finishes. Each printing technology has a different set of limitations and capabilities which will provide new manufacturing challenges when trying to print using 2D materials and their related composite materials. Stereolithography can be used to fabricate parts with high resolutions and good surface finishes, however, as of yet, the literature has focused mainly on ceramic-based composites rather than 2D materials. Therefore, it would be interesting to combine the structural and functional properties of GNP and BN with the AM technique SLA for the efficient manufacture of multi-functional composites. For potential applications in electronics, thermal management, medical, automotive, aerospace and engineering applications.

2.8 References

[1] K. S. Novoselov *et al.*, "Electric field effect in atomically thin carbon films," *Science*, vol. 306, no. 5696, pp. 666-669, 2004.

[2] V. Nicolosi, M. Chhowalla, M. G. Kanatzidis, M. S. Strano, and J. N. Coleman, "Liquid Exfoliation of Layered Materials," *Science*, vol. 340, no. 6139, pp. 1226419–1226419, 2013.

[3] H. Zhang, "Ultrathin Two-Dimensional Nanomaterials," *ACS Nano*, no. 10, pp. 9451-9469, 2015.

[4] J. N. Coleman *et al.*, "Two-dimensional nanosheets produced by liquid exfoliation of layered materials.," *Science*, vol. 331, no. 6017, pp. 568–571, 2011.

[5] T. Stephenson, Z. Li, B. Olsen, and D. Mitlin, "Lithium ion battery applications of molybdenum disulfide (MoS 2) nanocomposites," *Energy Environ. Sci.*, vol. 7, no. 1, pp. 209–231, 2014.

[6] A. K. Geim and K. S. Novoselov, "The rise of graphene.," *Nat. Mater.*, vol. 6, no. 3, pp. 183–91, 2007.

[7] Y. Wang, Z. Shi, and J. Yin, "Boron nitride nanosheets: large-scale exfoliation in methanesulfonic acid and their composites with polybenzimidazole," *J. Mater. Chem.*, vol. 21, no. 30, p. 11371, 2011.

[8] C. S. S. R. Kumar, *Mixed Metal Nanomaterials*. John Wiley & Sons, 2009.

[9] L. Liu, Y. P. Feng, and Z. X. Shen, "Structural and electronic properties of h - BN," *Phys. Rev. B*, vol. 68, no. 10, p. 104102, 2003.

[10] X.-F. Jiang *et al.*, "Recent Progress on Fabrications and Applications of Boron Nitride Nanomaterials: A Review," *J. Mater. Sci. Technol.*, vol. 31, no. 6, pp. 589–598, 2015.

[11] G. Giovannetti, P. A. Khomyakov, G. Brocks, P. J. Kelly, and J. van den Brink, "Substrate-induced band gap in graphene on hexagonal boron nitride: Ab initio density functional calculations," *Phys. Rev. B*, vol. 76, no. 7, p. 073103, 2007.

[12] B. Marinho, M. Ghislandi, E. Tkalya, C. E. Koning, and G. de With, "Electrical conductivity of compacts of graphene, multi-wall carbon nanotubes, carbon black, and graphite powder," *Powder Technol.*, vol. 221, pp. 351-358, 2012.

[13] M. J. Meziani *et al.*, "Boron nitride nanomaterials for thermal management applications.," *Chemphyschem*, vol. 16, no. 7, pp. 1339–46, 2015.

[14] J. C. Zheng *et al.*, "High thermal conductivity of hexagonal boron nitride laminates," *2D Mater.*, vol. 3, no. 1, p. 11004, 2016.

[15] H. Ebadi-Dehaghani and M. Nazempour, "Thermal Conductivity of nanoparticles Filled Polymers," in *Smart Nanoparticles Technology*, vol. 23, pp. 519–540, 2012.

[16] H. E.-D. and M. Nazempour, *Smart Nanoparticles Technology*. InTech, 2012.

[17] C. Yuan *et al.*, "Modulating the thermal conductivity in hexagonal boron nitride

via controlled boron isotope concentration," *Commun. Phys.*, vol. 2, no. 43, 00. 1-8, 2019.

[18] S. Stankovich *et al.*, "Graphene-based composite materials," *Nature*, vol. 442, no. 7100, 2006.

[19] J. M. Tour, "Top-Down versus Bottom-Up Fabrication of Graphene-Based Electronics," *Chem. Mater.*, vol. 26, no. 1, pp. 163–171, 2014.

[20] K. S. Novoselov, V. I. Fal'ko, L. Colombo, P. R. Gellert, M. G. Schwab, and K. Kim, "A roadmap for graphene.," *Nature*, vol. 490, no. 7419, pp. 192–200, 2012.

[21] J. T. Han *et al.*, "Extremely efficient liquid exfoliation and dispersion of layered materials by unusual acoustic cavitation.," *Sci. Rep.*, vol. 4, p. 5133, 2014.

[22] C. Y. Zhi, Y. Bando, C. C. Tang, H. Kuwahara, and D. Golberg, "Large-Scale Fabrication of Boron Nitride Nanosheets and Their Utilization in Polymeric Composites with Improved Thermal and Mechanical Properties," *Adv. Mater.*, vol. 21, no. 28, pp. 2889–2890, 2009.

[23] A. B. Bourlinos, V. Georgakilas, R. Zboril, T. a. Steriotis, A. K. Stubos, and C. Trapalis, "Aqueous-phase exfoliation of graphite in the presence of polyvinylpyrrolidone for the production of water-soluble graphenes," *Solid State Commun.*, vol. 149, no. 47–48, pp. 2172–2176, 2009.

[24] P. May, U. Khan, J. M. Hughes, and J. N. Coleman, "Role of Solubility Parameters in Understanding the Steric Stabilization of Exfoliated Two-Dimensional Nanosheets by Adsorbed Polymers," *J. Phys. Chem. C*, vol. 116, no. 20, pp. 11393–11400, 2012.

[25] A. C. Ferrari *et al.*, "Raman Spectrum of Graphene and Graphene Layers," *Phys. Rev. Lett.*, vol. 97, no. 18, p. 187401, 2006.

[26] D. Gonzalez Ortiz, C. Pochat-Bohatier, J. Cambedouzou, M. Bechelany, and P. Miele, "Exfoliation of hexagonal boron nitride (h-BN) in liquide phase by ion intercalation," *Nanomaterials*, vol. 8, no. 9, p. 716, 2018.

[27] L. H. Li, Y. Chen, G. Behan, H. Zhang, M. Petravic, and A. M. Glushenkov, "Large-scale mechanical peeling of boron nitride nanosheets by low-energy ball milling," *J. Mater. Chem.*, vol. 21, pp. 11862-11866, 2011.

[28] A. Ciesielski and P. Samorì, "Graphene via sonication assisted liquid-phase exfoliation," *Chemical Society Reviews*. vol. 43, pp. 381-398, 2014.

[29] Y. Hernandez *et al.*, "High-yield production of graphene by liquid-phase exfoliation of graphite," *Nat. Nanotechnol.*, vol. 3, no. 9, pp. 563–568, 2008.

[30] L. Cao, S. Emami, and K. Lafdi, "Large-scale exfoliation of hexagonal boron nitride nanosheets in liquid phase," *Mater. Express*, vol. 219, p. 1700482, 2014.

[31] C. Fu *et al.*, "Improving thermal conductivity of polymer composites by reducing interfacial thermal resistance between boron nitride nanotubes," *Compos. Sci. Technol.*, vol. 165, pp. 322-330, 2018.

[32] Z. Lin, A. Mcnamara, Y. Liu, K. Moon, and C.-P. Wong, "Exfoliated hexagonal

boron nitride-based polymer nanocomposite with enhanced thermal conductivity for electronic encapsulation," *Compos. Sci. Technol.*, vol. 90, pp. 123–128, 2014.

[33] X. Wang, C. Zhi, Q. Weng, Y. Bando, and D. Golberg, "Boron Nitride Nanosheets: novel Syntheses and Applications in polymeric Composites," *J. Phys. Conf. Ser.*, vol. 471, no. 1, p. 012003, 2013.

[34] C. Min, D. Yu, J. Cao, G. Wang, and L. Feng, "A graphite nanoplatelet/epoxy composite with high dielectric constant and high thermal conductivity," *Carbon N. Y.*, vol. 55, pp. 116–125, 2013.

[35] M. Shtein, R. Nadiv, M. Buzaglo, K. Kahil, and O. Regev, "Thermally Conductive Graphene-Polymer Composites: Size, Percolation, and Synergy Effects," *Chem. Mater.*, vol. 27, no. 6, pp. 2100–2106, 2015.

[36] L. Zhang, J. Zhu, W. Zhou, J. Wang, and Y. Wang, "Thermal and electrical conductivity enhancement of graphite nanoplatelets on form-stable polyethylene glycol/polymethyl methacrylate composite phase change materials," *Energy*, vol. 39, no. 1, pp. 294–302, 2012.

[37] N. Zhang, Y. Jing, Y. Song, Y. Du, and Y. Yuan, "Thermal properties and crystallization kinetics of pentaglycerine/graphene nanoplatelets composite phase change material for thermal energy storage," *Int. J. Energy Res.*, p. er.4946, 2019.

[38] Z. T. Yu *et al.*, "Increased thermal conductivity of liquid paraffin-based suspensions in the presence of carbon nano-additives of various sizes and shapes," *Carbon N. Y.*, vol. 53, pp. 277–285, 2013.

[39] X. Zheng and B. Wen, "Practical PBT/PC/GNP composites with anisotropic thermal conductivity," *RSC Adv.*, vol. 9, no. 62, pp. 36316–36323, 2019.

[40] F. Wang, L. T. Drzal, Y. Qin, and Z. Huang, "Enhancement of fracture toughness, mechanical and thermal properties of rubber/epoxy composites by incorporation of graphene nanoplatelets," *Compos. Part A Appl. Sci. Manuf.*, vol. 87, pp. 10–22, 2016.

[41] H. S. Kim, H. S. Bae, J. Yu, and S. Y. Kim, "Thermal conductivity of polymer composites with the geometrical characteristics of graphene nanoplatelets," *Sci. Rep.*, vol. 6, no. 1, p. 26825, 2016.

[42] J. Hou *et al.*, "Preparation and characterization of surface modified boron nitride epoxy composites with enhanced thermal conductivity," *RSC Adv.*, vol. 4, no. 83, pp. 44282–44290, 2014.

[43] N. Yang *et al.*, "Preparation and properties of thermally conductive polyimide/boron nitride composites," *RSC Adv.*, vol. 6, no. 22, pp. 18279–18287, 2016.

[44] H. B. Cho *et al.*, "Insulating polymer nanocomposites with high-thermal-conduction routes via linear densely packed boron nitride nanosheets," *Compos. Sci. Technol.*, vol. 129, pp. 205–213, 2016.

[45] G. W. Lee, M. Park, J. Kim, J. I. Lee, and H. G. Yoon, "Enhanced thermal conductivity of polymer composites filled with hybrid filler," *Compos. Part A*

Appl. Sci. Manuf., vol. 37, no. 5, pp. 727-734, 2006.

[46] Y. Zhang, W. Gao, Y. Li, D. Zhao, and H. Yin, "Hybrid fillers of hexagonal and cubic boron nitride in epoxy composites for thermal management applications," *RSC Adv.*, vol. 9, no. 13, pp. 7388–7399, 2019.

[47] K. Kalaitzidou, H. Fukushima, and L. T. Drzal, "A new compounding method for exfoliated graphite-polypropylene nanocomposites with enhanced flexural properties and lower percolation threshold," *Compos. Sci. Technol.*, vol. 67, no. 10, pp. 2045-2051, 2007.

[48] J. Liang *et al.*, "Electromagnetic interference shielding of graphene/epoxy composites," *Carbon N. Y.*, vol. 47, no. 3, pp. 922–925, 2009.

[49] W. Zheng and S.-C. Wong, "Electrical conductivity and dielectric properties of PMMA/expanded graphite composites," *Compos. Sci. Technol.*, vol. 63, no. 2, pp. 225–235, 2003.

[50] W. Zheng, X. Lu, and S.-C. Wong, "Electrical and mechanical properties of expanded graphite-reinforced high-density polyethylene," *J. Appl. Polym. Sci.*, vol. 91, no. 5, pp. 2781–2788, 2004.

[51] H. Bin Zhang *et al.*, "Electrically conductive polyethylene terephthalate/graphene nanocomposites prepared by melt compounding," *Polymer (Guildf).*, vol. 51, no. 5, pp. 1191–1196, 2010.

[52] G. Chen, W. Weng, D. Wu, and C. Wu, "PMMA/graphite nanosheets composite and its conducting properties," *Eur. Polym. J.*, vol. 39, no. 12, pp. 2329–2335, 2003.

[53] S. Vadukumpully, J. Paul, N. Mahanta, and S. Valiyaveettil, "Flexible conductive graphene/poly(vinyl chloride) composite thin films with high mechanical strength and thermal stability," *Carbon N. Y.*, vol. 49, no. 1, pp. 198–205, 2011.

[54] S. Chandrasekaran, C. Seidel, and S. Karl, "Preparation and characterization of graphite nano-platelet (GNP)/epoxy nano-composite: Mechanical, electrical and thermal properties," *Eur. Polym. J.*, vol. 49, pp. 3878–3888, 2013.

[55] S. Kashi, R. K. Gupta, N. Kao, S. A. Hadigheh, and S. N. Bhattacharya, "Influence of graphene nanoplatelet incorporation and dispersion state on thermal, mechanical and electrical properties of biodegradable matrices," *J. Mater. Sci. Technol.*, vol. 34, no. 6, pp. 1026–1034, 2018.

[56] T. Xia, D. Zeng, Z. Li, R. J. Young, C. Vallés, and I. A. Kinloch, "Electrically conductive GNP/epoxy composites for out-of-autoclave thermoset curing through Joule heating," *Compos. Sci. Technol.*, vol. 164, pp. 304–312, 2018.

[57] M. Shtein, R. Nadiv, M. Buzaglo, and O. Regev, "Graphene-Based Hybrid Composites for Efficient Thermal Management of Electronic Devices.," *ACS Appl. Mater. Interfaces*, vol. 7, no. 42, pp. 23725–30, 2015.

[58] M. Zhou *et al.*, "Highly conductive porous graphene/ceramic composites for heat transfer and thermal energy storage," *Adv. Funct. Mater.*, vol. 23, no. 18, pp. 2263–2269, 2013.

[59] X. Cui, P. Ding, N. Zhuang, L. Shi, N. Song, and S. Tang, "Thermal Conductive and Mechanical Properties of Polymeric Composites Based on Solution-Exfoliated Boron Nitride and Graphene Nanosheets: A Morphology-Promoted Synergistic Effect," *ACS Appl. Mater. Interfaces*, vol. 7, no. 34, pp. 19068–19075, 2015.

[60] M. Owais, J. Zhao, A. Imani, G. Wang, H. Zhang, and Z. Zhang, "Synergetic effect of hybrid fillers of boron nitride, graphene nanoplatelets, and short carbon fibers for enhanced thermal conductivity and electrical resistivity of epoxy nanocomposites," *Compos. Part A Appl. Sci. Manuf.*, vol. 117, pp. 11-22, 2019.

[61] L. Shao, L. Shi, X. Li, N. Song, and P. Ding, "Synergistic effect of BN and graphene nanosheets in 3D framework on the enhancement of thermal conductive properties of polymeric composites," *Compos. Sci. Technol.*, vol. 135, pp. 83–91, 2016.

[62] K. Wu, C. Lei, W. Yang, S. Chai, F. Chen, and Q. Fu, "Surface modification of boron nitride by reduced graphene oxide for preparation of dielectric material with enhanced dielectric constant and well-suppressed dielectric loss," *Compos. Sci. Technol.*, vol. 134, pp. 191–200, 2016.

[63] J. Yang *et al.*, "Largely enhanced thermal conductivity of poly (ethylene glycol)/boron nitride composite phase change materials for solar-thermal-electric energy conversion and storage with very low content of graphene nanoplatelets," *Chem. Eng. J.*, vol. 315, pp. 481–490, 2017.

[64] J. A. Lewis, "Direct Ink Writing of 3D Functional Materials," *Adv. Funct. Mater.*, vol. 16, no. 17, pp. 2193–2204, 2006.

[65] T. Wohlers and T. Gornet, "History of additive manufacturing," *Wohlers Rep. Addit. Manuf. 3D Print. State Ind. Annu. Worldw. Prog. Rep.*, 2011.

[66] I. Gibson, D. W. Rosen, and B. Stucker, *Additive manufacturing technologies*. Springer, 2010.

[67] S. C. Tjong, "Structural and mechanical properties of polymer nanocomposites," *Materials Science and Engineering R: Reports*. vol. 53, no. 3-4, pp. 73-197, 2006.

[68] L. Nayak, S. Mohanty, S. K. Nayak, and A. Ramadoss, "A review on inkjet printing of nanoparticle inks for flexible electronics," *J. Mater. Chem. C*, vol. 7, pp. 8771-8795, 2019.

[69] T. D. Ngo, A. Kashani, G. Imbalzano, K. T. Q. Nguyen, and D. Hui, "Additive manufacturing (3D printing): A review of materials, methods, applications and challenges," *Compos. Part B Eng.*, vol. 143, pp. 172–196, 2018.

[70] S. C. Ligon, R. Liska, J. Stampfl, M. Gurr, and R. Mülhaupt, "Polymers for 3D Printing and Customized Additive Manufacturing," *Chem. Rev.*, vol. 117, no. 15, pp. 10212–10290, 2017.

[71] X. Cui, T. Boland, D. DD'Lima, and M. K Lotz, "Thermal inkjet printing in tissue engineering and regenerative medicine," *Recent Pat. Drug Deliv. Formul.*, vol. 6, no. 2, pp. 149–155, 2012.

[72] A. Kamyshny and S. Magdassi, “Conductive nanomaterials for printed electronics,” *Small*, vol. 10, no. 17. 2014.

[73] S. F. S. Shirazi *et al.*, “A review on powder-based additive manufacturing for tissue engineering: selective laser sintering and inkjet 3D printing.,” *Sci. Technol. Adv. Mater.*, vol. 16, no. 3, p. 033502, 2015.

[74] J. M. Williams *et al.*, “Bone tissue engineering using polycaprolactone scaffolds fabricated via selective laser sintering,” *Biomaterials*,vol. 26, no. 23, pp. 4817-4827, 2005.

[75] Y. L. Kong, M. K. Gupta, B. N. Johnson, and M. C. McAlpine, “3D printed bionic nanodevices,” *Nano Today*, vol. 11, no. 3, pp. 330–350, 2016.

[76] F. Fina, C. M. Madla, A. Goyanes, J. Zhang, S. Gaisford, and A. W. Basit, “Fabricating 3D printed orally disintegrating printlets using selective laser sintering,” *Int. J. Pharm.*, vol. 541, no. 1-2, pp. 101-107, 2018.

[77] C. Hurt *et al.*, “Combining additive manufacturing and catalysis: a review,” *Catal. Sci. Technol.*, vol. 7, no. 16, pp. 3421–3439, 2017.

[78] E. García-Tuñón, E. Feilden, H. Zheng, E. D’Elia, A. Leong, and E. Saiz, “Graphene Oxide: An All-in-One Processing Additive for 3D Printing,” *ACS Appl. Mater. Interfaces*, vol. 9, no. 38, pp. 32977–32989, 2017.

[79] P. Jiang, Z. Ji, X. Zhang, Z. Liu, and X. Wang, “Recent advances in direct ink writing of electronic components and functional devices,” *Prog. Addit. Manuf.*, vol. 3, no. 38, pp. 32977-32989, 2018.

[80] X. You *et al.*, “Three-dimensional graphene-based materials by direct ink writing method for lightweight application,” *Int. J. Light. Mater. Manuf.*, vol. 1, no. 2, pp. 96–101, 2018.

[81] E. García-Tuñon *et al.*, “Printing in three dimensions with graphene.,” *Adv. Mater.*, vol. 27, no. 10, pp. 1688–93, 2015.

[82] S. H. Masood, “Advances in Fused Deposition Modeling,” in *Comprehensive Materials Processing*, vol. 10, no. 6, p. 1209, 2014.

[83] E. Ivanov *et al.*, “PLA/Graphene/MWCNT Composites with Improved Electrical and Thermal Properties Suitable for FDM 3D Printing Applications,” *Appl. Sci.*, vol. 9, no. 6, p. 1209, 2019.

[84] J. Liu, W. Li, Y. Guo, H. Zhang, and Z. Zhang, “Improved thermal conductivity of thermoplastic polyurethane via aligned boron nitride platelets assisted by 3D printing,” *Compos. Part A Appl. Sci. Manuf.*, vol. 120, pp. 140-146, 2019.

[85] E. Pei, J. Shen, and J. Watling, “Direct 3D printing of polymers onto textiles: Experimental studies and applications,” *Rapid Prototyp. J.*, vol. 21, no. 5, pp. 556-571, 2015.

[86] C. Lee Ventola, “Medical applications for 3D printing: Current and projected uses,” *P T*, vol. 39, no. 10, pp. 704-711, 2014.

[87] D. Popescu, A. Zapciu, C. Amza, F. Baciu, and R. Marinescu, “FDM process parameters influence over the mechanical properties of polymer specimens: A

review," *Polym. Test.*, vol. 69, pp. 157-166, 2018.

[88] Y. He, Y. Wu, J. Fu, Q. Gao, and J. Qiu, "Developments of 3D Printing Microfluidics and Applications in Chemistry and Biology: a Review," *Electroanalysis*, vol. 28, no. 8, pp. 1658-1678, 2016.

[89] S. Waheed *et al.*, "3D printed microfluidic devices: Enablers and Barriers," *Lab Chip*, no. 16, p. 1993, 2016.

[90] N. Yang, Y. Tian, and D. Zhang, "Novel real function based method to construct heterogeneous porous scaffolds and additive manufacturing for use in medical engineering," *Med. Eng. Phys.*, vol. 37, no. 11, pp. 1037–1046, 2015.

[91] J. H. Lee, R. K. Prud'homme, and I. A. Aksay, "Cure depth in photopolymerization: Experiments and theory," *J. Mater. Res.*, vol. 16, no. 12, pp. 3536–3544, 2011.

[92] T. R. Guess, R. S. Chambers, and T. D. Hinnerichs, "Epoxy and acrylate sterolithography resins: in-situ property measurements," Albuquerque, NM, and Livermore, CA (United States), 1996.

[93] X. Wu *et al.*, "Effects of soft-start exposure on the curing characteristics and flexural strength in ceramic projection stereolithography process," *J. Eur. Ceram. Soc.*, vol. 39, no. 13, pp. 3788–3796, 2019.

[94] A. R. Torrado and D. A. Roberson, "Failure Analysis and Anisotropy Evaluation of 3D-Printed Tensile Test Specimens of Different Geometries and Print Raster Patterns," *J. Fail. Anal. Prev.*,vol. 16, no. 1, pp. 154-164, 2016.

[95] M. L. Griffith and J. W. Halloran, "Freeform Fabrication of Ceramics via Stereolithography," *J. Am. Ceram. Soc.*, vol. 79, no. 10, pp. 2601–2608, 2005.

[96] G. A. Brady and J. W. Halloran, "Stereolithography of ceramic suspensions," *Rapid Prototyp. J.*, vol. 3, no. 2, pp. 61–65, 2005.

[97] M. L. Griffith and J. W. Halloran, "Scattering of ultraviolet radiation in turbid suspensions," *J. Appl. Phys.*, vol. 81, no. 6, pp. 2538–2546, 1997.

[98] M. L. Griffith and J. W. Halloran, "Ultraviolet curing of highly loaded ceramic suspensions for stereolithography of ceramics," in *Proc. Solid Freeform Fabr. Symp*, pp. 396–403, 1994.

[99] M. L. Griffith and J. W. Halloran, "Freeform Fabrication of Ceramics via Stereolithography," *J. Am. Ceram. Soc.*, vol. 79, no. 10, pp. 2601–2608, 2005.

[100] C. Hinczewski, S. Corbel, and T. Chartier, "Ceramic suspensions suitable for stereolithography," *J. Eur. Ceram. Soc.*, vol. 18, no. 6, pp. 583–590, 1998.

[101] J. P. Kruth, M. C. Leu, and T. Nakagawa, "Progress in additive manufacturing and rapid prototyping," *CIRP Ann. - Manuf. Technol.*, vol. 47, no. 2, pp. 525-540, 1998.

[102] E. Andrzejewska, "Free Radical Photopolymerization of Multifunctional Monomers," *Three-Dimensional Microfabr. Using Two-phot. Polym.*, pp. 62–81, 2016.

[103] *Stereolithography: Materials, Processes and Applications*. Springer Science &

Business Media, 2011.

[104] E. Andrzejewska, "Photopolymerization kinetics of multifunctional monomers," *Progress in Polymer Science (Oxford)*. vol. 26, no. 4, pp. 605-665, 2001.

[105] D. Bourell *et al.*, "Materials for additive manufacturing," *CIRP Ann.*, vol. 66, no. 2, pp. 659–681, 2017.

[106] J. P. Fisher, D. Dean, P. S. Engel, and A. G. Mikos, "Photoinitiated Polymerization of Biomaterials," *Annu. Rev. Mater. Res.*, vol. 31, no. 1, pp. 171–181, 2001.

[107] B. D. Fairbanks, M. P. Schwartz, C. N. Bowman, and K. S. Anseth, "Photoinitiated polymerization of PEG-diacrylate with lithium phenyl-2,4,6-trimethylbenzoylphosphinate: polymerization rate and cytocompatibility.," *Biomaterials*, vol. 30, no. 35, pp. 6702–7, 2009.

[108] P. Ferreira, J. F. J. Coelho, J. F. Almeida, and M. H. Gil, "3 Photocrosslinkable Polymers for Biomedical Applications." 2012

[109] M. Degirmenci, G. Hizal, and Y. Yagci, "Articles Synthesis and Characterization of Macrophotoinitiators of Poly(-caprolactone) and Their Use in Block Copolymerization," vol. 35, no. 22, pp. 8265-8270, 2002.

[110] A. Sanches-Silva *et al.*, "Study of the Migration of Photoinitiators Used in Printed Food-Packaging Materials into Food Simulants," *J. Agric. Food Chem.*, vol. 57, no. 20, pp. 9516–9523, 2009.

[111] A. Priola, G. Gozzelino, F. Ferrero, and G. Malucelli, "Properties of polymeric films obtained from u.v. cured poly(ethylene glycol) diacrylates," *Polymer (Guildf).*, vol. 34, no. 17, pp. 3653–3657, 1993.

[112] H. R. Ashjari, A. Ahmadi, and M. S. S. Dorraji, "Synthesis and employment of PEGDA for fabrication of superhydrophilic PVDF/PEGDA electrospun nanofibrous membranes by in-situ visible photopolymerization," *Korean J. Chem. Eng.*, vol. 35, no. 1, pp. 289–297, 2018.

[113] K. McAvoy, D. Jones, and R. R. S. Thakur, "Synthesis and Characterisation of Photocrosslinked poly(ethylene glycol) diacrylate Implants for Sustained Ocular Drug Delivery," *Pharm. Res.*, vol. 35, no. 2, p. 36, 2018.

[114] G. Taormina, C. Sciancalepore, M. Messori, and F. Bondioli, "3D printing processes for photocurable polymeric materials: technologies, materials, and future trends," *Journal of Applied Biomaterials and Functional Materials*. vol. 16, no. 3, pp. 151-160, 2018.

[115] N. Siddharth, M. Viola, Y. Mousa, and A. Ozan, "Chitosan:PEGDA hybrid-gel scaffolds printed by stereolithography," *Front. Bioeng. Biotechnol.*, 2016.

[116] G. Gonzalez *et al.*, "Development of 3D printable formulations containing CNT with enhanced electrical properties," *Polym. (United Kingdom)*, vol. 109, pp. 246–253, 2017.

[117] Y. Jiang and Q. Wang, "Highly-stretchable 3D-architected Mechanical Metamaterials," *Sci. Rep.*, vol. 6, no. 34147, 2016.

[118] A. P. Moreno Madrid, S. M. Vrech, M. A. Sanchez, and A. P. Rodriguez, "Advances in additive manufacturing for bone tissue engineering scaffolds," *Materials Science and Engineering C*. vol. 100, pp. 631-644, 2019.

[119] X. Wang, M. Jiang, Z. Zhou, J. Gou, and D. Hui, "3D printing of polymer matrix composites: A review and prospective," *Compos. Part B Eng.*, vol. 110, pp. 442–458, 2017.

[120] P. M. Grubb, H. Subbaraman, S. Park, D. Akinwande, and R. T. Chen, "Inkjet printing of high performance transistors with micron order chemically set gaps," *Sci. Rep.*, vol. 7, no. 1202, 2017.

[121] J. Stampfl *et al.*, "Photopolymers with tunable mechanical properties processed by laser-based high-resolution stereolithography," *J. Micromechanics Microengineering*, vol. 18, no. 125014, 2008.

[122] Z. Wang, R. Abdulla, B. Parker, R. Samanipour, S. Ghosh, and K. Kim, "A simple and high-resolution stereolithography-based 3D bioprinting system using visible light crosslinkable bioinks," *Biofabrication*, vol. 7, no. 4, 2015.

[123] B. Zhang, B. Seong, V. D. Nguyen, and D. Byun, "3D printing of high-resolution PLA-based structures by hybrid electrohydrodynamic and fused deposition modeling techniques," *J. Micromechanics Microengineering*, vol. 26, p. 35015, 2016.

[124] B. Derby and N. Reis, "Inkjet Printing of Highly Loaded Particulate Suspensions," *MRS Bulletin*. vol. 28, no. 11, pp. 815-818, 2003.

[125] C. Leonelli and M. Romagnoli, "Rheology parameters of alkali-activated geopolymeric concrete binders," in *Handbook of Alkali-Activated Cements, Mortars and Concretes*, pp. 133-169, 2014.

[126] W. Tesfai, P. Singh, Y. Shatilla, M. Z. Iqbal, and A. A. Abdala, "Rheology and microstructure of dilute graphene oxide suspension," *J. Nanoparticle Res.*, vol. 15, p. 1989, 2013.

[127] W. J. Tseng and K. C. Lin, "Rheology and colloidal structure of aqueous TiO2 nanoparticle suspensions," *Mater. Sci. Eng. A*, vol. 155, no. 1-2, pp. 186-192, 2003.

[128] B. C. Pak and Y. I. Cho, "Hydrodynamic and heat transfer study of dispersed fluids with submicron metallic oxide particles," *Exp. Heat Transf.*, vol. 11, no. 2, pp. 151-171, 1998.

[129] E. W. J. MARDLES, "Viscosity of Suspensions and the Einstein Equation," *Nature*, vol. 145, no. 3686, pp. 970–970, 1940.

[130] R. Deepak Selvakumar and S. Dhinakaran, "Effective viscosity of nanofluids — A modified Krieger–Dougherty model based on particle size distribution (PSD) analysis," *J. Mol. Liq.*, vol. 225, pp. 20–27, 2017.

[131] I. M. Krieger and T. J. Dougherty, "A Mechanism for Non-Newtonian Flow in Suspensions of Rigid Spheres," *Cit. Trans. Soc. Rheol.*, vol. 3, p. 137, 1959.

[132] G. Hou, W. Tao, J. Liu, Y. Gao, L. Zhang, and Y. Li, "Tailoring the dispersion of nanoparticles and the mechanical behavior of polymer nanocomposites by

designing the chain architecture," *Phys. Chem. Chem. Phys.*, vol. 19, pp. 32024-32037, 2017.

[133] L. W. T. Ng *et al.*, "Printing of Graphene and Related 2D Materials: Technology, Formulation and Applications," 2018.

[134] A. Kozbial *et al.*, "Study on the surface energy of graphene by contact angle measurements," *Langmuir*, vol. 30, no. 28, pp. 8598–8606, 2014.

[135] R. Atif and F. Inam, "Reasons and remedies for the agglomeration of multilayered graphene and carbon nanotubes in polymers," *Beilstein J. Nanotechnol.*, vol. 7, pp. 1174-1196, 2016.

[136] C. Teng, D. Xie, J. Wang, Z. Yang, G. Ren, and Y. Zhu, "Ultrahigh Conductive Graphene Paper Based on Ball-Milling Exfoliated Graphene," *Adv. Funct. Mater.*, vol. 7, p. 1700240, 2017.

[137] S. G. Prolongo, A. Jimenez-Suarez, R. Moriche, and A. Ureña, "In situ processing of epoxy composites reinforced with graphene nanoplatelets," *Compos. Sci. Technol.*, vol. 86, p. 185-191, 2013.

[138] Y. Yao, Z. Lin, Z. Li, X. Song, K. S. Moon, and C. P. Wong, "Large-scale production of two-dimensional nanosheets," *J. Mater. Chem.*, vol. 22, pp. 13494-13499, 2012.

[139] H. Guo, R. Lv, and S. Bai, "Recent advances on 3D printing graphene-based composites," *Nano Mater. Sci.*,vol.1, no. 2, pp. 101-115, 2019.

[140] S. Singh, S. Ramakrishna, and F. Berto, "3D Printing of polymer composites: A short review," *Mater. Des. Process. Commun.*, 2019.

[141] J. Czyzewski, P. Burzyński, K. Gaweł, and J. Meisner, "Rapid prototyping of electrically conductive components using 3D printing technology," *J. Mater. Process. Technol.*,vol. 209, no. 12-13, pp. 5281-5285, 2009.

[142] Y. S. Rim, S. H. Bae, H. Chen, N. De Marco, and Y. Yang, "Recent Progress in Materials and Devices toward Printable and Flexible Sensors," *Adv. Mater.*, vol. 28, no. 22, pp. 4415–4440, 2016.

[143] B. G. Compton and J. A. Lewis, "3D-Printing of Lightweight Cellular Composites," *Adv. Mater.*, vol. 26, no. 34, pp. 5930–5935, 2014.

[144] A. S. Dalaq, D. W. Abueidda, and R. K. Abu Al-Rub, "Mechanical properties of 3D printed interpenetrating phase composites with novel architectured 3D solid-sheet reinforcements," *Compos. Part A Appl. Sci. Manuf.*, vol. 84, pp. 266–280, 2016.

[145] W. Li *et al.*, "Flexible Circuits and Soft Actuators by Printing Assembly of Graphene," *ACS Appl. Mater. Interfaces*, p. acsami.6b04235, 2016.

[146] C. Zhu *et al.*, "Highly compressible 3D periodic graphene aerogel microlattices," *Nat. Commun.*, vol. 6, no. 1, p. 6962, 2015.

[147] T. Carey *et al.*, "Fully inkjet-printed two-dimensional material field-effect heterojunctions for wearable and textile electronics," *Nat. Commun.*, vol. 8, no. 1202, 2017.

[148] L. M. Guiney, N. D. Mansukhani, A. E. Jakus, S. G. Wallace, R. N. Shah, and M. C. Hersam, "Three-Dimensional Printing of Cytocompatible, Thermally Conductive Hexagonal Boron Nitride Nanocomposites," *Nano Lett.*, vol. 18, no. 6, pp. 3488-3493, 2018.

[149] C. W. Foster *et al.*, "3D Printed Graphene Based Energy Storage Devices," *Sci. Rep.*, vol. 7, no. 42233, 2017.

[150] A. E. Jakus, E. B. Secor, A. L. Rutz, S. W. Jordan, M. C. Hersam, and R. N. Shah, "Three-Dimensional Printing of High-Content Graphene Scaffolds for Electronic and Biomedical Applications," *ACS Nano*, vol. 9, no. 4, pp. 4636–4648, 2015.

[151] A. Harvey *et al.*, "Non-resonant light scattering in dispersions of 2D nanosheets," *Nat. Commun.*, vol. 9, no. 1, p. 4553, 2018.

[152] Z. Weng, Y. Zhou, W. Lin, T. Senthil, and L. Wu, "Structure-property relationship of nano enhanced stereolithography resin for desktop SLA 3D printer," *Compos. Part A Appl. Sci. Manuf.*, vol. 88, pp. 234–242, 2016.

[153] H. Korhonen *et al.*, "Fabrication of graphene-based 3D structures by stereolithography," *Phys. status solidi*, vol. 213, no. 4, pp. 982-985, 2015.

[154] D. Lin *et al.*, "3D stereolithography printing of graphene oxide reinforced complex architectures.," *Nanotechnology*, vol. 26, no. 43, p. 434003, 2015.

[155] J. Z. Manapat, J. D. Mangadlao, B. D. B. Tiu, G. C. Tritchler, and R. C. Advincula, "High-Strength Stereolithographic 3D Printed Nanocomposites: Graphene Oxide Metastability," *ACS Appl. Mater. Interfaces*, vol. 9, no. 11, pp. 10085–10093, 2017.

[156] J. Bustillos, D. Montero-Zambrano, A. Loganathan, B. Boesl, and A. Agarwal, "Stereolithography-based 3D printed photosensitive polymer/boron nitride nanoplatelets composites," *Polym. Compos.*, vol. 40, no. 1, pp. 379–388, 2019.

[157] "Additive Manufacturing Technologies: An Overview | 3D Hubs." [Online]. Available: https://www.3dhubs.com/knowledge-base/additive-manufacturing-technologies-overview. [Accessed: 12-Oct-2018].

[158] X. Lin, J. Kavalakkatt, M. C. Lux-Steiner, and A. Ennaoui, "Inkjet-Printed $Cu_2ZnSn(S, Se)_4$ Solar Cells," *Adv. Sci.*, vol. 2, no. 6, p. 1500028, 2015.

[159] H. S. Kim, J. S. Kang, J. S. Park, H. T. Hahn, H. C. Jung, and J. W. Joung, "Inkjet printed electronics for multifunctional composite structure," *Compos. Sci. Technol.*, vol. 69, no. 7–8, pp. 1256–1264, 2009.

[160] B. S. Cook, J. R. Cooper, and M. M. Tentzeris, "An Inkjet-Printed Microfluidic RFID-Enabled Platform for Wireless Lab-on-Chip Applications," *IEEE Trans. Microw. Theory Tech.*, vol. 61, no. 12, pp. 4714–4723, 2013.

[161] A. H. Espera, A. D. Valino, J. O. Palaganas, L. Souza, Q. Chen, and R. C. Advincula, "3D Printing of a Robust Polyamide-12-Carbon Black Composite via Selective Laser Sintering: Thermal and Electrical Conductivity," *Macromol. Mater. Eng.*, vol. 304, no. 4, p. 1800718, 2019.

[162] A. D. Valentine *et al.*, "Hybrid 3D Printing of Soft Electronics," *Adv. Mater.*,

2017.

[163] A. A. Konta, M. García-Piña, and D. R. Serrano, "Personalised 3D printed medicines: Which techniques and polymers are more successful?," *Bioengineering*. vol. 4, no. 4, p. 79, 2017.

[164] S. Gantenbein, K. Masania, W. Woigk, J. P. W. Sesseg, T. A. Tervoort, and A. R. Studart, "Three-dimensional printing of hierarchical liquid-crystal-polymer structures," *Nature*, vol. 561, no. 7722, pp. 226–230, 2018.

[165] F. Ning, W. Cong, J. Qiu, J. Wei, and S. Wang, "Additive manufacturing of carbon fiber reinforced thermoplastic composites using fused deposition modeling," *Compos. Part B Eng.*, vol. 4, pp. 369-378, 2015.

[166] Stratasys, "What is FDM?: Fused Deposition Modeling Technology for 3D Printing | Stratasys." [Online]. Available: https://www.stratasys.com/fdm-technology. [Accessed: 23-Sep-2019].

[167] "UV damage | Johnson and Johnson Vision Care Companies." [Online]. Available: https://www.jnjvisioncare.co.uk/education/uv-damage. [Accessed: 13-Oct-2018].

[168] "2019 Dental 3D Printing Guide: All You Need to Know | All3DP." [Online]. Available: https://all3dp.com/2/dental-3d-printing-all-you-need-to-know/. [Accessed: 24-Nov-2019].

3

Materials and Method

3.1 2D Material Synthesis

Hexagonal boron nitride powder (Alfa Aesar, 99.5 % (metal basis)) starting flake size ~7.45 was exfoliated using liquid-phase exfoliation method. Deionised water and 2-propanol (Alfa Aesar, 99+ %) were mixed in the ratio 1:1, 150 mg/ml of hBN powder was added to the solution and sonicated (30 Hz, 37 W power) in an ultra-sonication bath (Thermo Fisher Scientific) for 1 hour at 25 °C. During sonication, a water cooling system was used to obtain a constant temperature. After sonication, a white suspension was obtained consisting of a homogenous phase and some large aggregates. Bulk material was removed by centrifugation at 1000 rpm for 20 minutes to leave a homogeneous dispersion of hBN. The hBN flakes were then collected using vacuum filtration (cellulose filter paper, Whatman) and washed through with deionised water to remove the excess solvent. The hBN flakes were then characterised using AFM and SEM to determine the average lateral size to be ~4.28 µm. This proved to be the optimal exfoliation method for producing flakes with large lateral sizes after previously trying different exfoliation times and techniques including tip sonication.

Graphene nanoplatelets (xGNP, grade M 25, XG Sciences) starting flake size ~5.75 µm were prepared using the same liquid-phase exfoliation method as previously mentioned. The average flake size of the GNP after exfoliation was determined to be ~4.31 µm.

3.2 UV-Curable Composite Ink Formulation

To produce photo-cross linkable inks suitable for SLA the ink must consist of two main components; a monomer resin consisting of molecules with highly sensitive acrylate end groups or epoxide end groups and a photoinitiator (PI). For the SLA (Viper Si2, 3D systems) used in this research, the photoinitiator was required to begin initiation at 354.7 nm wavelength. Poly (ethylene glycol) diacrylate (Sigma-Aldrich, M_n 575) was selected due to its already established use as a photocurable resin in SLA[1][2][3][4]. The photoinitiator selected for this study was Phenylbis (2, 4, 6-trimethylbenzoyl) phosphine oxide (97% powder, Mw 418.5, Sigma-Aldrich) also known as BAPO and Irgacure 819. BAPO was chosen due to its high reactivity at 295 nm and 370 nm suitable for the SLA, some pre-trials of other photoinitiators including Irgacure 184 and 2959 were eliminated due to the quality of print achieved.

BAPO (1 wt. %) was added to PEGDA and mixed for 2 hours at room temperature using a magnetic stirrer until a homogenous yellow resin was obtained. Due to the highly reactive properties of BAPO even within the visible light range all dispersions needed to be covered with aluminium foil to avoid unwanted curing whilst mixing. The resulting resin made the basis of all further photocurable inks (UV-ink).

The exfoliated hexagonal boron nitride and GNP flakes were then added in varying concentrations (table 4) to the UV-ink and speed mixed using DAC 150 SP Mixer (Synergy Devices Limited). To achieve inks with good dispersions, a small amount of the UV-resin was first added to the nano-platelets within a PP (polypropylene) speed mixing container and mixed for 3 minutes at 2000 rpm. This enabled a thick paste of either hBN or GNP to be formed (figure 35). The subsequent UV resin was then added to the paste and mixed for a further 10 minutes at 2500 rpm in 120s cycles with a 30s rest period in between each cycle to avoid overheating of the speed mixer. For increased concentrations of hBN or GNP faster speeds or longer mixing times can be used to ensure a smooth homogenous ink is formed without agglomerates.

Table 4 Concentration of 2D materials in PEGDA resin used to describe the naming of the composites.

Ink	BN (wt. %)	GNP (wt. %)	vol. %	PEGDA (wt. %)
BN 0.1	0.10		0.05	99.90
BN 1	1.00		0.53	99.00
BN 2	2.00		1.07	98.00
BN 4	4.00		2.13	96.00
BN 8	8.00		4.27	92.00
BN 20	20.00	-	10.67	80.00
GNP 0.1	-	0.10	0.05	99.80
GNP 1	-	1.00	0.53	99.00
GNP 2	-	2.00	1.07	98.00
GNP 4	-	4.00	2.13	96.00
GNP 8	-	8.00	4.27	92.00

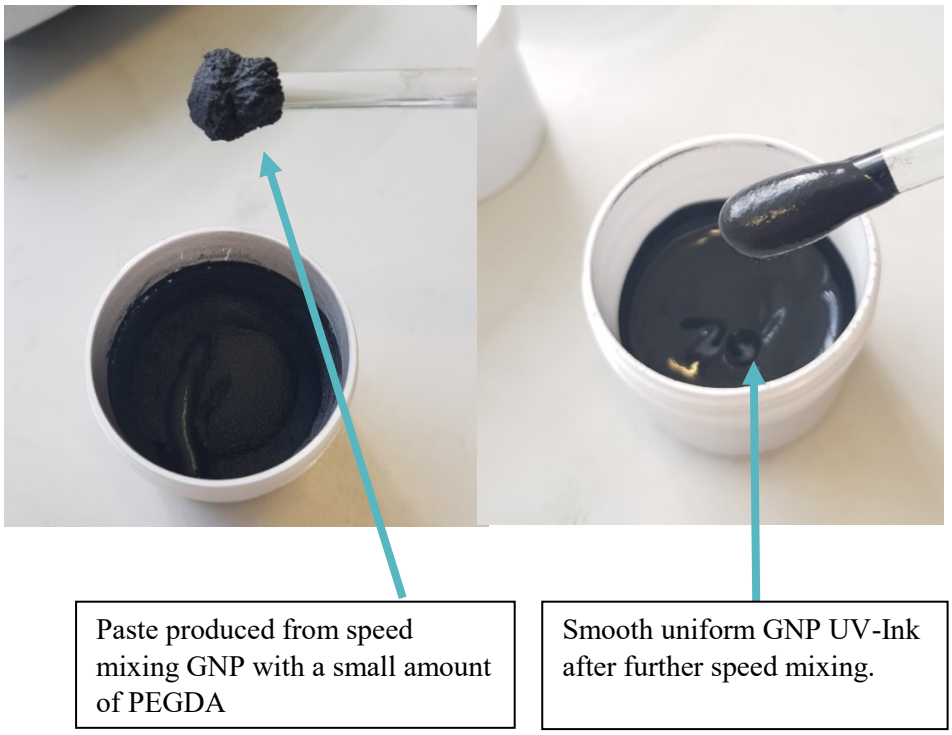

Figure 35 Speed mixing results of GNP and UV curable ink.(Left image) Results from mixing a small amount of PEGDA with GNP flakes to produce a course paste, (right image) Smooth resin after the rest of the UV has been added to the paste.

3.3 Hybrid Inks

Hybrid inks containing both hBN and GNP as fillers were chosen due to their high theoretical thermal conductivities. Hexagonal boron nitride has a theoretical thermal conductivity of 600 W/mK in-plane and 30 W/mK in the out plane direction, whilst graphene shows thermal conductivities between 200-2000 W/Km in-plane and 2-800 W/Km out of plane [5]. These high thermal conductivities make hBN and GNP attractive fillers for increasing the thermal conductivity of polymers. Hybrids of GNP and hBN were developed to achieve high thermal conductivities for thermal management applications in electronics whilst eliminating any electronic conductivity.

Hybrid inks containing both hBN and GNP were synthesised using PEGDA and BAPO as previously mentioned. Bulk hBN (44µm, Alfa Aesar, 99.5 % (metal basis)) was used as the primary filler and mixed with the UV-ink using DAC 150 SP Mixer (Synergy Devices Limited) for 10 minutes at 2500 rpm in 120 s cycles with a 30 s rest period. The secondary filler either eGNP or eBN were added in varying ratios 1:1, 1:4,

1:9, 1:19 and 0.2 :19.8. The maximum solid loading of the inks was 20 wt. % in respects to the UV-ink.

3.4 Printing

Like most 3D printing techniques, SLA requires a 3D CAD model of an object to be printed. In this work, the majority of CAD files were generated using Autodesk Inventor Professional and converted into an stl. file. This file was then imported to *'3D Lightyear'* a programme set up to communicate the stl. file to the SLA printer. Here a computerised build platform was generated to imitate the one in the SLA Viper Si2 (3D Systems). The supports could then be generated and edited were required to assist in the printing. The CAD model with supports could then be sliced into a series of layers to be printed.

Setting up the SLA firstly requires filling the vat with a photoactive resin, this could take the form of either a petri dish for 2D prints or a larger vat for 3D prints. To avoid bubbles within the resin the inks were always transferred carefully into the vat. The build plate could then be aligned to sit approximately 0.5 mm on the top surface of the resin. The temperature control was then set between 25-30 °C as the SLA will not print outside of this range. The main parameters of the resin the E_c, critical exposure energy and D_p, depth of penetration of the laser could then be selected, the optimised values of these were found from running a test called '*Window Panes'*.

Window Panes

The Window Panes test was created to find an appropriate photoinitiator (PI) and PI concentration to print using UV curing of the SLA laser. The test is used to find the depth of penetration (D_p), the distance where the laser's energy attenuates to $1/e$ of the surface energy, and the critical exposure energy (E_c), the minimum energy required to initiate polymerisation.[6] These parameters are calculated using the working curve equation (12) and represent the optimum printing parameter for the resin, as the D_p and E_c parameters are the only adjustable printing parameters directly related to the chemistry of the resin. All new resins should go through the Window Panes test before printing a 3D part to help optimise the final resolution. The window panes tests involve printing five 'panes' (one layer thick films) (figure 36) each of different thickness. The set thickness of each pane should be 80, 100, 120, 140 and 160 µm (Cd1 the thinnest up to Cd5 the thickest pane), each pane is cured using

different energy intensities known as the exposure energy E_0. The thickness of each pane is then measured, this thickness is known as the cure depth (C_d), the maximum resolution in the z-axis. The C_d of each pane is then plotted against its related E_0 to produce a working curve (Figure 37). The gradient of the curve is represented by the D_p depth of penetration of the laser and the x-intercept representing the critical exposure energy E_c. The E_c and D_p values are used to calibrate the SLA for each resin formulation as the chemistry of the resin and type of filler and concentration of filler will affect these parameters.

$$C_d = D_p \ln\left[\frac{E_0}{E_c}\right] \quad (12)$$

The windows pane test was used to calculate the optimum printing parameters for each of

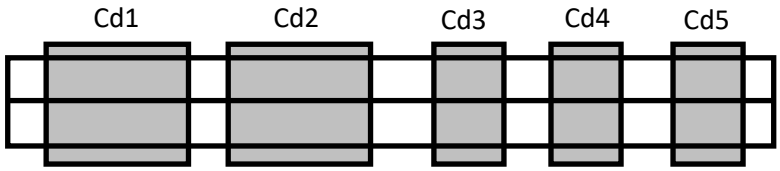

Figure 36 Schematic of printed window panes showing a series of 5 panes Cd1 representing the thinnest pane to Cd5 the thickest pane

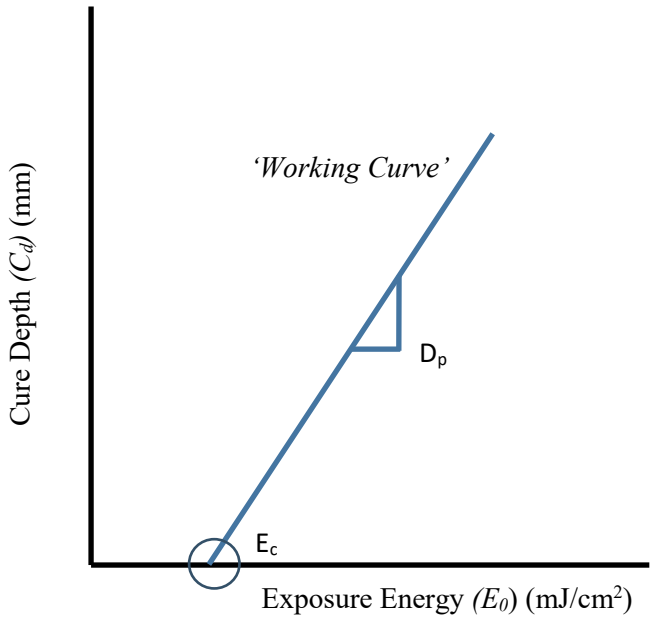

Figure 37 Graph showing a typical representation of the working curve from the window panes test. The measured cure depth (C_d) is plotted against the exposure energy (E_0) on an ln scale. The gradient of the curve provides the D_p value, how far the laser can penetrate through the resin where the intensity of the laser reaches 1/e of its original value. The x-intercept is the E_c value were below this exposure energy curing will not occur.

the composite inks to obtain the best resolution possible. The results of the tests were

also used to study the scattering effects of the laser interacting with the GNP and hBN fillers, to gain a deeper understanding of the requirements and challenges of 3D printing with 2D materials.

Post-processing

Post-processing of all printed parts via stereolithography firstly involves the removal of all supports. If the supports were relatively soft and under cured these could be easily removed by hand and washing carefully, however, if the supports were more rigid scissors or clippers were used to remove the supports. Following on from this all printed parts were then washed in a bath of isopropanol to remove any excess un-polymerised resin that remained on the surface. The parts were then moved to a UV oven were they further cured for 15 minutes to fully polymerise the parts and leave a smooth finish without any tacky surfaces.

3.5 Characterisations

Scanning Electron Microscopy (SEM)

Scanning electron microscopy is used to image the surface of a material on a micron and sub-micron level. Standard optical microscopy is limited by the longer wavelengths of visible light. Electrons can be used to image samples at a much higher resolution at sub-micron levels due to their shorter wavelengths. The improvement of resolution from imaging the surface of a sample can range from microns in optical microscopy to nm in scanning electron microscopy.

SEM uses a condenser lens to focus a beam of electrons onto the surface of the sample; this, therefore, limits the area of sample that can be imaged at any one time (figure 38). A raster mode is used to image the surface of a sample line by line to produce an image. There are three main signals produced when the electron beam interacts with the surface of a sample these include secondary electrons (SE), backscattered electrons (BSE) and characteristic X-rays. Secondary electrons are the most commonly used signal for imagining in SEM. Secondary electrons are produced as a result of inelastic scattering, they are the electrons from the conduction or valance bands with energies below 50 eV and are picked up by the secondary electron detector. BSEs are the elastic scattering of electrons (through more than 90°) with energies greater than 50 eV.[7] BSEs interact with the nuclei of the atom of a sample; therefore larger atoms with a greater atomic number are more likely to produce BSEs due to their larger cross-sectional area.[7]

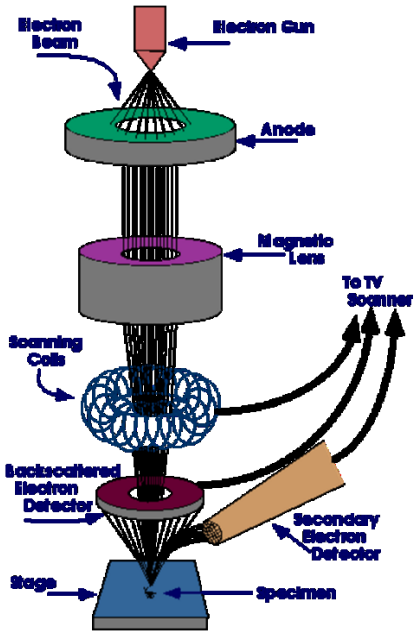

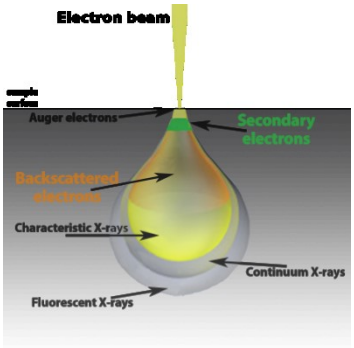

Figure 38 Schematic showing the working set-up of SEM (above), schematic showing the interaction of the incident electron beam with the sample and the associated characteristic interactions used to create the SEM image (below).[8]

SEM samples have been prepared via carbon coating to ~16nm to avoid the accumulation of charges on the surface of the sample which hinders the imaging of the structure of the surface by producing bright spots / noisy images. The SEM microscope used was Zeiss Ultra 55. All sample images were obtained using the secondary electron mode with a voltage ranging between 1 kV and 5 kV and a working distance of 8 mm.

Atomic Force Microscopy (AFM)

Atomic force microscopy (AFM) is used to detect the physical properties of a sample such as height, friction, lateral size, by scanning a cantilever with a sharp edge over the surface of a sample and detecting the deflections of the cantilever from the reflections of the laser (figure 39). AFM usually will use a tip as the sharp edge which is made out of silicon or silicon nitride and has an approximate radius of 10s of nm. The resolution of the image is therefore limited by the radius of the tip. Tapping mode is commonly used in imagining in AFM it works by vertically oscillating the tip across the surface of the sample at a frequency between 50,000 to 500,000 cycles/sec. As the tip reaches the surface of the sample the oscillation amplitude is reduced due to a loss in energy caused by the tip contacting the surface.

Advantages of AFM include easy sample preparation, works in air, vacuum and liquids, accurate height information is produced, 3D imaging. The main disadvantages of using AFM is the limited vertical range, slow scan speeds and the tip can easily damage and may even damage the sample.

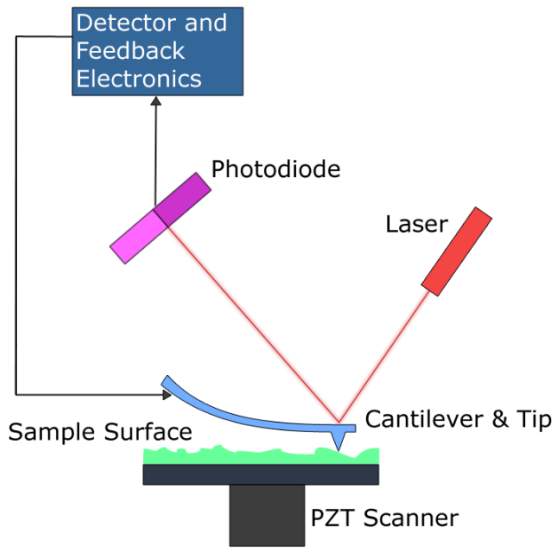

Figure 39 Schematic showing the working principles of AFM.

AFM has been used in this work as a characterisation technique for all 2D materials. The AFM used was the Dimension FastScan by Bruker. All samples were spin-coated onto a silicon substrate and tested under tapping mode. The height profiles and morphology of both graphene nanoplatelets and boron nitride flakes were analysed to gain a better understanding of the 2D materials used within the inks.

Fourier Transform Infrared Spectrometer (FT-IR)

FT-IR is a quantitative analytical technique, which is used to acquire information on the composition of a material. It works by shinning a monochromatic beam through a sample in either liquid or solid form to a detector beneath the sample; the absorbance of the sample is recorded at a specific single frequency (figure 40). During exposure to infrared molecules in the sample will selectively absorb radiation at specific wavelengths. This causes the vibrational energy levels of the molecule to jump from the ground state to an excited one. The difference in vibrational energy will produce the frequency of the peak. This data is received by a detector called an interferometer, and is converted using Fourier transformation to produce a fingerprint spectrum of the sample, in transmittance (%) or absorbance over wavenumber (cm^{-1}).

FT-IR was used on all samples to create a fingerprint of the characteristic bonds present. This could be used to see if the parts were fully cured of if further post-processing of the printed parts was needed. All samples were measured using the Nicolet 5700 (Thermo electron corporation) FT-IR with OMNIC software. An average of 32 scans between 4000-500 cm^{-1} was completed in transmission mode.

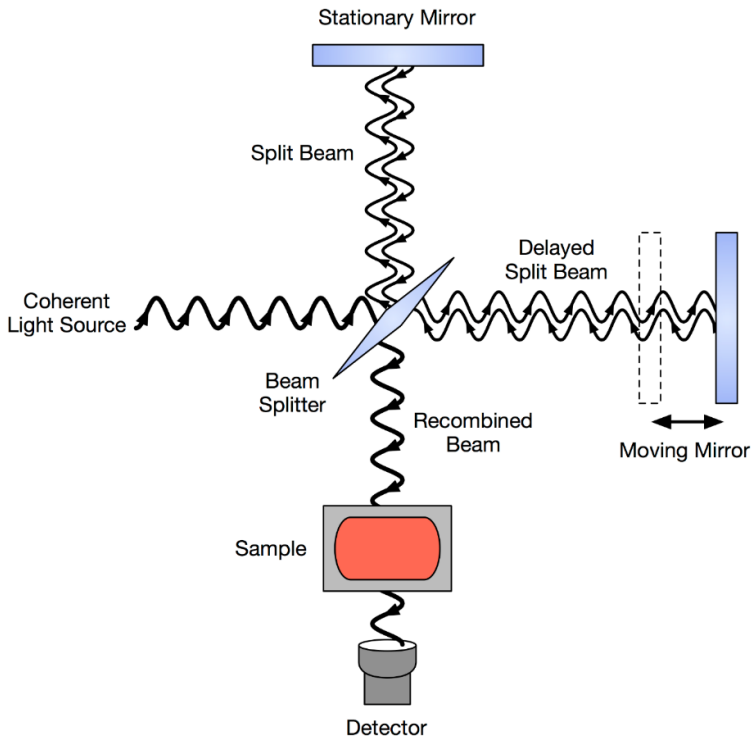

Figure 40 Schematic showing the principle workings of an FTIR spectrometer.

Ink Rheology

Rheology is an important polymer processing tool for 3D printing inks, finding correlations between the processing of the polymer and the suitability to the 3D printer. Rheology is the study of deformation and flow of a material used to characterise the mechanical properties through describing the flow in relation to strains, stresses and time.[9] There are three main methods to test the rheology of polymer resins including capillary, rotational and extensional rheometers (figure 41). In this work, a rotational rheometer was used to study the properties of the inks as this technique has widely been reported throughout current literature.[10][11][12] Testing with rotational rheometers involves placing a paste or fluid between either two parallel plates or one cone and one flat plate. The sample is then sheared between the plates.

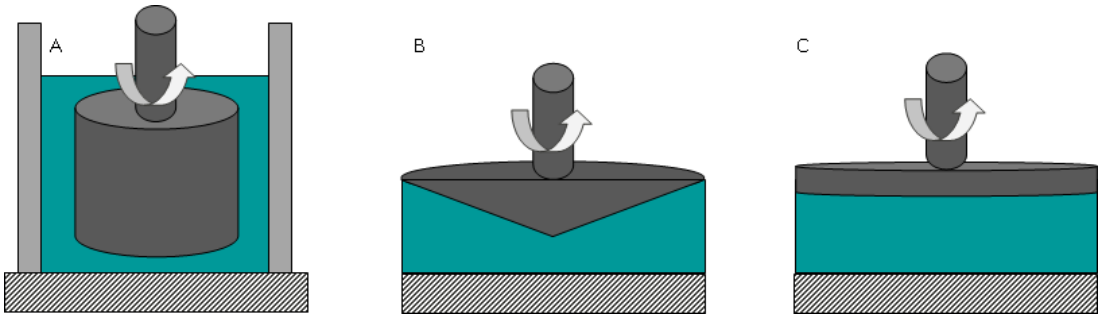

Figure 41 Schematic representing the main three types of rotational techniques: (a) concentric cylinder (b) torsion using cone geometry (c) torsion using parallel plates.

The shear stress, shear rate, strain and viscosity of the sample have been described below in the following equations:

$$Shear\ stress(\sigma) = \frac{F}{A} = \frac{N}{m^2} = Pa$$

$$Shear\ rate(\acute{\varepsilon}) = \frac{v}{h} = \frac{ms^{-1}}{m} = s^{-1}$$

$$Strain = \frac{\Delta x}{h} = \frac{m}{m} = dimensionless$$

$$Viscosity(\eta) = \frac{\tau}{\ddot{\Upsilon}} = \frac{Pa}{s^{-1}} = Pas$$

Where v is the velocity, h is the distance, Δx is the change in distance, F is the force and A is the area.

The rheological properties of the UV curable inks were characterised using a stress-controlled rheometer Discovery HR3 by TA systems and analysed using TRIOS software (figure 42). A 60mm flat Peltier plate was used with a gap of 500 µm. For more viscous inks and pastes, smaller plates could be used to save on materials, however, due to the relatively low viscosity of some of the UV-inks a larger plate was used to allow for spreading of the fluid ink, excess material was removed to fit within the geometry of the plate. A flow sweep was used to measure the apparent viscosity of the inks in relation to the shear rate at 25°C to mimic the conditions of the SLA. These measurements were carried out using a strain rate of 0.02-200s^{-1}. The main requirement for SLA resins is that the ink must be able to flow to deposit a fresh new layer of resin onto the previously cured layer. Therefore there is a large range of viscosity for the inks as long as it's below 3000mPas.[13] Oscillatory measurements of the inks were also taken at 1 Hz with variations of the oscillatory stress logarithmically from 0.1-1000Pa.

Figure 42 Discovery DH-3 Rheometer by TA Systems.

UV-Visible Spectroscopy

Ultraviolet-visible (UV-Vis) absorption is a characterisation technique that can be used to identify particle sizes of nanomaterials. UV-vis can also be used to identify the specific wavelength or range of wavelength that photocurable inks for the SLA will cure at. This can be a very useful tool in matching the correct photoinitiator for each resin (figure 43).

UV-vis absorption spectroscopy measures the attenuation of a beam of light that passes through a sample, the absorption measurements can be taken over a specific wavelength or across the desired range. The main principles of UV-vis spectroscopy include the transition of electrons in a molecule from a lower energy level to a higher level.

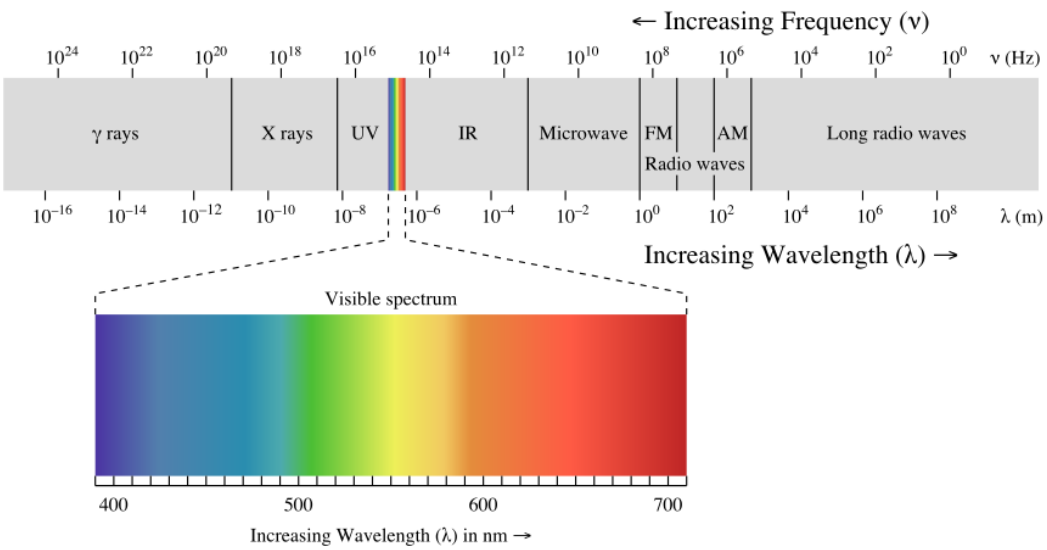

Figure 43 Spectrum of electromagnetic radiation.

UV-vis has been used to analyse the compatibility of the ink with the SLA's laser system. The SLA system used in this work uses a laser with a wavelength of 354.7nm. Therefore all formulations of inks had to be able to cure at this wavelength. The analysis of samples was performed on the PerkinElmer Lambda25 UV/VIS spectroscopy from 700-200 nm. All samples were diluted x100 and analysed using quartz glass cells (Hellma Analytics).

Differential Scanning Calorimetry (DSC)

Differential scanning calorimetry is a thermal analysis characterisation technique which can be used to evaluate the different phases a polymer may go through during heating and cooling cycles. In particular, the glass transition temperature T_g, melting temperature T_m and crystallisation temperature T_c, can all be identified through analysing the resulting thermograph (figure 44).

DSC measures the temperature and heat flows of a material in relation to their transitions as a function of time and temperature in a controlled atmosphere. It is a quantitative technique which collects information regarding the physical and chemical changes that involve exothermic or endothermic processes. DSC is based on the use of two separate chambers, one containing a reference and the other containing the sample to be analysed. The difference in the quantity of heat required to increase the temperature of both samples is recorded in terms of temperature. Dependent on the endothermic or exothermic nature of the material being analysed an increased or decreased amount of heat will be required to maintain the temperature increase constant. This data can then be used to produce a thermograph identifying the different phase changes the material is subjected to, similar to that seen in figure 44.

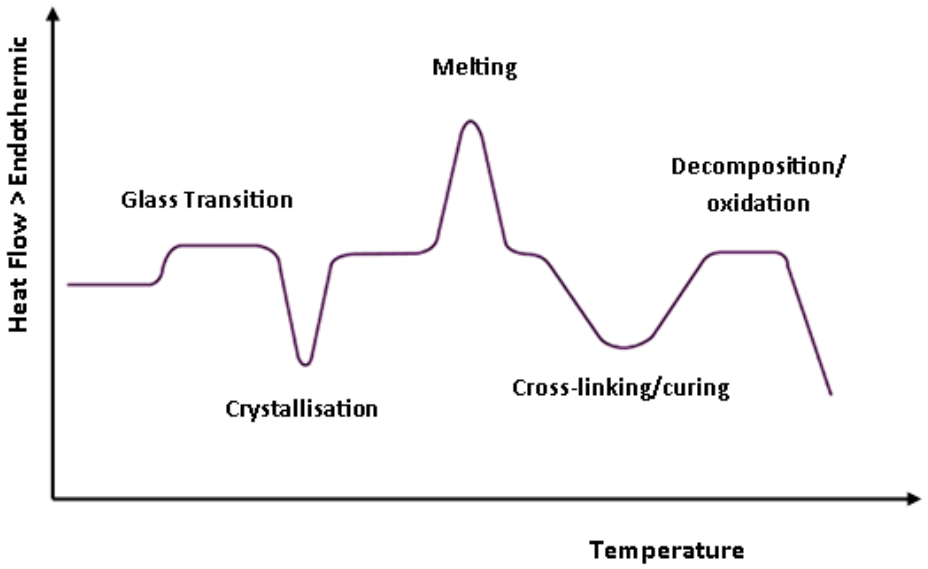

Figure 44 DSC thermogram showing the transitions of a typical thermoplastic in relation to temperature changes.

In this work, DSC was used to analyse the T_g and thermal properties of the UV-inks, hybrid inks. The DSC used was the TA Q100 series; the heat cycle used was heat, cool, heat in the range of -150 °C to 200 °C with a heating/cooling rate of 5 °C/min.

For calculating the specific heat capacity of the printed samples for thermal conductivity measurements, the samples were measured using a modulated heat ramp sample from 30 °C -200 °C with a heating rate of 5 °C/min.

Thermal Gravimetric Analysis TGA

TGA is a quantitative analysis by weight of a material[14], the technique is used to monitor the change in mass over a set temperature range and atmosphere. TGA measurements are mainly used to determine the composition of a material and to foresee how thermally stable a material will be up to temperatures of 1200 °C. Weight loss exhibited in TGA can be due to decomposition, breaking of chemical bonds or evaporation due to the loss of volatiles at high temperatures. Weight gain, however, is mainly due to oxidation therefore this can be eliminated by using inert atmospheres. In this work, TGA was mainly used for compositional analysis and thermal stability of the printed parts.

All samples were weighed and measured in aluminium 100 µl pans and tested using TGA Q500 by TA systems. Samples were tested in a nitrogen atmosphere with a constant heating rate of 10 °C/ min. The temperature range at which the samples were tested was between 0-1000 °C.

Density Measurements

To calculate the density of each samples Archimedes' principle was used by calculating the displaced volume of an object in a liquid of known density. To do this the mass of the sample dry and infiltrated with water were measured using a balance. All samples were placed under vacuum to help infiltrate the samples with water. To determine the density of the samples the following equation was used:

$$\rho = \frac{m_d \times (\rho_w - 0.001225)}{0.99983 \times (m_d - m_w)} + 0.001225$$

Where ρ_w represents the density of water and $(m_d - m_w)$ provides the buoyancy G. The density of water is assumed to be 1000 g/cm^3. The density of air under these tests conditions is 0.001225.

Thermal Analysis: Laser Flash

To analyse the thermal diffusivity and conductivity of the printed samples the laser flash system LFA427 by Netzsch was used to study the thermal transport properties. Laser flash is a widely used technique to measure the thermal diffusivity of a material at a specified temperature. A laser pulse is first shot in an upwards direction for the underside of the sample. The temperature change in the upper surface of the sample is then measured using an infrared detector. A graph of change in temperature against time is produced from the signal (figure 45). The half time ($t_{1/2}$) can then be used along with the thermal diffusivity (a), the thickness of the sample (d) and thermal conductivity (λ) using the following formula:

$$\lambda(T) = a(T) \times c_p(T) \times \rho(T)$$

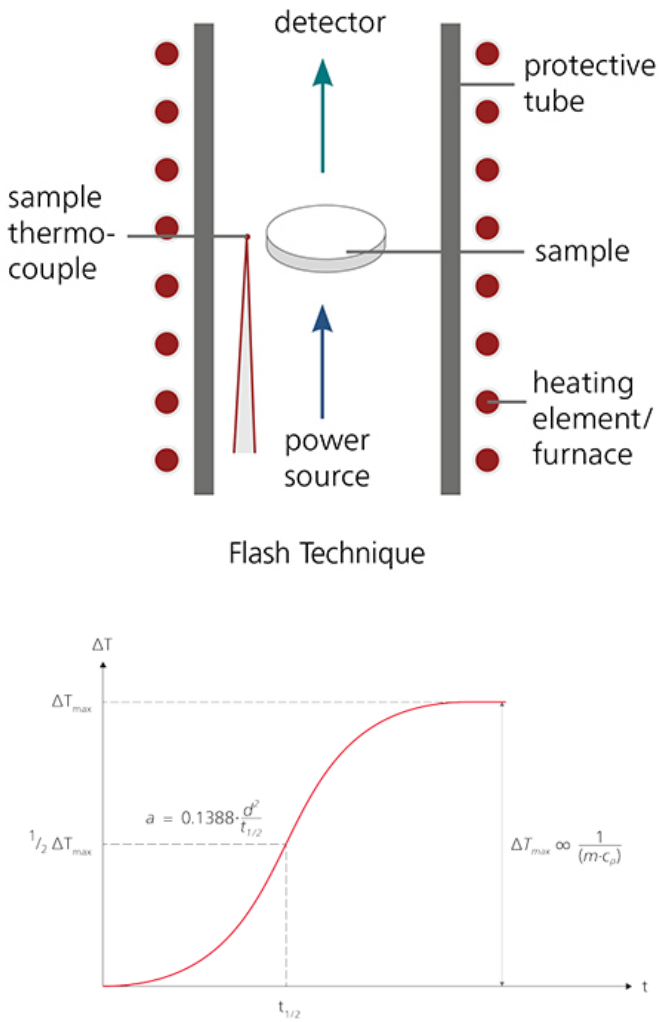

Figure 45 Schematic of working principle of the laser flash technique (above). Representation of a typical graph produced from laser flash technique (below). [15]

The specific heat capacity of each sample was measured using modulated DSC and density measurements were taken before using the laser flash. All samples were printed in disks 10mm in radius with approximately a 1 mm thickness, to compensate for over curing some samples were ground down to the desired thickness. Each sample was then coated in a thin layer of carbon before testing. An average of five measurements was taken at 30 °C, 60 °C 0 °C, 90 °C, 120 °C and 150 °C, using 400 V laser. Each sample was measured and plotted using the Cowen principle. The thermal conductivity of the printed parts was then calculated using the above formulae.

Thermal Analysis: Thermal Imaging

Thermal images were captured using a FLIR T440 thermal camera. The emissivity was set for each sample using a hot plate and thermocouple as a reference. Printed heat sink samples were placed on top of an rGO aerogel which was mounted between two steel plate electrodes connected to a power supply (figure 46). A set current was then passed through the aerogel creating a joule heating effect providing uniform distributed heat across the sample. The current output was adjusted to heat the aerogel to 30, 60, 90, 120°C and held for 10 minutes before imaging.

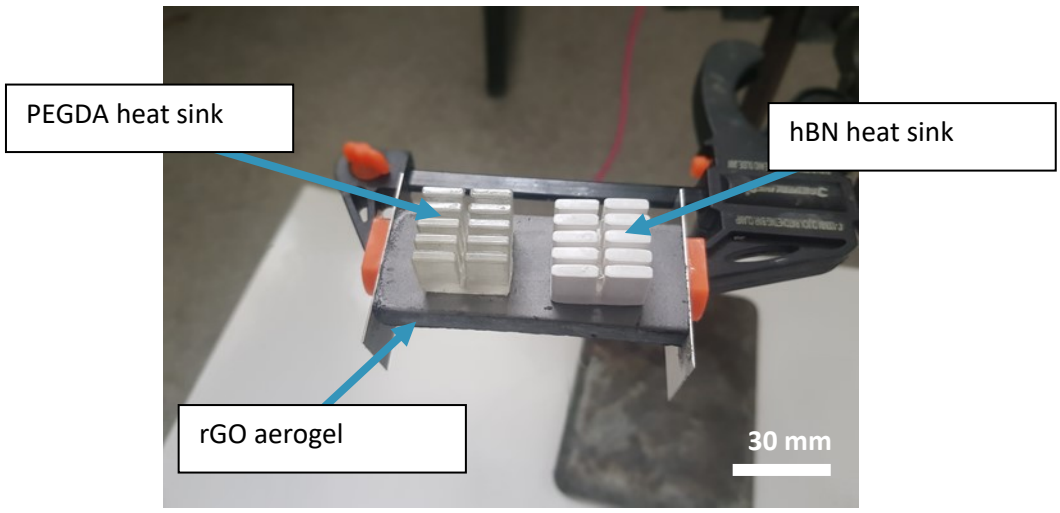

Figure 46 Setup for thermal imaging of heat sinks on rGO aerogel.

Mechanical Tests

Tensile Tests

Samples were tested in tension using an Instron 3344 machine. For samples tested in tension a 100 N load cell was used to apply a load to a sample secured between two clamps in tension at a constant rate of 0.5 mm/min (figure 47). An extensometer was used to measure the displacement of the sample as the load increased, data points were collected every 2 ms. To avoid slipping during testing emery paper was glued to the clips to allow for better contact to the smooth surface of the printed parts. All specimen sizes were prepared in accordance with ASTM D638 type IV with a 25 mm gauge length. The tensile properties tested included, ultimate tensile strength, yield strength, elongation and Poisson's ratio.

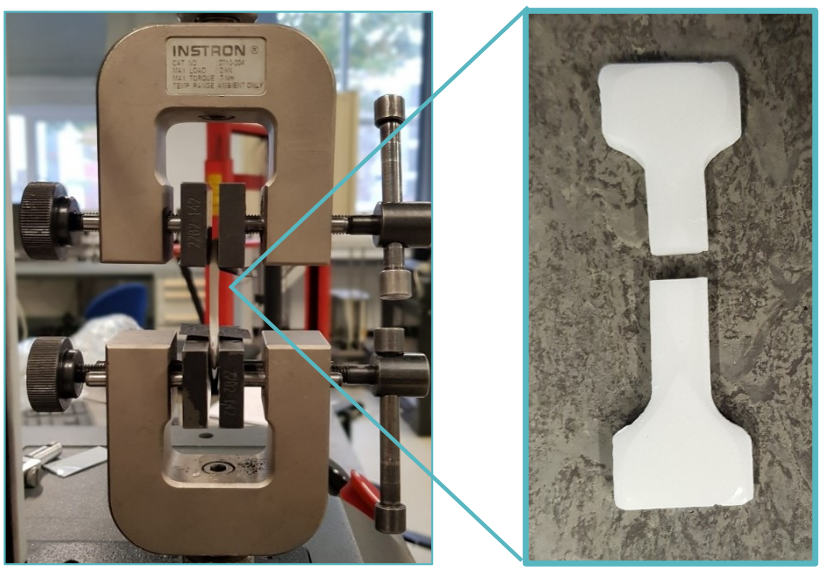

Figure 47 Photograph of typical set up for tensile tests.

Equations:

$$Ulrimate\ Tensile\ Strength = \frac{Maximum\ Load}{Cross - sectional\ Area}$$

$$Modulus\ of\ Elasticity\ (E) = \frac{Stress}{Strain}$$

Three-Point Bend Test

To calculate the flexure strength of the printed parts, samples were testes using the 3-point bend method on the Instron 3344 machine. The samples were printed to size and tested according to D790 ASTM standard with a 16:1 ratio of thickness to gauge length. A 40 mm span was used with a 3 mm triangle radius. A 100 N load cell was used with a cross-head motion of 0.2 mm/s (figure 48).

To calculate the flexure strength the following equation was used:

$$\sigma = \frac{3FL}{2wd^2}$$

Whereby σ is the flexure strength measured in MPa, F is the maximum force applied (N), l is the length of the sample (mm), w is the width of the sample and d is the depth of the sample (mm).

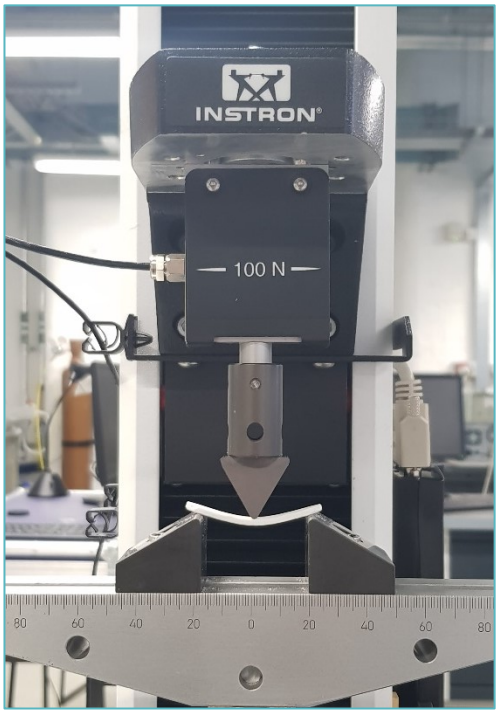

Figure 48 Photograph of typical set up of 3-point bend test.

Electrical Conductivity

Electrical resistivity test was conducted on printed cylindrical samples with a diameter of 10 mm and approximately 1 mm thick. Silver paint was applied directly onto the surface of the sample and copper tape applied to the painted area (figure 49). Crocodile clips were then placed on each of the copper tape tabs to complete the circuit. Samples were measured using the two-point probe method by sweeping the potential difference from 1 V - 50 V. The maximum current compliance was set to 1 $x10^{-5}$ A. When measuring DC resistance across the 3D printed parts, powerline induced AC noise was reduced by integrating the DC signal over one complete power line cycle (NPLC = 1). This method measures the voltage drop across the sample V, and the current through the sample I.

The resistivity of the sample can then be calculated using the following equation:

$$\rho = \frac{RA}{L}$$

Where ρ is the resistivity, R is the resistance, A is the cross-sectional area and L is the length or distance the current has to pass through the sample.

This method was chosen as it works well for materials with high electrical resistivity. The 4-point probe method is more applicable for conductive materials and films.

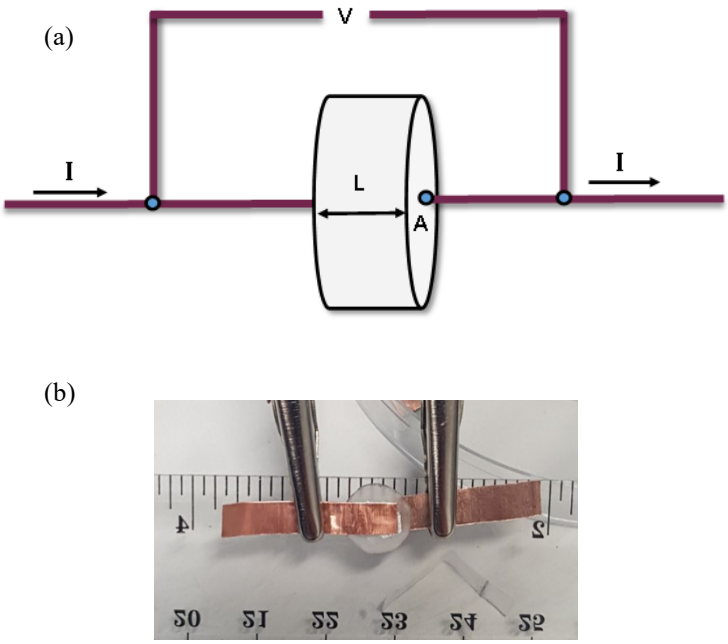

Figure 49 (a) Schematic of 2-point probe electrical resistivity measurement set-up. (b) Photograph of measurement set up using 3D printed BN part.

3.6 References

[1] K. Wang *et al.*, “A novel method for preparation of cross-linked PEGDA microfibers by low-temperature photopolymerization,” *Mater. Lett.*, vol. 161, pp. 317–320, 2015.

[2] A. Priola, G. Gozzelino, F. Ferrero, and G. Malucelli, “Properties of polymeric films obtained from u.v. cured poly(ethylene glycol) diacrylates,” *Polymer (Guildf).*, vol. 34, no. 17, pp. 3653–3657, 1993.

[3] S.-J. Lee *et al.*, “3D printing nano conductive multi-walled carbon nanotube scaffolds for nerve regeneration,” *J. Neural Eng.*, vol. 15, no. 1, p. 016018, 2018.

[4] Z. Wang, R. Abdulla, B. Parker, R. Samanipour, S. Ghosh, and K. Kim, “A simple and high-resolution stereolithography-based 3D bioprinting system using visible light crosslinkable bioinks,” *Biofabrication*, vol. 7, no. 4, p. 45009, 2015.

[5] M. Kawaguchi, S. Kuroda, and Y. Muramatsu, “Electronic structure and intercalation chemistry of graphite-like layered material with a composition of BC6N,” *J. Phys. Chem. Solids*,vol. 69, no. 5-6, pp. 1171-1178, 2008.

[6] J. Bennett, “Measuring UV curing parameters of commercial photopolymers used in additive manufacturing,” *Addit. Manuf.*, vol. 18, pp. 203–212, 2017.

[7] R. F. Egerton, *Physical principles of electron microscopy: An introduction to TEM, SEM, and AEM, second edition*. 2016.

[8] S. Maurya and A. Paunikar, *AUTOMOTIVE FASTENERS DEFECTS AND FAILURE ANALYSIS*. 2016.

[9] A. J. B. Spaull, H. A. Barnes, J. F. Hutton and K. Walters," An introduction to Rheology" *Journal of chemical technology and biotechnology.*, vol. 50, no. 3. p. 437, 1991.

[10] B. Zhang *et al.*, “Highly stretchable hydrogels for UV curing based high-resolution multimaterial 3D printing,” *J. Mater. Chem. B*, vol. 6, no. 20, pp. 3246–3253, 2018.

[11] J. T. Muth *et al.*, “Embedded 3D printing of strain sensors within highly stretchable elastomers,” *Adv. Mater.*, vol. 26, no. 36, pp. 6307–6312, 2014.

[12] J. A. Lewis, “Direct Ink Writing of 3D Functional Materials,” *Adv. Funct. Mater.*, vol. 16, no. 17, pp. 2193–2204, 2006.

[13] M. L. Griffith and J. W. Halloran, “Freeform Fabrication of Ceramics via Stereolithography,” *J. Am. Ceram. Soc.*, vol. 79, no. 10, pp. 2601–2608, 2005.

[14] P. J. Haines, “Thermogravimetry,” in *Thermal Methods of Analysis*, Dordrecht: Springer Netherlands, 1995, pp. 22–62.

[15] “Principle of the LFA Method - NETZSCH Analyzing & Testing.” [Online]. Available: https://www.netzsch-thermal-analysis.com/en/landing-pages/principle-of-the-lfa-method/. [Accessed: 13-Nov-2018].

4

GNP and hBN Ink Formulation for Stereolithographic Printed Parts

4.1 Introduction

The formulation of UV-curable inks containing 2D materials for SLA printing reported in the literature is relatively scarce; this is partially due to the compatibility of the platelets and their effects on the rheological properties, causing high viscosities outside of the printable range required for SLA printing. Also, when there are large differences in the refractive index between the UV polymer and the filler, this can result in large amounts of scattering of the laser resulting in under curing.[1] Literature reports show that previous emphasis has been made on achieving high loadings of ceramic materials in SLA resins.[2][3][4][5] Platelets and 2D materials differ significantly from traditional spherical ceramics particles, their high aspect ratios will have implications on their capabilities to increase their loading in the composite.

As knowledge and interest of 2D materials continue to grow, the need to manufacture and use these materials to create functional products becomes paramount for applications in industry including biotechnology, electronics, thermal management systems and rapid-prototyping. Although 3D printing offers advanced, manufacturing solutions there is still a gap that needs to be bridged between the current technologies and the compatibility of printing advanced multi-functional materials. This is because most 3D printing technologies are designed to print simple polymeric resins or ceramic solutions, therefore the printing of 2D materials may not meet the requirements of the 3D printer.

This chapter aims to explore the properties of SLA inks containing 2D materials and how these properties affect the printability of the inks (Figure 50). Focus has been made on the interactions the nanoplatelets have on the UV-curable resins, including the rheological properties and scattering/absorption effects during curing.

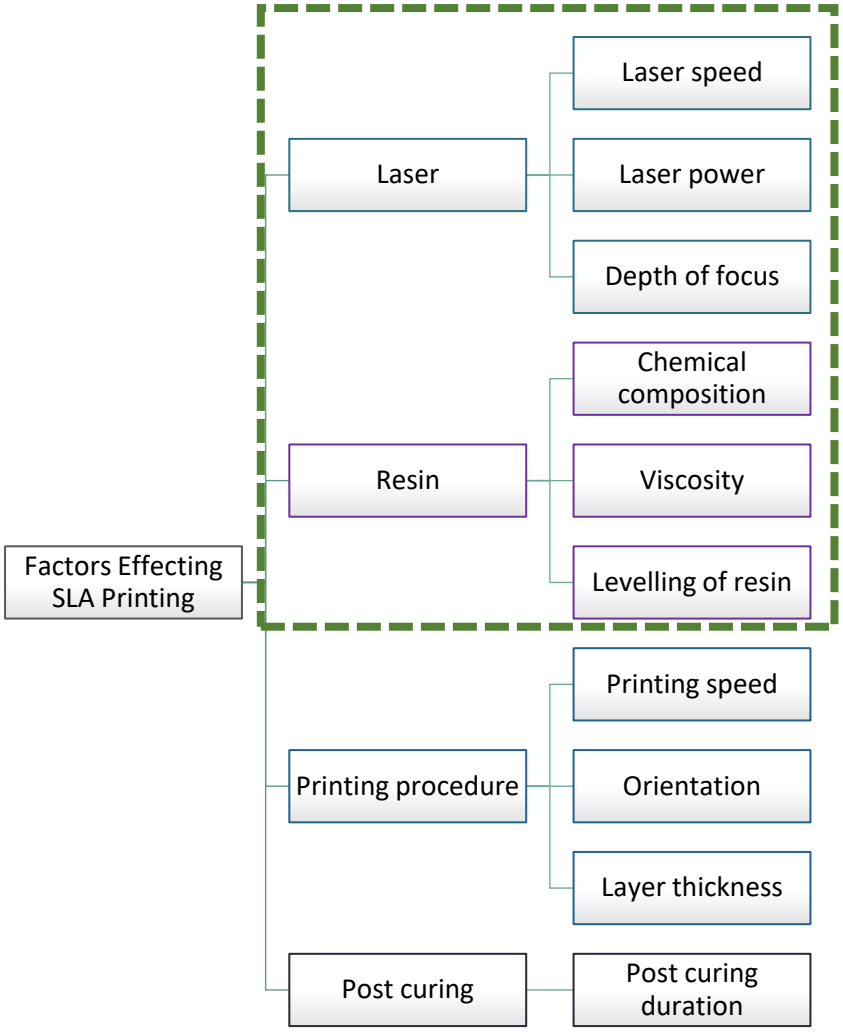

Figure 50 Overview of factors relating to SLA printing. The highlighted region will be explored and discussed in this chapter.

4.2 UV Ink Selection

The first step in producing UV-curable inks containing BN and GNP involves the synthesis of a UV-curable resin usually involving a monomer and photoinitiator. In this study, PEGDA was selected as the monomer due to the vast number of publications used as a UV-curable acrylate resin in SLA applications.[6][7][8][9] The concentration and type of photoinitiator were selected from preliminary tests including the window panes test as described in detail in chapters 2 and 3. The wavelength of the laser used in this research was 354.7 nm (not adjustable) therefore the photoinitiator selected needed to absorb photons within this range to produce radicals for curing. Three photoinitiators were originally selected to determine which would be most effective with the monomer PEGDA 575. The photoinitiators included Irgacure 819 commonly known as BAPO, Irgacure 2959 and Irgacure 184 which can be seen in table 5.

Table 5 Properties of Photoinitiators.

Photoinitiator	Irgacure 819 (BAPO)	Irgacure 2959	Irgacure 184
Chemical name	Bis (2, 4, 6-trimethylbenzoyl)-phenylphosphineoxide.	1-[4-(2-Hydroxyethoxy)-phenyl]-2-hydroxy-2-methyl-1-propane-1-one	1-Hydroxy-cyclohexyl-phenyl-ketone
Molecular weight M_n	418.5	224.3	204.3
Chemical structure	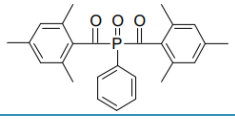	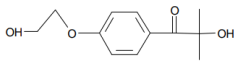	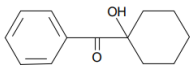
Absorption wavelengths (nm)	295, 370	276	230, 304
Comments	Photosensitivity at longer wavelengths. Yellow powder	White powder	White powder

The results from the window panes graphs in figure 51 show that BAPO is more reactive under UV light from the SLA's laser compared to Irgacure 2959 and 184. The increased cure depth (C_d) of the BAPO resin suggests that more radicals were produced, resulting in panes with increased thickness (figure 51). This is due to BAPO having an absorption peak at 370 nm, which is closely matched to the wavelength of the laser at 354.7 nm. BAPO was selected for further studies due to its high reactivity resulting in panes with large thicknesses, this was found to be promising for high

concentrations of filler materials as the introduction of fillers will rapidly decrease the C_d value due to known scattering effects.[1]

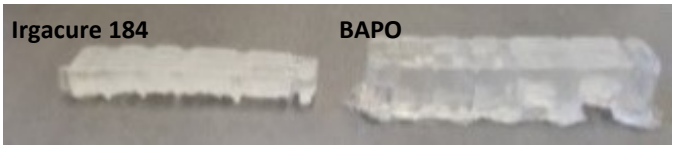

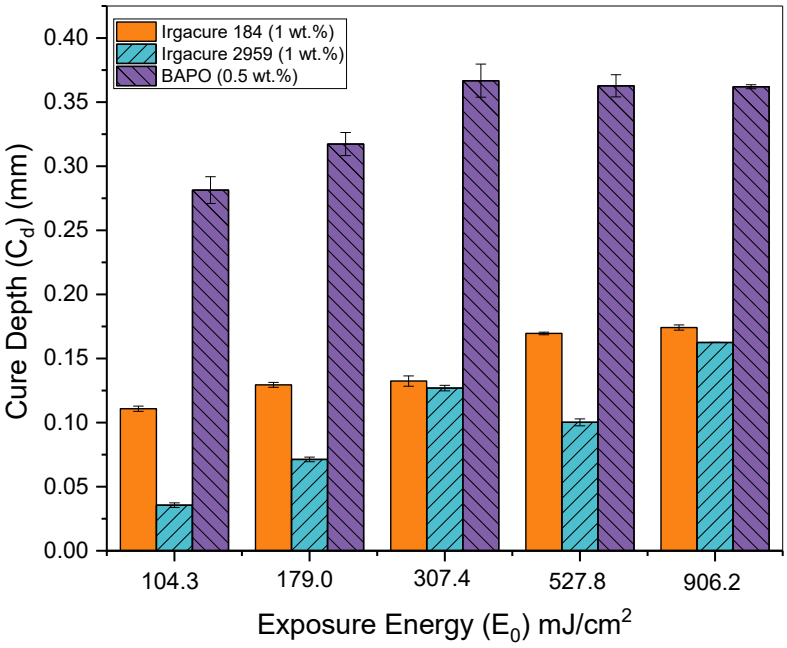

Figure 51 The effect of using different photoinitiators to cure PEGDA 575. Starting printing parameters: Ec: 12 mJ/ cm^2, Dp: 3.7 mm

4.2.1 Free Radical Polymerisation Reaction:

When BAPO is exposed to UV light during the SLA process, it absorbs the light and generates free radicals, which react with the PEGDA molecules opening the C-C bonds. The monomers will then continue to connect resulting in large molecules until the reaction is terminated. [10]. The reaction process for PEGDA and BAPO has been demonstrated in figure 52. When BAPO is dispersed in PEGDA and exposed to UV light, radicals are produced and attach onto the acrylate end groups of the PEGDA molecule, creating a cross-linked network of the cured polymer. Once the reference UV ink was formulated, the nanoplatelets BN and GNP were prepared to formulate composite inks with differing particle sizes and refractive indexes.

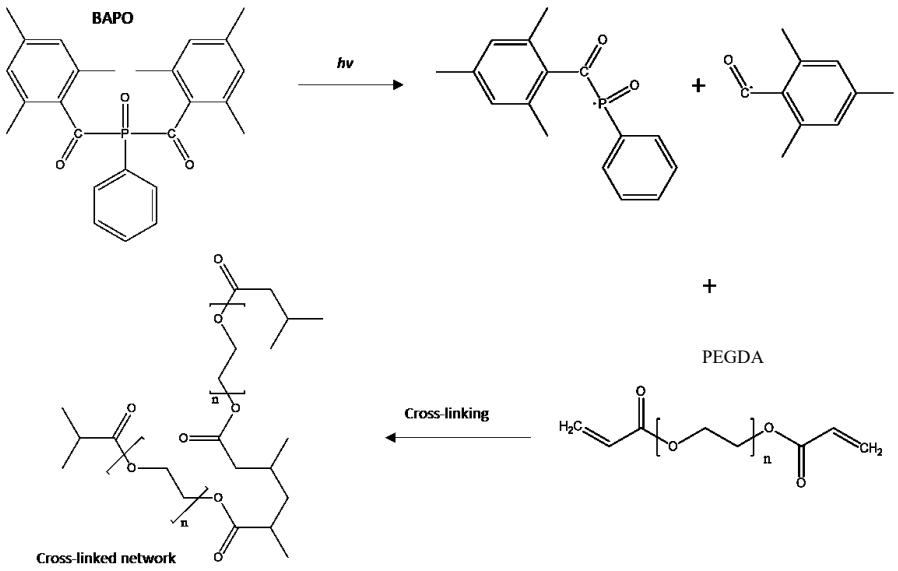

Figure 52 Mechanism of free-radical polymerisation of PEGDA and BAPO, hv represents the photon from the UV light. [17]

4.3 Characterisation of GNP and hBN Nanoplatelets

The morphology and flake size distribution of both GNP and BN particles were measured using SEM and AFM. The SEM micrographs (figure 53) show flakes with irregular geometries which appear flat and wide, with visible stacking of multiple flakes upon one another. The data collected from SEM provided a mean average lateral platelet size of 7.45 µm and 5.74 µm for BN and GNP respectively (table 6). The lateral size values from the SEM data has been calculated by measuring individual flakes. To understand the rheological and scattering effects of using different particle sizes in SLA inks, BN was exfoliated using bath sonication and filtered to produce smaller flakes with reduced thickness, and lateral size denotes as eBN. The SEM micrographs in figure 53 show a mean average lateral size of 4.28 µm for eBN. Particle sizing of nanoplatelets is important as it will affect the rheology of the inks and the scattering of the laser during printing affecting the overall printability of the inks. Although thin flakes with large lateral sizes would be beneficial for thermal and electrical properties due to good connections for electron pathways, large flakes can be detrimental to the printing process. This can result in inhomogeneous dispersions in the PEGDA resin, large amounts of scattering and poor adhesion between layers.

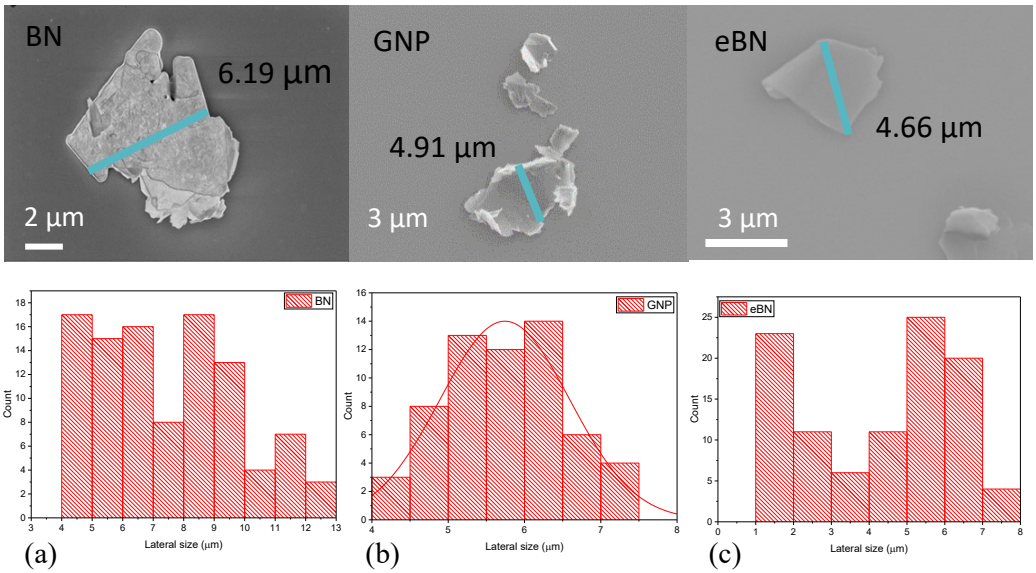

Figure 53 Typical SEM images of the lateral flake size distribution of (a) BN, (b) GNP and (c) eBN.n=100

Table 6 Mean average data of size distributions of GNP, BN and eBN flakes from SEM.

2D material	SEM: Lateral size (µm)	Error
GNP	5.74	0.84
BN	7.45	2.25
eBN	4.28	1.98

4.4 Compatibility of GNP and hBN with PEGDA

To produce a composite ink for SLA, GNP and BN flakes need to be dispersed homogeneously with good stability within the UV resin to avoid sedimentation at the bottom of the vat during printing, particularly as curing occurs on the top surface. In large commercial SLA printers, there may be a mixing system designed into the printer to help with possible sedimentation, however, for small-scale, research-based printing this is not viable. The results from the sedimentation tests showed that the inks began to sediment at ~8 hours before noticeable sedimentation started to occur which can be seen in figure 54. After 36 hours, the BN and GNP flakes had formed clear sediment. Therefore, prints longer than 8 hours would require additional mixing or the addition of dispersants to retain a homogenous ink.

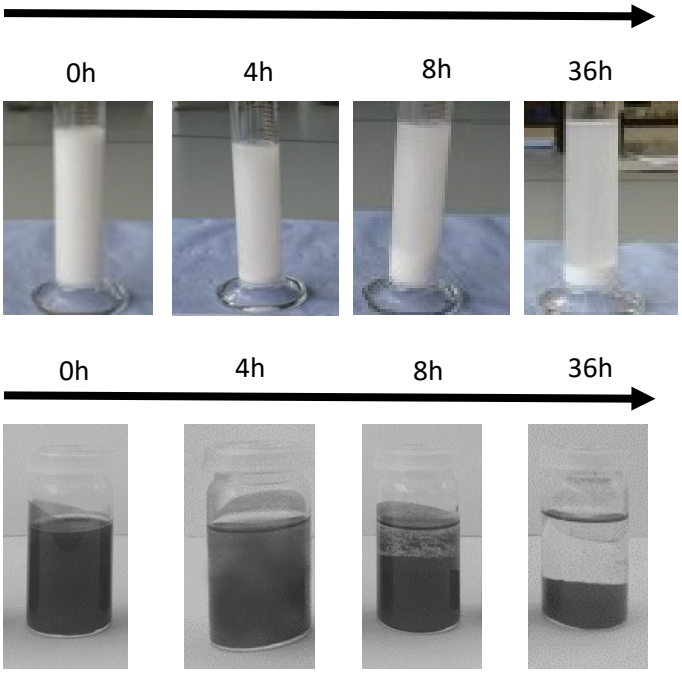

Figure 54 Sedimentation results of BN (top) and GNP (bottom) in PEGDA at 0, 4, 8 and 36 hours

UV-Vis was used to analyse the absorption peak of the composite inks to understand the optimum wavelength at which free-radicals are generated for curing. The absorption peaks of the composite resins are shown to be at 366 nm for the UV-resin and BN-based resin whereas the peak for GNP-based ink has been shifted to 367 nm (figure 55). As the SLA uses an Nd: YVO4 laser with a wavelength of 354.7 nm all the inks are well within the range for producing radicals for curing during printing. The baseline of the inks at wavelengths greater than ~400 nm shows little to no absorbance, however, as the inks pass through the UV region there is absorbance relating to the absorbance of the photoinitiator.

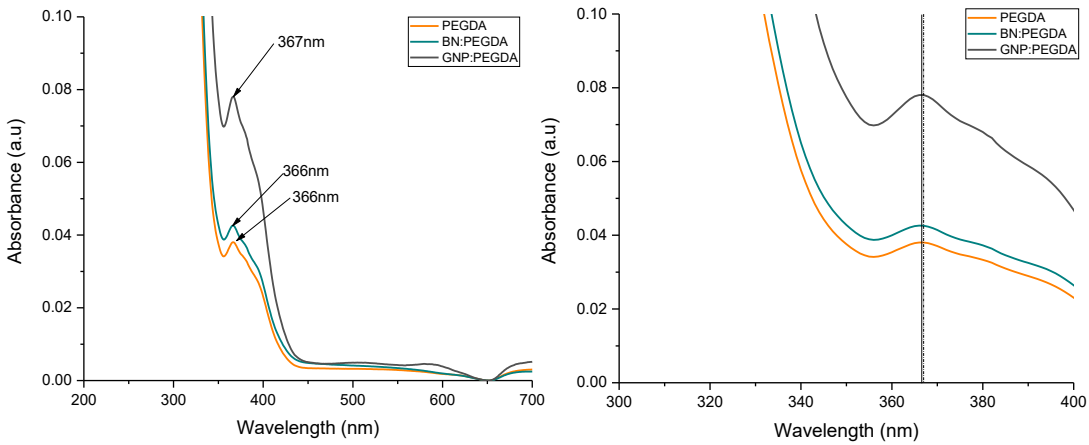

Figure 55 Normalised UV-Vis spectrum of UV ink PEGDA, BN: PEGDA (1 wt. %) and GNP: PEGDA (1 wt. %), full UV-vis spectra (left) zoomed in image (right).

4.5 Rheology of Inks

The basic rheological property for the printing of SLA inks is viscosity η, which is defined by:

$$\eta = \frac{\tau}{\gamma} \tag{13}$$

Where γ is the shear strain rate experienced at τ the shear stress, τ.

Viscosity

The viscosity of 2D material-based composite inks is a key consideration for printing using SLA. The build plate platform is required to travel down into the liquid vat allowing the resin to pass over the top of the previously printed layer. Therefore, if the ink is too viscous it will be difficult to flow under the applied stress from the build platform. This can cause a build-up of excess resin in some areas or no coverage at all. It has been reported that for SLA the viscosity of the resin should be less than 3-5 Pa.s at a shear rate of 15 1/s to mimic the printing conditions. [5][11]

Figure 56 displays the effect that GNP and BN have on the viscosity of the PEGDA resin. By measuring the flow of the inks over an increasing shear rate we can determine the viscosity at the operating shear rate of the SLA. For BN-based inks, all concentrations (up to 20 wt. %) fell into the printable region (below 3-5 Pa.s). For GNP-based inks, the maximum printable concentration is at 4 wt.% much less than that of BN. In comparison to literature, Chartier et al. achieved a printable viscosity with a solid loading of 53 vol.% or 80 wt.% using alumina particles.[5] This solid loading is much higher than that achieved with BN and GNP. The high aspect ratio and platelet geometries cause a drastic increase in viscosity compared to spherical particles due to inefficient packing systems. This has also been reported by Wierenga et al. where they saw an increase in the intrinsic viscosity when using platelets by up to 2.5 times that of the spherical particles. [12]

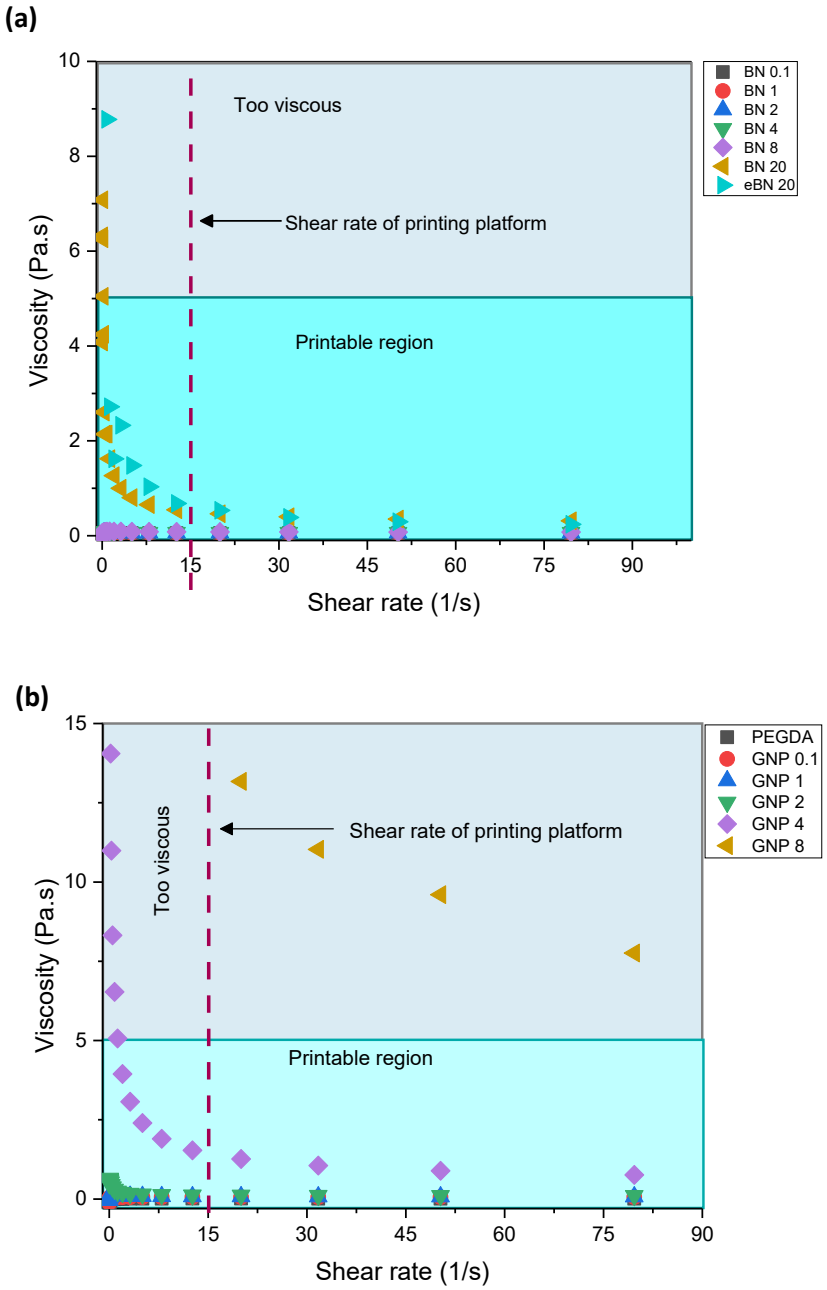

Figure 56 Effects of filler volume fraction on the viscosity of (a) BN-based inks and (b) GNP-based inks. The numbers next to GNP and BN represent the weight percentage of the platelets in the PEGDA inks, e.g. BN 2= 2 wt. % BN and 98 wt. % of PEGDA.

Figure 57 shows a direct comparison of the BN 20 and eBN 20 ink showing that an increase in aspect ratio does not have a large effect on the viscosity of the ink as they both display similar values at high and low shear rates. This could be because the decrease in particle size (BN 20, 7.45 µm and eBN 20, 4.28 µm) is not significant enough to cause a substantial change in viscosity.

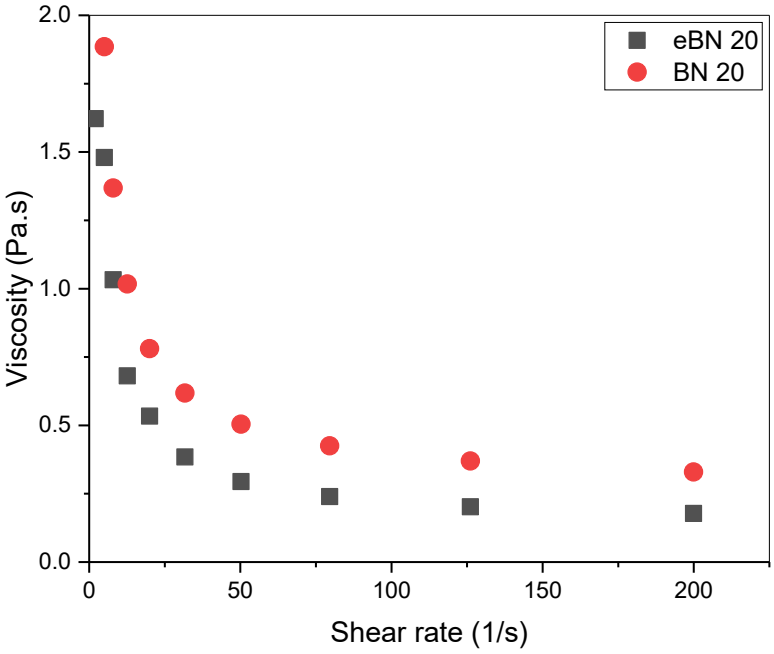

Figure 57 Effect of particle size dependency on the viscosity of BN-based inks.

Viscoelastic Properties of Inks

When oscillation amplitude ramps are applied to the inks (figure 58), the loss modulus *G''* is always greater than the storage modulus *G'* for concentrations of BN-based inks up to 8 wt. % and for GNP-based inks up to 4 wt. % in the applied stress range 1-1000 Pa. Therefore the inks display a 'liquid-like' behaviour at all stress frequencies at low concentrations. However at 8 wt. % GNP, *G'* is greater than *G''* at low-stress frequencies (>10 Pa) meaning the ink displays a 'solid-like' behaviour and eventually transitions to 'liquid-like' at high-stress frequencies. This transition can also be seen in the BN-based inks at 20 wt.%. In SLA printing it is paramount that all inks display a liquid-like behaviour as flow is an important function of the inks for the recoating of a new layer of resin, as the build plate needs to pass down into the vat of resin. Therefore the printing properties of inks containing up to 4 wt. % GNP and 20 wt.% BN will be further investigated as they meet the rheological requirements for SLA.

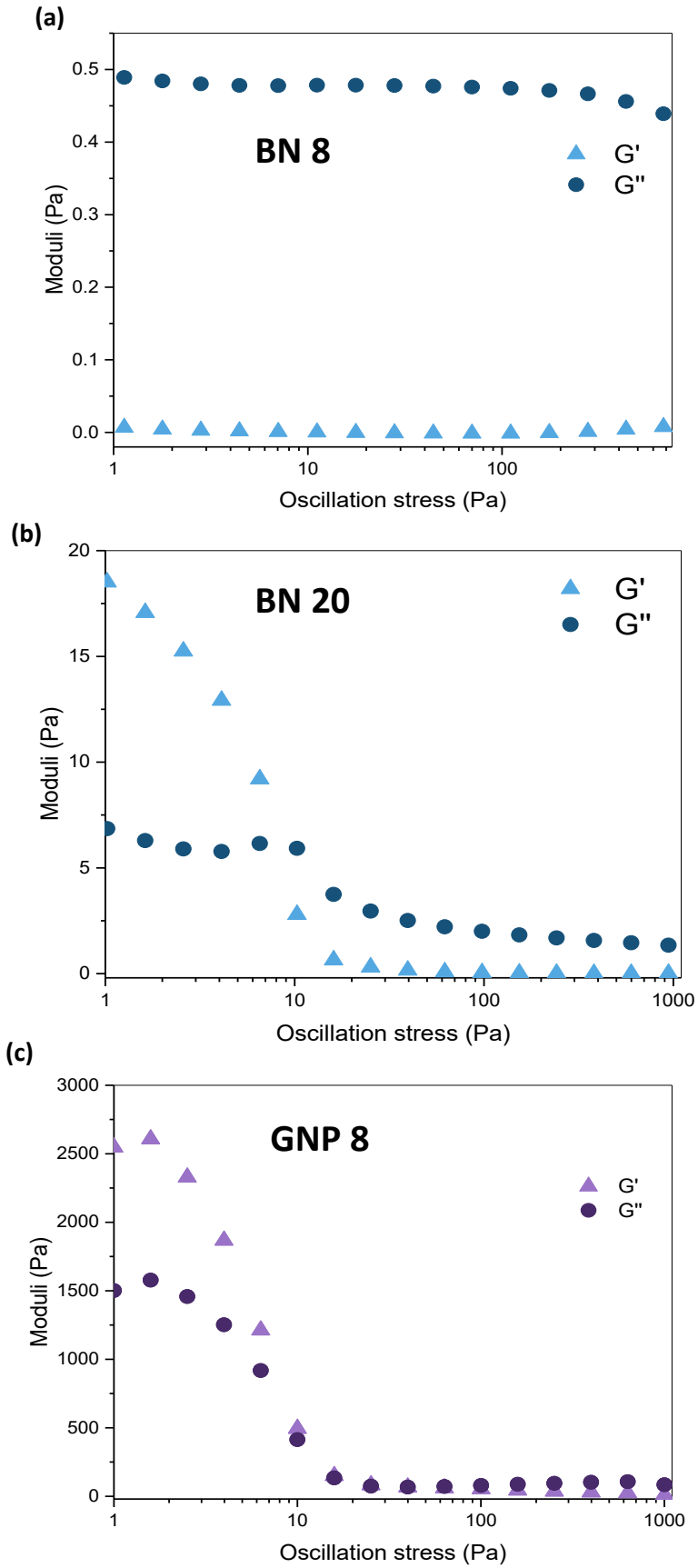

Figure 58 Oscillation amplitude ramp of (a) BN 8 (b) BN 20 and (c) GNP 8.

Shear Thinning Parameter n

We can analyse the rheological properties of a fluid when stress is applied to characterise the type of behaviour it will display. Fluids are usually categorised into three main categories Newtonian fluids where $n = 1$, shear-thinning $0 < n < 1$ and shear-thickening or dilatant $n > 1$. Newtonian fluids display a linear relationship between shear stress and shear rate, shear-thinning fluids will show a decrease in viscosity with increasing shear rate and shear thickening fluids will have an increase in viscosity with increasing shear rate. The Herschel-Bulkley model has been applied to the flow ramp rheological data (figure 59 and appendix 9.2) to calculate *n* the shear-thinning coefficient, K the viscosity parameter and τ_γ the yield stress.

$$\tau = \tau_\gamma + K\Upsilon^n \tag{14}$$

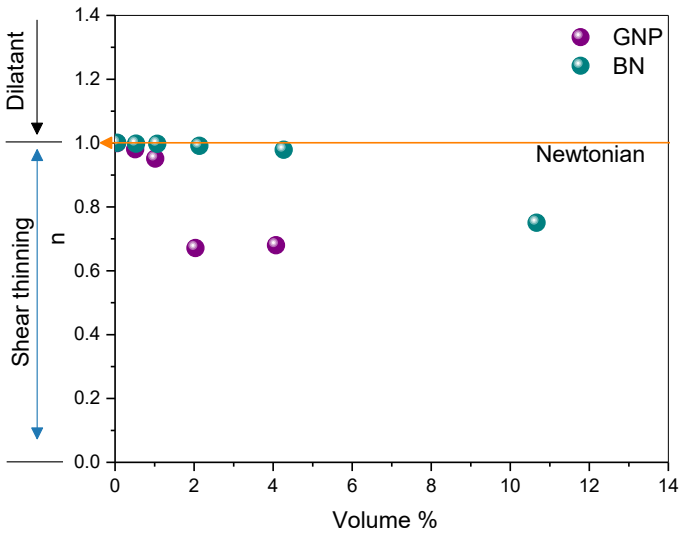

Figure 59 Difference in the shear thinning parameter n with varying BN and GNP concentrations.

With increasing concentrations of both GNP and BN particles, the ink displays shear thinning characteristics. However, at low concentrations the inks behave like a Newtonian fluid. When the inks display shear thinning behaviour they will flow under stress and recover back when the stress is removed at a specific shear rate or stress. The *n* parameters of the GNP and BN-based inks are within the range of 1 to 0.7, meaning that all inks are shear-thinning and will flow under stress. This is important

for SLA printing as the build plate needs to pass down through the resin easily for the recoating of a new layer of resin.

Comparison of models to find yield stress, τ_y

The yield stress was calculated using the Herschel-Bulkley equation by plotting shear stress against shear rate (figure 60). The yield stress is the stress in which plastic deformation will occur; the ink will not recover elastically past this point. The yield stress of a fluid can be calculated using different methods including Herschel-Bulkley model, Bingham model, tangential method and modulus cross-over the point where G' intercepts G''(dynamic yield stress)(tables 7 & 8). As the inks will flow readily, the yield stress can be calculated using flow ramps. At higher concentrations, oscillation amplitude ramps can be used to find the yield stress (figure 58) as the inks have a higher solid content allowing the ink to act as a solid and cross over at its yield point to flow like a liquid.

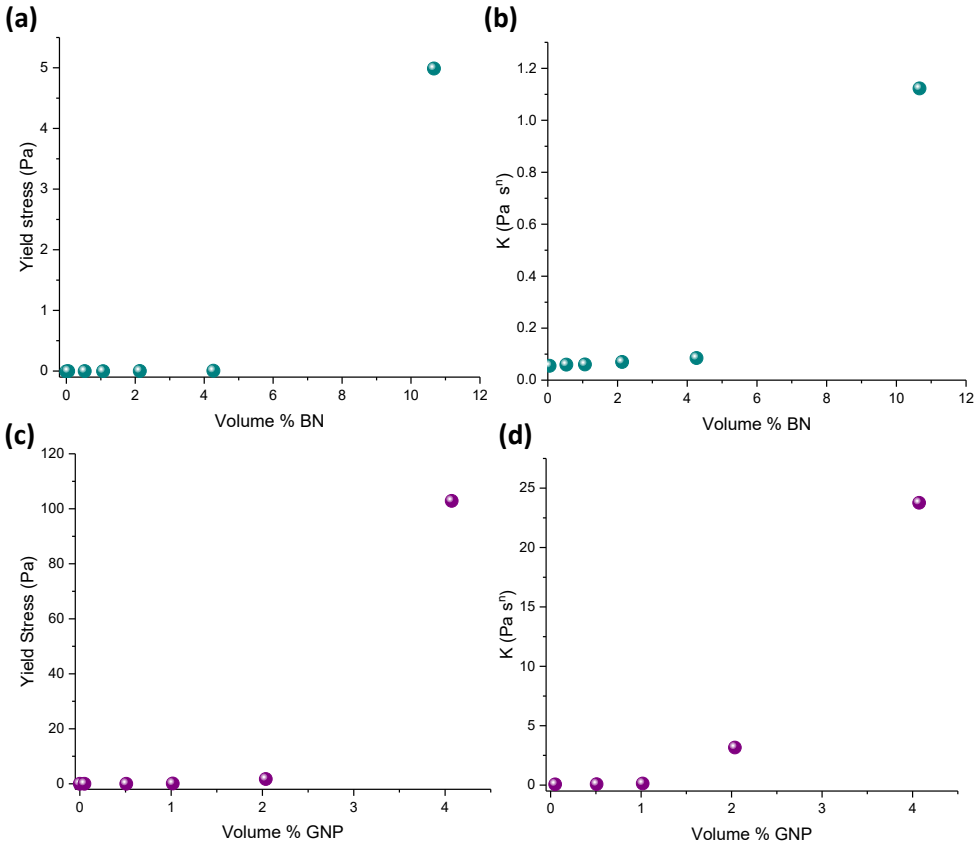

Figure 60 Yield stress as a function of concentration of (a) BN and (b) GNP particles, derived from Herschel-Bulkley. Difference in reference viscosity K, with (c) BN and (d) GNP.

When the volume percent of the platelets increases for both BN and GNP-based inks the yield stress increases meaning it requires more stress to deform the ink due to the

reinforcement of the platelets. At low concentrations, the static yield stress calculated for the inks is negative, for the Herschel-Bulkley and Bingham models, this information is meaningless for the yield stress. Therefore the data plotted does not fit the model at low concentrations.

Table 7 Comparison of models to find τ_γ for BN inks.

	BN 0.1	BN 1	BN 2	BN 4	BN 8	BN 20	eBN 20
Herschel-Bulkley							
Yield stress	-0.0023	-0.0014	-0.0033	-0.0006	0.0048	4.9874	11.1625
R^2	1.0000	1.0000	1.0000	1.0000	0.9999	0.9914	0.6608
Bingham							
Yield stress	-0.0034	0.0003	-0.0007	0.0131	0.0324	7.0082	10.6501
R^2	1.0000	0.9999	0.9999	0.9999	0.9999	0.9806	0.6303
Tangent method							
Yield stress	0.6817	0.3404	0.5044	0.6430	0.5175	5.4482	1.1201
Modulus cross–over							
Yield stress	N/A	N/A	N/A	N/A	N/A	7.6611	4.5646

Table 8 Comparison of models to find τ_γ for GNP inks.

	GNP 0.1	GNP 1	GNP 2	GNP 4	GNP 8
Herschel-Bulkley					
Yield stress	-0.0021	0.0199	0.0965	1.7359	102.8553
R^2	1.0000	0.9999	0.9999	0.9992	0.9874
Bingham					
Yield stress	-0.0019	0.0448	0.1785	6.5215	139.346
R^2	1.0000	0.9999	0.9994	0.968	0.9509
Tangent method					
Yield stress	0.4224	0.4732	0.4186	0.2852	4.4709
Modulus cross –over					
Yield stress	N/A	N/A	0.1269	N/A	37.0046

Calculating the yield stress for BN-based resins shows that all three models present similar values with a difference of 2.67 Pa between the highest and smallest value at 20 wt.% (10.67 vol. %) (figure 61). The same cannot be said for GNP-based inks, which result in similar values up to 4 wt. % (2.13 vol. %) however, as the concentration of GNP increases to 8 wt. % the disparity between the tangent method and Bingham model is significant (134.88 Pa) (figure 61). The disparity between the models of the yield stress at high solid loadings of platelets is likely due to the difference in the method of find τ_γ. Although the R^2 value is high for the Herschel-Buckley model and Bingham model for GNP-based inks, it is difficult to establish the goodness of fit for the tangent method and modulus cross-over. Therefore, it can be said that the

Herschel-Buckley and Bingham model is a more accurate fitting to the experimental data.

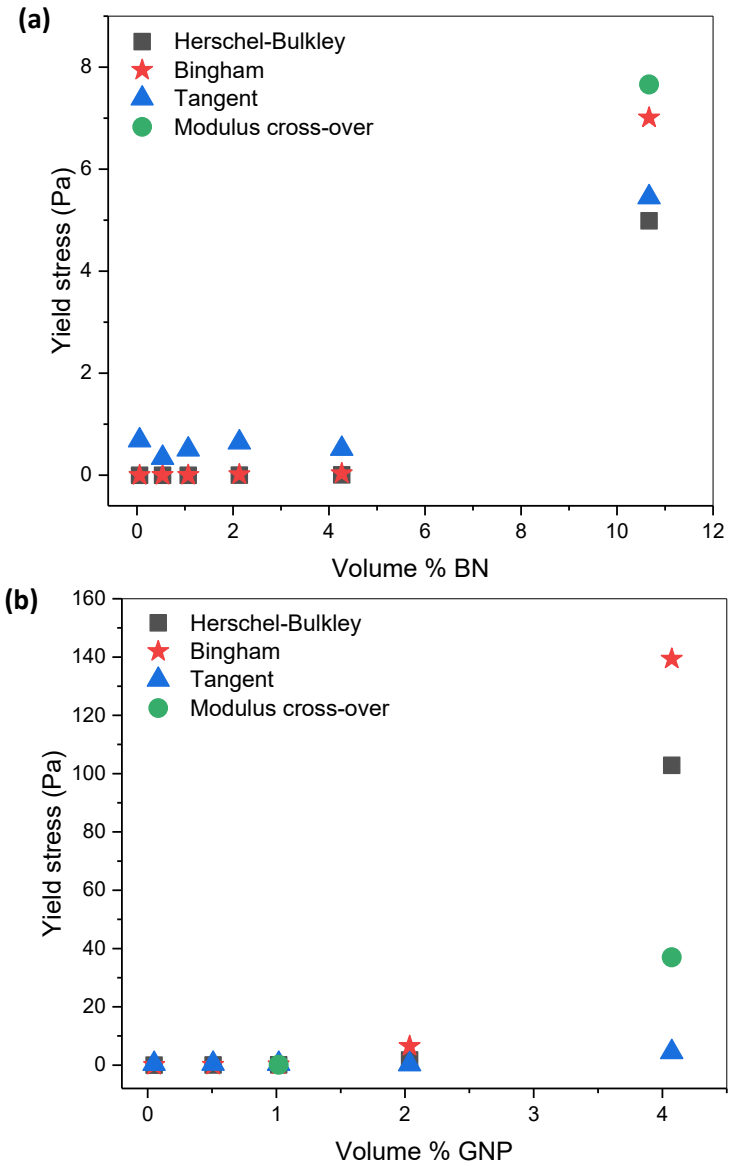

Figure 61 Comparison of models to find τ_y with increasing volume % of (a) BN particles and (b) GNP particles.

4.6 Scattering Effects of Printing GNP and hBN-based Inks using the Window Panes Test

Once the rheological properties of the inks were analysed the next step to determine the printability of the ink is through the analysis of the *'Window Panes'* test. The test is used to find the resolution in the z-axis and the optimum printing parameters for manufacturing 3D structures. To calculate the optimum printing parameters for new SLA resins, two variables can be adjusted the depth of penetration D_p, and the

critical exposure energy E_c, which will control the resolution in the z-axis (or layer thickness). Both of these parameters are reliant on the composition and chemistry of the resins. D_p is the distance where the laser's energy attenuates to $1/e$ of the surface energy and is determined by the intrinsic properties of the resin, including the refractive index of the UV polymer, the solid loading and geometry of the particles or flakes. As these factors can interfere with the incident laser acting as obstacles for the laser to travel through the resin. The photoinitiator and monomer resin determine the *Ec,* the critical exposure energy to initiate curing.[13] The chemistry of the resin will determine how many radicals are produced and the associated end groups available for free radical polymerisation under UV exposure.

Previously; published research has focused on the addition of ceramic particles in an acrylate polymer, epoxy or a combination of both. This is because ceramic particles can be dispersed within these resins at high loadings up to ~80 wt. % with the help of surfactants or dispersants to reduce the viscosity of the resin.[13] The polymer component of the printed part is often burnt out leaving the ceramic portion to be sintered to produce a porous ceramic part. The refractive index of alumina and silica, which are traditionally used in these resins, are matched to that of their monomer counterparts. This reduces the scattering of the laser during printing resulting in good printability with high solid loadings. When the difference between the refractive index of the monomer and filler materials is large this will cause the D_p value to decrease reducing the likelihood of curing during printing. This is of particular concern for the resins containing GNP as the refractive index is 2.7 much higher than PEGDA 575 at 1.47 (table 9). The following fillers for PEGDA 575 resin system were investigated:

1. BN- a low refractive index filler for thermal management applications
2. GNP- a high refractive index filler for thermal management and electrical applications.

Table 9 General properties of UV inks and filler materials that effect scattering behaviours.

Material	**Density (g/cm^3)**	**Lateral platelet size <d> (µm)**	**Refractive index *n***	**Δ*n* (n_{filler}-$n_{polymer}$)**	**Δ*n*/n_0**
PEGDA 575	1.12	-	1.47 (n_0)	-	1.00
BN	2.10	7.45	1.80	0.33	1.22
eBN	2.10	4.28	1.80	0.33	1.22
GNP	2.2 0	5.74	2.70	1.23	1.84

To calculate the optimum printing parameters for each ink the E_c and D_p were calculated using the working curve (15) to achieve the desired C_d or layer thickness by setting initial arbitrary values D_p=3.7 mm and E_c=12 mJ/cm^2 (figure 62). The newly calculated D_p and E_c values from the Window Panes test provided D_p values outside of the printing range of the printer (> 20 mm). Therefore, to find the optimum printing parameters the E_c was adjusted using 20% increments until the desired C_d was achieved. However, the results from the working curve were used to explain the relationship between the E_c, E_0, D_p, C_d and the 2D material fillers. From an initial analysis of the *'windowpane'* graphs (figure 62), there is a clear relationship between the C_d and E_0, and this depends on the volume fraction of the nanoplatelets. As the volume fraction of GNP and BN increases, the slope of C_d vs E_0 decreases, providing an inversely proportional relationship. As the slope dictates the D_p, the increase in the volume fraction of nanoplatelets results in a smaller depth of penetration of the laser. The increase in E_0, on the other hand, causes the C_d to increase proportionally. These relationships can help us to identify the scattering effects that occur during the printing process through the application of semi-empirical mathematical modelling (equation (16).

Working curve equation:

$$C_d = D_p \ln\left[\frac{E_0}{E_c}\right] \tag{15}$$

Scattering equation:

$$C_d = \frac{2\langle d\rangle}{3Q}\frac{1}{\phi} ln\left(\frac{E_0}{E_c}\right) \tag{16}$$

Where $\langle d\rangle$is the average size of the nanoplatelets, E_0 is the energy density, E_c is the critical exposure energy, Q is the extinction coefficient efficiency term, ϕ is the volume fraction of the filler and C_d is the cure depth of the printed window pane.

These equations have been applied to the experimental data to analyse the effect that ϕ, $\langle d \rangle$ and E_0 have on the scattering effects of printing using nanoplatelets, and which parameter has the most influence on the printability of the ink. For all calculations $\langle d \rangle$ is equated to the mean average lateral length of the flakes mentioned in section 4.3. It is important to know that typically the cross-section for scattering uses the diameter of spherical particles.

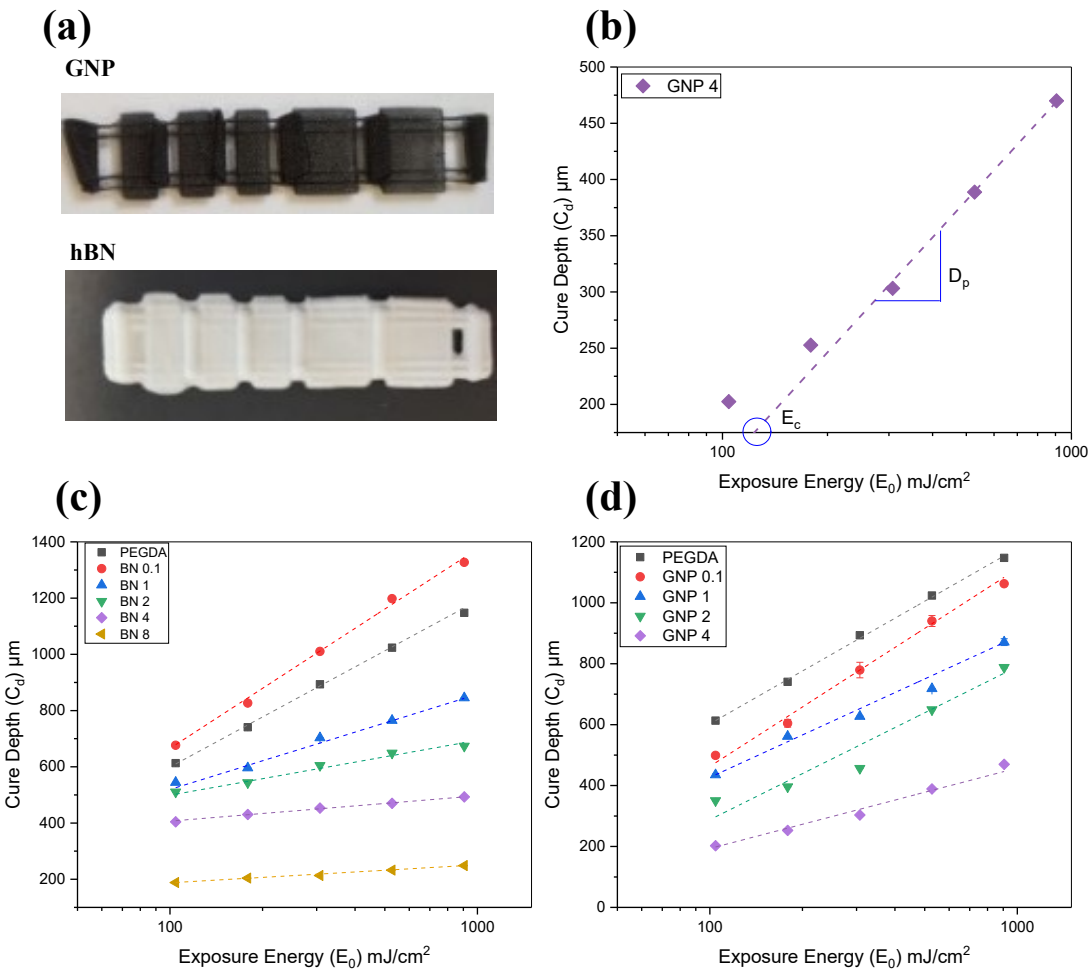

Figure 62 (a) Images of printed window pane labelled GNP and hBN. (b) Example of plotted window panes graph to find the E_c and D_p values for composite inks. (c) Cure depth as a function of concentration with increasing E_0 for BN-based inks and (d) GNP-based inks. Initial set parameters were E_c: 12 mJ/cm^2 and D_p: 3.7 mm.

4.6.1 Concentration Dependence of 2D Material-based Inks

The '*window panes*' test can be useful to study the effects the concentration of the filler has on the thickness of each printed layer. Achieving high loadings of nanoplatelets in SLA resins gives functionality to the printed part, producing electrically and thermally conductive components. However, an increase in the

concentration of nanoplatelets will affect the amount of scattering during printing which can lead to under curing of the inks as the photons will be blocked by the fillers from reaching the absorbing UV polymer matrix.

For both BN and GNP-based inks, the relationship between the inverse volume fraction and C_d is expected to show a linear relationship according to equation (16) (figures 63 & 64). Both GNP and BN show similar values for the C_d with a slight reduction in the GNP for C_d over the concentration range 0.1 -8 wt. % (197-26, 1/vol. %). From the original printing parameters (E_c=12 mJ/cm^2, D_p =3.7 mm) 8 wt. % was the maximum loading of GNP, above this, the inks would not cure. The reduction in C_d for the GNP inks is related to the square of the refractive index between the filler and UV polymer Δn^2 being greater than that of BN.

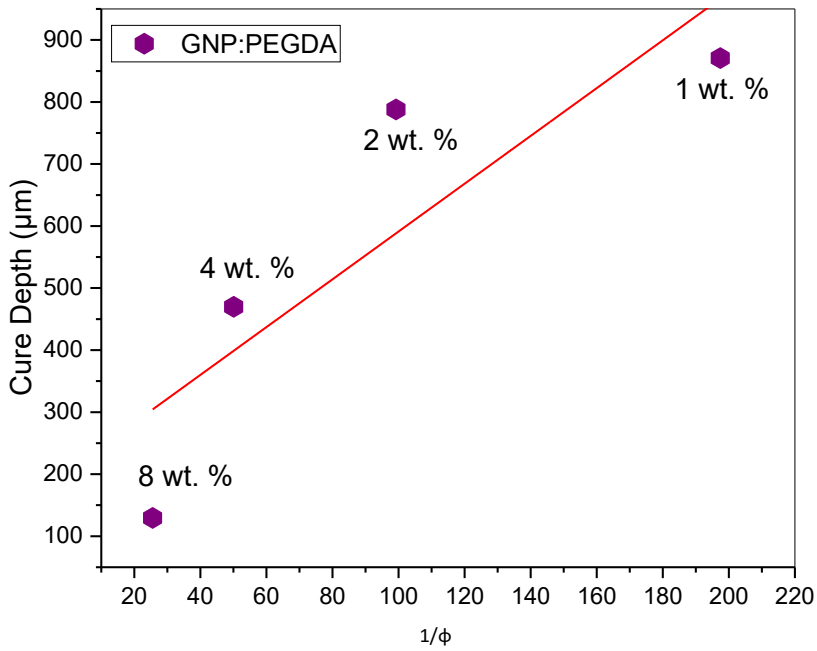

Figure 63 Cure depth vs inverse volume fraction for GNP concentrations at 980 mJ /cm^2 and λ=365 nm. Initial printing parameters: E_c: 12 mJ/cm^2 and D_p: 3.7 mm.

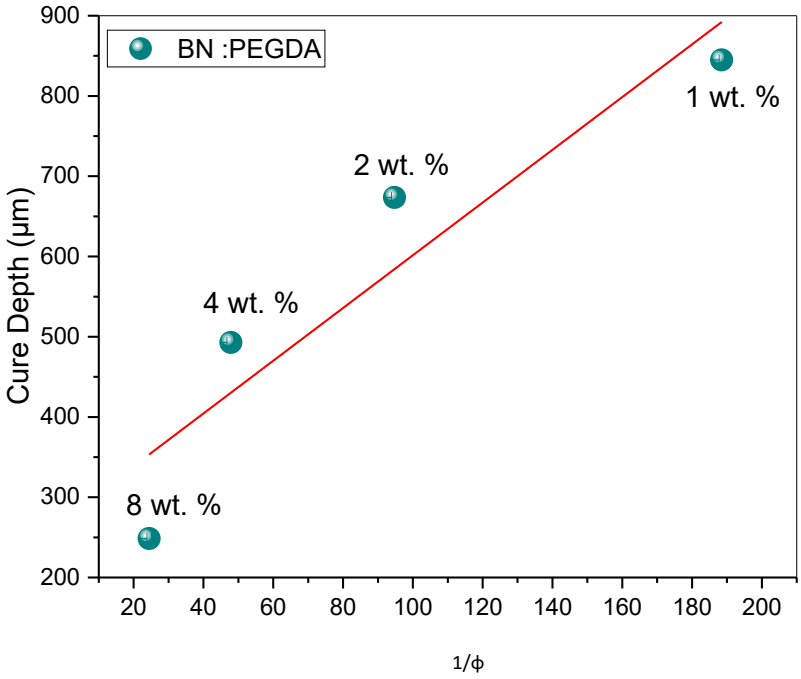

Figure 64 Cure depth vs inverse volume fraction for BN concentrations at E_0 980mJ /cm^2 and λ= 365 nm. Initial printing parameters: E_c: 12 mJ/cm^2 and D_p: 3.7 mm.

A linear fit has been employed in figures 63 & 64 according to the relationship shown in (16). The data in figures 63 & 64 does not show a clear linear relationship this is because the model is based on the interactions of the laser with spherical particles associated with their diameter. However, for BN and GNP flakes the average length of the flakes are used to replace the diameter used in the model. There are no current models that use platelets/flakes in the replacement of spherical particles, therefore, the non-ideal behaviour displayed is likely to be related to the degree of rotation of the flakes varying the area of interaction of the laser affecting the scattering behaviour.

4.6.2 Dose Dependence (E_0) of 2D Material-based Inks

Dose dependence is the amount of energy provided by the laser (E_0) which contributes to the thickness of the C_d. Figure 65 shows the dose-dependency of printing both BN and GNP inks with 4 wt. % solid loading. As expected from the Beer-Lamberts equation (15), the C_d increases with increasing exposure energy. The cure depth is also predicted to increase as the difference in the refractive index between PEGDA and the filler material is reduced. At 307 mJ/cm^2 the C_d values for BN and GNP are 453 µm and 303 µm respectively, following the expected trend, as the

difference in the refractive index Δn between the 2D material and the photopolymer is 0.33 (BN) and 1.23 (GNP) (table 9).

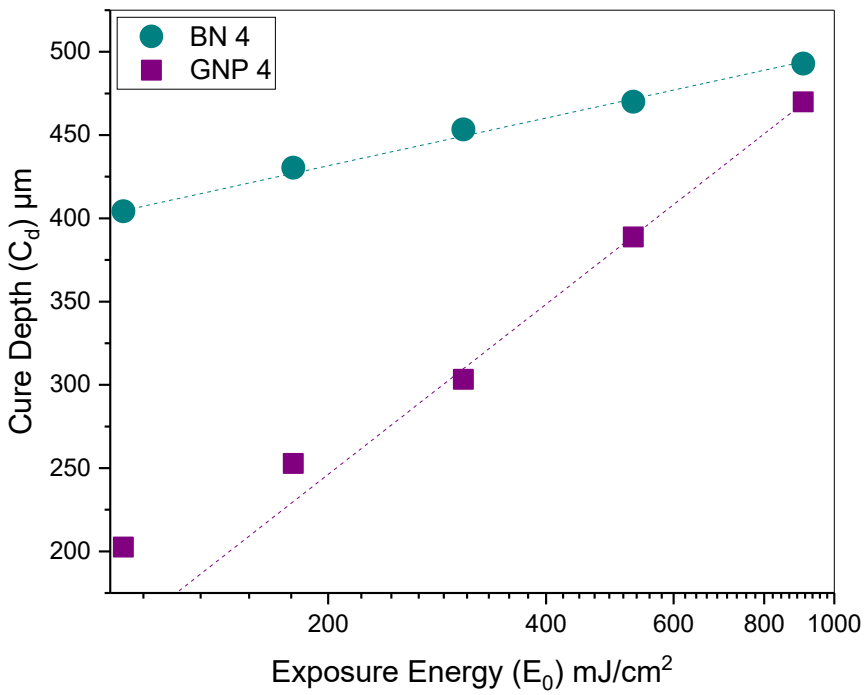

Figure 65 Cure depth of BN 4 wt. % and GNP 4 wt. %. Initial printing parameters: E_c: 12 mJ/cm^2 and D_p: 3.7 mm.

4.6.3 Particle Size Dependence of 2D Material-based Inks

The inks BN 20 and eBN 20 were measured to determine the effects that nanoplatelet size has on the curing process. The mean lateral size, <d> of BN 20 was 7.45 (+/- 2.25) µm and eBN 20 was 4.28 (+/- 1.98) µm (table 9). As expected for plots of C_d vs E_o both inks show a linear fit, however, the exfoliated BN with a smaller <d> value produced window panes with a larger C_d (figure 66). This is contradictory to $C_d \propto d$. This has also been reported by Halloran et al. where the reduction in particle size of alumina suspensions from 0.61 to 0.46 µm increased the C_d.[1] This could be due to increased scattering effects of the larger lateral sized BN nanoplatelets causing fewer photons to reach the absorbing UV polymer for curing. This effect has been observed by Harvey et al. where they saw an increase in the scattering coefficient with increased lateral size of the BN nanoplatelets.[14]

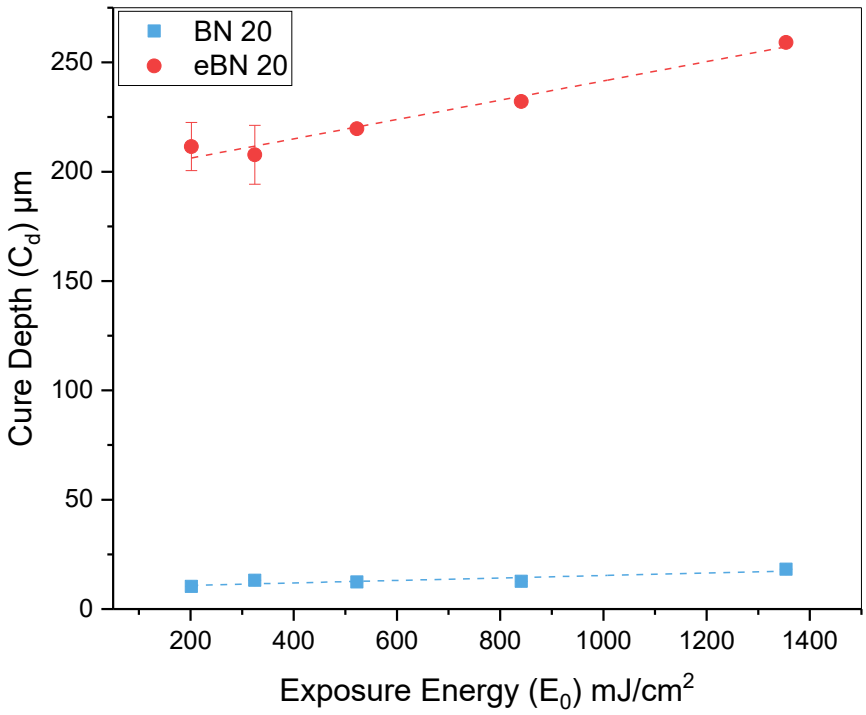

Figure 66 Cure depth of BN 20 and eBN 20 inks. Initial printing parameters: E_c: 30 mJ/cm^2 and D_p: 4.2 mm.

4.5.4 Scattering and the Extinction Coefficient Efficiency *Q*

The extinction coefficient *Q* is a scattering efficiency term that represents the ratio of energy scattered by the nanoplatelets to the total energy in the incident ray.[15] To quantify the effects that nanoplatelets have on the scattering of the laser during printing is complex. This is because many models for calculating *Q,* the extinction coefficient efficiency term are based on several assumptions. These assumptions include the assumption that electromagnetic radiation interacts with a single spherical particle that is suspended in a medium that is not absorbing. For both BN and GNP-based inks, this is not the case, as nanoplatelets with irregular geometries and high aspect ratios are suspended in the absorbing medium PEGDA/BAPO. These assumptions suggest that the effects of scattering control the penetration depth D_p. During printing, the nanoplatelets will first cause scattering from the oncoming radiation reducing the intensity of the laser. The remaining radiation will then travel into the resin until a critical limit of exposure is reached for curing or gelation of the monomer known as E_c.

Q is a dimensionless term that can be affected by the size of the particle, concentration of filler and the ratio between the filler and the UV resins refractive index. There are many ways to describe the type of scattering that occurs, one of which is Rayleigh scattering, however for this to occur the size of the nanoplatelets should be less than or equal to the wavelength of the incident beam. Therefore, for the composites inks, calculating Q for Rayleigh scattering is not appropriate. For the Rayleigh-Gans region, (Q_{ray}) scattering is associated with x and the ratio between the refractive indices.

$$Q_{ray} = \frac{1}{2}\rho^2 = \frac{1}{2}x^2\Delta n^2 \tag{17}$$

Where ρ is related to the difference in refractive index between the 2D material and UV-curable resin.

$$\rho = x\Delta n = x(n_p - n_0) \tag{18}$$

Where, $x = \pi\langle d\rangle/\lambda$

For Q to be valid $\rho < 1$, therefore, the difference in refractive index needs to be small which will mean the value of Q will be less than 1.[1]

Another way to describe the scattering effects term Q is through Mie scattering (Q_{mie}), the size parameter x is approximately that of the incident wavelength but is not limited by the size of the nanoplatelets or large differences in refractive index.

$$Q_{mie} = 2 - \frac{4\sin\rho}{\rho} + \frac{4}{\rho^2}(1 - \cos\rho) \tag{19}$$

Griffith and Halloran[1] also suggested (Q_n) with the equation:

$$Q_n = \frac{\Delta n^2}{n_0^2} \tag{20}$$

Here Q is described by the difference in the square of the refractive index between UV resin and particle.

Q_{geo} is used to describe the type of scattering when the size parameter x is greater than that of the incident wavelength, providing the equation:

$$Q_{geo} = \pi\langle d\rangle^2 \quad (21)$$

$Q_{mie}, Q_{ray}, Q_{geo}$ and Q_n will be compared to the experimental values Q_{exp} to determine the closest fit between theoretical and experimental results to explain the scattering behaviour. Q_{exp} will be determined from experimentally measured values of BN and GNP-based inks using equation (22) and rearrangement of equation (16).

$$Q_{exp} = \frac{2\langle d\rangle}{3\emptyset C_d}\frac{1}{\phi} ln\left(\frac{E_0}{E_{crit}}\right) \quad (22)$$

Q Dependence on E_0

To determine the effect that E_0 has on Q, the inks BN 2 wt. % and GNP 2 wt. % were analysed. The average lateral particle size of BN 2 and GNP 2 was used as $\langle d\rangle$, Δn was 0.333 and 1.233 respectively, λ=354.7 nm shown in table 9. For both GNP and BN inks, the change in Q_{exp} was very small for the range of E_0 values analysed. This suggests that E_0 does not affect the outcome of Q alone and is affected more by Δn^2 or$\langle d\rangle$. Q_{exp} closely matched the values of Q_{mie} for both inks, whilst Q_{ray}, Q_{geo} and Q_n were orders of magnitude different from Q_{exp} (tables 10 & 11).

Table 10 Calculated Q values for BN 2 wt. %.

BN 2 wt.%						
E_0 (mJ/cm²)	C_d (µm)	Q_{exp}	Q_{mie}	Q_{ray}	Q_n	Q_{geo}
104.28	510.75	2.10	2.01	421.44	0.05	12343.51
179.04	543.63	2.47				
307.40	604.75	2.66				
527.79	648.88	2.90				
906.17	673.63	3.19				

Table 11 Calculated Q values for GNP 2 wt. %.

GNP 2 wt. %						
E_0 *(mJ/cm²)*	C_d *(µm)*	Q_{exp}	Q_{mie}	Q_{ray}	Q_n	Q_{geo}
104.28	350.50	2.36	2.01	3647.24	0.70	1516.67
179.04	395.88	2.61				
307.40	456.38	2.72				
527.79	649.00	2.23				
906.17	787.88	2.10				

Q Dependence on Δn^2

To understand the effect that *n* has on *Q* BN 8 and GNP 8 inks were analysed. The average lateral particle size of BN 8 and GNP 8 was used for $\langle d \rangle$, Δn was 0.333 and 1.233 respectively, the cure depth was taken using E_0= 906.173 mJ/cm^2, λ= 354.7 nm.

Table 12 shows that as the difference in the refractive index increases the C_d decreases. The magnitude of the experimental term for *Q* best matches that of Q_{mie} for both GNP and BN-based inks. Q_n, which is directly related to the square of the difference in refractive index between the UV resin and nanoplatelets, is orders of magnitude lower than Q_{exp}. This demonstrates that the size and volume fraction of nanoplatelets in the resin affects the *Q* term, which is not captured in the Q_n model.

Table 12 Calculated Q values for BN 8 and GNP 8 inks.

	n_0	Δn	$\langle d \rangle$ (μm)	∅	C_d	Q_{exp}	Q_{mie}	Q_{ray}	Q_n	Q_{geo}
BN 8	1.47	0.33	7.45	0.04	248.64	2.12	2.01	421.44	0.05	1516.67
GNP 8	1.47	1.23	5.75	0.04	99.25	1.98	2.01	3647.24	0.70	12343.51

Q as a Function of Particle Size

The effect that the particle size has on *Q* has been analysed by taking measurements of the BN 20 and eBN 20 ink as the *n* value and E_0 value remains consistent with only changes to the particle size. The average lateral particle size of BN 20 and eBN 20 was used as $\langle d \rangle$, the difference in refractive index was 0.333 and cure depth was taken using E_0= 1353.87 mJ/cm^2, λ= 354.7 nm. The results for *Q* from the experimental values best matched that of Mie scattering. The larger lateral size of the BN flakes produced a smaller value for C_d but a higher value for *Q*. *Q* in regards to the Rayleigh-Gans region and Q_{geo} is very large, up to five orders of magnitude different from the experimental value for *Q,* seen in table 13, therefore, they are not valid models for these inks.

Table 13 Calculated Q values for BN 20 and eBN 20 inks.

	$\langle d \rangle$ (μm)	∅	C_d	Q_{exp}	Q_{mie}	Q_{ray}	Q_n	Q_{geo}
BN 20	7.45	0.10	18.22	10.39	2.01	421.44	0.05	1516.67
eBN 20	4.28	0.10	259.13	0.42	1.98	139.10	0.05	500.57

4.7 General Discussion

The 'printability' of SLA resins is highly dependent on the rheological properties of the inks, particle size, the refractive index of both UV resin and filler materials and their associated absorption and scattering effects. It is difficult to distinguish which property of the inks is most crucial to achieving good printability and instead requires cohesion between them all.

To ensure inks have good printability they should include the following properties:

1. Ensure there is a good dispersion of flakes in UV resins.
2. Low viscosities of < 5 Pa at shear rates of 15 s^{-1}.
3. Minimise the difference in refractive index between UV resin and filler material.
4. Minimise scattering effects by controlling size, concentration and refractive index.

The rheological behaviour of SLA inks must be able to flow at shear-rate of 15 s^{-1}, this is to enable the deposition of a new layer of resin using the build plate and re-coating system. This has proven not to be an issue for inks containing BN as solid loadings of up to 20 wt. % fell below the 5 Pa limit. GNP-based inks, on the other hand, produced high viscosities that did not fall within the printable range at 8 wt. %. As the concentration of solid loading increased, the *G'* of the inks was larger than *G''* at low shear stress, displaying 'solid-like' behaviour. As previously mentioned, the inks are required to flow at low shear rates and stress, therefore to maximise the solid-loading content (dependent on the function of the final application) a diluent could be added to decrease the viscosity and *G'*. Modelling of the yield stress showed that at low solid loadings for both GNP and BN-based inks, the yield stress was small and tended towards 0, and even provided some minus values for the Herschel-Bulkley model which are meaningless. From these results, at low solid loadings, BN and GNP-based inks cannot be considered to be Herschel-Bulkley fluids as they do not have a yield stress and therefore are not shear-thinning and behave more like Newtonian fluids which can be found when plotting the shear-thinning coefficient *n*. There are many methods for calculating the yield stress of a fluid, however, the results in tables 7 & 8 and figure 61 shows that they are not all closely comparable. This is because, for some methods such as the modulus cross-over, the fluid must act as a solid at low shear rates

in order to cross over to display a liquid-like behaviour at high shear rates. For most the inks discussed in this chapter, a liquid-like behaviour was displayed at low shear rates, which is beneficial for the SLA printing process as the inks need to flow at low shear rates for the deposition of a new layer of resin.

Understanding the scattering effects of 2D materials in SLA inks is crucial in improving printability. By matching, the refractive index of the UV resin to the filler material there should be a decrease in scattering effects, resulting in an appropriate C_d avoiding under/over curing. The refractive index difference between PEGDA/BAPO and GNP was greater than that of BN, allowing higher loadings of BN to be printable and limiting GNP to 8 wt. %. Looking further at matching other 2D materials such as MoS_2, BP, GO and Mxenes etc. we can predict the likelihood of scattering and understand the maximum concentration and C_d that can be achieved.

As an alternative to changing the filler material, we could also change the UV pre-polymer PEGDA to reduce the Δn^2. The reduction in the lateral size of the platelets should also see a reduction in scattering, allowing the photons to be absorbed by the medium. However, this poses a problem, as most layered 2D materials are irregular in geometry and not consistent in size for the large quantities needed for SLA printing. One method to tackle this issue is by sizing the flakes through centrifugation. This was achieved by Khan et al. where they used centrifugation to size order their flakes at 3000, 1000 and 500 rpm by removing the supernatant between each run. The small flakes were collected from the supernatant and the larger flakes remained within the sediment. The incremental decrease in centrifugation speed resulted in larger flakes to be collected from the supernatant each time.[16]

When comparing scattering models for both GNP and BN-based inks the factor that had the most significant influence on scattering was the lateral size of the flakes. When comparing the C_d of the BN 20 and eBN 20 window panes results there is a significant difference in Q, much more so than comparing the C_d of BN 8 and GNP 8 with a large difference in Δn^2. However, that being said the model that best described the type of scattering of the experimental values is Mie scattering. This is because the model takes into consideration large differences in n and the size of particles. Whereas Q_n only takes into consideration the difference in n and Q_{geo} is related to only the size of the

platelets, and for Q_{ray} the size parameter needs to be less than 1 which was not the case for the BN and GNP platelets.

The *'window panes'* test is useful in calculating the exact printing parameters E_c and D_p value for the desired C_d at a given E_0. However, in practice, the results produced a depth of penetration value outside of the limits of the printer (maximum 20 mm). This limitation leads to the pursuit of other techniques to find the optimum printable parameters, including increasing the E_c value of 20 % at a time to find a reasonable C_d. Which resulted in the findings that printing GNP-based inks required an extremely large amount of power for the $E_0 \sim 90$ mJ/cm^2 to achieve a reasonable thickness for a single oriented layer (C_d). Therefore, for printing with GNP-based inks with high solid loadings to be possible, a more powerful laser combined with the reduction in viscosity, possibly due to the addition of diluents, would be required.

To summarise this chapter has reviewed the overall printability of the composite inks, including finding the maximum solid loading of both BN and GNP in the PEGDA resin and establishing the optimum printing parameters to print 3D structures. Subsequently, these findings can be applied to 3D print BN and GNP composites, to help characterise their mechanical, electrical and thermal properties, discussed in chapter 5.

4.8 References

[1] M. L. Griffith and J. W. Halloran, "Scattering of ultraviolet radiation in turbid suspensions," *J. Appl. Phys.*, vol. 81, no. 6, pp. 2538–2546, 1997.

[2] G. A. Brady and J. W. Halloran, "Stereolithography of ceramic suspensions," *Rapid Prototyp. J.*, vol. 3, no. 2, pp. 61–65, 2005.

[3] F. Doreau, C. Chaput, and T. Chartier, "Stereolithography for Manufacturing Ceramic Parts," *Adv. Eng. Mater.*, vol. 2, no. 8, pp. 493–496, 2000.

[4] M. L. Griffith and J. W. Halloran, "Freeform Fabrication of Ceramics via Stereolithography," *J. Am. Ceram. Soc.*, vol. 79, no. 10, pp. 2601–2608, 2005.

[5] C. Hinczewski, S. Corbel, and T. Chartier, "Ceramic suspensions suitable for stereolithography," *J. Eur. Ceram. Soc.*, vol. 18, no. 6, pp. 583–590, 1998.

[6] S. M. Kim *et al.*, "Synthesis of large-area multilayer hexagonal boron nitride for high material performance.," *Nat. Commun.*, vol. 6, p. 8662, 2015.

[7] V. Chan, P. Zorlutuna, J. H. Jeong, H. Kong, and R. Bashir, "Three-dimensional photopatterning of hydrogels using stereolithography for long-term cell encapsulation," *Lab Chip*, vol. 10, no. 16, p. 2062, 2010.

[8] K. Wang *et al.*, "A novel method for preparation of cross-linked PEGDA microfibers by low-temperature photopolymerization," *Mater. Lett.*, vol. 161, pp. 317–320, 2015.

[9] H. Seo, S. G. Heo, H. Lee, and H. Yoon, "Preparation of PEG materials for constructing complex structures by stereolithographic 3D printing," *RSC Adv.*, vol. 7, no. 46, pp. 28684-28688, 2017.

[10] W. Yang, H. Yu, W. Liang, Y. Wang, and L. Liu, "Rapid fabrication of hydrogel microstructures using UV-induced projection printing," *Micromachines*, vol. 6, pp. 1903-1913, 2015.

[11] M. L. Griffith and J. W. Halloran, "Ultraviolet curing of highly loaded ceramic suspensions for stereolithography of ceramics," in *Proc. Solid Freeform Fabr. Symp*, 1994, pp. 396–403.

[12] A. M. Wierenga, T. A. J. Lenstra, and A. P. Philipse, "Aqueous dispersions of colloidal gibbsite platelets: synthesis, characterisation and intrinsic viscosity measurements," *Colloids Surfaces A Physicochem. Eng. Asp.*, vol. 134, no. 3, pp. 359–371, 1998.

[13] C. Hinczewski, S. Corbel, and T. Chartier, "Ceramic suspensions suitable for stereolithography," *J. Eur. Ceram. Soc.*, vol. 18, no. 6, pp. 583–590, 1998.

[14] A. Harvey *et al.*, "Non-resonant light scattering in dispersions of 2D nanosheets," *Nat. Commun.*, vol. 9, no. 1, p. 4553, 2018.

[15] G. Taormina, C. Sciancalepore, M. Messori, and F. Bondioli, "3D printing processes for photocurable polymeric materials: technologies, materials, and future trends," *Journal of Applied Biomaterials and Functional Materials*.vol. 16, no. 3, pp. 151-160, 2018.

[16] U. Khan, A. O'Neill, H. Porwal, P. May, K. Nawaz, and J. N. Coleman, "Size selection of dispersed, exfoliated graphene flakes by controlled centrifugation," *Carbon N. Y.*, vol. 50, no. 2, pp. 470–475, 2012.

[17] H. Zhou *et al.*, "Hydrogen abstraction of carbon/phosphorus-containing radicals in photoassisted polymerization †," vol. 6, pp. 68952-68959, 2016.

5

Properties of 3D Printed GNP and hBN-based Composites

5.1 Introduction

In the previous chapter the ink formulation and printability of BN and GNP containing SLA inks were discussed on a '2D' single printed layer basis. This chapter will now discuss the mechanical, thermal and electrical properties of three-dimensional stereolithographic parts produced from these inks. Understanding the effects of resin formulation on print properties, and to be able to design inks that are printable with the hardware available.

Through 3D printing, we can manufacture complex geometries producing minimal waste material over short processing times. However, the mechanical properties of these printed parts tend to display brittle and weak behaviour. The addition of fillers is commonly used to increase the strength properties and alter the function of the printed parts to be thermally or electrically conductive. At present, there have been few reports on the properties of printing 2D material-based resins[1][2][3] using SLA especially in regards to the 'high' concentrations (above 2 wt. %) reported in this research. This chapter demonstrates the scaling effects of trying to print multi-layered 3D structures, focusing on the print quality which is determined by the resolution in the *x, y* and *z*-planes. This has been done through the analysis of support structures with consideration of adaptations of the SLA printer, including raster patterns and elevator speeds.

This chapter aims to fill these gaps found in the literature by analysing the mechanical, thermal and electrical properties of the 3D printed, 2D material-based composites, comparing the results to current composites both printed and manufactured using alternative methods.

5.2 Adjusting the 3D Printability of Composites

The C_d and D_p values discussed in chapter 4 have been calculated to print one layer thick films, therefore to translate this into 3D structures further controls and adjustments are required for good printability of 3D parts. These controls include adjustments to the support structures, print speeds and raster patterns.

Unlike other methods of additive manufacturing such as FDM where layer by layer adhesions use mechanical deposition, SLA printed parts use chemical covalent bonds in the adhesion between layers. This, in theory, should result in a fully dense isotropic printed part. During printing the SLA parameters are set to allow for a partial cure of each layer, creating what is known as the 'green state' (figure 67). Therefore when the next layer of resin is deposited on top of the previous surface, which is in its green state, full polymerisation of the previous layer will occur. This process forms covalent bonds not only in the *x, y*- plane but also in the *z*-axis, leading to isotropy via a continuous polymer network, free of voids.[4] The quality of SLA printed parts is generally high when compared to other techniques, offering smooth finishes and high resolutions in *x*, *y* and *z*-direction ~10 µm in *z*-axis compared to 3DP 100-250 µm or 80 µm SLS.[5] However, this is with a compromise to the speed of the prints requiring longer processing times as the resolution increases.[4]

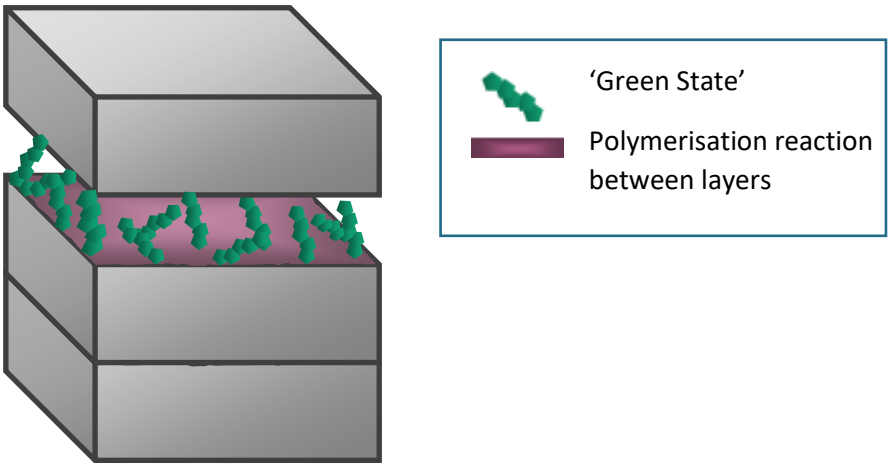

Figure 67 Scematic of curing between individual layers during the SLA printing process.(adapted from Formlabs) [4]

5.2.1 Support Generation

When using additive manufacturing to print 3D parts it is crucially important to incorporate a sturdy support system to avoid collapsing during printing. In stereolithography, supports are made from the same resin and designed to break away easily using thin structures. The supports are used to anchor the part to the build plate and support any overhangs (greater than 45°) or bridges in the design.[6] For all prints, support structure designs were generated using Lightyear software, the supports were in a point formation and could be edited manually to change the thickness of the strands and positions of each strand. When printing the composite inks, the software-generated supports collapsed under the component causing bowing of parts and slippage between layers, leaving floating parts within the vat of resin. By increasing the thickness of the support strands and the addition of more supports, a visible reduction in the bowing effect was seen due to the alleviation of stresses at a single build point. The supports are represented below in figure 68 and a comparison of the original, software determined and final, improved support structure parameters are displayed in table 14. Notably, the thickness of the strands and intersects (table 14) were increased in order to support the printed parts sufficiently during printing.

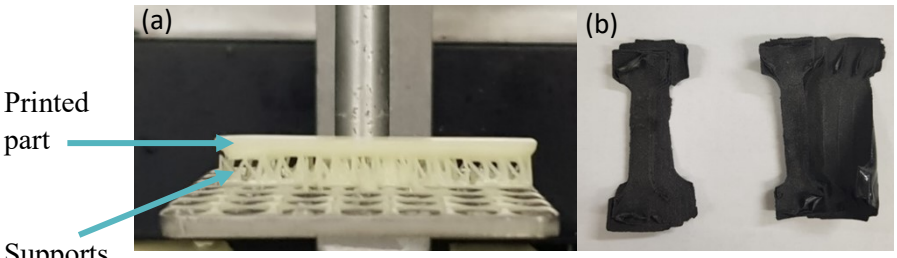

Figure 68 (a) Example of point supports for flexure-test samples BN 1, and (b) slippage between layers of GNP 1 tensile test specimen.

Table 14 Adjustments of parameters in structural supports of SLA printed parts

Fine Point Supports	***Original (mm)***	***New (mm)***
Strand thickness	0.40	1.00
Strand spacing	3.05	3.05
Top interface intersect	0.40	1.00
Top interface exposed height	0.61	0.61
Bottom interface intersect	0.61	0.61
Bottom interface exposed	0.61	0.61
Projection offset height	5.08	5.08
Projection thickness	0.40	1.00
Triangular offset width	5.08	5.08

5.2.2 Print Speeds & Raster Pattern

The speed of printing is governed mainly by the C_d outcomes mentioned in chapter 4 i.e. the smaller the C_d the longer the print time. However, the speed at which the elevator lowers the build plate into the resin can be adjusted. The built-in modes for the Viper Si2 printer were as follows:

- Slow: 0.76 mm/s
- Medium: 1.52 mm/s
- Normal: 2.54 mm/s

For all composite resins '*normal*' mode was used since printing at slower speeds caused excess resin to build up, resulting in warped parts.

To optimise the print resolution and to help reduce warpage of the printed parts, the raster pattern of the laser was also adjusted shown in table 15. Studies have shown that, by changing the raster pattern from a long raster pattern to a short one, the degree of warpage can be significantly reduced.[7] The number of layer hatches, up and down fills with the laser were adjusted to see which combination printed flat beam parts with minimal defects. The beam design was chosen as flat structures are known to be difficult to print due to their tendencies to contract in the centre causing warpage because of the different curing rates, which is why beams are often printed at a 90° angle to the build plate.[8]

Table 15 Dimensional results from changing the raster pattern of the SLA laser.

Parameters	**Test**			
	Original (1)	2	3	4
Layer thickness	0.10	0.10	0.10	0.10
Line width compensation	0.13	0.13	0.13	0.13
Additional boarders	3.00	3.00	3.00	3.00
Number of up hatches	0.00	2.00	0.00	0.00
Number of down hatches	0.00	2.00	0.00	0.00
Number of layer hatches	2.00	2.00	2.00	4.00
Number of up fills	2.00	2.00	4.00	2.00
Number of down fills	2.00	2.00	4.00	2.00
Over cure: Prime layer boarder	0.28	0.28	0.28	0.28

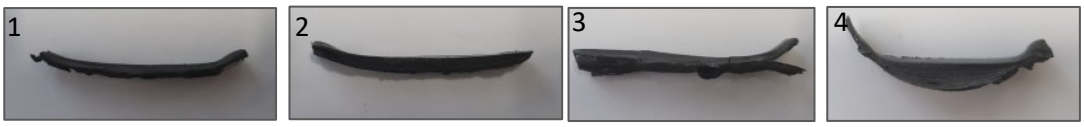

Figure 69 Photographs of the outcomes of changing the raster pattern of the SLA laser using 1 wt. % GNP ink.

The increase in the number of layer hatches caused large amounts of bowing in test 4, with a thickness of 5.62 mm at the centre of the bar. This is because increasing the number of hatches can cause over-curing as the laser passes over the printed area more times, which can lead to the part contracting inwards as seen in figure 69, test piece 4.[9] The increase in the number of up and down fills also caused a splitting effect between layers due to over curing between layers in test 3. The best outcome of the raster pattern variations was test piece 2 as visually this produced the most 'beam-like structure' therefore all further printing parameters would use this combination.

5.2.3 Resolution

The experimental resolution and accuracy of the printed parts were determined by measuring the width, height and depth of flexural specimens in comparison to the original CAD file, the results of which have been displayed in table 16. Optical microscopy was used to measure the average layer thickness of the printed parts, which was ~100 µm for all composite inks (figure 70).

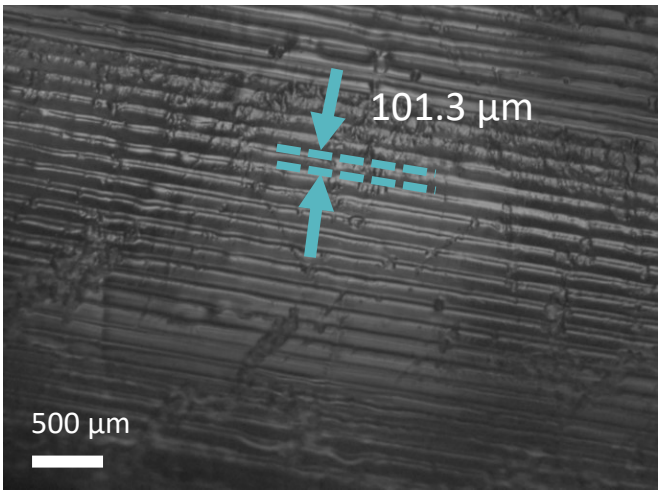

Figure 70 Optical microscope image of 3D printed layers of UV ink.

Table 16 Measured resolution of 3D printed composites.

	Width (x-*y*) (mm)	Accuracy (+/-mm)	Depth (*z*) (mm)	Accuracy (+/-mm)	E_c (mJ/cm^2)	D_p (mm)
CAD	6.00	-	3.00	-	-	-
UV Ink	6.27 (+/- 0.08)	0.27	2.84 (+/- 0.04)	0.16	12	3.7
BN 1	6.69 (+/- 0.17)	0.69	2.85 (+/- 0.10)	0.15	12	3.7
BN 2	6.92 (+/- 0.02)	0.92	2.73 (+/- 0.08)	0.27	12	3.7
BN 4	7.16 (+/- 0.10)	1.16	2.74 (+/- 0.08)	0.26	12	3.7
BN 8	6.54 (+/- 0.22)	0.54	2.62 (+/- 0.08)	0.38	12	3.7
BN 20	6.67 (+/- 0.15)	0.67	3.01 (+/- 0.10)	0.01	30	4.2
GNP 1	6.61 (+/- 0.01)	0.61	2.23 (+/- 0.15)	0.77	12	3.7
GNP 2	7.29 (+/- 0.25)	1.29	2.80 (+/- 0.33)	0.20	12	3.7

The resolution in the *x, y*-plane is also known as width of cure W_c is controlled by the assumed Gaussian curve that the laser produces. The width of cure can be theoretically calculated using the following equation:

$$W_c = \sqrt{2} \times w_0 \times \sqrt{ln\left(\frac{E_0}{E_c}\right)} \tag{23}$$

Whereby W_c is the width of cure, w_0 is the radius of the beam (0.25 mm using standard resolution at $1/e^{-2}$), E_0 is the exposure energy (mJ/cm^2) and E_c is the critical exposure energy (mJ/cm^2).[10] However, this equation does not take into consideration the effect of fillers and is therefore only valid as a theoretical equation for the pure PEGDA/BAPO resin width of cure.

Figure 71 shows a plot of the theoretical cure width of the UV curable PEGDA polymer using the E_c values 12 mJ/cm^2 and 30 mJ/cm^2 which matches the conditions used to print the samples in table 16. Here the theoretical value for the width of cure of the UV resin increases with increasing E_0, and decreases with an increase in E_c, a decreased W_c value should correspond to a higher degree of accuracy in the x, y-plane. However, the measured W_c from the experimental data in table 16 does not agree with this relationship, as the W_c increases slightly with an increase in E_c (figure 71) when considering the values of the BN 8 and BN 20 composites. This is because the effects that fillers have on the W_c is not incorporated into (equation 23). From the

experimental data, the trends observed in the GNP composites show an increase in W_c with solid loading when using the same printing parameters. Similarly, the trends in the BN-based inks show an increase in W_c with solid loading up to 4 wt. %. Broadening behaviour of the width of cure has been reported by Gentry et al. where they observed a decrease in W_c as the difference in the refractive index $(\Delta n/n_0)$of their ceramics increased.[11] Here, the GNP-based composites display a decrease in W_c (6.61 mm) compared to the BN-based composite (6.69 mm) at 1 wt. % filler loading.

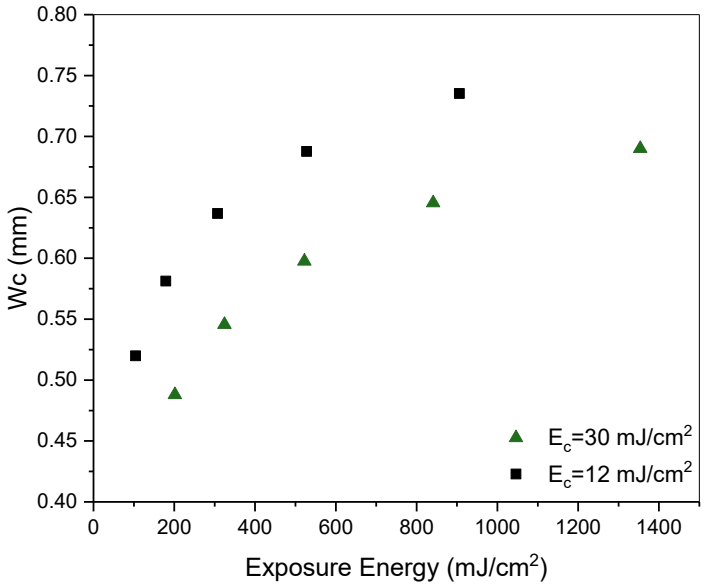

Figure 71 Theoretical width of cure of UV ink when the E_c=12 mJ/cm^2 (set parameters for all GNP-based inks and BN-based inks below 8 wt. %) and E_c=30 mJ/cm^2 (set parameters for BN 20 wt. % inks).

In order to print high accuracy 3D parts (5.2.4), careful consideration must be taken into supporting the structure during printing. Insufficient supports can lead to bowing effects and slippage between layers during printing which is not only time-consuming but costly for the manufacturer. The raster pattern of the laser and speed of print must also be considered because this will determine the overall resolutions and surface finishes of the printed parts. By considering and adjusting these factors the work presented here has produced a z-resolution of ~100 µm (figure 70) and an *x, y*-resolution which ranges from 0.61 to 1.29 mm for GNP and 0.54 mm to 1.16 mm for BN depending on the concentration of filler used (table 16).

5.2.4 Examples of Printed Parts

Below, figure 72 displays some examples of SLA printed GNP composites showing the printed samples for mechanical testing and heat sinks for potential thermal management applications for electronics. Figure 73 displays BN printed parts showing the capabilities of the SLA printer.

Figure 72 3D printed GNP-based composites 1 wt. %.

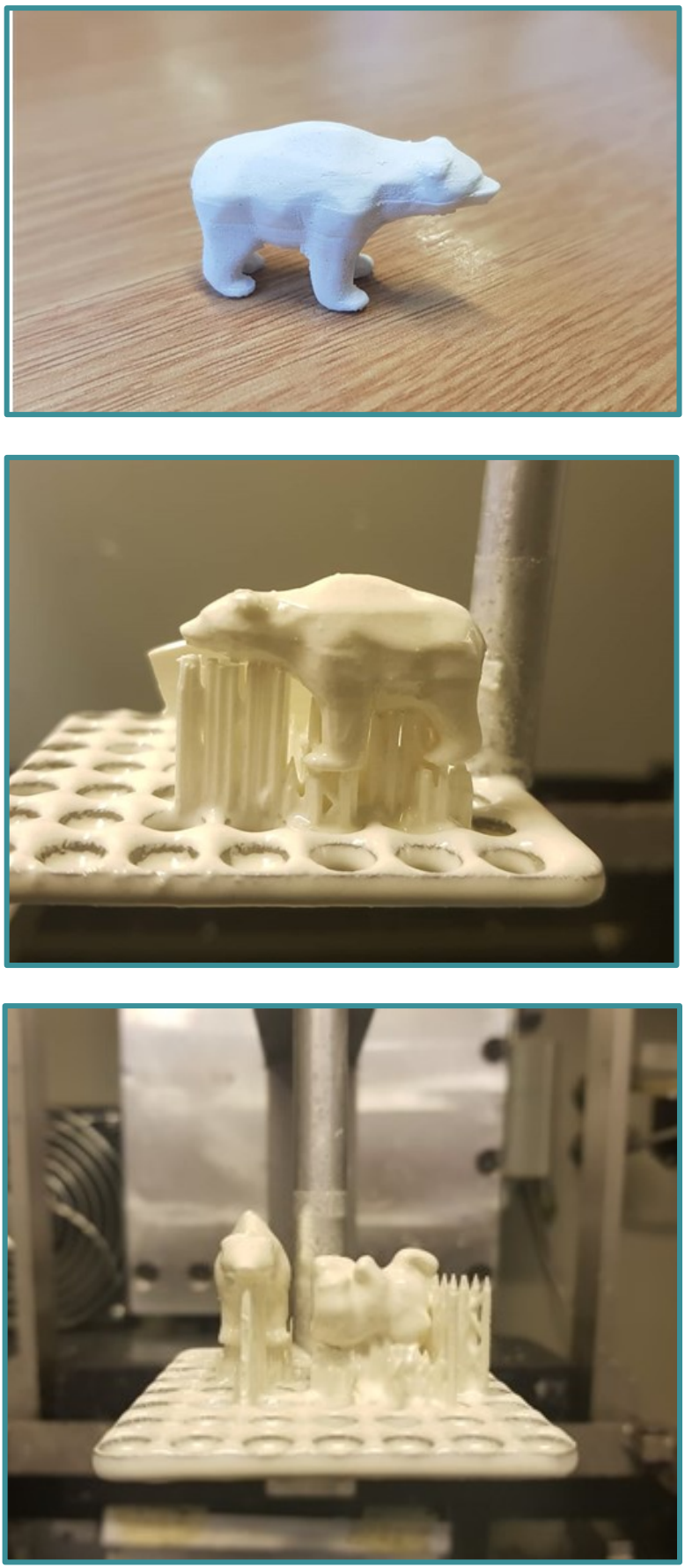

Figure 73 3D printed BN-based composites 20 wt. %.

5.3 Properties of 2D-Material Printed Composites

This section discusses the properties of the printed 3D parts including the chemical, mechanical, electrical and thermal properties. To understand the effects of printing with 2D material fillers with the aim to improve these properties when compared to typical SLA ceramic-based resins.

5.3.1 Thermomechanical and Spectroscopic Analysis

Although a solid loading of 8 wt. % GNP was achieved in the '2D printing' preliminary tests, during scale-up there was poor adhesion between the layers due to under-curing resulting in failed prints. Adjustments to the E_c and D_p values were made in an attempt to combat this, however, the limits of the printer were reached before successful prints were achieved. The maximum possible solid loading of GNP in printed composites was therefore limited to 4 wt. % for 3D structures. Although only inks up to 4 wt. % are printable, compositions up to 8 wt. % were tested by curing the composite directly in the DSC pan using a UV oven to extend the dataset.

The glass transition temperature (T_g) of printed composites has been investigated to understand the effect of nanoplatelets on the thermal properties of the composites (figure 74). The T_g values for the reference polymer without the inclusion of fillers (-38°C) falls within a similar range for low molecular weight PEGDA previously reported (-40 to -30 °C) [12]. The T_g of the composite increases 7.3% (-36 °C) and 38.6% (-24 °C) with the addition of 8% BN and GNP, respectively. BN20 composites reach a T_g of -20 °C. The inclusion of nanoplatelets has shown to restrict the chain mobility of the polymeric matrixes in composites leading to the increase in T_g.[13][14]

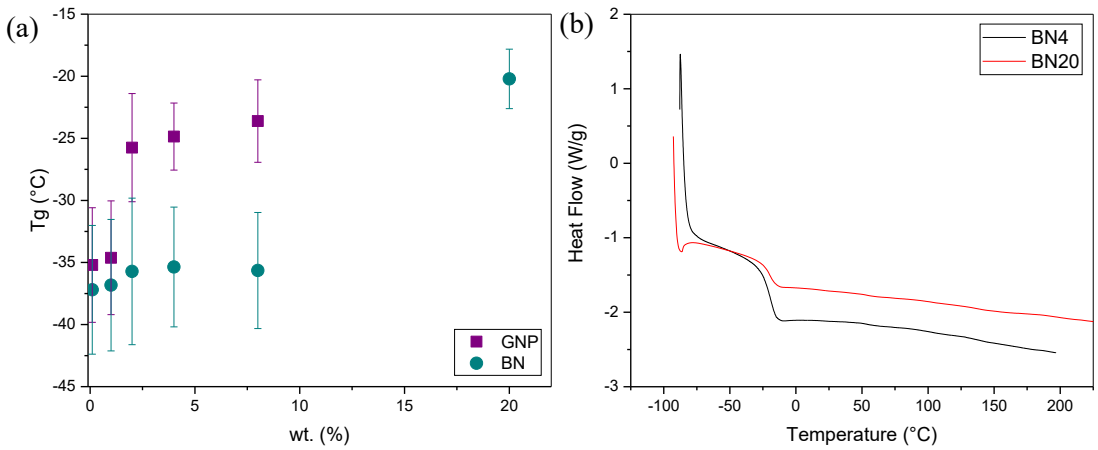

Figure 74 (a) Tg results of printed composites with varying concentrations of GNP and BN. (b) Example of DSC results of BN 20 wt. % and 4 wt. % displaying 2rd heating curve.

The FTIR spectra of the cured UV ink (PEGDA/BAPO), a BN-based composite and a GNP-based composite are shown in figure 75. FTIR was used to determine if the BN and GNP-based inks were cured during printing by displaying the associated PEGDA peaks in both composites. The bands at 804.1 cm^{-1} and 1371.2 cm^{-1} are related to the B-N-B bending peak and the B-N bond respectively.[15] The peaks at 1410 cm^{-1} and 1640 cm^{-1} are the vibrations of the –COOH bonds[16] and graphitic double bonds[17] in the GNP-based composite. The strong peak at 2863 cm^{-1} and 1091cm^{-1} is related to the CH_2[18] and -C-O-C[19] bonds respectively, the arrows are assigned to the carbonyl stretching band of PEGDA.[20] Showing that the PEGDA polymer has been cured during printing even with the addition of the filler materials.

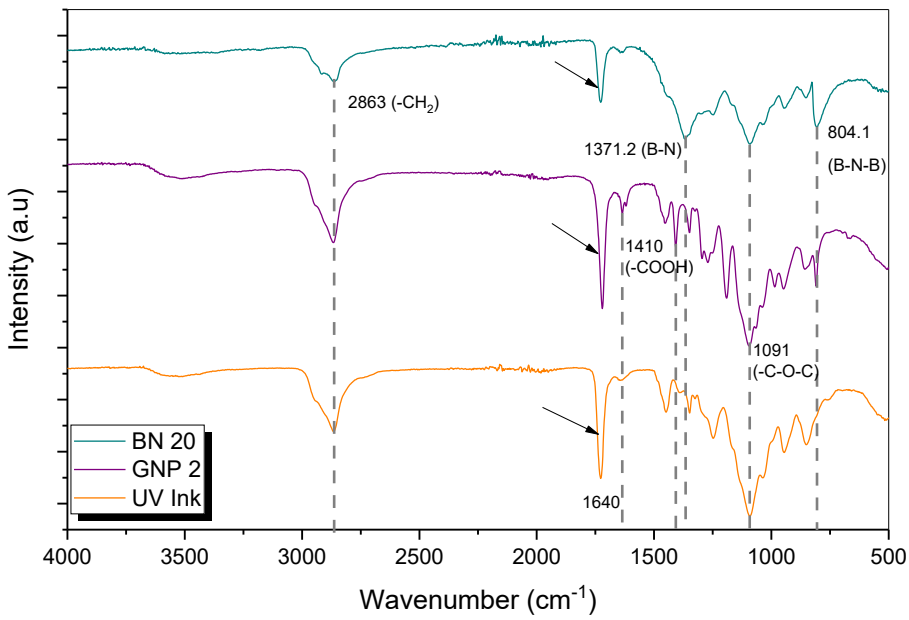

Figure 75 FTIR of UV polymer, BN-based composite and GNP-based composite.

TGA data were used to assess what proportion of the initial filler content in the inks remained in the composites after printing (figure 76). The printed parts were heated to burn out the polymer and determine the weight percentage of solid particles that remained. The results showed that the solid content was lower than expected (table 17) suggesting that some of the inks had deposited a sediment of nanoplatelets at the bottom of the resin vat during printing. At lower concentrations the composites show little sign of sedimentation as the weight retained after burning out is similar to the amount of filler added to the ink, BN 4 (as an example) retained 4 wt. % BN platelets. However at 20 wt. % BN, only 82 % of the original platelets can be accounted for, suggesting improvements in dispersing the platelets in the resin are needed (table 17).

Table 17 Weight retention of composites from TGA data.

Composite (wt. %)	Weight remained (wt. %)
BN 2	3.1
BN 4	4.0
BN 8	5.9
BN 20	16.4
eBN 20	16.0
BN 100	99.8
GNP 1	1.2
GNP 2	2.3
GNP 100	92.1

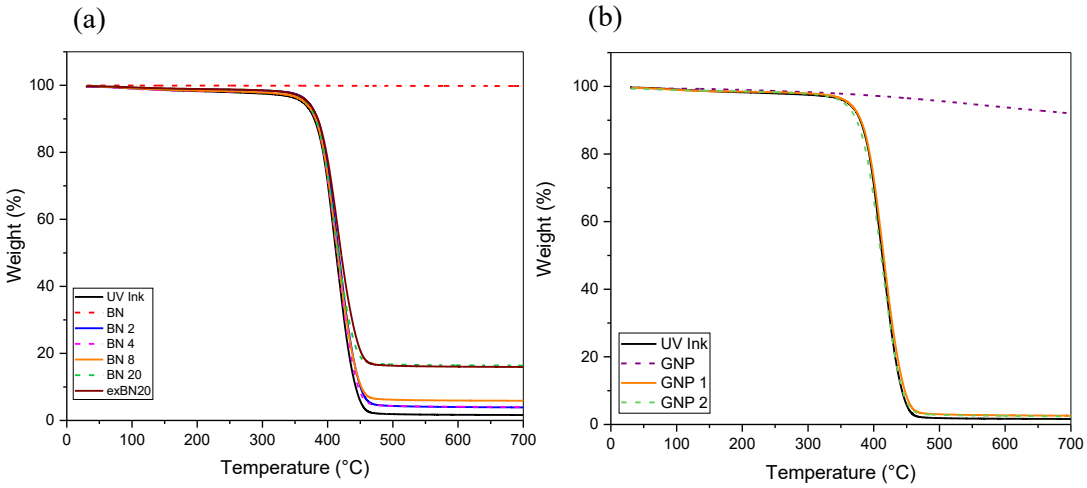

Figure 76 TGA data of (a) BN -based polymer composites and (b) GNP-based composites, showing the loss in mass as a percentage with increasing temperature.

5.3.2 Mechanical Properties

In general commercial SLA, resins tend to have high stiffness once cured but are brittle.[21][22] The additions of filler materials can improve functional properties

but can have a detrimental effect on the mechanical properties.[21] Therefore it is important to analyse the mechanical properties to determine the resins suitability for various applications. The mechanical properties of the printed composites were tested in both tensile and flexure to gain a deeper understanding of the effects of nanoplatelets in SLA resins. Due to difficulties printing with high loadings of GNPs, only flexure samples of 0.125, 0.25, 0.5, 1 and 2 wt. % and tensile specimens up to 1 wt. % were able to be prepared. The data is presented in figure 77 & 78.

The flexural modulus for the BN printed composites was between 38-64 MPa and the flexural strength was calculated at 1.4-3.0 MPa (figure 77). The increase in modulus with increasing BN loading was as expected from the rule of mixtures.[23] The largest value for flexural modulus occurred at 20 wt. % (63.8 MPa) which was a 49 % increase from the UV polymer (42.8 MPa). The flexural modulus for GNP-based composites was 10-43 MPa and the flexural strength calculated to be 0.2-2.5 MPa. The flexural modulus of the GNP-based composites decreased with increased loadings of GNP, this was not as expected and is likely to be due to weak interfacial bonding and poor adhesion between printed layers due to under-curing.[24][25]

The flexural strength or the maximum amount of bending the composite material can withstand reaches a maximum at 4 wt. % (2.99 MPa) for BN-based composites, after this the flexural strength decreases (figure 77). Similarly to the flexural modulus, the flexural strength of the GNP-based composites decreased with increased solid loading. The reduction in flexural strength with increasing filler content for both the BN and GNP composites is possibly related to poor dispersions of flakes in the polymer matrix and weak interfacial bonding.[24]

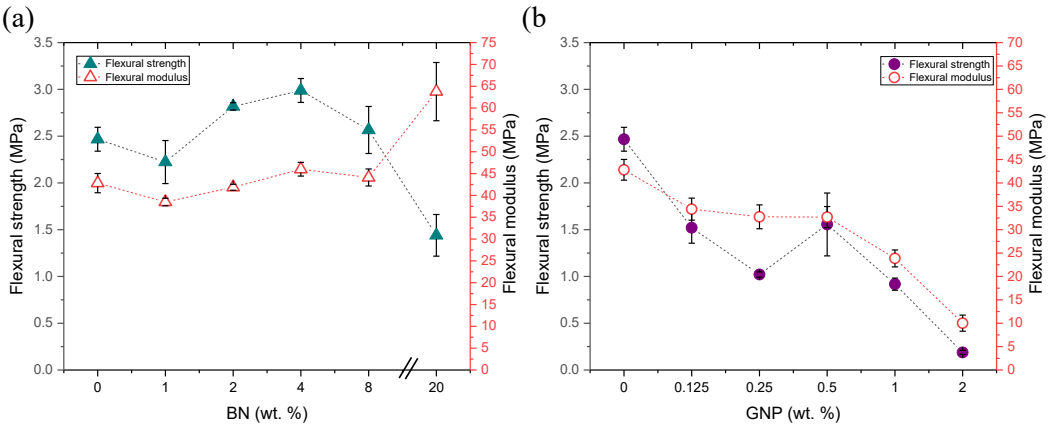

Figure 77 Three-point bend results of (a) BN and (b) GNP printed composites via SLA.

Tensile testing of GNP-based composites was particularly problematic as the specimens would break under the pressure of the tensometer clamps. For this reason, tensile specimens were prepared with a maximum concentration of 1 wt. % GNPs. To gain an understanding of the effects of GNP inside the polymer matrix 0.125 wt. %, 0.25 wt. % and 0.5 wt. % samples were additionally prepared and tested.

The tensile modulus of GNP-based composites was between 318-590 kPa and the tensile strength was calculated to be 445-946 kPa. The tensile modulus for BN composites was between 3-20 kPa and the tensile strength was calculated at 677-1663 kPa (figure 78).

The Young's modulus increased with increasing concentration of BN as expected, this relationship has been previously reported by Weng et al. and Taormina et al. where their SLA printed nanocomposites all showed an increase in ultimate tensile strength (UTS) with filler concertation.[26][27] The BN nanoplatelets have caused the composite to become stiffer and more resistant to the load applied. However, interestingly, as the weight percent of GNP increased, a reduction in the modulus could be observed and this is likely to be due to the delamination of layers during printing and/or under curing.[24][25]

At 20 wt. % loading of BN (1663.2 kPa) the UTS improved by 146% when compared to the UV polymer (677.1 kPa) (figure 78). However, there was a slight reduction in the UTS with increasing solid loading of GNP of 1% at 1 wt. % loading (668.6 kPa), this slight reduction is likely to be attributed to weak interfacial bonding between the polymer and platelets.[28]

Overall the composites containing BN produced mechanical properties far superior to those that contained GNP (flexure strength: 2.8 MPa and 0.9 MPa respectively), meaning the interfacial bonding between the UV polymer and the BN platelets was better than that of GNP. This result also gives insight into the curing process during printing, as discussed in chapter 4 the GNP inks were difficult to cure at high loadings and often resulted in under-cured parts. When printing in 3D with multiple layers, the individual layers begin to delaminate from one another as they are not sufficiently bonded together. The tensile strength of the composites is lower than the flexural strength as expected. This is because in a tensile test the maximum tensile stresses are experienced throughout the volume of the sample. Whereas the maximum tensile

strength in flexure tests are concentrated in small regions on the top surface above the neutral axis of the test specimen. If there are defects present in the sample it is more likely that a large defect will be found and cause catastrophic failure in tensile testing due to the effective volume being tested compared to three-point bend tests.

Investigations of the fractured surface of the test pieces were conducted using SEM to

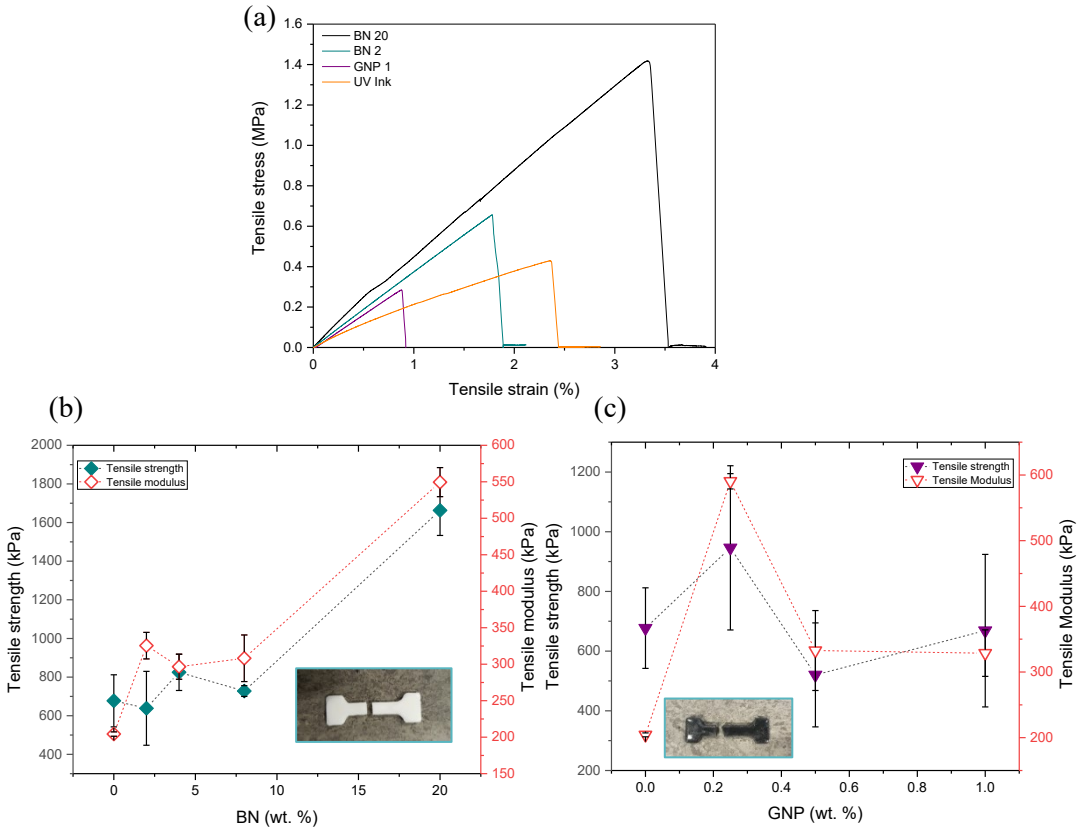

Figure 78 Example of stress stress/strain curves of printed composites (a). Tensile test results of (b) BN (c) GNP printed composites via SLA.

find microstructural information of the composites to help understand the properties observed on the macro scale in the mechanical tests.

By analysing the fracture surface of BN and GNP composites we can observe that the BN nanoplatelets have been dispersed within the polymer matrix, however, some visible agglomerates as marked by the arrows in figure 79, can be seen in the form of clusters of flakes in BN 2 wt. %. The BN-based composites showed a rough fracture surface with visible pull-out of flakes leaving platelet shaped voids. The arrangement of platelets showed no visible alignment, an example of the lack of control of filler orientation in the SLA printing process. As the solid loading of the composites increase the fracture surface shows a high density of nanoplatelets resulting in a rough

surface. At lower solid loadings the fracture surface has more smooth regions of the polymer.

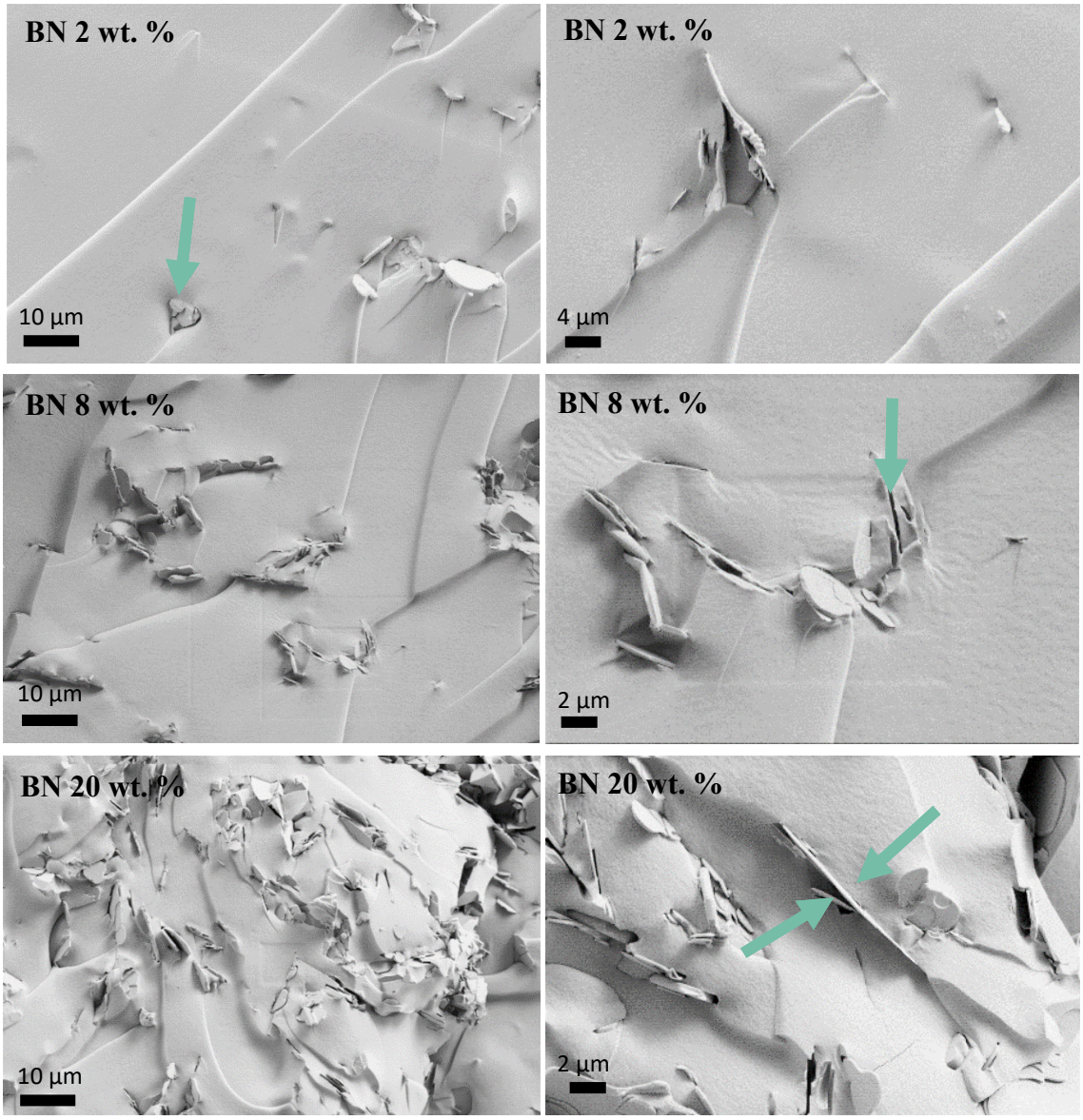

Figure 79 SEM micrographs of the flexural fracture surface of 3D printed composites with 2, 8 and 20 wt. % BN (top, middle and bottom images, respectively). Arrows indicate agglomerates for BN 2, pull-out for BN 8 and flakes for BN 20.

At 1 wt. % the fracture surface of the GNP composite appears to have clusters of flakes and large areas of the smooth polymer surface. These agglomerates are likely to be the reason why the mechanical properties decreased with an increasing filler content of GNP.[24][25] The fracture surfaces of both composites show little in the way of voids or cavities suggesting that the printed parts have been fully cured (figure 80).

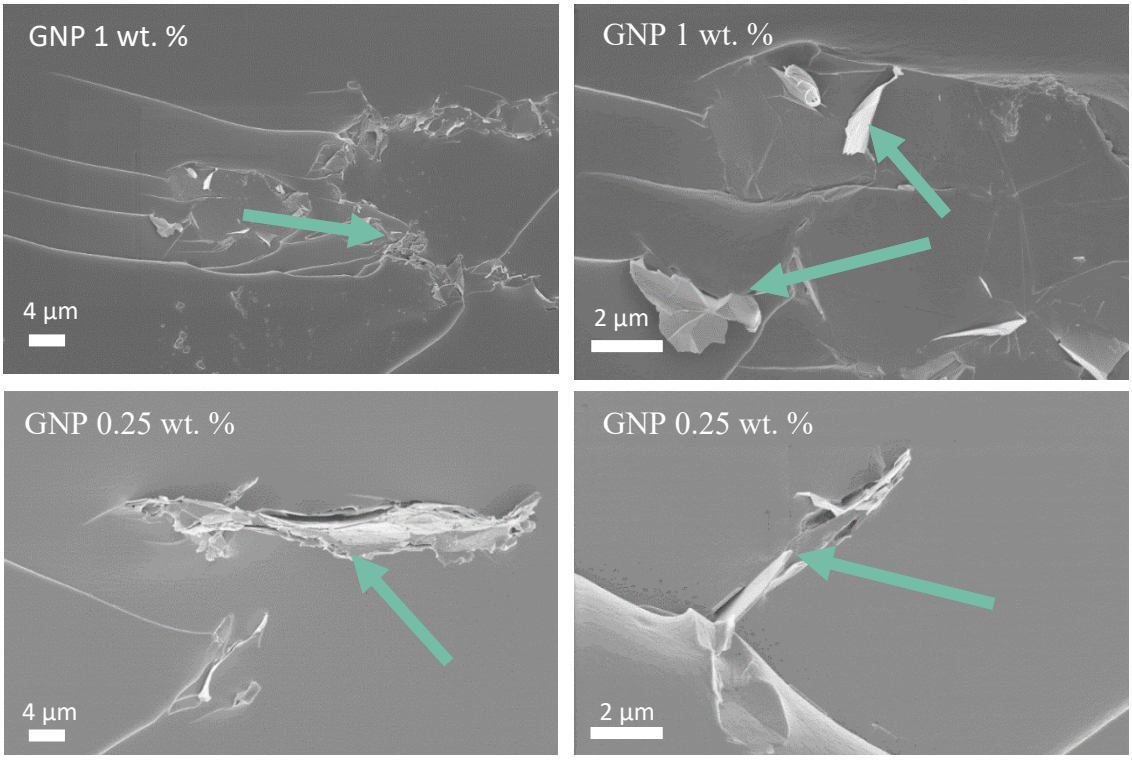

Figure 80 SEM micrographs of the flexural fracture surface of 3D printed composites with 1, 0.25 wt. % GNP (top and bottom images, respectively). Arrows indicate agglomerates for GNP 0.25, flakes for GNP 1.

5.3.3 Electrical Properties

The electrical properties of the printed parts were measured using the 2-point probe method as previously mentioned in chapter 3. As expected from the physical and chemical properties of BN discussed in chapter 2, the BN composites, showed high electrical resistance when a voltage was passed through the sample (5.73-1.88 x10^{-11} S/m) (figure 81). The GNP-based printed resins showed a steep increase in electrical conductivity as the GNP concentration increased shown in figure 81 (a). If we consider 10^{-4} S/m to be conductive, at low concentrations (1 wt. %- 8 wt. %)the GNP loading is still not enough to be considered electrically conductive (2.81 x10^{-10} S/m).[29] The maximum printable solid-loading of GNP for the 2-point probe specimens was 4 wt. %, from literature this is lower than the average percolation thresholds reported for GNP-polymer composites. Chen et al. achieved a conductivity of ~1 S/cm with 10 wt.% GNP in Poly(methyl methacrylate),[30] whilst Park et al. and Viculis et al. reached conductivities of 5 x10^{-3} S/cm with 10 wt. % GNP in Poly(propylene)[31] and 0.06 S/cm with 14.8 wt.% GNP in Poly(vinyl chloride),[32] respectively. Although Chandrasekaren et al. managed to achieve electrical conductivities of 1.8 x10^{-3} with as little as 1 wt. % GNP in epoxy,[33] it is clear that the solid loading of GNP typically needs to be much higher (~10 wt. %) to achieve a

reasonable conductivity. However, the printing with the SLA inks at 10 wt. % or higher is currently not possible without serious revisions to the ink formulation and SLA printer. Whilst the low filler concentration of GNP may not be electrically conductive, this may be advantageous for thermal applications when considering recent reports on GNP composites with high thermal conductivities at low filler loadings.[34][33][35]

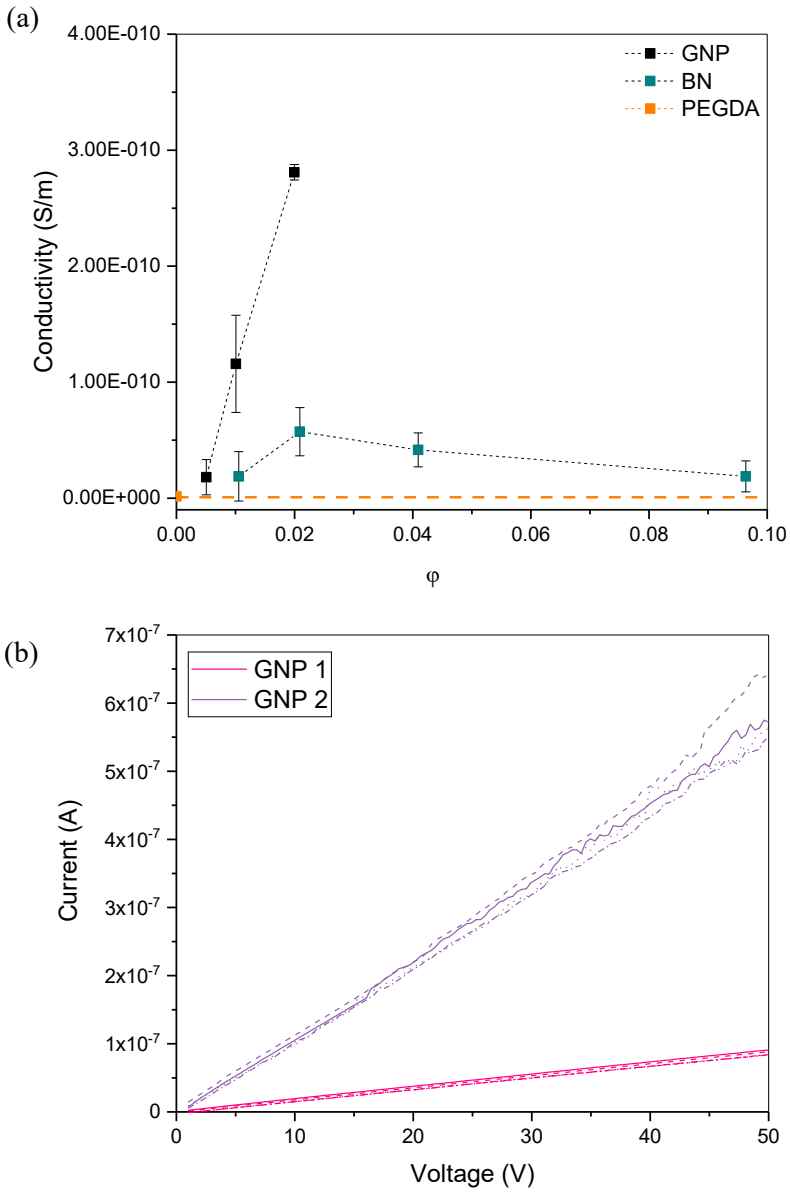

Figure 81 (a) Electrical conductivity as a function of filler volume of BN and GNP. (b) Typical current/voltage graph from two-point probe tests for GNP 1 wt.% and GNP 2 wt.%.

5.3.4 Thermal Conductivities of Printed Composites

In general, polymers are usually poor thermal conductors but have excellent and diverse printing properties.[36][37] The intrinsically high thermal properties of

GNP and BN nanoplatelets discussed in chapter 2 make for ideal filler materials for achieving thermally conductive printed parts. The thermal conductivity of the composites was measured at 30 °C intervals from 30 °C to 150 °C using the laser flash method, the results of which are displayed in figures 82 & 83. From the SEM images displayed in figure 82, it can be observed that the platelets are not aligned in any one direction. The thermal conductivity, therefore, cannot be measured in regards to in-plane or out-of-plane relative to the platelets.

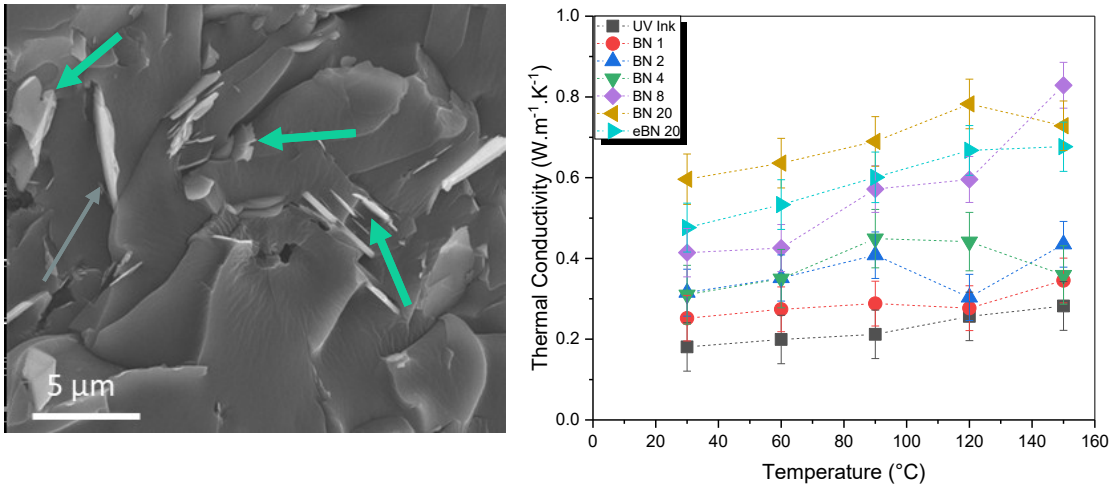

Figure 82 SEM image of BN 20 the arrows highlighting the random orientation of flakes within the polymer matrix (left). Measured thermal conductivity of BN composites (right).

The thermal conductivity of both GNP and BN–based composites increased significantly with solid loading (figures 82 & 83). The thermal conductivity of the base UV polymer was 0.21 W. m^{-1}. K^{-1} measured at 90 °C. At 4 wt. % filler loadings, the GNP composite (0.55 W. m^{-1}. K^{-1}) displays an increase in thermal conductivity of nearly 22 % compared to the BN composite (0.45 W. m^{-1}. K^{-1}). This is expected as GNP has a theoretical thermal conductivity of 3000 $W.m^{-1}.K^{-1}$ according to the manufacturers (XG Sciences). BN, on the other hand, has a theoretical thermal conductivity of 400 $W.m^{-1}.K^{-1}$.[38]

Figure 83 describes the effect of filler size on the thermal conductivity of the BN composites. BN 20 composites present higher thermal conductivity as compared to eBN 20. At 0.78 W. m^{-1}. K^{-1} (120 °C) BN 20 is 14% more thermally conductive. The increase in thermal conductivity occurs as, for the same filler concentration, the eBN

are slightly smaller and thinner, leading to a higher surface area in contact with the polymer than the BN20, resulting in an increased interfacial thermal resistance.[39]

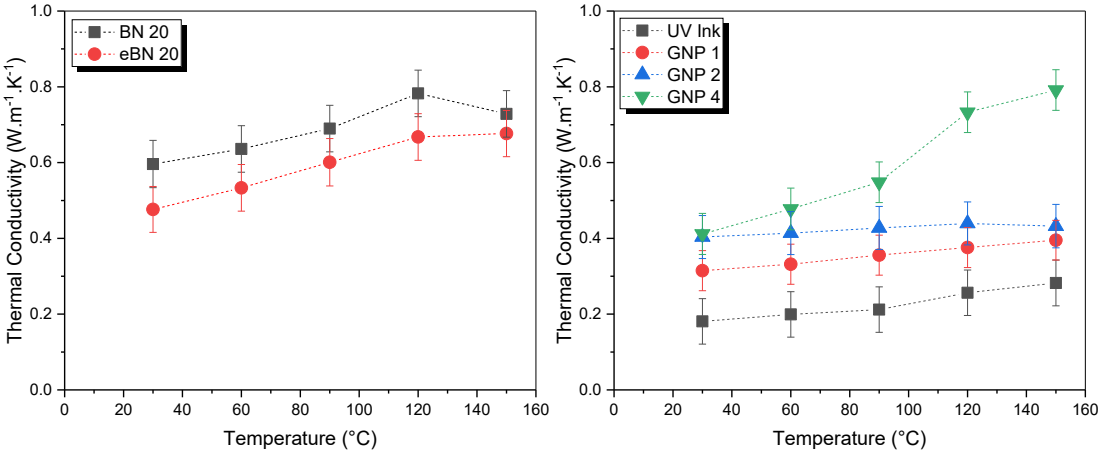

Figure 83 Thermal conductivity of BN 20 and eBN 20 (left). Thermal conductivity of GNP-based composites (right).

Figure 84 describes the thermal enhancement factor of the composites - the percentage increase in thermal conductivity of the composites relative to the UV polymer only, measured at 90 °C. The thermal conductivity of the BN-composite at 20 wt. % is nearly three and a half times greater than that of the UV polymer. Even as little as 4 wt. % GNP content will result in an increase of nearly three times that of the polymer without any filler.

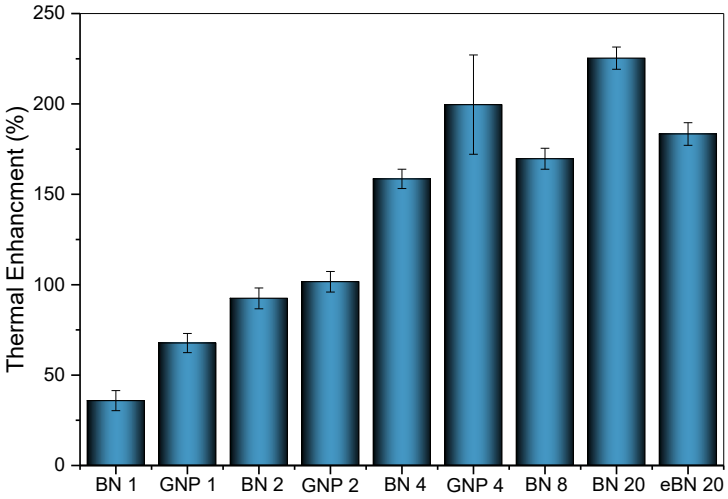

Figure 84 Thermal enhancement factor (%) of BN and GNP-based composites compared to UV polymer (calculations based on thermal conductivity measured at 90 °C).

The ability to predict the thermal conductivity of a composite as a function of its filler content can be useful when designing components for specific functions such as parts

used in thermal management applications. Theoretical and semi-empirical models such as the Maxwell-Eucken model and Agari's equation have been used to gain a deeper understanding of this effect related to the BN composites only. This is because so far BN-based composites have displayed good printability, mechanical and thermal properties with the potential to be used in thermal management applications.

Table 18 Thermal conductivity components of composites measured at 90 °C, were ρ (g/cm^3) is the density of the composite, C_p (T) (J/g °C) is the specific heat capacity, a (T) is the thermal diffusivity (mm/cm^2) and λ (T) is the thermal conductivity (W.m^{-1}.K^{-1}) (see appendix for full range of values).

Composite	*ρ*	*C_p (T)*	*a (T)*	*λ (T)*
UV Polymer	1.39	2.23	0.08	0.21
BN 1	1.11	2.24	0.12	0.29
BN 2	1.45	2.80	0.11	0.45
BN 4	1.13	2.93	0.12	0.41
BN 8	1.10	2.39	0.22	0.57
BN 20	1.23	2.34	0.24	0.69
eBN 20	1.21	2.13	0.23	0.60
GNP 1	1.05	2.25	0.15	0.36
GNP 2	1.11	2.32	0.17	0.43
GNP 4	1.07	3.27	0.16	0.55

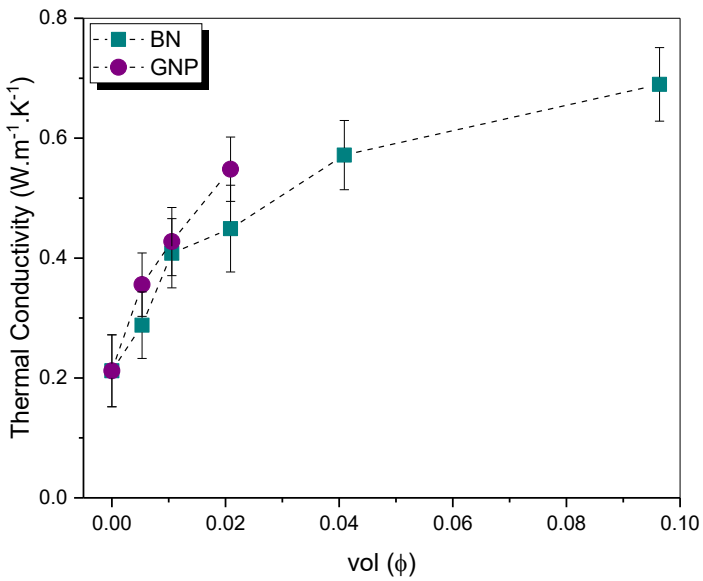

Figure 85 Thermal conductivity as a function of volume fraction of nanoplatelets, measured at 90 °C.

The results from the thermal conductivities of the composites at 90°C (table 18 & figure 85) have been evaluated using the Maxwell-Eucken model (equation 24)[40] and Agari's equation (equation 25)[41], both models are widely used for approximating the thermal conductivity of particulate composites.[42][41][43]:

$$\lambda = \frac{\lambda_p[2\lambda_p + \lambda_f + 2V_f(\lambda_f - \lambda_p)]}{2\lambda_p + \lambda_f - V_f(\lambda_f - \lambda_p)} \quad (24)$$

$$log\,\lambda_c = V_f.C_2.log\,\lambda_f + (1 - V_f).log(C_1\lambda_p) \quad (25)$$

Where λ_p is the thermal conductivity of the polymer matrix, λ_f is the thermal conductivity of the filler (in this case the theoretical conductivity of 400 W/m K was used), λ is the thermal conductivity of the composite and V_f is the volume fraction of filler. In regards to Agari's equation, the value of C_2 is the ability of the composites to form conductivity networks. In general, the C_2 value should be between 0~1 however the higher the value of C_2 the more easily the composite forms conductive pathways. The C_1 value is related to the inherent structure of the polymer including the crystallinity and crystal size.[44]

In this work, the thermal conductivities were estimated using Agari's equation (eq. (25). The thermal conductivity of the BN filler was considered to be 400 W/m K[38], and the experimental value for the UV polymer PEGDA was used (0.21 W/m K) due to difficulties obtaining reported theoretical values of the polymer matrix.

C_1 has been calculated (see appendix 9.4) to be 1.68, and C_2 to be 1.44 using the data displayed in figure 85. The calculated C_2 value is greater than 1 meaning that BN forms thermally conductive networks easily within the composite, meaning that BN is an effective filler material for improving the thermal conductivity of 3D printable inks in SLA. The value of C_1 is also greater than 1 therefore the addition of BN fillers has some effect on the secondary structure of PEGDA, changing its thermal conductivity.[46] Reports by Agari et al. describe the C_1 value to be always ~1 for polymer composites, however, the increase in C_1 value in this data could be related to the geometry or type of filler being tested. As Agari et al. tested fillers of Al_2O_3, SiO_2, copper and graphite in polyethylene (PE).[42]

The experimental values for the thermal conductivity of the composite are higher than the Maxwell-Eucken model (figure 86), this is because the model assumes the shape of the filler is sphere instead of platelets.[40] The model also presumes that the flakes do not interact with one another and are randomly distributed within a homogenous matrix.[45] Agari's equation is a semi-empirical model that considers the interaction of the platelets with the polymer through the adjustable constants C_1 and C_2 that can be used for fitting thermal conductivity data. The fitting of the Agari's equation in figure 86 is closer to the experimental values than Maxwell-Eucken's model, showing that incorporation of the constants C_1 and C_2 provides a better model for fitting the thermal conductivities of 2D material-based polymer composites as presented in this work. The R^2 value of the Agari fitting is 0.76 showing a reasonable fitting to the experimental data, the value at 1 wt. % BN, however, looks like an outlier therefore the reliability of this fitting could be improved by taking more thermal conductivity measurements between 1 wt. % and 2 wt. % or by discarding the 1 wt. % value.

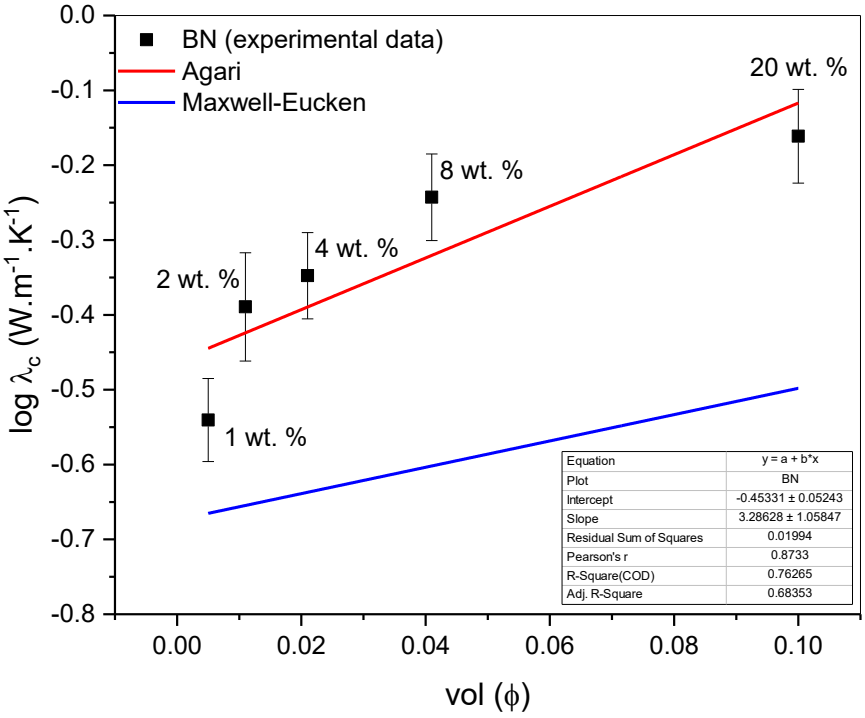

Figure 86 Results of the thermal conductivities of BN composites, black line represents the experimental values obtained, the blue and red lines represent the fitting of Agari's equation and Maxwell-Eucken to the experimental values.

5.4 General Discussion

3D printing multi-functional composites are challenging due to the high loadings needed for efficient thermal and electrical properties which are required for applications in electronics and thermal management of electronics.[47][48] The

increase in solid loading will affect not only the rheological properties of the inks and produce large amounts of scattering of the incident light leading to under-curing but will affect the resolution of the printed parts.[49][50] The tendency of the platelets to aggregate will decrease the interfacial bonding between layers resulting in delamination, impeding the overall mechanical properties.[51] Nevertheless, this work has reported a 3D printable UV curable ink with improved thermal and mechanical properties using up to 20 wt. % BN and 4 wt. % GNP as filler materials. The 3D printed GNP-based composites show promise for thermally conductive applications, however, they are yet to be optimised for laser-based printing methods which would improve print quality and their associated mechanical properties.

Adjusting the 3D Printability of Composites

Despite the optimisation of the printing parameters, there are still several factors that can affect the success of a print using SLA. One example is the atmosphere of which parts are printed in, for example, oxygen inhibition is an issue in SLA acrylate-based inks and can lead to under-curing during the free-radical polymerisation process. Another example is the spot size of the laser which will affect the resolution in the *x, y*-plane as it determines the smallest feature in the horizontal axis, however, this could not be changed for the work present here. Whilst the filler material and initial UV resin will affect the resolution in the *z*-plane.[52]

Mechanical Properties

The nanoplatelets should act as a harder and stiffer phase to the polymer matrix allowing the matrix to transfer some of the stress to the platelets which bear a percentage of the load. However, the improved mechanical properties are governed by the interfacial bonding between the polymer matrix and the nanoplatelets. With increasing concentration of GNP the tensile strength and flexure strength decreases, therefore the GNPs are acting as defects to the composite rather than reinforcing additives. This is likely to be due to under-curing during the printing and post-processing stages. Poor interfacial bonding between the platelets and polymer matrix or large agglomerates of GNP can also cause premature failure as they act as stress raisers.[24] For effective reinforcement of filler materials, the platelets should be small and evenly distributed throughout the polymer matrix, however, nanoplatelets tend to

agglomerate due to their high aspect ratios and surface energies, which has been observed in the GNP-based composites.[53]

Thermal Properties

The thermal properties of BN-based composites have been reported to form effective thermal pathways at concentrations of 20 wt. %[54] which is the maximum printability of the inks in this work. Zhang et al. achieved a thermal enhancement factor of 765 % and a thermal conductivity of 1.66 $W.m^{-1}.K^{-1}$ using agglomerated BN platelets of 40 wt. %.[54] We report a thermal enhancement of ~233 % using BN platelets with a thermal conductivity of 0.7 $W.m^{-1}.K^{-}$ at 90°C and loadings of 20 wt.%. The improvement in thermal conductivity of the printed parts has been compared to those reported in the literature in figure 87 for BN-based composites and figure 88 for GNP-based composites. The results show that, even at relatively low loadings of BN, high thermal conductivity has been achieved. The low concentration of GNPs still offers good thermal conductivity in the PEGDA polymer matrix. For both BN and GNP there are very few reports on the thermal conductivity of composites that have been 3D printed using SLA and therefore our results cannot be compared effectively with the literature.

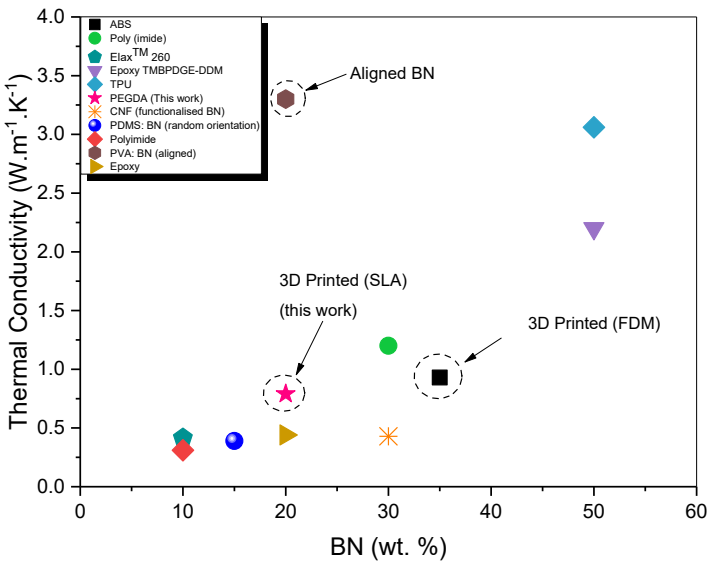

Figure 87 Comparison of thermal conductivities of BN-based polymer composites including ABS (35 wt. %)[55], Poly (imide) (30 wt. %)[56], Elax™ 260 (20 wt. %)[57] , Epoxy TMBPDGE-DDM (50 wt.%)[58], TPU (50 wt.%)[59] , PEGDA (20 wt. %)(this work), CNF (cellulose Nano-fibre functionalised BN (30 wt. %))[60], PDMS (15 wt. %)[61], Polyimide (10 wt. %)[62], PVA (20 wt. %)[63], Epoxy (20 wt. %)[64].

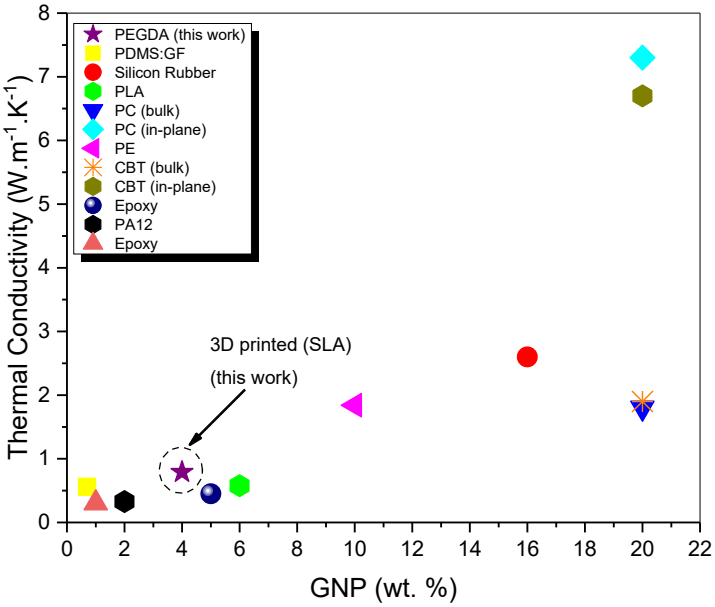

Figure 88 Comparison of thermal conductivities of GNP-based polymer composites including PEGDA (4 wt. %) (This work), PDMS: graphene foam (0.7 wt. %)[65], Silicon Rubber (16 wt. %)[66], PLA (6 wt. %)[67], PC (20 wt.%)[35], PE (10 wt. %)[68], Cyclic butylene terephthalate (CBT) (20 wt. %)[69], Epoxy (5 wt. %)[70], PA12 (2 wt. %)[71], Epoxy (1 wt. %)[72].

Effect of Filler Loading

It is clear that with both BN and GNP platelets the thermal conductivity increases with increasing solid loading of fillers (figure 82 & 83). This is because thermally conductive pathways are needed for phonons to travel via filler to filler contacts which is greatly increased as the concentration of fillers are increased.[73] However, the trade-off for increasing filler content is reduced printability (discussed in chapter 4) and brittle composites that are costly to make.

Effect of Filler Size

The results from the BN 20 and eBN 20 composites showed an increase in thermal conductivity of 14 % with the increased lateral size of the flakes in the BN 20 composite. The size of the platelets is known to affect the thermal conductivity of the composite, small particles will result in a reduction of thermal conductivity due to the interfacial area being greater, causing obstructions and scattering effects of phonons.[74] This has commonly been reported in the literature. Wu et al. reported an increase in thermal conductivity of their GNP-polyetherimide composites[75] with increasing lateral size as well as Li et al. who saw an increase in thermal conductivity of their polyimide films using micro-sized over nano-sized BN.[56]

Effect of Filler Orientation

The thermal conductivity of the composite can be heavily influenced by the orientation of the platelet. When the platelets are oriented to the in-plane direction of the flow of heat they can produce high thermal conductivities as shown in figure 87. Quill et al. reported a 64 % increase in thermal conductivity when printing 35 wt. % BN-ABS in-plane using FDM.[55] Similarly, Liu et al. reported an increase in thermal conductivity of ~280 % for their TPU- BN hot-pressed composites when their platelets where aligned in-plane.[76] No doubt the ability to orientate platelets during printing could greatly enhance the thermal properties of the composite, however currently there is little control of flake orientation in SLA printing, which has been shown in the characterisation of the fracture surfaces of the composites, therefore this could be considered for future developments in SLA printing.

To summarise the mechanical, electrical and thermal properties of the printed composites are not defined by one single characteristic of the filler or polymer matrix rather it is a combination of many factors including shape of the filler, size, solid loading, surface chemistry and intrinsic thermal conductivity of filler.[73] If the GNP or BN platelets were functionalised to the PEGDA matrix an improvement should be seen in the overall mechanical, electrical and thermal properties. As shown in this chapter, high solid loadings of both BN and GNP could also prove to improve thermal conductivity for applications in thermal management. However, the printability of these compositions for SLA rapidly decreases at concentrations above 2 wt. % GNP and 20 wt. % BN as previously mentioned in chapter 4. Furthermore, the increase in filler loading will lead to brittle composites as described in section 5.3.1. The results of the BN 20 wt. % composite has shown to have good printability with enhanced mechanical and thermal properties, the electrically insulating behaviour of the BN indicates this composite has the potential for thermal management applications in electronics which will be explored in chapter 6.

5.5 References

[1] J. Z. Manapat, J. D. Mangadlao, B. D. B. Tiu, G. C. Tritchler, and R. C. Advincula, "High-Strength Stereolithographic 3D Printed Nanocomposites: Graphene Oxide Metastability," *ACS Appl. Mater. Interfaces*, vol. 9, no. 11, pp. 10085–10093, 2017.

[2] H. Korhonen *et al.*, "Fabrication of graphene-based 3D structures by stereolithography," *Phys. status solidi*, vol. 213, no. 4, pp. 982-9985, 2015.

[3] D. Lin *et al.*, "3D stereolithography printing of graphene oxide reinforced complex architectures.," *Nanotechnology*, vol. 26, no. 43, p. 434003, 2015.

[4] "Validating Isotropy in SLA 3D Printing | Formlabs." [Online]. Available: https://formlabs.com/blog/isotropy-in-SLA-3D-printing/. [Accessed: 17-Apr-2019].

[5] X. Wang, M. Jiang, Z. Zhou, J. Gou, and D. Hui, "3D printing of polymer matrix composites: A review and prospective," *Compos. Part B Eng.*, vol. 110, pp. 442–458, 2017.

[6] Y. Xie and X. Chen, "Support-free interior carving for 3D printing," *Vis. Informatics*, vol. 1, no. 1, pp. 9–15, 2017.

[7] Y.-M. Huang and C.-P. Jiang, "Curl distortion analysis during photopolymerisation of stereolithography using dynamic finite element method," *Int. J. Adv. Manuf. Technol.*, vol. 21, no. 8, pp. 586-595, 2003.

[8] P. T. Lan, S. Y. Chou, L. L. Chen, and D. Gemmill, "Determining fabrication orientations for rapid prototyping with stereolithography apparatus," *CAD Comput. Aided Des.*, vol. 29, no.1, pp. 53-62, 1997.

[9] D. A. Schaub, K. R. Chu, and D. C. Montgomery, "Optimizing Stereolithography Throughput," *J. Manuf. Syst.*, vol. 16, no. 4, pp. 290–303, 1997.

[10] C. Hinczewski, S. Corbel, and T. Chartier, "Ceramic suspensions suitable for stereolithography," *J. Eur. Ceram. Soc.*, vol. 18, no. 6, pp. 583–590, 1998.

[11] S. P. Gentry and J. W. Halloran, "Depth and width of cured lines in photopolymerizable ceramic suspensions," *J. Eur. Ceram. Soc.*, vol. 33, no. 10, pp. 1981-1988, 2013.

[12] T. Keim and K. Gall, "Synthesis, characterization, and cyclic stress-influenced degradation of a poly(ethylene glycol)-based poly(beta-amino ester)," *J. Biomed. Mater. Res. Part A*, vol. 92A, no. 2, pp. 702–711, 2010.

[13] K. H. Liao, S. Aoyama, A. A. Abdala, and C. Macosko, "Does graphene change T g of nanocomposites?," *Macromolecules*, 2014.

[14] S. Fu, Z. Sun, P. Huang, Y. Li, and N. Hu, "Some basic aspects of polymer nanocomposites: A critical review," *Nano Mater. Sci.*, vol. 1, no. 1, pp. 2-30, 2019.

[15] M. C. Vu *et al.*, "Self-Assembly of Carbon Nanotubes and Boron Nitride via Electrostatic Interaction for Epoxy Composites of High Thermal Conductivity

and Electrical Resistivity," *Macromol. Res.*, vol. 26, no. 6, pp. 521–528, 2018.

[16] S. Araby, Q. Meng, and L. Zhang, "Polymeric ion functionalized graphite nanoplatelets with flowability Related content Elastomeric composites based on carbon nanomaterials," vol. 5, p. 85013, 2018.

[17] Q. Wang *et al.*, "Preparation of high antistatic HDPE/polyaniline encapsulated graphene nanoplatelet composites by solution blending," vol. 7, pp. 2796-2803, 2017.

[18] Y.-H. Hsueh, W.-C. Liaw, J.-M. Kuo, C.-S. Deng, and C.-H. Wu, "Hydrogel Film-Immobilized Lactobacillus brevis RK03 for γ-Aminobutyric Acid Production.," *Int. J. Mol. Sci.*, vol. 18, no. 11, 2017.

[19] Z. A. A. Hamid and K. W. Lim, "Evaluation of UV-crosslinked Poly(ethylene glycol) Diacrylate/Poly(dimethylsiloxane) Dimethacrylate Hydrogel: Properties for Tissue Engineering Application," *Procedia Chem.*, vol. 19, pp. 410–418, 2016.

[20] S. F. Dana, D.-V. Nguyen, J. S. Kochhar, X.-Y. Liu, and L. Kang, "UV-curable pressure sensitive adhesive films: effects of biocompatible plasticizers on mechanical and adhesion properties," *Soft Matter*, vol. 9, no. 27, p. 6270, 2013.

[21] G. Taormina, C. Sciancalepore, M. Messori, and F. Bondioli, "3D printing processes for photocurable polymeric materials: technologies, materials, and future trends," *Journal of Applied Biomaterials and Functional Materials*.vol. 16, no. 3, pp. 151-160, 2018.

[22] J. Borrello, P. Nasser, J. Iatridis, and K. D. Costa, "3D Printing a Mechanically-Tunable Acrylate Resin on a Commercial DLP-SLA Printer," *Addit. Manuf.*, vol. 23, pp. 374–380, 2018.

[23] S. Y. Fu, B. Lauke, E. Mäder, C. Y. Yue, and X. Hu, "Tensile properties of short-glass-fiber- and short-carbon-fiber-reinforced polypropylene composites," *Compos. Part A Appl. Sci. Manuf.*, vol. 31, no. 10, pp. 1117-1125, 2000.

[24] Z. Feng, Y. Li, C. Xin, D. Tang, W. Xiong, and H. Zhang, "Fabrication of Graphene-Reinforced Nanocomposites with Improved Fracture Toughness in Net Shape for Complex 3D Structures via Digital Light Processing," *C*, vol. 5, no. 2, p. 25, 2019.

[25] A. Kernin *et al.*, "The effect of graphene network formation on the electrical, mechanical, and multifunctional properties of graphene/epoxy nanocomposites," *Compos. Sci. Technol.*, vol. 169, pp. 224–231, 2019.

[26] Z. Weng, Y. Zhou, W. Lin, T. Senthil, and L. Wu, "Structure-property relationship of nano enhanced stereolithography resin for desktop SLA 3D printer," *Compos. Part A Appl. Sci. Manuf.*, vol. 88, pp. 234–242, 2016.

[27] G. Taormina, C. Sciancalepore, F. Bondioli, and M. Messori, "Special Resins for Stereolithography: In Situ Generation of Silver Nanoparticles," *Polymers (Basel).*, vol. 10, no. 2, p. 212, 2018.

[28] J. Bustillos, D. Montero-Zambrano, A. Loganathan, B. Boesl, and A. Agarwal, "Stereolithography-based 3D printed photosensitive polymer/boron nitride

nanoplatelets composites," *Polym. Compos.*, vol. 40, no. 1, pp. 379–388, 2019.

[29] P. C. Ma *et al.*, "Enhanced electrical conductivity of nanocomposites containing hybrid fillers of carbon nanotubes and carbon black," *ACS Appl. Mater. Interfaces*, 2009.

[30] G. Chen, C. Wu, W. Weng, D. Wu, and W. Yan, "Preparation of polystyrene/graphite nanosheet composite," *Polymer (Guildf).*, vol. 44, no. 6, pp. 1781–1784, 2003.

[31] S. Park and R. S. Ruoff, "Chemical methods for the production of graphenes," *Nat Nanotechnol*, vol. 4, 2009.

[32] L. M. Viculis, O. M. Mayer, H. T. Hahn, and R. B. Kaner, "Intercalation and exfoliation routes to graphite nanoplatelets," *J Mater Chem*, vol. 15, 2005.

[33] S. Chandrasekaran, C. Seidel, and S. Karl, "Preparation and characterization of graphite nano-platelet (GNP)/epoxy nano-composite: Mechanical, electrical and thermal properties," *Eur. Polym. J.*, vol. 49, pp. 3878–3888, 2013.

[34] M. T. Hung, O. Choi, Y. S. Ju, and H. T. Hahn, "Heat conduction in graphite-nanoplatelet-reinforced polymer nanocomposites," *Appl. Phys. Lett.*, 2006.

[35] H. S. Kim, H. S. Bae, J. Yu, and S. Y. Kim, "Thermal conductivity of polymer composites with the geometrical characteristics of graphene nanoplatelets," *Sci. Rep.*, vol. 6, no. 1, p. 26825, 2016.

[36] C. Fu *et al.*, "Improving thermal conductivity of polymer composites by reducing interfacial thermal resistance between boron nitride nanotubes," *Compos. Sci. Technol.*, vol. 165, pp. 322-330, 2018.

[37] C. M. González-Henríquez, M. A. Sarabia-Vallejos, and J. Rodriguez-Hernandez, "Polymers for additive manufacturing and 4D-printing: Materials, methodologies, and biomedical applications," *Progress in Polymer Science*. vol. 94, pp. 57-116, 2019.

[38] J. C. Zheng *et al.*, "High thermal conductivity of hexagonal boron nitride laminates," *2D Mater.*, vol. 3, no. 1, p. 11004, 2016.

[39] L. Chen *et al.*, "Analytic modeling for the anisotropic thermal conductivity of polymer composites containing aligned hexagonal boron nitride," *Compos. Sci. Technol.*, vol. 122, pp. 42-49, 2016.

[40] W. Zhou, S. Qi, Q. An, H. Zhao, and N. Liu, "Thermal conductivity of boron nitride reinforced polyethylene composites," *Mater. Res. Bull.*, vol. 42, no. 10, pp. 1863-1837, 2007.

[41] Y. Zhang, W. Gao, Y. Li, D. Zhao, and H. Yin, "Hybrid fillers of hexagonal and cubic boron nitride in epoxy composites for thermal management applications," *RSC Adv.*, vol. 9, no. 13, pp. 7388–7399, 2019.

[42] Y. Agari, A. Ueda, and S. Nagai, "Thermal conductivity of a polymer composite," *J. Appl. Polym. Sci.*, vol. 49, no. 9, pp. 1625–1634, 1993.

[43] X. Wang *et al.*, "Aerogel Perfusion-Prepared h-BN/CNF Composite Film with Multiple Thermally Conductive Pathways and High Thermal Conductivity,"

Nanomaterials, vol. 9, no. 7, p. 1051, 2019.

[44] D. Tang *et al.*, "Preparation and properties of epoxy/BN highly thermal conductive composites reinforced with SiC whisker," *Polym. Compos.*, vol. 37, no. 9, pp. 2611–2621, 2016.

[45] R. Kochetov, A. V. Korobko, T. Andritsch, P. H. F. Morshuis, S. J. Picken, and J. J. Smit, "Modelling of the thermal conductivity in polymer nanocomposites and the impact of the interface between filler and matrix," *J. Phys. D. Appl. Phys.*, vol. 44, p. 395401, 2011.

[46] Y. Agari and T. Uno, "Estimation on thermal conductivities of filled polymers," *J. Appl. Polym. Sci.*, vol. 32, no. 7, pp. 5705-5712, 1986.

[47] A. L. Moore and L. Shi, "Emerging challenges and materials for thermal management of electronics," *Materials Today*. vol. 17, no. 4, pp. 163-174, 2014.

[48] Z. A. Ghaleb, M. Mariatti, and Z. M. Ariff, "Properties of graphene nanopowder and multi-walled carbon nanotube-filled epoxy thin-film nanocomposites for electronic applications: The effect of sonication time and filler loading," *Compos. Part A Appl. Sci. Manuf.*,vol. 58, pp. 77-83, 2014.

[49] A. Harvey *et al.*, "Non-resonant light scattering in dispersions of 2D nanosheets," *Nat. Commun.*, vol. 9, no. 1, p. 4553, 2018.

[50] M. L. Griffith and J. W. Halloran, "Scattering of ultraviolet radiation in turbid suspensions," *J. Appl. Phys.*, vol. 81, no. 6, pp. 2538–2546, 1997.

[51] T. D. Ngo, A. Kashani, G. Imbalzano, K. T. Q. Nguyen, and D. Hui, "Additive manufacturing (3D printing): A review of materials, methods, applications and challenges," *Compos. Part B Eng.*, vol. 143, pp. 172–196, 2018.

[52] B. Sager, D. W. Rosen, M. Shilling, and T. R. Kurfess, "Experimental studies in stereolithography resolution," in *Proceedings of the Solid Freeform Fabrication Symposium*, pp. 70–81, 2003.

[53] R. S. Chen, M. F. H. Mohd Ruf, D. Shahdan, and S. Ahmad, "Enhanced mechanical and thermal properties of electrically conductive TPNR/GNP nanocomposites assisted with ultrasonication," *PLoS One*, vol. 14, no. 9, p. e0222662, Sep. 2019.

[54] H. Zhang *et al.*, "Optimization of Boron Nitride Sphere Loading in Epoxy: Enhanced Thermal Conductivity and Excellent Electrical Insulation," *Polymers (Basel).*, vol. 11, no. 8, p. 1335, 2019.

[55] T. J. Quill *et al.*, "Thermal and mechanical properties of 3D printed boron nitride – ABS composites," *Appl. Compos. Mater.*, vol. 25, no. 5, pp. 1205–1217, 2018.

[56] T.-L. Li and S. L.-C. Hsu, "Enhanced thermal conductivity of polyimide films via a hybrid of micro- and nano-sized boron nitride.," *J. Phys. Chem. B*, vol. 114, no. 20, pp. 6825–9, 2010.

[57] S. Ghose, K. A. Watson, D. C. Working, J. W. Connell, J. G. Smith, and Y. P. Sun, "Thermal conductivity of ethylene vinyl acetate copolymer/nanofiller

blends," *Compos. Sci. Technol.*, vol. 68, no. 7–8, pp. 1843–1853, 2008.

[58] T. Qin, H. Wang, J. He, R. Wang, Q. Qu, and X. Tian, "Preparation and application of high thermal conductivity TMBPDGE-DDM@h-BN composites," *Mater. Res. Express*, vol. 6, 2019.

[59] T. Fei, Y. Li, B. Liu, and C. Xia, "Flexible polyurethane/boron nitride composites with enhanced thermal conductivity," *High Perform. Polym.*, p. 095400831986204, 2019.

[60] K. Wu *et al.*, "Achieving a Collapsible, Strong, and Highly Thermally Conductive Film Based on Oriented Functionalized Boron Nitride Nanosheets and Cellulose Nanofiber," *ACS Appl. Mater. Interfaces*,vol.9 no. 35, pp. 30035-330045, 2017.

[61] H. Shen, C. Cai, J. Guo, Z. Qian, N. Zhao, and J. Xu, "Fabrication of oriented hBN scaffolds for thermal interface materials," *RSC Adv.*, vol. 6, no. 20, pp. 16489–16494, 2016.

[62] M. H. Tsai, I. H. Tseng, J. C. Chiang, and J. J. Li, "Flexible polyimide films hybrid with functionalized boron nitride and graphene oxide simultaneously to improve thermal conduction and dimensional stability," *ACS Appl. Mater. Interfaces*, vol. 6, no. 11, pp. 8639-8645, 2014.

[63] H. Shen, J. Guo, H. Wang, N. Zhao, and J. Xu, "Bioinspired Modification of h-BN for High Thermal Conductive Composite Films with Aligned Structure," *ACS Appl. Mater. Interfaces*, vol. 7, no. 10, pp. 5701-5708, 2015.

[64] T. Huang *et al.*, "Boron nitride@graphene oxide hybrids for epoxy composites with enhanced thermal conductivity," *RSC Adv.*, vol. 6, no. 42, pp. 35847–35854, 2016.

[65] Y.-H. Zhao, Z.-K. Wu, and S.-L. Bai, "Study on thermal properties of graphene foam/graphene sheets filled polymer composites," *Compos. Part A Appl. Sci. Manuf.*, vol. 72, pp. 200–206, 2015.

[66] M. Varenik, R. Nadiv, I. Levy, G. Vasilyev, and O. Regev, "Breaking through the Solid/Liquid Processability Barrier: Thermal Conductivity and Rheology in Hybrid Graphene–Graphite Polymer Composites," *ACS Appl. Mater. Interfaces*, vol. 9, no. 8, pp. 7556–7564, 2017.

[67] E. Ivanov *et al.*, "PLA/Graphene/MWCNT Composites with Improved Electrical and Thermal Properties Suitable for FDM 3D Printing Applications," *Appl. Sci.*, vol. 9, no. 6, p. 1209, 2019.

[68] F. E. Alam *et al.*, "In situ formation of a cellular graphene framework in thermoplastic composites leading to superior thermal conductivity," *J. Mater. Chem. A*, vol. 5, no. 13, pp. 6164–6169, 2017.

[69] Y. J. Noh, H. S. Kim, B.-C. Ku, M.-S. Khil, and S. Y. Kim, "Thermal Conductivity of Polymer Composites With Geometric Characteristics of Carbon Allotropes," *Adv. Eng. Mater.*, vol. 18, no. 7, pp. 1127–1132, 2016.

[70] F. Wang, L. T. Drzal, Y. Qin, and Z. Huang, "Mechanical properties and thermal conductivity of graphene nanoplatelet/epoxy composites," *J. Mater. Sci.*, vol. 50, no. 3, pp. 1082–1093, 2015.

[71] D. Zhu *et al.*, “Thermal and mechanical properties of polyamide 12/graphene nanoplatelets nanocomposites and parts fabricated by fused deposition modeling,” *J. Appl. Polym. Sci.*, vol. 134, no. 39, p. 45332, 2017.

[72] F. Wang, L. T. Drzal, Y. Qin, and Z. Huang, “Effects of functionalized graphene nanoplatelets on the morphology and properties of epoxy resins,” *High Perform. Polym.*, vol. 28, no. 5, pp. 525–536, 2016.

[73] S. Kemaloglu, G. Ozkoc, and A. Aytac, “Properties of thermally conductive micro and nano size boron nitride reinforced silicon rubber composites,” *Thermochim. Acta*, vol. 4999, no. 1-2, pp. 40-47, 2010.

[74] H. Chen *et al.*, “Thermal conductivity of polymer-based composites: Fundamentals and applications,” *Prog. Polym. Sci.*, vol. 59, pp. 41–85, 2016.

[75] H. Wu and L. T. Drzal, “High thermally conductive graphite nanoplatelet/polyetherimide composite by precoating: Effect of percolation and particle size,” *Polym. Compos.*, vol. 34, no. 12, pp. 2148–2153, 2013.

[76] J. Liu, W. Li, Y. Guo, H. Zhang, and Z. Zhang, “Improved thermal conductivity of thermoplastic polyurethane via aligned boron nitride platelets assisted by 3D printing,” *Compos. Part A Appl. Sci. Manuf.*,vol. 120, pp. 140-146, 2019.

6

Hybrid SLA Inks for Thermal Management Applications

6.1 Introduction

Thermal management in electronic systems is crucially important as the trend for more powerful electronics in ever-smaller packaging requires efficient heat transfer to stop overheating and short-circuiting of the electronics.[1][2][3] Heat sinks are a common technique for heat transfer where thermally conductive components, usually made from aluminium or copper, are added to circuits to transfer the heat away from the circuit to the surrounding area. Potting materials are also commonly used for heat transfer. Here, a circuit board is encapsulated by a thermally conductive material (usually a polymer) and works by displacing the air around the working electronics and reducing moisture and mechanical shocks.

Dispersing thermally conductive fillers within a polymer matrix enables the manufacture of lightweight and cost-effective thermal management components. The ability to 3D print these composites offers an exciting opportunity for manufacturing complex structures with highly efficient heat transfer systems that are not possible with traditional methods. Graphene and BN have high thermal conductivities with low densities, making them ideal filler materials for polymers. However, GNPs are electrically conductive (10^7 S/m)[4] by nature which is detrimental for thermal applications in electronics as this can lead to short-circuiting of the device. The addition of a secondary electrically insulating filler can provide a solution to the aforementioned problem. BN and GNP complement each other electronically and thermally and have previously been used together to produce hybrid composites for thermal management applications in electronics.[5][6]

This chapter aims to develop printable GNP and BN hybrid SLA inks to improve thermal conductivities for applications in thermal management systems. However in contrast to what has previously been reported in the literature (chapter 2) regarding hybrids where GNP is the primary filler and BN is used as secondary filler, here BN has been selected as the primary filler. This is because of the BN 20 wt. % ink mentioned in chapters 4 and 5 produced the best mechanical and thermal properties while attaining a good printability.

6.2 Printing of Hybrids

6.2.1 Hybrid Selection

In total, seven hybrids were synthesised using a combination of exfoliated GNP (eGNP) and BN (eBN) platelets and bulk BN (BN) (table 19). Exfoliated GNP and BN was used as the secondary filler as this method of using smaller nanoplatelets mixed with larger nanoplatelets has been reported to work effectively.[5][7] As discussed in chapter 5, the maximum printable solid loading of 2D material fillers was 20 wt. % (BN 20).At this solid loading, the printed composite also displayed the highest thermal conductivity, therefore to optimise the printed composites for thermal management applications hybrids with a maximum filler loading of 20 wt. % were explored. However, the maximum 3D printable loading of GNP was 4 wt. %, which will affect the overall maximum loading achieved for the BN-GNP hybrids. Therefore hybrids that contained high loadings of eGNP the maximum solid loading was reduced to compensate for the printability of the ink.

Table 19 Varying ratios of hybrids containing bulk BN, eBN and eGNP.

	BN (wt. %) (7.45 µm)	**eGNP (wt. %) (4.31 µm)**	**eBN (wt. %) (4.28 µm)**
Hybrid 1	19.0	-	1.0
Hybrid 2	19.0	1.0	-
Hybrid 3	16.0	-	4.0
Hybrid 4	16.0	4.0	-
Hybrid 5	2.0	2.0	-
Hybrid 6	9.0	1.0	-
Hybrid 7	19.8	0.2	-

Each of the hybrids was first printed using the *'Window Panes'* test, to assess the printability of the hybrids. The results of which indicated that Hybrid 1 and Hybrid 7 (figure 89) had the best printability (appendix 9.3). Hybrids 2, 4, 5 and 6 exhibited poor printability and fell apart during handling. Whilst hybrid 3 did have good printability the results discussed in chapter 5 showed BN to have a higher thermal conductivity than eBN, therefore hybrid 1 was selected over hybrid 3 for further studies as it had less eBN content. For this reason, Hybrid 1 and Hybrid 7 will be

compared to BN 20, the most promising ink for thermal management applications due to its high thermal conductivity from chapter 5.

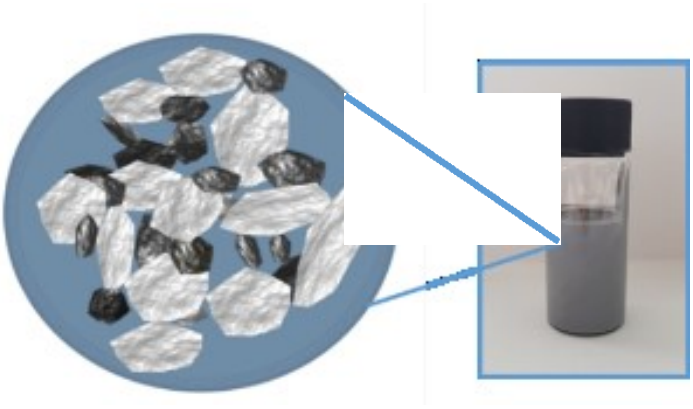

Figure 89 Representation of hybrid BN and µGNP flakes within the UV polymer ink.

6.2.2 Rheology

The rheological behaviour of Hybrid 7 (H7) and Hybrid 1 (H1) both display a viscosity of less than 5 Pa at a shear rate of 15 s^{-1} from the flow sweeps seen in figure 90. Therefore they both fall within the printable range as published by Hinczewski et al.[8] A slight increase in viscosity can be seen from the H7 ink when compared to the BN 20 ink, this correlates to the findings in chapter 4 where GNP-based inks displayed an increase in viscosity over the BN inks at the same solid loading. However in contrast H1 shows a higher viscosity than H7, despite having no GNP content. The particle size effects of BN 20 discussed in chapter 4 showed a slight increase in viscosity with decreasing platelet size. This collates to the higher viscosity seen in H1 compared to BN 20. The viscosities for all the inks are within a small range of one another (Δ2 Pa at 15 s^{-1}) suggesting that the small additions of the exfoliated fillers do not significantly influence the rheology of the inks.

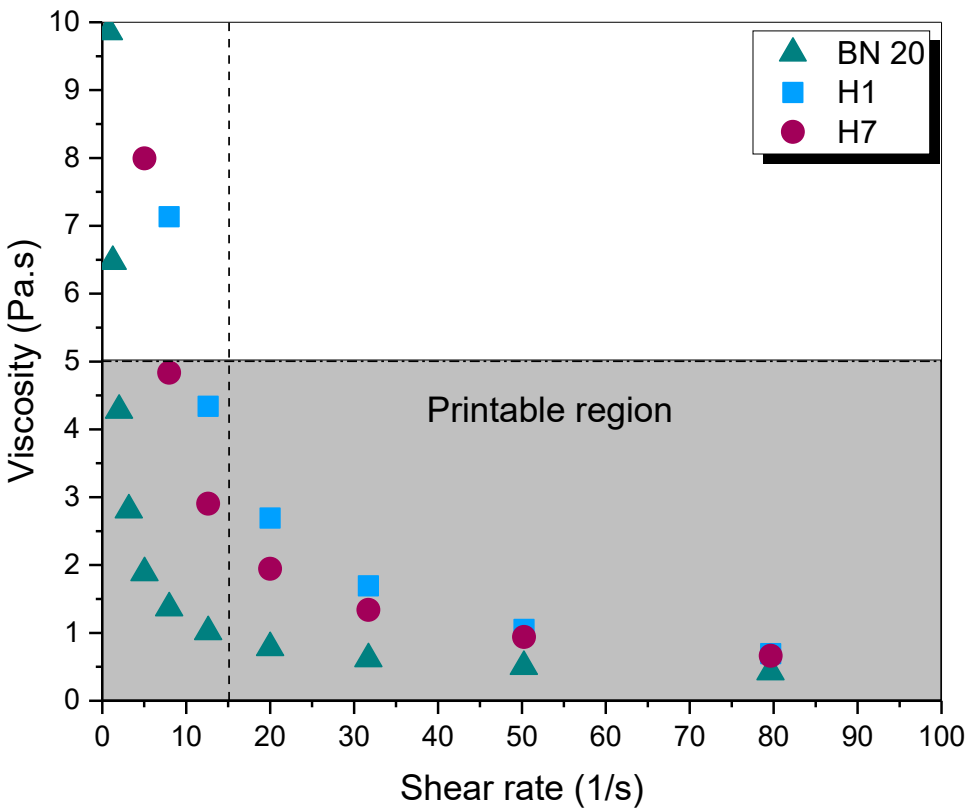

Figure 90 Rheological flow data of Hybrids.

6.2.3 Window Panes

To obtain the resolution in the *z*-axis and determine the speed of print using SLA, the hybrid inks underwent the '*Window Panes*' test. The results from plotting the cure depth C_d against the exposure energy E_0 (figure 91) showed a lower C_d when eGNP is added as a secondary filler in hybrid 7 compared to when eBN is used as a secondary filler in hybrid 1. This is in agreement with the lower cure depth of the GNP inks discussed in chapter 4. At different exposure energies (E_0) the C_d of hybrid 1 is larger than BN 20, however, is not the case for all E_0. The results in chapter 4 displayed a significant increase in C_d for the eBN20 ink compared to BN 20 ink. However, this is not observed in figure 91, therefore the small additions of the eBN have not significantly affected the scattering behaviour of the overall ink when compared to BN 20. Whereas there is a consistent reduction in the C_d for hybrid 7 compared to BN 20, implying the addition of GNP has a dominant effect on the scattering behaviour. The highest resolution in the *Z*-plane was 9.19 µm and 8.69 µm for H1 and H7 respectively.

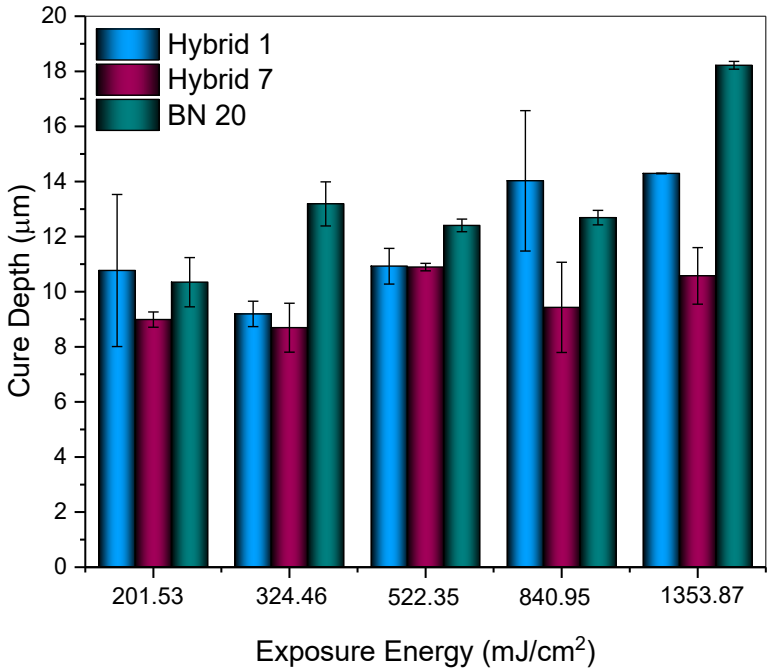

Figure 91 Cure depths from 'Window panes' test of hybrid 1, 7 and BN 20.

The printing outcomes of hybrid 7 and 1 are displayed in figure 92 and 93 respectively. Figure 92 shows a printed heat sink fabricated using hybrid 7 ink on the SLA build platform, the part is slightly grey in colour attributed to the small amounts of eGNP (black) inside the predominantly BN-based ink (white). Additional supports were required for the hybrid 7 ink to avoid bowing and warpage occurring during printing. The photographs show a good outcome of the print, the parts are supported by fine supports attached to the build plate and the printed columns or fins are upright and self-supported. Figure 93 represents an SEM image of the individual layers produced in the SLA printing process. It can be noted that there are some visible gaps or voids between the layers highlighted by the arrows. These voids illustrate poor adhesion between layers or trapped air pockets during the printing process. The difference in the square of the refractive index Δn^2 between the BN and GNP nanoplatelets and the polymer, PEGDA could also attribute to the voids presented in figure 93. If the layers aren't fully bonded to one another during curing this can have a significant impact on the thermal, electrical and mechanical properties of the printed composite. Although the H1 and H7 showed comparable viscosity and good printability with BN20, further improvements to dispersions are necessary to optimize the adhesion between layers.

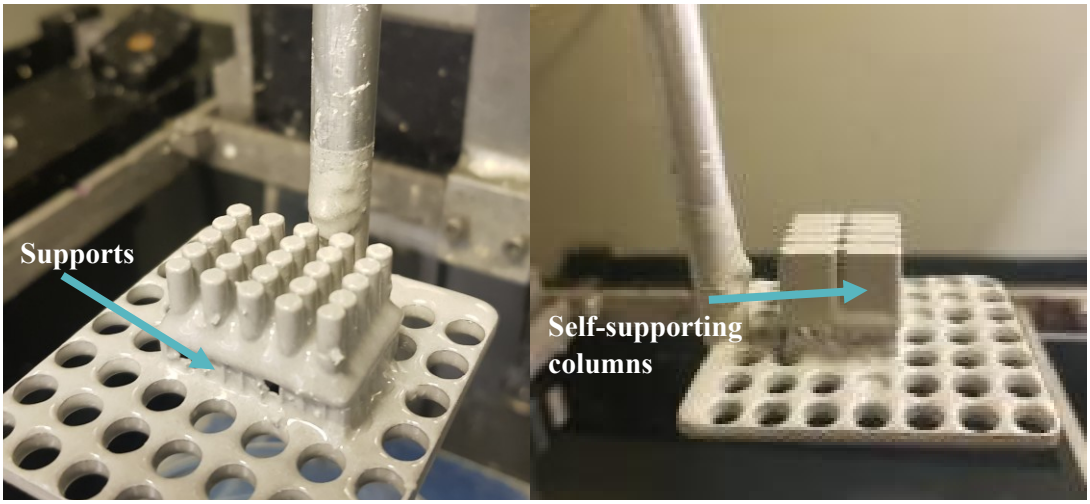

Figure 92 Example of printed part using hybrid 7 ink.

(a) Hybrid 1 **(b) Hybrid 7**

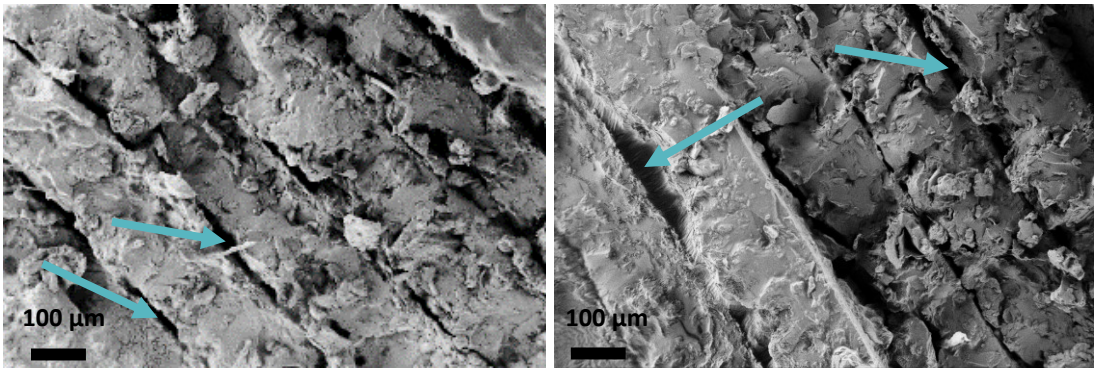

Figure 93 SEM image of printed layers of (a) hybrid 1 and (b) hybrid 7. The blue arrows point towards the voids between the layers.

6.3 Properties of Hybrids

The thermal, mechanical, electrical and chemical properties of the hybrids were analysed to determine the impact of having a primary and secondary filler compared to a singular filler material.

TGA data were used to assess what proportion of the initial filler content in the inks remained in the composite after printing (figure 94). The printed composites were heated under an inert atmosphere to burn out the polymer so only the nanoplatelets remained. All three samples BN 20, Hybrid 1 (H1) and Hybrid 7 (H7) contained the same starting solid loading however the results from the TGA (figure 94) showed there was a slight disparity in the total weight that remained after the polymer had been burnt-out. The total mass that remained for hybrid 1 and 7 and BN 20 after burn out was 13 %, 20 % and 17 % respectively. The reduction in mass of hybrid 1 from the

original solid loading of 20 wt. % represents significant sedimentation during the printing process.

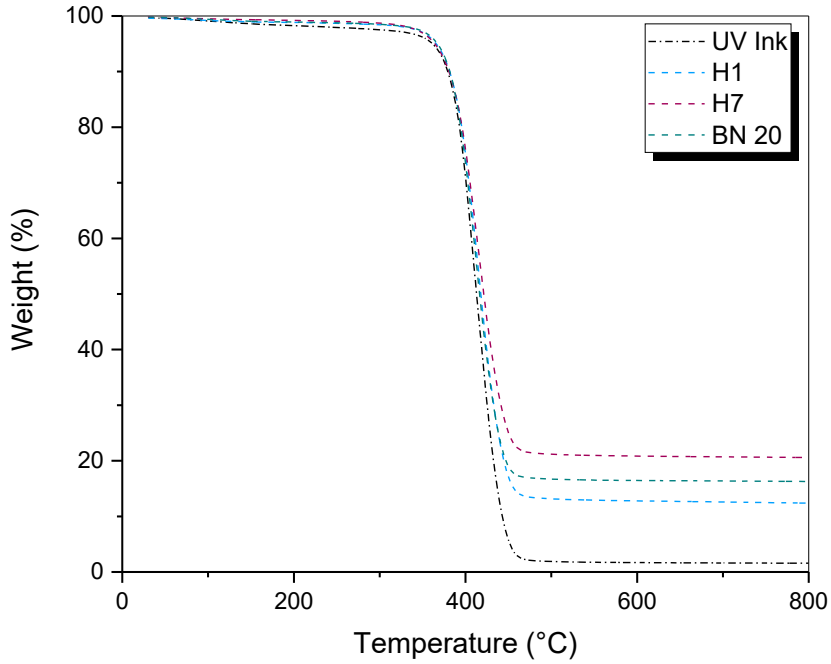

Figure 94 TGA data of hybrid composites, showing the loss in mass as a percentage with increasing temperature.

The FTIR spectra of hybrid 1, hybrid 7 and the UV polymer PEGDA/BAPO are shown in figure 95. FTIR was used to determine if the hybrid inks had cured during printing by displaying the associated PEGDA peaks in both hybrid spectra's. The peaks from both hybrids 1 and 7 (figure 95) display the main B-N-B bending peak at 806.1 cm^{-1} and the B-N stretching peak at 1371.1 cm^{-1}. There is no distinguishable characteristic peak of the vibration of the –COOH bonds and the graphitic double bonds from the eGNP platelets in hybrid 7 at 1410 cm^{-1} and 1640 cm^{-1} respectively. The CH_2 and –C-O-C bands at 2863 cm^{-1} and 1091 cm^{-1} respectively represent the characteristic bands of the PEGDA polymer.

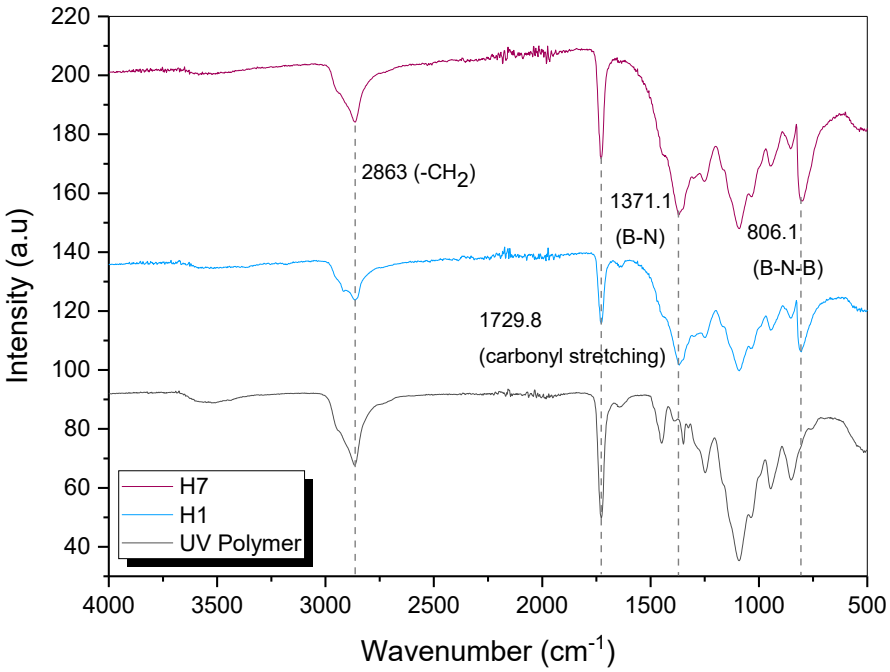

Figure 95 FTIR showing the infrared spectrum of Hybrids 1, 7 and the UV polymer.

The glass transition temperatures of the hybrids were measured using DSC and have been displayed in table 20. The results of which are comparable to the BN 20 composite at the same solid loading. The reported T_g of PEGDA is between -40 ºC and -30 ºC[9] therefore the increase in T_g of the hybrids show that the BN and eGNP platelets cause a loss in the mobility of the polymer chains. This will, therefore, affect the mechanical properties of the composite.[10]

Table 20 T_g results of composites BN 20 and Hybrids 1 and 7.

Composite	**T_g (°C)**
PEGDA/BAPO	-38 ± 4.5
Hybrid 1	-21 ± 3.0
Hybrid 7	-22 ± 2.7
BN 20	-20 ± 5.9

6.3.1 Surface Morphology of Hybrids

Figure 96 shows the fracture surface morphology of hybrid 1. It can be seen that the composite has a relatively rough structure. This indicates a good dispersion of

BN platelets throughout the polymer matrix which will improve the mechanical properties. It is, however, difficult to identify the two different BN flake sizes used in the hybrid. Figure 96 displays the fracture surface of hybrid 7, here both the eGNP and BN platelets have been dispersed throughout the matrix. It is difficult to identify the two flake types but the smaller darker flakes highlighted in the image can be said to represent the eGNP platelets, as eGNP are smaller than BN nanoplatelets. Whilst the brighter larger flakes are assigned to BN due to charging effects during imaging. BN is electrically insulating, causing accumulation of static electric charges on the surface of the sample.[11] It can be noted that for both hybrids there doesn't appear to be any voids or porosities from trapped air bubbles during the printing process, which is important for thermal and mechanical properties. Although there are visible voids described in figure 93 between the layers of the composites, the SEM images show a smaller cross-sectional area which may only represent an individual layer with no voids. Suggesting that the printing of the individual layers are homogeneous, but there are issues with bonding between the layers (figure 93).

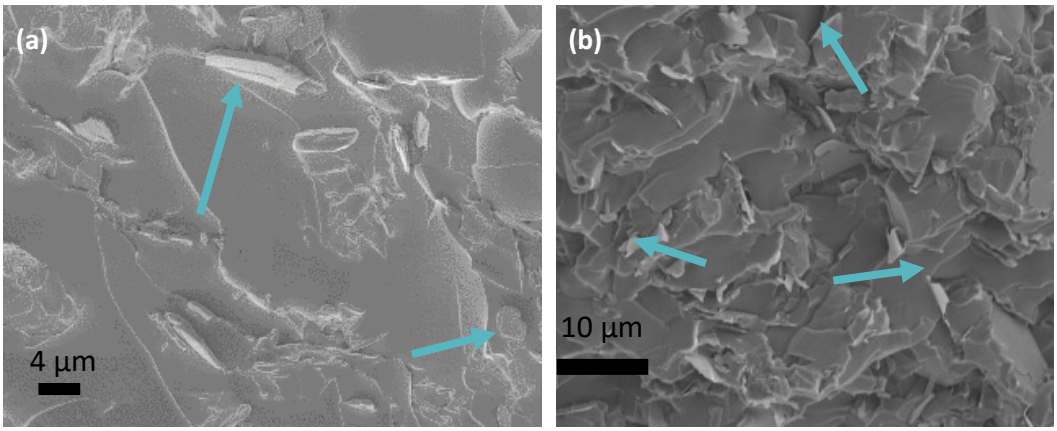

Figure 96(a) Fracture surface of hybrid 7 the white regions pointed with blue arrows represents the BN flakes. (b) Fracture surface of hybrid 1 the white regions pointed with blue arrows represents the BN flakes.

6.3.2 Mechanical Properties of Hybrids

The mechanical properties of the hybrids are shown in figures 97 & Figure 98. It can be observed from figure 97 the ultimate tensile strength (UTS) of hybrid 1 was 1970 kPa, the UTS of hybrid 7 was 1170 kPa and the UTS of BN 20 was 1660 kPa. For all samples, there was an improvement in the tensile strength compared to the polymer without filler (677 kPa). Therefore the addition of filler materials can improve the mechanical properties. The varied lateral sizes of BN platelets in hybrid 1 (table 19) produced the greatest increase in UTS of 18 % compared to the BN 20 composites

and a 68 % increase compared to hybrid 7. The decrease in UTS of hybrid 7 compared to BN 20 can be attributed to the results discussed in chapter 5, where the UTS decreased with an increasing weight percentage of GNP due to poor adhesion between the layers.[12][13] The addition of 0.2 wt. % GNP platelets with the BN platelets has resulted in poor interfacial bonding between the platelets and the polymer matrix. The difference in refractive index between the platelets could have also caused the scattering of the laser during printing leading to under curing or problems with bonding between layers, as discussed in 6.2.3 (figure 97).[14] There is an increase in Young's modulus (stiffness) for both hybrids compared to just the polymer PEGDA. Hybrid 7 does show a slight decrease in Young's modulus compared to hybrid 1 and BN 20 however they all fall within the range of 460-540 kPa, this is likely to be due to problems with printing GNP. The large difference in refractive index between GNP and the polymer can lead to large amounts of scattering causing under curing, resulting in the fabrication of weaker parts.[15][16]

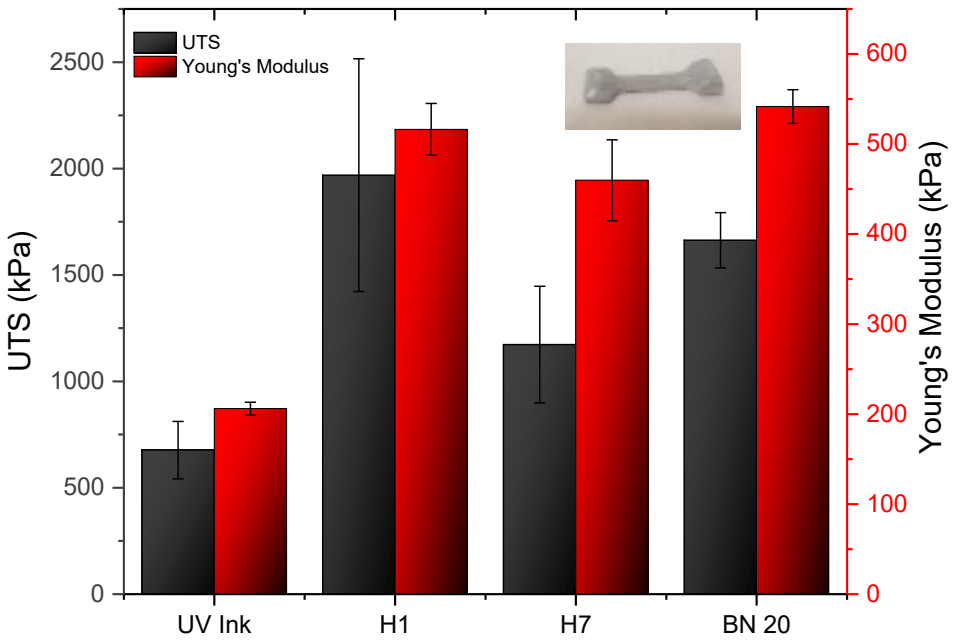

Figure 97 Tensile data of Hybrids 1, 7, composite BN 20 and the UV ink PEGDA/BAPO.

Hybrid 1 presented a maximum flexure strength of 3.08 MPa which is a 25 % increase in strength compared to the UV printed polymer (figure 98). Hybrid 7 however, displayed a maximum flexure strength of 1.83 MPa resulting in a decrease in flexure strength of 35 % compared to the UV polymer. This reduction in the flexure strength is attributed to the poor adhesion between printing layers as a result of scattering of

the laser during printing.[17][12] For both hybrids 1 and 7, there is an increase in the flexure modulus of 42 % (60 MPa) and 10 % (47 MPa) respectively. Therefore both hybrids have increased the overall stiffness of the UV polymer.

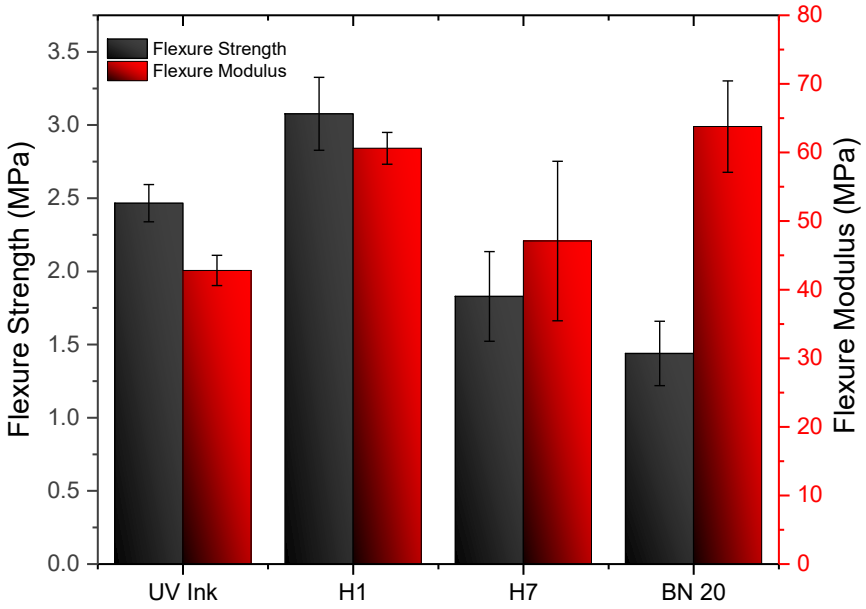

Figure 98 Flexure results of Hybrids 1, 7, composite BN 20 and the UV ink PEGDA/BAPO.

6.3.3 Electrical and Thermal Properties of Hybrids

The electrical and thermal properties of BN and GNP are notably the most exploited characteristics for functional polymer composites.[18][19][20][21] Previous reports have used BN and GNP together for a synergetic effect of driving phonons in the composites.[5][22][23] When the fillers are used together, they retain high thermal conductivity whilst breaking any electrical pathways with the addition of BN interfering between the GNP nanoplatelets. Therefore the hybrids are not electrically conductive suitable for uses in electronics, as the hybrids will be able to manage the excess heat produced by the electrical device without short-circuiting due to its electrically insulating properties. The intrinsic electrical and thermal properties of the fillers and PEGDA polymer have been listed below in table 21.

Table 21 Intrinsic properties of polymer matrix and fillers.

Material	ρ (g/cm^3)	λ (W/mK)	σ (S/m)	Ref.
BN	2.10	400	10^{-15}	[24][25]
GNP	2.20	3000/6	10^{7}	[4]
PEGDA	1.12	~0.1-0.2	10^{-8}	[26]

The thermal (figure 99) and electrical properties have been calculated using the laser flash method and 2-point probe method respectively. The results from table 22 show that both hybrids 1 and 7 are not electrically conductive. This is as expected as hybrid 1 contains no electrically conductive particles and hybrid 7 only contains a small quantity (0.2 wt. %) of eGNP, far below the percolation threshold for electrical conductivity ~10 wt. %.[27][28] The thermal properties of the hybrids show a definite increase in thermal conductivity compared to the polymer matrix. However, the inclusion of eGNP in hybrid 7 has not caused an increase in thermal conductivity when compared to hybrid 1 and BN 20 at the same solid loading. Interestingly, hybrid 1 (0.71 W. $m^{-1}.K^{-1}$) displays an increase in thermal conductivity of 32 % when compared to hybrid 7 (0.54 W. $m^{-1}.K^{-1}$) containing eGNP (figure 99). This is not as expected, as previous literature reports GNP and BN hybrids are more thermally conductive than just BN-based composites.[5] Figure 100 shows Hybrid 1 has the greatest thermal enhancement factor of 235 %, close to that of BN 20 at 225 % when compared to the UV polymer without filler. The thermal conductivity results discussed in chapter 5 describes GNP-based composites to be more thermally conductive than BN composites at the same solid loading, implying hybrids with both GNP and BN should be more thermally conductive than just BN-based hybrids. This indicates that the GNP, as a secondary filler, may have caused problems during the printing and curing stage and therefore were not dispersed effectively throughout the polymer, however further investigations into this may be required.

Table 22 Thermal and electrical properties of hybrid composites. Were ρ (g/cm^3) is the density of the composite, C_p (T) (J/g °C) is the specific heat capacity, a (T) is the thermal diffusivity (mm/cm^2) and λ (T) is the thermal conductivity ($W.m^{-1}.K^{-1}$).

Composite	ρ (kg/m^3)	C_p (T) (J/g °C)	a (T) (mm/cm^2)	λ(T) ($W.m^{-1}.K^{-1}$)	Error	Resistivity (Ω.m)
UV Ink	1.18	2.23	0.08	0.21	0.07	6.65×10^{11}
Hybrid 1	1.34	2.15	0.25	0.71	0.07	1.81×10^{10}
Hybrid 7	1.22	2.03	0.22	0.54	0.06	2.46×10^{10}
BN 20	1.21	2.34	0.23	0.69	0.06	3.33×10^{9}

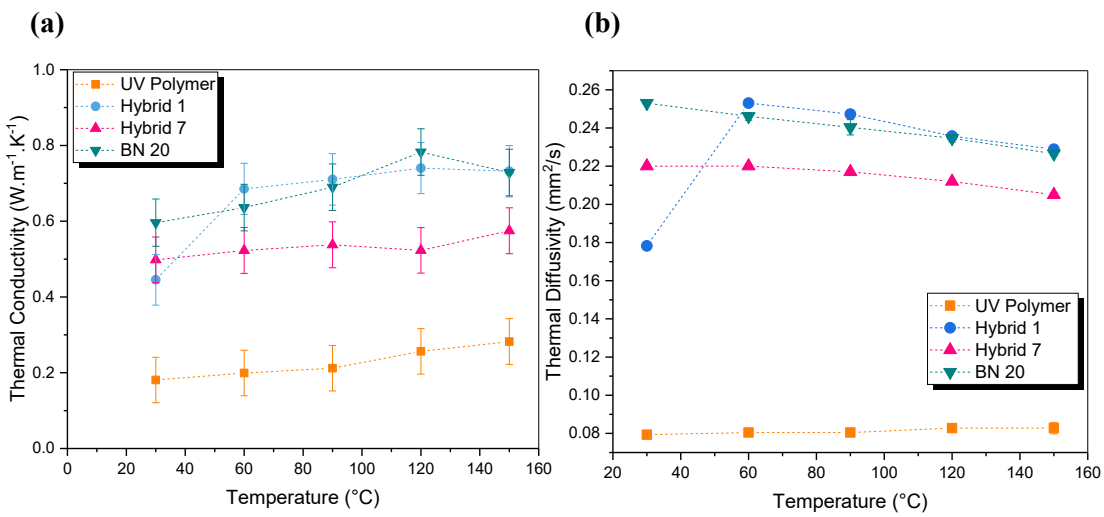

Figure 99 (a) Thermal conductivity of hybrid composites. (b) Thermal Diffusivity of hybrids.

To summarise, the properties of both hybrids 1 and 7 are similar to that of the BN 20 composite. All three samples showed an improvement in tensile and flexure strengths and thermal conductivity when compared to just the polymer PEGDA. The hybrids also displayed a high electrical resistivity suitable for potential applications in thermal management of electronics (table 22). Shows that there are some voids between the layers of the hybrids which will affect the properties discussed, potentially if this could be improved a higher thermal enhancement factor could be achieved. The heat dissipation of these materials will now be explored further by printing current methods (heat sinks) for thermal management applications of electronic.

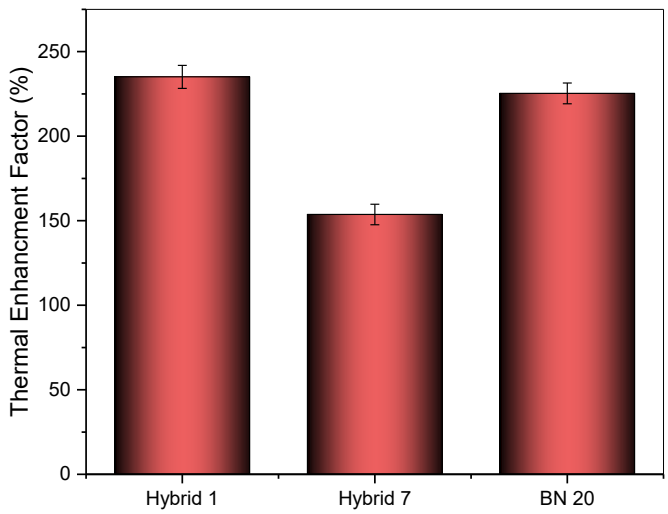

Figure 100 Thermal enhancement factor of hybrid composites. Hybrid 1 (19:1, BN: eBN) Hybrid 7 (19.8:0.2, BN: eGNP) and BN 20 (20 wt.% BN)

6.4 Heat Sinks

Without the aid of heat sinks or efficient cooling systems, modern electronics with fast processors will overheat and fail. The working limit of electronic devices is between 85- 100 °C, when the temperature increases to even 1 °C above the working limit the devices life span is significantly reduced and reliability falls by 5 %.[29] Therefore the need for efficient thermal management in modern electronic devices is paramount. Heat sinks are often used for this reason to remove excess heat via conduction.[30][31][32][33] Commonly heat sinks tend to be made from metallic materials such as aluminium or copper. Both these materials have intrinsically high thermal conductivities, however, both materials are electronically conductive and are therefore not always a suitable choice in electronics. This has led to research in thermally conductive polymer composites as they offer an exciting alternative with good processing abilities and a reduction in mass. Kalsom et al. used SLA to print heat sinks made from 30% (w/v) diamond nano-particles within a commercial resin. They observed a significant increase in heat transfer of their composite with nano-particle content, resulting in reaching the desired temperature in 30 % less time than their composites containing 10 % (w/v). [31] To investigate the effectiveness of the hybrid composites for thermal management applications, a typical heat sink design consisting of a plate-fin array,[34] was chosen to monitor heat dissipation when placed directly on top of a heat source (figures 101 & 102). Heat sinks are often used in electronics to remove excess heat from a device for improved working efficiency, safety and to avoid short-circuiting from over-heating.

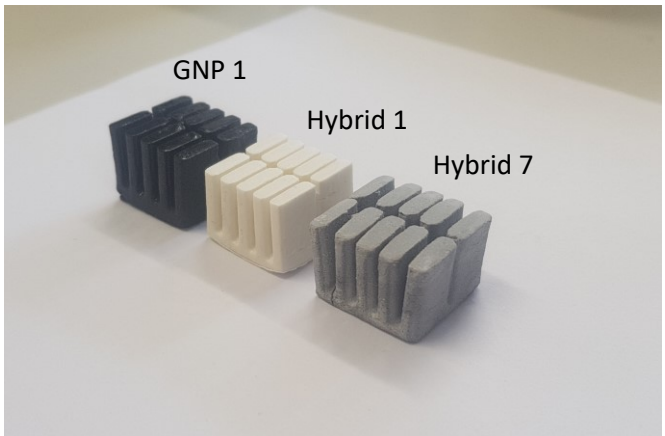

Figure 101 Photograph of composite heat sinks, from left to right GNP 1, H 1 and H7. The heat design shown here is the plate fin array consisting of 10 fins in total.

A reduced graphene oxide (rGO) aerogel was used to represent a heat source for the composite heat sinks (figure 102) (7 x 2.5 x 1cm). Reduced graphene oxide aerogels consist of an ultra-lightweight porous 3D structure of nanocarbons that display joule heating properties.[35] By adjusting the current that is passed through the steel plates and the aerogel a joule heating effect is attained, that provides uniform heat across the sample at a specified temperature. The current was adjusted to heat the aerogel to 90 °C based on a temperature reading from an Infrared thermometer (IR) thermometer, the temperature profiles were then recorded using point measurements from an IR thermometer at the base and top of the heat sinks to observe the dissipation of heat over time. The heat released from the heat sinks was measured using an infrared thermometer (model: 568, Fluke). The resultant heat transferred from the heat sinks to the surrounding area is driven mainly by natural convection and radiation. This is where there is no forced air in the system through fans. The air between the fins of the heat sinks increases due to the temperature increase from the heat source. Higher temperature air is less dense than the surrounding cooler air causing the air to rise out from the heat sink. This change in density of the air causes the airflow to cool the heat sink.[34]

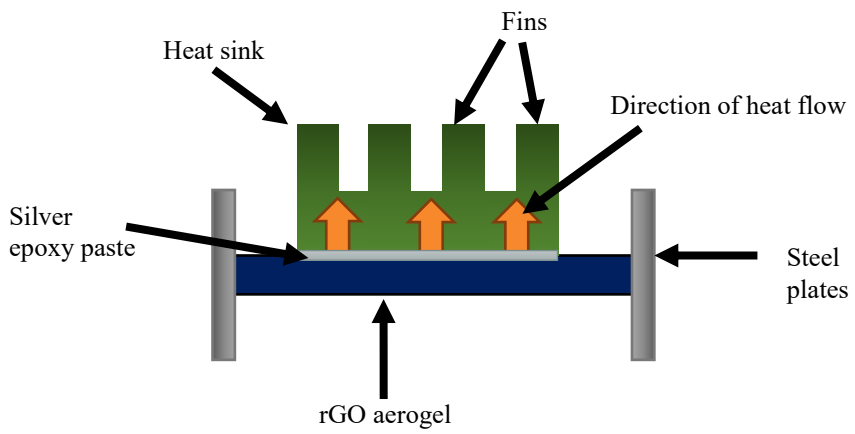

Figure 102 Schematic of the heat flow through the heat sink as a result of joule heating of the rGO aerogel.

The images from the IR camera (FLIR T440) in figure 104 show a temperature gradient from the base to the top of the fins show in the heat dissipation through the heat sink. Point measurements were taken at the base of the heat sinks over a period of time until the composites reached the set temperature of 90 °C. The results displayed in figure 103 show that all three of the composite heat sinks reached the target temperature before the PEGDA polymer. The BN 20 composite had the greatest

increase in temperature over time with an average of 19.14 °C/min compared to the PEGDA polymer. Hybrid 7 and hybrid 1 also displayed an increased temperature of 6.49 °C/min and 8.08 °C/min respectively when compared to the PEGDA UV polymer (figure 103). The BN 20 composite reached the set temperature three times quicker than the PEGDA heat sink and twice as quick as hybrid 1 and 7. It can be observed that both hybrids 1 and 7 perform comparatively to one another, however, the BN 20 composite still outperforms the printed hybrids. This is likely due to the larger flake size and aspect ratio of the bulk BN platelets which reduces phonon scattering and creates good thermal pathways.[36] As expected, the results of the heat dissipation are directly related to the thermal conductivities reported, the BN 20 ink achieved the greatest thermal conductivity and dissipated the heat the quickest. The reduction in performance of the hybrids may also be related to the print quality achieved, as there is visible air pocket between the layers which reduce the effectiveness of the thermal conductivity as air is a poor conductor of heat (figure 93).

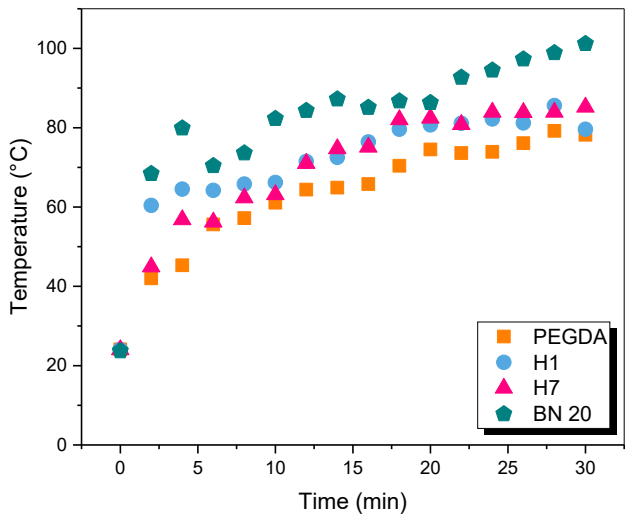

Figure 103 Temperature profiles of different composite heat sinks.

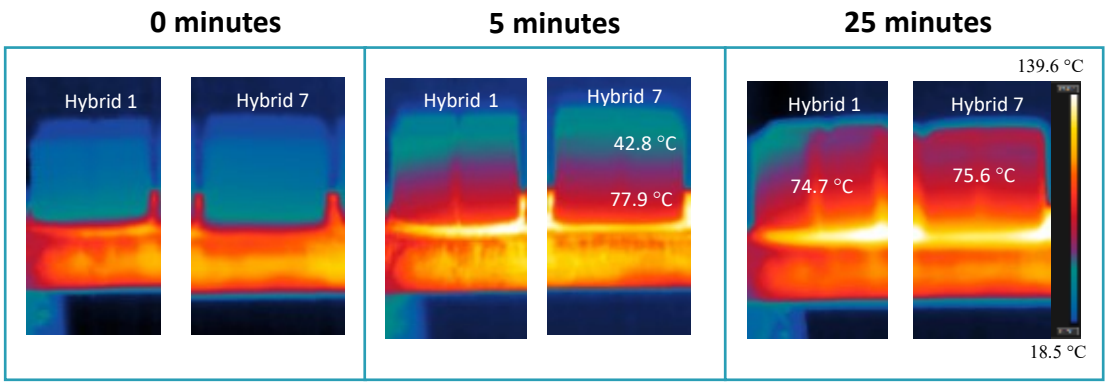

Figure 104 IR camera images of Hybrid 1and Hybrid 7 heat sinks

6.4.1 Heat Sink Design

The design consideration of the heat sinks is equally as vital as the material selection for ensuring efficient heat transfer and heat dissipation. One of the key advantages of being able to 3D print the thermally conductive inks is the freedom and flexibility of altering the designs of the heat sinks quickly and with no extra costs of new tooling and dies. It has been reported by Costa et al. that by adjusting the geometric parameters of the heat sink, including the height, thickness and number of fins, the overall performance of the heat sinks can be improved.[37] By reducing the thickness of the fins from 2 mm to 1mm and increasing the number of fins from 40 to 70 they saw a considerable reduction in thermal resistance, however, this also meant there was an increase in the mass of the heat sink of 24%. Luo et al. also reported a decrease in thermal resistance of 10% when they increased the number of fins from 3 to 18.[38] Therefore to test the effect of heat sink design on hybrid composite heat sinks and compare with the results of previous reports on increasing fin numbers, heat sinks designs included a simple block design and arrangement of the fins in a 5 x 4 and 3 x 3 array, two heat sinks with increasing number of fins (increasing the surface area) (Table 23). All heat sink designs were fabricated using hybrid 1 ink and a control using just the polymer PEGDA, as hybrid 1 displayed the best heat dissipation of the two hybrids tested (Figure 103).

Figure 105 is a visual representation of the thermal conduction between the heat sink designs directly on the heat source rGO aerogel, the temperature variations were recorded using an infrared thermometer, measuring at the base of the heat sink. Being heated by the rGO aerogel the heat sinks temperatures increase at different rates. The heat sink with a 5 x 4 array of fins reached the set temperature (110 °C) in 43 % less time than the 3 x 3 array and the simple block design (figure 105) (table 23). This is as expected as previously mentioned reports showed an improvement in heat dissipation with an increased number of fins. [33][37][38] The heat distribution of the heat sinks is uniform for the simple block design, however, the tips of the fins in the 5 x 4 and 3 x 3 array are considerable cooler showing temperatures difference of 15 °C and 13.5 °C respectively. This is because the surface area is larger with an increasing number of fins, allowing air to circulate, cooling the heat sink and transferring the heat into the surrounding air. To further test the potential applications of the heat sink designs in microelectronics thermal resistance measurements could be measured by

fixing the heat sinks to a working electronic device and measure the device's temperature over time.

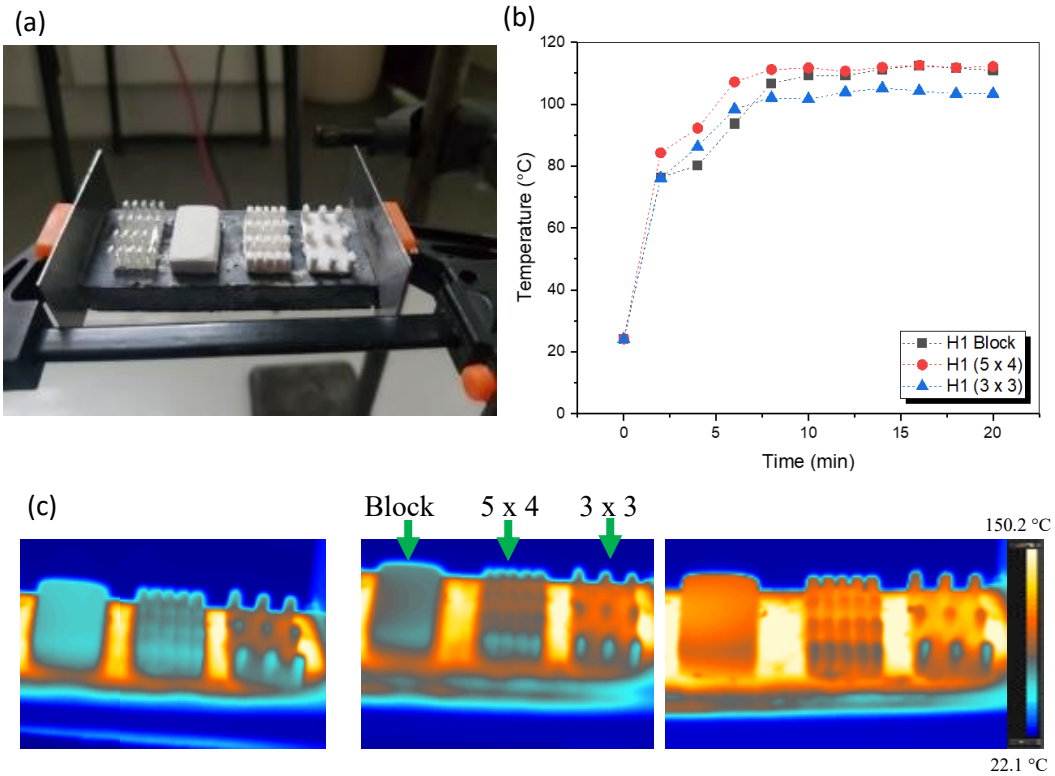

Figure 105 (a) Heat sink designs of hybrid 1 composite with rGO aerogel joule heater providing homogeneous source of heat to the sinks (b) temperature profile of the different designs of heat sinks displaying heat dissipation over time, (c) IR images of the heat dissipation of different designs of heat sinks printed using Hybrid 1.

Table 23 Measurements of hybrid 1 heat sinks with varying fin numbers.

Heat Sink	Length (mm)	Width (mm)	Depth (mm)	Fin length (mm)	Fin width (mm)
5 x 4	21.0	11.2	5.4	2.5	1.2
3 x 3	22.2	11.3	5.5	3.1	1.9
Block	21.1	12.1	5.3	-	-

6.5 General Discussion

Hybrid material composites are an effective way of tuning the properties of a material to suit a given application. BN and GNP have often been used together to form synergetic, thermally conductive, electrically insulating, hybrid materials for thermal management applications in electronics. [39][40][19] In this work these properties have been exploited to produce printable UV curable SLA inks. The final printed composites have seen an increase in thermal conductivity with good heat dissipation compared to the UV PEGDA polymer whilst retaining mechanical properties similar to that of bulk BN without a secondary filler.

6.5.1 Printability of Hybrids

The rheological properties of the hybrid inks produced viscosities well below 5 Pa s^{-1} at the printing shear rate of 15 s^{-1}, comparable with single filler composite BN 20. Therefore the small additions of a secondary filler material did not play a large role in the overall viscosity of the inks. When printing the hybrids, hybrid 1 produced parts with smooth finishes similar to that of BN 20. However, the printing parameters E_c and D_p had to be adjusted to compensate for the eGNP in the ink. Notably, the layer thickness of hybrid 7 was smaller than hybrid 1 and BN 20 from the window panes test. This was expected as the GNP-based inks produced panes of reduced thickness compared to BN-based inks discussed in chapter 4. Overall the printability of the hybrids was good as the ratios of eGNP to BN and eBN to BN were tuned to resemble the printability of the BN 20 ink. To the best of our knowledge, there have been no reports in the literature on SLA 3D printable hybrid composites consisting of 2D-material based materials.

6.5.2 Properties of Hybrid Composites

The overall properties of the hybrid composites were reflective of the properties obtained by the BN 20 composite. Interestingly hybrid 1 displayed superior mechanical properties over hybrid 7 and BN 20 in both flexure and tension. The bonding between the two fillers plays an important part in the final reinforcement of the polymer. The decrease in mechanical properties of hybrid 7 was attributed to the difference in the refractive index of the BN, eGNP and PEGDA during printing causing a degree of scattering from the SLA laser affecting the adhesion between layers. Importantly both hybrids maintained a high electrical resistivity suitable for the use in electronic devices and as potting materials.

To maximise the thermal conductivity of the hybrid composites the solid loading was optimised to 20 wt. % total while attaining electrical resistivity and good mechanical properties. The addition of eGNPs in hybrid 7 was to improve the overall thermal conductivity as seen by Shtein et al. where they used GnPs as their primary filler and nm-BN for their secondary filler. Shtein et al. saw a significant increase in the thermal conductivity of their GNP and BN hybrid composite compared to their µm-BN and nm-BN hybrid.[5] However, in this work, when BN is used as a primary filler and eGNP as a secondary filler, there is a decrease in thermal conductivity. The reason

for this is likely related to how the composites have been manufactured. The SLA printing technique uses UV radiation to cure the composites and the degree of cure, penetration depths of the radiation into the resin, and overall print quality are heavily affected by the difference in the square of the refractive indexes between the polymer and filler material. Therefore even with a small quantity of eGNP platelets the difference in the refractive index between them and the BN platelets and PEGDA polymer is likely to cause scattering of the UV radiation leading to under curing and poor adhesion between the printed layers. When this occurs, the network of filler material within the printed part may be broken or disrupted by voids or air pockets. These voids will scatter phonons and therefore impede the thermal conductivity of the printed hybrid composite. To obtain a high thermal conductivity for the hybrid 7 resin adjustments to the printing process will be required in order to minimize scattering effects.

Similar to Shtein et al. there was an increase in thermal conductivity of the BN and eBN-hybrid (hybrid 1) compared to just bulk BN dispersed within the UV polymer.[5] The theory behind this is that the smaller platelets fit in between the larger ones providing a pathway between the flakes, reducing the distance travelled through the matrix. Overall hybrid 1 produced the highest mechanical and thermal properties whilst maintaining good workability and printability as an ink for SLA.

6.5.3 Hybrids for Thermal Management Applications

The heat sinks in this work showed that BN 20 reached the set temperature in 50% less time than hybrid 1 and 7. The amount of power dissipated is a function of the geometry and pathway between the device and heat sink. The adaptations to the design of the heat sinks, by increasing the number of fins and therefore surface area further improved the heat dissipation by reaching the set temperature in 43% less time than the simple block design or a (5 x 4) array measured from the base of the heat sink. This agreed with the reports in the literature that an increase in heat sink fins (surface area to volume ratio) improves the dissipation of heat.[33][37][38] Further improvements to reduce the contact resistance between the heat sink and the heat sources could be made by trying different thermal compounds and pastes, improving the efficiency of the heat sink.

The thermal conductivity reported here (0.71 $W.m^{-1}.K^{-1}$ at 90 °C, BN 20) is still quite low and therefore the heat dissipation is not sufficient enough for thermal management in modern electronics. For efficient LED systems with a medium power density, a thermal conductivity of 3 W/mK is required.[41] The inks produced in this study are currently limited by the maximum solid loading. The percolation threshold for thermal conductivity of eBN-BN and eGNP-BN hybrids has been reported to be ~17 vol. % which is higher than the 10.7 vol. % used in this work.[5] Therefore with improvements to the solid loading and orientation of the platelets the enhancement in thermal conductivity can be significantly increased to be able to be used in thermal management applications. The ability to 3D print graded complex structures, components with gradual differences in the composition and structure over volume, with minimal waste is also a very attractive prospect for 3D printing new generation thermal management systems.[42][43]

6.6 References

[1] H. Chen *et al.*, "Thermal conductivity of polymer-based composites: Fundamentals and applications," *Prog. Polym. Sci.*, vol. 59, pp. 41–85, 2016.

[2] A. L. Moore and L. Shi, "Emerging challenges and materials for thermal management of electronics," *Materials Today*. vol. 17, no. 4, pp. 163-174, 2014.

[3] S. V. Garimella *et al.*, "Thermal challenges in next-generation electronic systems," *IEEE Trans. Components Packag. Technol.*,vol. 3, no. 4, pp. 801-815, 2008.

[4] K. A. Imran and K. N. Shivakumar, "Enhancement of electrical conductivity of epoxy using graphene and determination of their thermo-mechanical properties," *J. Reinf. Plast. Compos.*, vol. 37, no. 2, pp. 118–133, 2017.

[5] M. Shtein, R. Nadiv, M. Buzaglo, and O. Regev, "Graphene-Based Hybrid Composites for Efficient Thermal Management of Electronic Devices.," *ACS Appl. Mater. Interfaces*, vol. 7, no. 42, pp. 23725–30, 2015.

[6] M. Owais, J. Zhao, A. Imani, G. Wang, H. Zhang, and Z. Zhang, "Synergetic effect of hybrid fillers of boron nitride, graphene nanoplatelets, and short carbon fibers for enhanced thermal conductivity and electrical resistivity of epoxy nanocomposites," *Compos. Part A Appl. Sci. Manuf.*, vol. 117, pp. 11-22, 2019.

[7] R. Kumar, S. K. Nayak, S. Sahoo, B. P. Panda, S. Mohanty, and S. K. Nayak, "Study on thermal conductive epoxy adhesive based on adopting hexagonal boron nitride/graphite hybrids," *J. Mater. Sci. Mater. Electron.*, vol. 29, no. 19, pp. 16932–16938, 2018.

[8] C. Hinczewski, S. Corbel, and T. Chartier, "Ceramic suspensions suitable for stereolithography," *J. Eur. Ceram. Soc.*, vol. 18, no. 6, pp. 583–590, 1998.

[9] T. Keim and K. Gall, "Synthesis, characterization, and cyclic stress-influenced degradation of a poly(ethylene glycol)-based poly(beta-amino ester)," *J. Biomed. Mater. Res. Part A*, vol. 92A, no. 2, pp. 702–711, 2010.

[10] E. Çakmakçı, Ç. Koçyiğit, S. Çakır, A. Durmus, and M. V. Kahraman, "Preparation and characterization of thermally conductive thermoplastic polyurethane/h-BN nanocomposites," *Polym. Compos.*, vol. 35, no. 3, pp. 530–538, 2014.

[11] K. H. Kim, Z. Akase, T. Suzuki, and D. Shindo, "Charging effects on SEM/SIM contrast of metal/insulator system in various metallic coating conditions," *Mater. Trans.*,vol. 51, no. 6, pp. 1080-1083, 2010.

[12] Z. Feng, Y. Li, C. Xin, D. Tang, W. Xiong, and H. Zhang, "Fabrication of Graphene-Reinforced Nanocomposites with Improved Fracture Toughness in Net Shape for Complex 3D Structures via Digital Light Processing," *C*, vol. 5, no. 2, p. 25, 2019.

[13] A. Kernin *et al.*, "The effect of graphene network formation on the electrical, mechanical, and multifunctional properties of graphene/epoxy

nanocomposites," *Compos. Sci. Technol.*, vol. 169, pp. 224–231, 2019.

[14] S. P. Gentry and J. W. Halloran, "Absorption effects in photopolymerized ceramic suspensions," *J. Eur. Ceram. Soc.*, vol. 33, no. 10, pp. 1989–1994, 2013.

[15] A. Harvey *et al.*, "Non-resonant light scattering in dispersions of 2D nanosheets," *Nat. Commun.*, vol. 9, no. 1, pp. 4553, 2018.

[16] M. L. Griffith and J. W. Halloran, "Scattering of ultraviolet radiation in turbid suspensions," *J. Appl. Phys.*, vol. 81, no. 6, pp. 2538–2546, 1997.

[17] C. Sun and X. Zhang, "The influences of the material properties on ceramic micro-stereolithography," *Sensors Actuators A Phys.*, vol. 101, no. 3, pp. 364–370, 2002.

[18] Z. Lin, Y. Liu, K. Moon, and C.-P. Wong, "Enhanced thermal transport of hexagonal boron nitride filled polymer composite by magnetic field-assisted alignment," in *2013 IEEE 63rd Electronic Components and Technology Conference*, 2013, pp. 1692–1696.

[19] S. G. Mosanenzadeh, S. Khalid, Y. Cui, and H. E. Naguib, "High thermally conductive PLA based composites with tailored hybrid network of hexagonal boron nitride and graphene nanoplatelets," *Polym. Compos.*, vol. 37, no. 7, pp. 2196-2205, 2016.

[20] J. Yang *et al.*, "Largely enhanced thermal conductivity of poly (ethylene glycol)/boron nitride composite phase change materials for solar-thermal-electric energy conversion and storage with very low content of graphene nanoplatelets," *Chem. Eng. J.*, vol. 315, pp. 481–490, 2017.

[21] E. Ivanov *et al.*, "PLA/Graphene/MWCNT Composites with Improved Electrical and Thermal Properties Suitable for FDM 3D Printing Applications," *Appl. Sci.*, vol. 9, no. 6, p. 1209, 2019.

[22] J. Wang, F. Ma, W. Liang, and M. Sun, "Electrical properties and applications of graphene, hexagonal boron nitride (h-BN), and graphene/h-BN heterostructures," *Mater. Today Phys.*, vol. 2, pp. 6–34, 2017.

[23] X. Cui, P. Ding, N. Zhuang, L. Shi, N. Song, and S. Tang, "Thermal Conductive and Mechanical Properties of Polymeric Composites Based on Solution-Exfoliated Boron Nitride and Graphene Nanosheets: A Morphology-Promoted Synergistic Effect," *ACS Appl. Mater. Interfaces*, vol. 7, no. 34, pp. 19068–19075, 2015.

[24] J. C. Zheng *et al.*, "High thermal conductivity of hexagonal boron nitride laminates," *2D Mater.*, vol. 3, no. 1, p. 11004, 2016.

[25] W. Zhou, J. Zuo, X. Zhang, and A. Zhou, "Thermal, electrical, and mechanical properties of hexagonal boron nitride-reinforced epoxy composites," *J. Compos. Mater.*, vol. 48, no. 20, pp. 2517-2526, 2014.

[26] V. Guarino, M. A. Alvarez-Perez, A. Borriello, T. Napolitano, and L. Ambrosio, "Conductive PANi/PEGDA Macroporous Hydrogels For Nerve Regeneration," *Adv. Healthc. Mater.*, vol. 2, no. 1, pp. 218–227, 2013.

[27] G. Chen, C. Wu, W. Weng, D. Wu, and W. Yan, "Preparation of polystyrene/graphite nanosheet composite," *Polymer (Guildf).*, vol. 44, no. 6, pp. 1781–1784, 2003.

[28] S. Park and R. S. Ruoff, "Chemical methods for the production of graphenes," *Nat Nanotechnol*, vol. 4, pp. 217-224, 2009.

[29] H. E. Ahmed, B. H. Salman, A. S. Kherbeet, and M. I. Ahmed, "Optimization of thermal design of heat sinks: A review," *International Journal of Heat and Mass Transfer*. vol. 118, pp. 129-153, 2018.

[30] S. Ghaffari Mosanenzadeh and H. E. Naguib, "Effect of filler arrangement and networking of hexagonal boron nitride on the conductivity of new thermal management polymeric composites," *Compos. Part B Eng.*, vol. 85, pp. 24–30, 2016.

[31] U. Kalsoom, A. Peristyy, P. N. Nesterenko, and B. Paull, "A 3D printable diamond polymer composite: A novel material for fabrication of low cost thermally conducting devices," *RSC Adv.*,vol. 6, pp. 38140-38147, 2016.

[32] W. Wu, G. Zhang, X. Ke, X. Yang, Z. Wang, and C. Liu, "Preparation and thermal conductivity enhancement of composite phase change materials for electronic thermal management," *Energy Convers. Manag.*,vol. 101, pp. 278-284, 2015.

[33] A. Arshad, H. M. Ali, M. Ali, and S. Manzoor, "Thermal performance of phase change material (PCM) based pin-finned heat sinks for electronics devices: Effect of pin thickness and PCM volume fraction," *Appl. Therm. Eng.*,vol. 112, pp. 143-155, 2017.

[34] A. Al-damook and F. S. Alkasmoul, "Heat transfer and airflow characteristics enhancement of compact plate-pin fins heat sinks – a review," *Propuls. Power Res.*,vol. 7, no. 2, pp. 138-146, 2018.

[35] R. Menzel *et al.*, "Joule heating characteristics of emulsion-templated graphene aerogels," *Adv. Funct. Mater.*, vol. 25, no. 1, pp. 28–35, 2015.

[36] L. Chen *et al.*, "Analytic modeling for the anisotropic thermal conductivity of polymer composites containing aligned hexagonal boron nitride," *Compos. Sci. Technol.*, vol. 122, pp. 42-49, 2016.

[37] V. A. F. Costa and A. M. G. Lopes, "Improved radial heat sink for led lamp cooling," *Appl. Therm. Eng.*, 2014.

[38] Q. Luo *et al.*, "Experimental investigation on the heat dissipation performance of flared-fin heat sinks for concentration photovoltaic modules," *Appl. Therm. Eng.*, vol. 157, p. 113666, 2019.

[39] T. Huang *et al.*, "Boron nitride@graphene oxide hybrids for epoxy composites with enhanced thermal conductivity," *RSC Adv.*, vol. 6, no. 42, pp. 35847–35854, 2016.

[40] S. N. Leung, S. Ghaffari, and H. E. Naguib, "Development of novel multifunctional biobased polymer composites with tailored conductive network of micro-and-nano-fillers," in *Proc.SPIE*, vol. 8689, 2013.

[41] A. J. Fischer, Y. Zhong, L. Zhang, W. Wu, and D. Drummer, "Heat propagation in thermally conductive polymers of PA6 and hexagonal boron nitride," *Fire Mater.*, vol. 43, no. 8, pp. 928-935, 2019.

[42] J. Feng, J. Fu, Z. Lin, C. Shang, and B. Li, "A review of the design methods of complex topology structures for 3D printing," *Vis. Comput. Ind. Biomed. Art*, vol. 1, no. 5, pp. 1-16, 2018.

[43] E. Pei, G. H. Loh, D. Harrison, H. De Amorim Almeida, M. D. M. Verona, and R. Paz, "A study of 4D printing and functionally graded additive manufacturing," *Assem. Autom.*, vol. 37, no. 2, pp. 147-153, 2017.

7

Conclusion

The goal of this thesis was to explore multi-functional UV curable resins containing GNP and BN for SLA printing. The physical and chemical properties of the printed composites have been analysed to determine the suitability for potential applications with a focus on the thermal and electrical properties. Further developments of BN-GNP hybrid inks have been synthesised and tested for their synergetic effects of high thermal conductivities and electrical resistivity's for applications in thermal management of electronics.

It is clear from the work presented in chapter 2, that there have been few publications on the development of 2D material-based inks for SLA and the implications of printing this class of materials. Chapter 4 has explored the implications of printing platelets as opposed to traditional spherical ceramic particles. The maximum solid loading of the BN-based inks was 20 wt. % the main reason for this was related to the scattering effects of the ink as opposed to the rheological properties. The viscosity of the ink was considerably below the printing viscosity of 5 Pa s^{-1} suggesting that BN inks would still be printable with further increases in concentration. However the small C_d of the 20 wt. % inks (10-18 µm) implies that large amounts of scattering of the incoming UV light occurred. It has been noted that GNP platelets have a significant effect on the viscosity, even at relatively low loadings of 8 wt. % the viscosity was outside of the printing parameters for SLA, this lead to maximum solid loading of GNP to be 4 wt. %. For both inks scattering effect, models were applied to the curing behaviour established by the window panes tests. The results concluded that the experimental scattering behaviour that occurred during printing was best described through Mie scattering. The limitations to these results are related to the semi-empirical models

published focusing on the assumptions of spherical particles as opposed to platelets. The Δn^2 between the polymer and filler material had a significant effect on scattering and therefore should be minimised to ensure good printability of the inks when using SLA.

The BN-based inks provided a better overall printability with smooth surface finishes compared to those that contained GNP. This had a direct impact on the overall mechanical and thermal properties. With increasing concentration of BN, the tensile modulus and strength increased by 169 % and 146 % respectively. However for GNP composites, there was a reduction in tensile strength and modulus with increasing concentration, this was attributed to the formation of aggregates and poor adhesions between the printed layers. There was however a significant increase in thermal conductivity with increasing filler loading of both materials. With a maximum thermal enhancement of 233% (0.7 W m^{-1} K^{-1}) for BN 20 composite and 200 % (0.55 W m^{-1} K^{-1}) for GNP 4. GNP composites displayed a thermal enhancement that was 22 % greater than that of BN composites at the same solid loading, this is associated with the higher intrinsic thermal conductivity of GNP. The low weight percentage of GNP in the composite inks (4 wt. %) meant that the percolation threshold for electrical conductivity was not achieved ~10 wt. %.[1] [2] [3]Therefore all printable composites were electrically resistive (2.81 x10^{-10} S/m) for potential applications in thermal management of electronic devices.

The results from chapter 6 showed that hybrid inks based on a variation in size and materials could be printed using SLA. The findings showed that hybrid 1 which contained both bulk BN and exfoliated BN had the greatest increase in tensile strength and thermal conductivity 191 % and 238 % respectively. Although there have been reports of improvements in thermal conductivity of GNP-BN hybrids, this was not as effective in the SLA printed composites. Hybrid 7 displayed a high thermal conductivity of 0.54 W m^{-1} K^{-1}. The decrease in thermal conductivity compared to hybrid 1can be attributed to issues with the printability of the ink, for example, increased scattering effects and reduced interfacial bonding between both of the platelets and the polymer matrix.

To test the effectiveness of the composites for potential applications in thermal management of electronics, heat sinks were printed using hybrids 1 and 7 inks to

monitor the heat dissipation over time. The findings concluded that both hybrids reached the set temperature in less time than the polymer, however, the BN 20 composite heat sink was the most effective in heat dissipation of the rGO aerogel. Three designs of heat sinks were tested using hybrid 1 ink to observe the geometric effects on heat dissipation. The findings showed that the heat sink with the larger surface area (5 x 4) array reached the set temperature 43 % faster than the other designs.

7.1 References

[1] G. Chen, C. Wu, W. Weng, D. Wu, and W. Yan, "Preparation of polystyrene/graphite nanosheet composite," *Polymer (Guildf).*, vol. 44, no. 6, pp. 1781–1784, 2003.

[2] S. Park and R. S. Ruoff, "Chemical methods for the production of graphenes," *Nat. Nanotechnol.*, vol. 4, no. 4, pp. 217–224, 2009.

[3] L. M. Viculis, J. J. Mack, O. M. Mayer, H. T. Hahn, and R. B. Kaner, "Intercalation and exfoliation routes to graphite nanoplatelets," *J. Mater. Chem.*, vol. 15, no. 9, p. 974, 2005.

8

Suggestion for Future Works

The work presented in this research demonstrated the use of SLA printing to produce functional composite parts with enhanced thermal conductivities. While this work has shown the possibilities and challenges associated with printing 2D materials using SLA, further work is required to extend and improve the functionalities and therefore applications of printing next-generation materials. Suggestions for future work will now be discussed based on the work carried out in this research.

In chapter 4 the effects of scattering and absorption behaviour of GNP and BN inks were discussed and calculated using previously published models. Although these models were applied to the experimental findings, further investigation into the absorption and scattering effects could be studied to gain a deeper understanding of what happens during the printing process in order to improve it. The scattering coefficients can be measured using an integrating sphere. Work by Harvey *et al.* used an integrating sphere for various 2D nanosheet dispersions to find the size effects of the materials and their associated scattering behaviours.[1] The reduction of Δn^2 between the polymer and fillers helps to reduce scattering effects, therefore it would be interesting to review the refractive index of other photopolymers and 2D material fillers to produce inks with excellent printability with increased solid loading and functionalities.

To improve the dispersions and homogeneity of the inks experiments with different dispersants and functionalisation of fillers to the polymer resin could be further studied. This is important to also improve the interfacial bonding between the polymer and filler to enhance the mechanical, electrical and thermal conductivities discussed in chapter 5.

For the work in chapter 5, it would be interesting to investigate the alignment of 2D material fillers during the printing process in SLA. As 2D materials are anisotropic the mechanical, thermal and electrical properties of the composites could be greatly improved through tuning the orientation of the platelets. This is challenging in SLA due to the lack of control of orientation as the flakes are suspending in a vat. Nevertheless, work by Lin *et al*. have aligned BN flakes using magnetic particles attached to the fillers to control orientation using a magnetic field. They modified the surface of BN flakes using iron oxide which was responsive to a magnetic field and found an increase of 104 % in the thermal conductivity of their aligned BN composites.[2] Liu *et al.* used an electric field to induce the orientation of their BN/SiC- epoxy composites to improve the thermal and mechanical properties.[3] The alignment of filler materials in SLA could drastically change the outlook for functional 3D printing that can be used in everyday applications that have not been achieved thus far.

The results in chapter 6 showed that improvements in thermal conductivity and mechanical properties were achieved through the creation of BN hybrids based on platelets of different lateral sizes and aspect ratios. It would be beneficial to study the effects of incorporating a secondary filler material with further reductions in the lateral size and/or aspect ratio, to see if smaller flakes can bridge the gaps between the larger ones more efficiently than what was achieved in chapter 6. It would also be advantageous to improve the printing parameters of the GNP-BN hybrid ink to improve the thermal and mechanical properties similar to what others have reported discussed in chapter 6.[4] This could be achieved by studying the effects of incorporating varied lateral sizes of platelets and optimising the ratio of primary to secondary filler.

Primary research was conducted on the effectiveness of heat dissipation using different geometries of heat sinks for electronic devices in chapter 6. This work could be optimised further by printing components with varied internal geometries, graded structures and complexities that can be accomplished through 3D design and printing.

The outlook for 3D printing 2D material composites is an exciting prospect for an array of applications from thermal management, electronics, biomedical devices etc. Work is still yet to be completed to commercial resins for 3D printing applications

however when this is succeeded it will open up a new route for manufacturing multi-functional parts, quickly and with minimal waste.

8.1 References

[1] A. Harvey *et al.*, "Non-resonant light scattering in dispersions of 2D nanosheets," *Nat. Commun.*, vol. 9, no. 1, p. 4553, 2018.

[2] Z. Lin, Y. Liu, S. Raghavan, K. S. Moon, S. K. Sitaraman, and C. P. Wong, "Magnetic alignment of hexagonal boron nitride platelets in polymer matrix: Toward high performance anisotropic polymer composites for electronic encapsulation," *ACS Appl. Mater. Interfaces*, vol. 5, no. 15, pp. 7633-7640, 2013.

[3] X. Liu *et al.*, "Thermal and electrical properties of nanoparticle oriented Epoxy/BN/SiC composites for superconducting magnet," *IEEE Trans. Appl. Supercond.*, vol. 29, no. 2, 2019.

[4] M. Shtein, R. Nadiv, M. Buzaglo, and O. Regev, "Graphene-Based Hybrid Composites for Efficient Thermal Management of Electronic Devices.," *ACS Appl. Mater. Interfaces*, vol. 7, no. 42, pp. 23725–30, 2015.

9
Appendix

The following appendix describes some of the calculations used within the main thesis and some novel findings that have not been reported on as they are not directly relevant to the thesis story.

9.1 Particle Sizing Data

The thickness of both GNP and BN were measured using AFM, the size of which is reported in table 24.

Table 24 Particle sizing of BN and GNP flakes

2D material	SEM: Lateral size (µm)	Error	AFM: Thickness (nm)	Error	Aspect ratio
GNP	5.74	0.84	153.63	30.71	115.82
BN	7.45	2.25	68.79	7.40	108.30

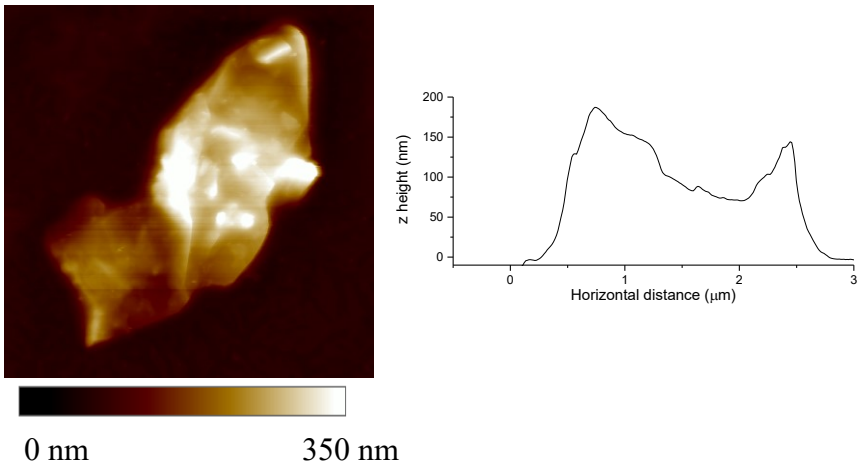

Figure 106 Representative AFM data for GNP nanoplatelets n=14.

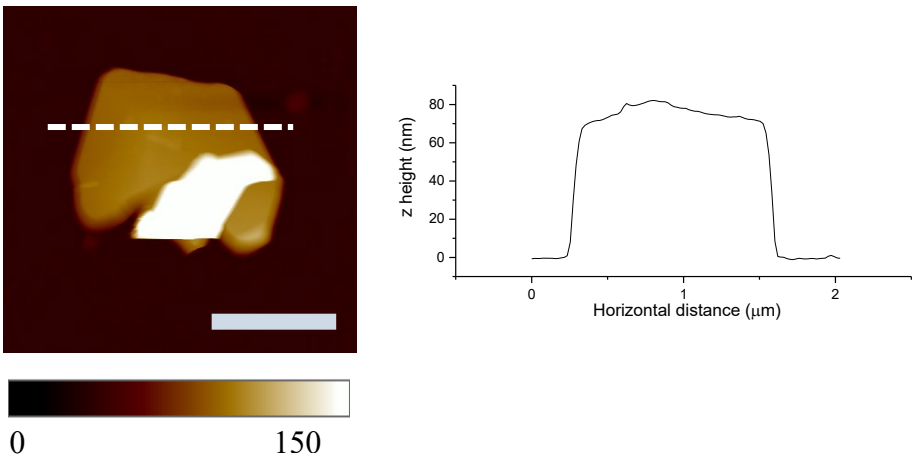

Figure 107 Representative AFM data for BN nanoplatelets n=12.

9.2 Herschel-Bulkley Fitting of Composite Inks

Figures 108 & 109 represent the Herschel-Bulkley fitting of the rheological raw data of all UV inks containing both BN and GNP. The results of which were used for empirical modelling to find τ_y the yield stress discussed in chapter 4.

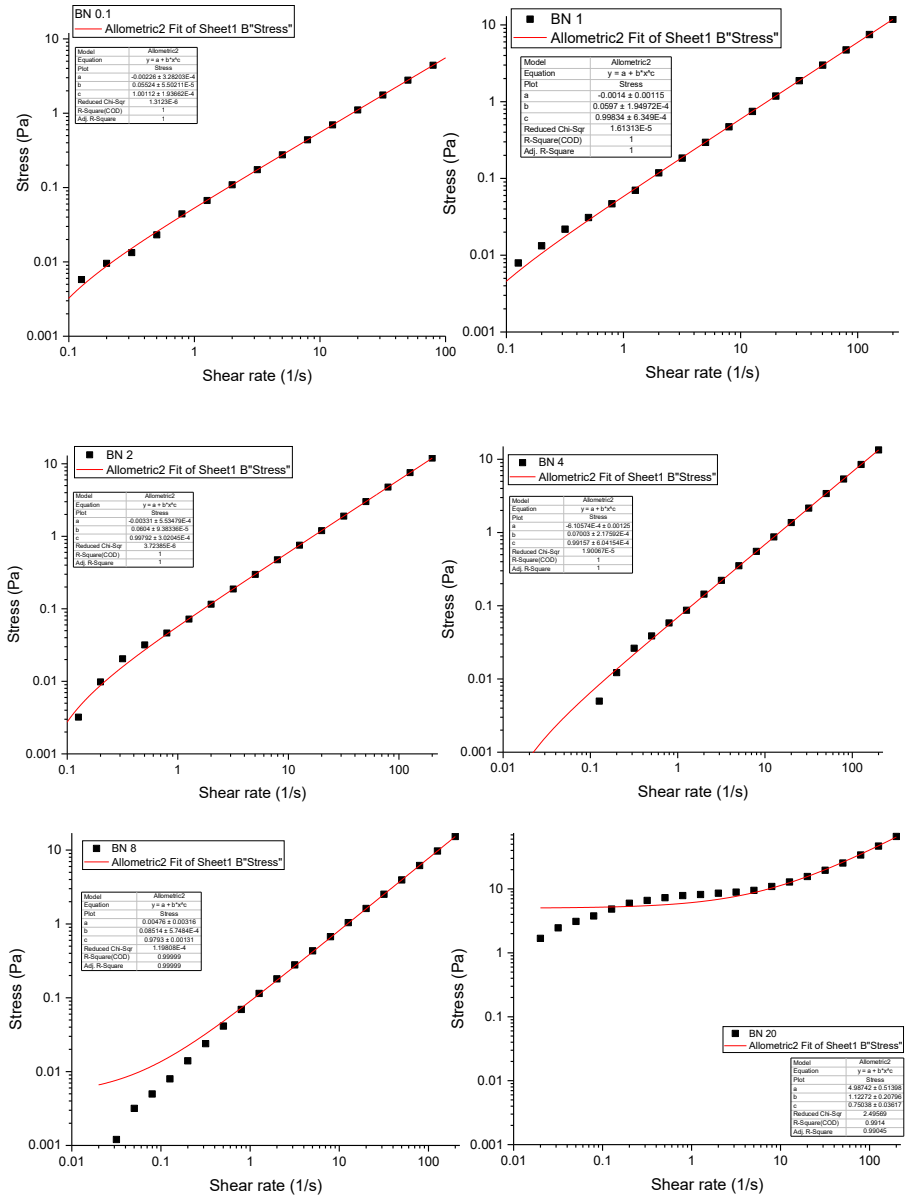

Figure 108 Herschel–Bulkley fitting of all BN-based inks, raw data from flow sweeps.

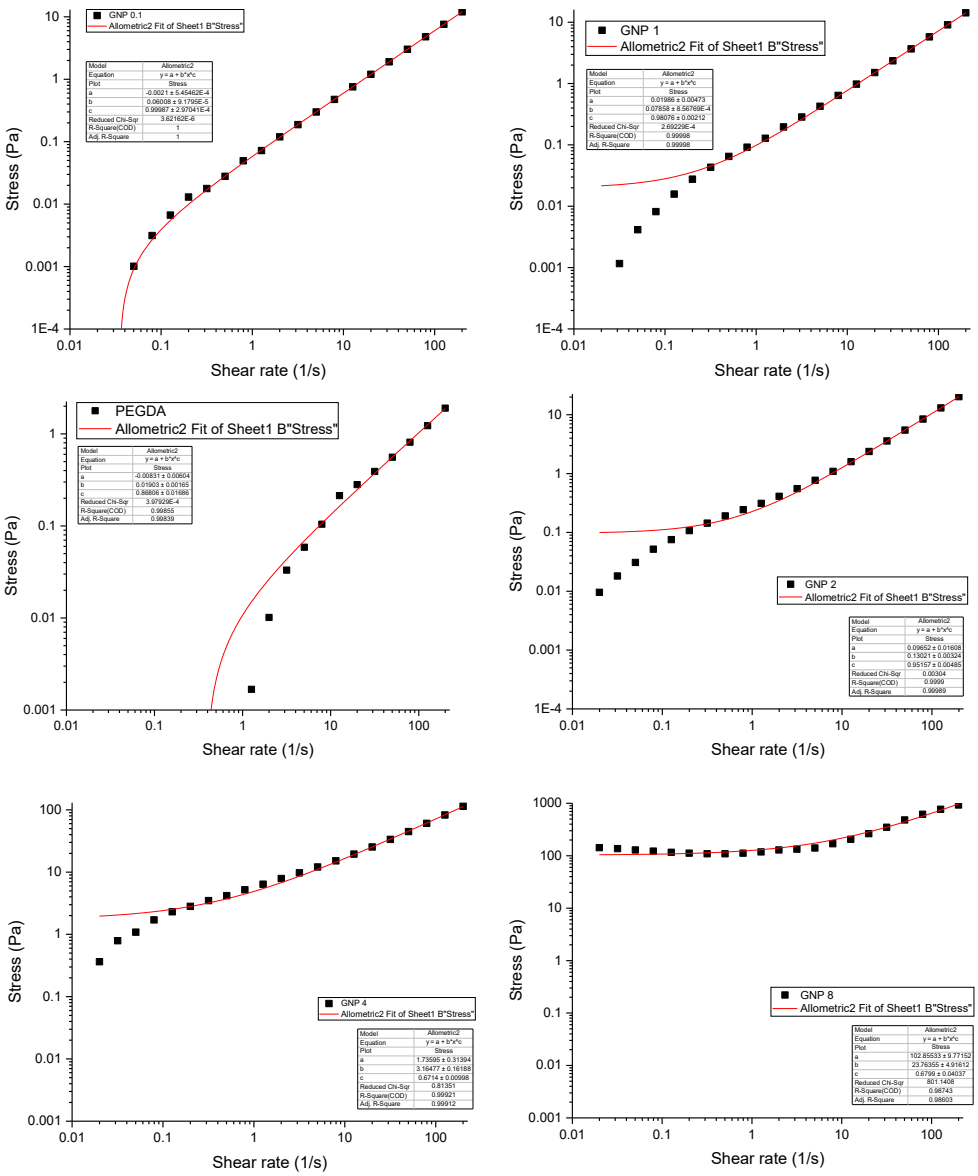

Figure 109 Herschel–Bulkley fitting of PEGDA and GNP-based inks, raw data from flow sweeps.

9.3 Optimum Printing Parameters from the '*Window Panes'* Test

The optimum C_d and D_p were calculated using the window panes test. For inks, containing BN and GNP up to 8 wt. % solid loading the initial values for E_c and D_p were 12 mJ/cm^2 and 3.7 mm respectively. Inks containing solid loadings greater than 8 wt. % had the initial printing parameters 30 mJ/cm^2 and 4.2 mm respectively. The limitations of the SLA printer meant that a maximum D_p of 20 mm could be applied. Therefore, to find the optimum printing parameters of the composite inks the initial D_p of either 3.7 mm or 4.2 mm remained and the E_c was increased in increments of 20 % until the optimum C_d was achieved. These parameters were then applied to the printed parts described in chapters 5 and 6.

Table 25 The calculated D_p and E_c values from the Window Panes test results, derived from Beer-Lamberts equation.

Ink	D_p (mm)	E_c (mJ/cm^2)
BN 0.1	170.3	6.2
BN 1	122.7	4.4
BN 2	126.9	3.3
BN 4	138.7	4.8
BN 8	124.3	4.6
BN 20	3.2	8.0
eBN 20	25.1	0.1
GNP 0.1	170.3	6.2
GNP 1	68.6	8.9
GNP 2	18.3	0.5
GNP 4	73.2	7.3
GNP 8	30.0	2.8

Empirical models for defining scattering behaviour of composite resins in SLA

The cure depth of an SLA resin can be modelled using the following equations:

$$C_d = \frac{2\langle d \rangle}{3\tilde{Q}} \frac{n_0^2}{\Delta n^2} ln\left(\frac{E_0}{E_{crit}}\right) \tag{26}$$

Where $\langle d \rangle$ is the average size of the diameter of the particles, Δn^2 is the square of the difference in refractive index between the particle and resin. E_0 is the energy density and $\tilde{Q}$ is the scattering efficiency term.[1]

Working curve equation:

$$C_d = D_p \ln\left[\frac{E_0}{E_{crit}}\right] \tag{27}$$

Equation (15) is the most widely used equation for predicting the optimum printing parameters to control layer thickness and therefore the speed of print. Alternatively, the working curve equation can be adapted to include the extinction coefficient by:

$$C_d = \left[\frac{1}{\gamma}\right] ln\left(\frac{E_0}{E_{crit}}\right) \tag{28}$$

From the Beer-Lamberts equation the effective extinction coefficient, γ_{eff} can be calculated using the following equation:

$$\gamma_{eff} = 3\tilde{Q}\Delta n^2/2\langle d\rangle n_0^2 \tag{29}$$

$$E_{crit} = E_0 exp(-\gamma C_d), \tag{30}$$

$$C_d = \gamma^{-1} ln\left(\frac{E_0}{E_{crit}}\right) \tag{31}$$

The extinction coefficient can be described by;

$$\gamma = \frac{3}{2}\frac{\phi Q}{\langle d\rangle} \tag{32}$$

Where Q is the extinction coefficient efficiency term, ϕ is the volume fraction of the filler.

After substitution the equation becomes:

$$C_d = \frac{2\langle d \rangle}{3Q} \frac{1}{\phi} ln\left(\frac{E_0}{E_{crit}}\right) \quad (33)$$

These equations have been applied to the experimental data to analyse the effect that ϕ, $\langle d \rangle$ and E_0 have on the scattering effects of printing using nanoplatelets. For all calculations $\langle d \rangle$ is equated to the mean average lateral length of the flakes mentioned in section 4.3. It is important to know that typically the cross-section for scattering uses the diameter of spherical particles.

9.4 Thermal Properties of BN and GNP Composites

Figures 110 & 111 show the thermal diffusivity results from the laser flash method used to calculate the thermal conductivity of the composites. An increase in thermal diffusivity with increasing solid loading of 2D material can be observed from the graph.

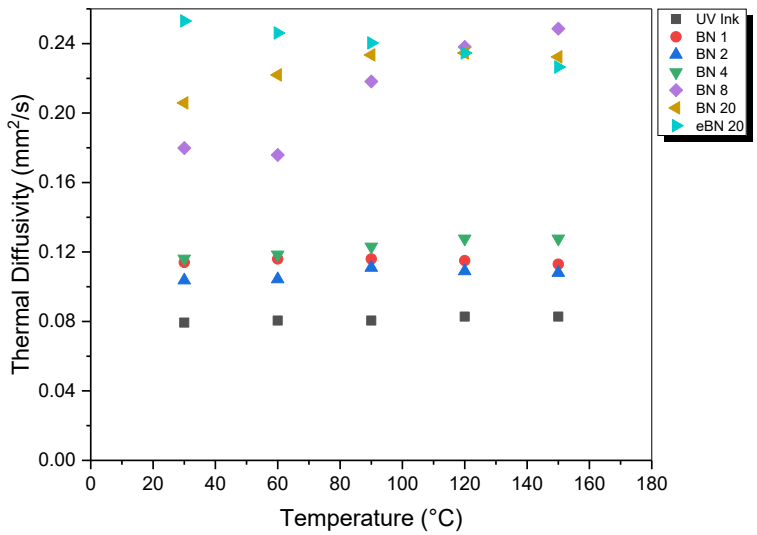

Figure 110 Thermal diffusivity of BN-based inks measured from 30°C to 150 °C.

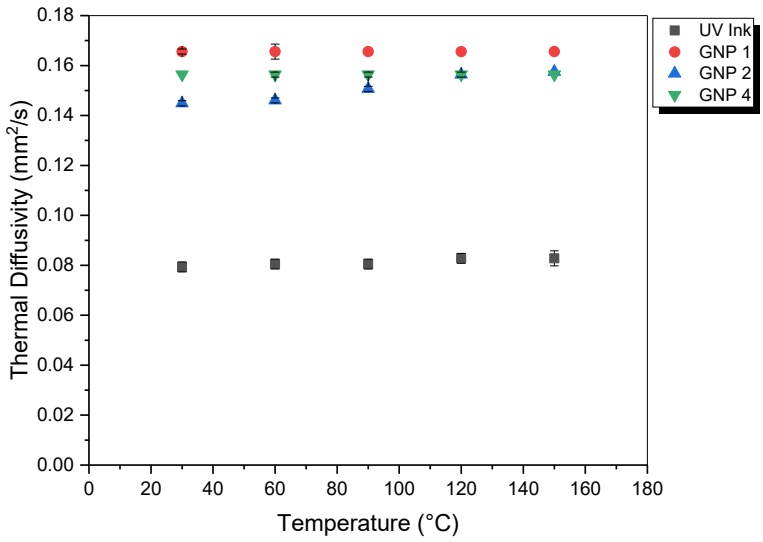

Figure 111 Thermal diffusivity of GNP-based inks measured from 30°C to 150 °C.

Figure 112 describes the coefficient of thermal expansion of the PEGDA resin matrix, GNP 1 composite and BN 20 composite, measured using dilatometry. The CTE describes the degree of expansion of the composite as a result of being heated at constant pressure. The composite containing GNP 1 wt. % had the largest increase in thermal expansion, however, there is little difference in the CTE between the composites, meaning that the addition of 2D materials does not have a significant effect on the CTE at the described solid loadings up to 20 wt. % BN and 1 wt. % GNP.

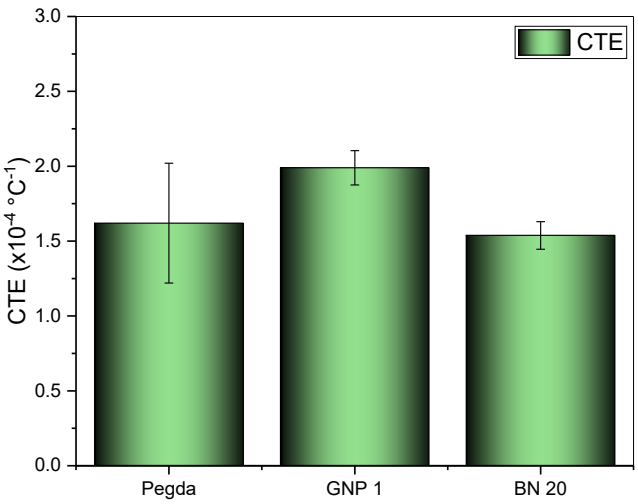

Figure 112 Coefficient of thermal expansion of composites.

Fitting of Agari's equation to BN composites

$$log\,\lambda_c = V_f.C_2.log\,\lambda_f + (1 - V_f).log(C_1\lambda_p)$$

From the table, Equation fitted: $y = mx + c$

Plot is $\log\lambda_c$ vs V_f so y = $\log\lambda_c$ and x = V_f

By expanding the brackets the equation becomes:

$$log\,\lambda_c = V_f.C_2.log\,\lambda_f + log(C_1\lambda_p) - V_f.log(C_1\lambda_p)$$

Re-arranging using the common dominatorV_f:

$$log\,\lambda_c = V_f.[C_2.log\,\lambda_f - log(C_1\lambda_p)] + log(C_1\lambda_p)$$

$$log\,\lambda_c = log(C_1\lambda_p) + V_f.[C_2.log\,\lambda_f - log(C_1\lambda_p)]$$

Re-arrange to the from $y = mx + c$

$$log\,\lambda_c = V_f.[C_2.log\,\lambda_f - log(C_1\lambda_p)] + log(C_1\lambda_p)$$

$$m = log(C_1\lambda_p)$$

$$c = C_2.log\,\lambda_f - log(C_1\lambda_p)$$

The gradient from Figure 113 represents m and the x-intercept is c

Calculating C_1 and C_2 values.

C_1:

$$10^a = C_1\lambda_p$$

$$C_1 = 10^a/\lambda_p$$

C_2:

$$c = C_2.\log\lambda_f - \log(C_1\lambda_p)$$

$$c = C_2.\log\lambda_f - m$$

$$\frac{c - m}{\log\lambda_f} = C_2$$

Using BN 20 wt. % thermal conductivity from the experimental data (1.71 W/m K) C_1 and C_2 are found to be:

m = -0.45331, c = 3.286, λ_f = 400 (W/m K), λ_p= 0.21 (W/m K)

C_1 = 1.677

$C_2 = 1.437$

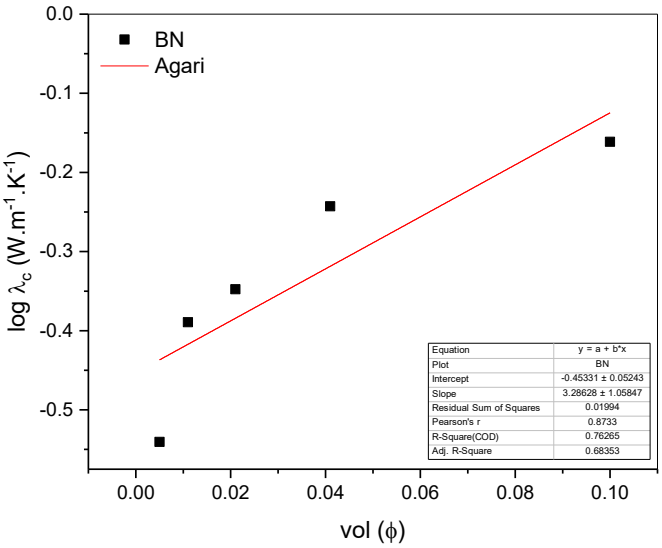

Figure 113 Agari's equation applied to the thermal conductivity of BN composites to find the C_1 and C_2 values.

The glass transition temperature values for all GNP and BN-based composites discussed in chapter 5 are listed in table 26.

Table 26 Glass transition temperatures (°C) of all composites containing GNP and BN.

Filler concentration (wt. %)	T_g of BN composites (°C)	T_g of GNP composites (°C)
1	-36.83	-34.62
2	-35.72	-25.75
4	-35.36	-24.86
8	-35.65	-23.61
20	-20.21	-

9.5 Properties of Hybrid Composites

Figure 114 displays the SEM image of the GNP nanoplatelets after exfoliation. These nanoplatelets are used in chapter 6 for hybrid 7.

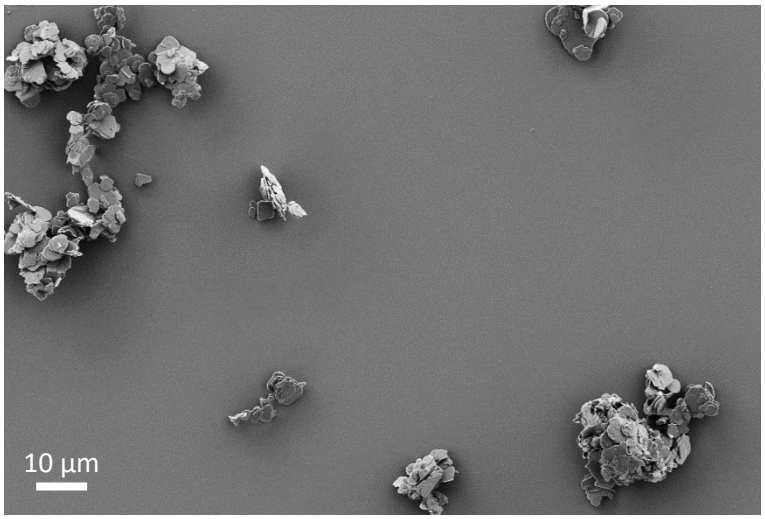

Figure 114 SEM image of eGNP nanoplatelets

The Window Panes test results describe the C_d of each of the hybrids with increasing E_0 (figure 115). The graph shows that hybrids with high amounts of GNP produce a smaller C_d than hybrids that only containing BN and eBN. Hybrids 1, 3 and 7 all produced a suitable layer thickness for printing using SLA. Hybrids 2, 4, 5 and 6 fell apart during measurements as they were too delicate. Therefore from the results Hybrids, 1 and 7 were chosen for further studies that have been discussed in chapter 6

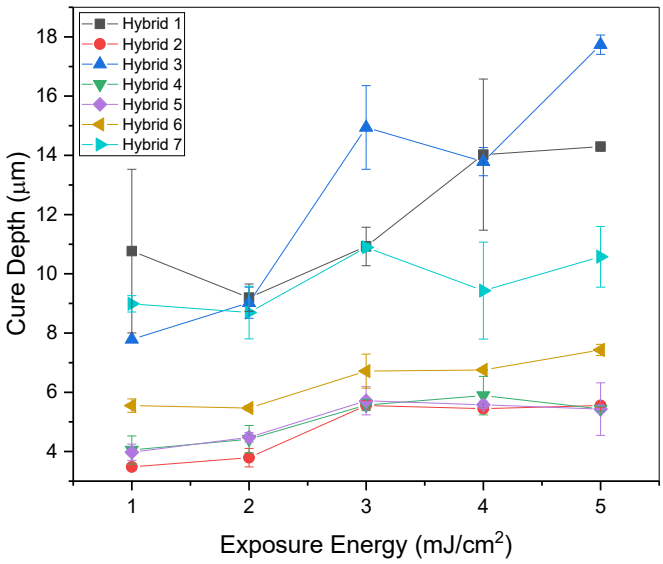

Figure 115 Working curve of all iterations of hybrids from the window panes test.

Figure 116 describes the mass loss as a percent of all of the hybrid composites when heated in an inert atmosphere to 800 °C.

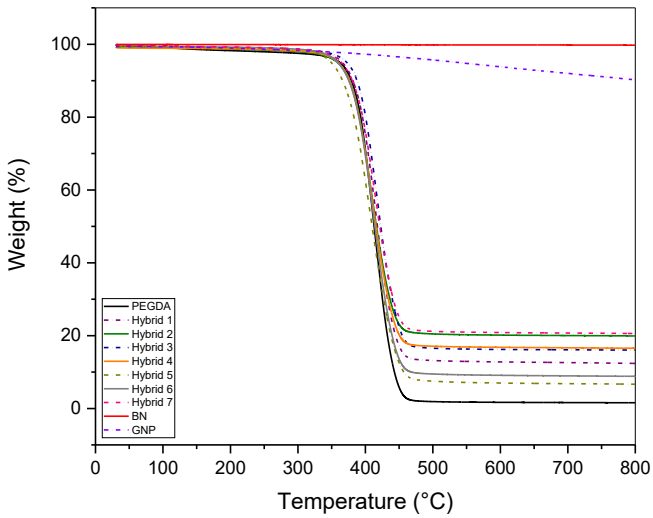

Figure 116 TGA results showing change in mass over temperature of all hybrid compositions.

The results displayed in figure 117 describes the T_g of each of the hybrid composites, the influence of GNP and BN has little effect on the glass transition temperature as this is dominated by the polymer PEGDA.

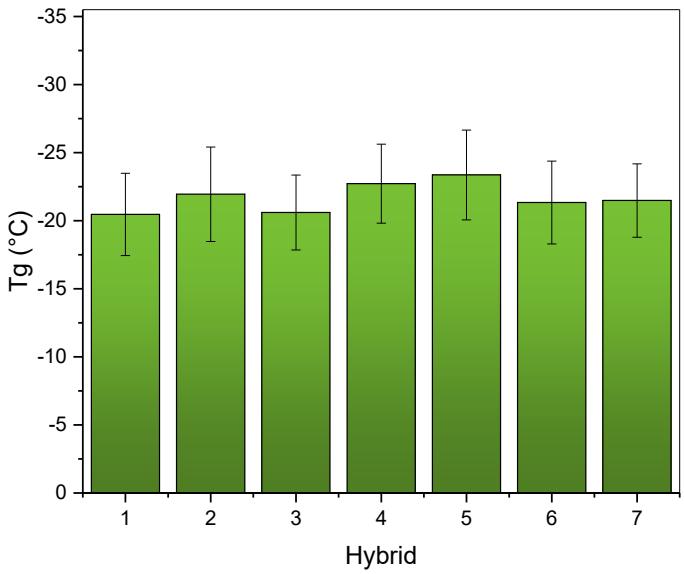

Figure 117 Glass transition temperature of hybrid composites.

Figures 118 & 119 display the arrangement of BN nanoplatelets in the PEGDA matrix visualised through CT data. The highlighted regions show the presence of large air

pockets, the largest void has been measured to be 167 µm in diameter. The scans show that the BN flakes (white regions) have been dispersed evenly throughout the printed part showing going homogeneity

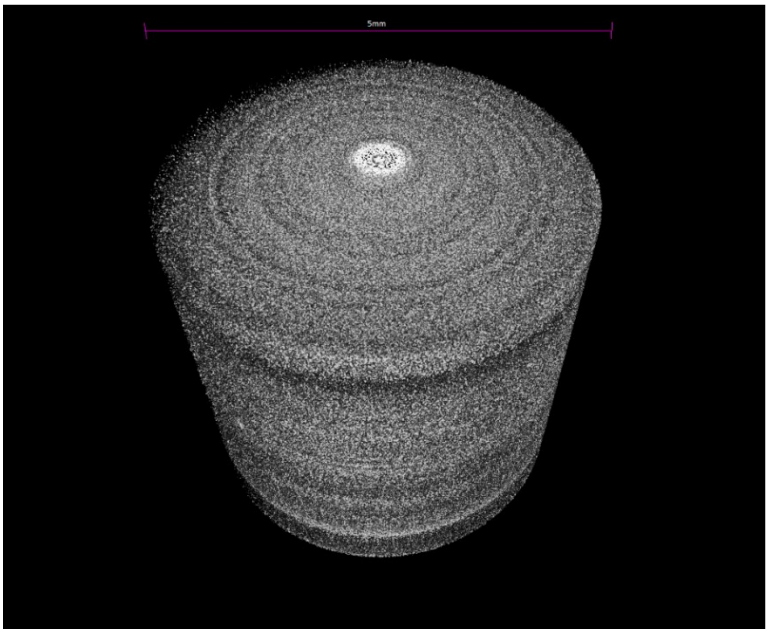

Figure 118 CT data of Hybrid 1. The white areas represent the BN flakes dispersed within the polymer matrix (black areas) scale bar is 5 mm.

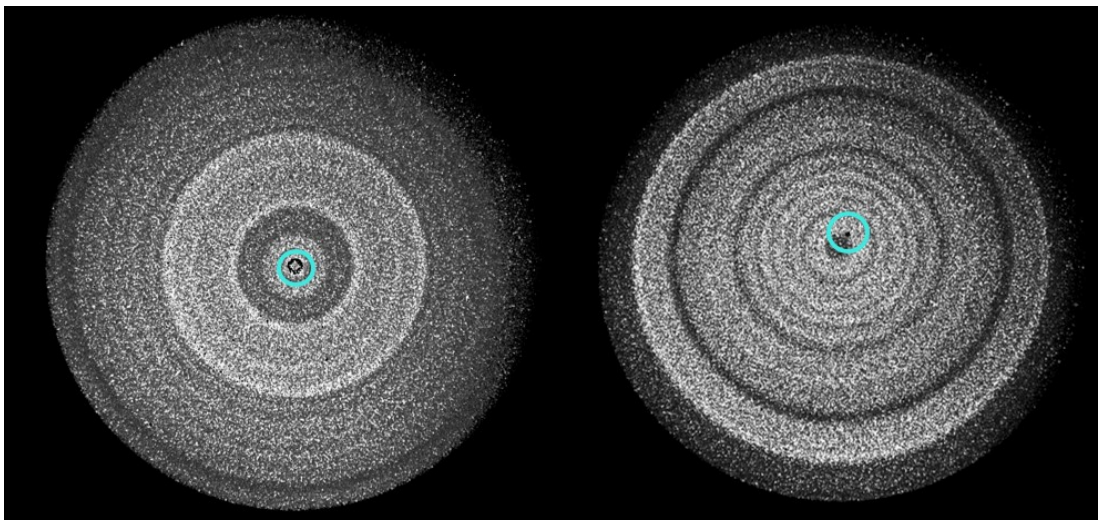

Figure 119 CT data of Hybrid 1, the blue circles highlight the voids within the sample. The white areas represent the BN flakes dispersed within the polymer matrix (black areas).

Figure 120 describes the input power required to heat the rGO aerogel to specific temperatures using joule heating. This data was then applied to the heat dissipation results discussed in chapter 6.

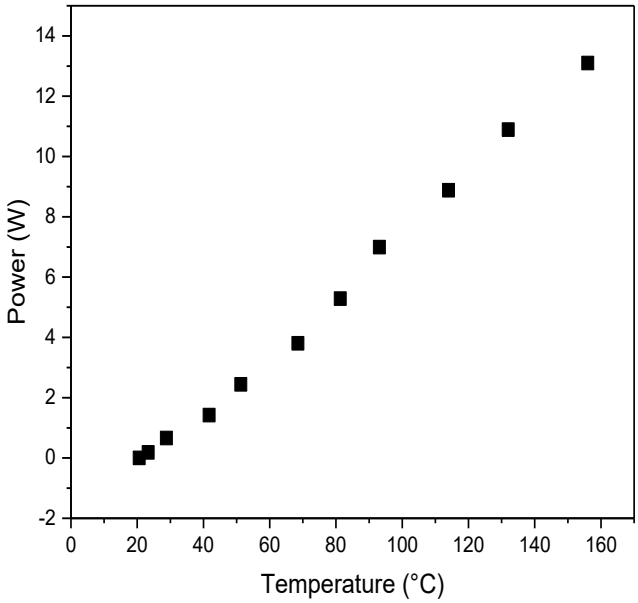

Figure 120 Joule heating of rGO Aerogel

Visible heat gradients of a printed polar bear heated on top of the rGO aerogel printed using hybrid 1 ink.

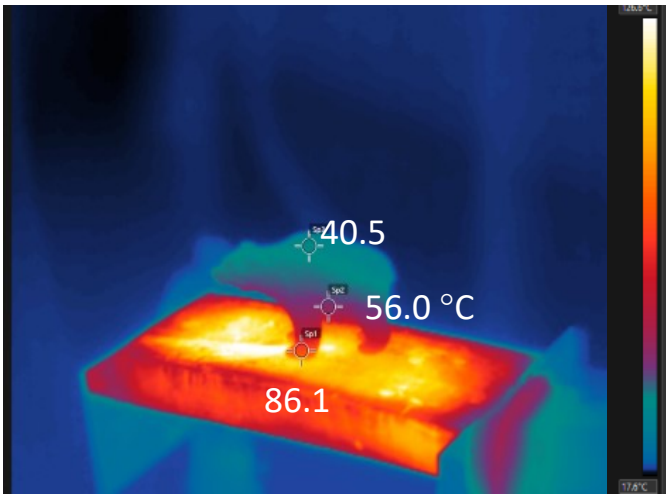

Figure 123 Image of 3D printed BN polar bear on rGO aerogel showing the difference in temperature gradients.

9.6 References

[1] M. L. Griffith and J. W. Halloran, "Scattering of ultraviolet radiation in turbid suspensions," *J. Appl. Phys.*, vol. 81, no. 6, pp. 2538–2546, 1997.